Stable High-Order Finite-Difference Interface Schemes with Application to the Richtmyer-Meshkov Instability

Thesis by

Richard Michael Jack Kramer

In Partial Fulfillment of the Requirements

for the Degree of

Doctor of Philosophy

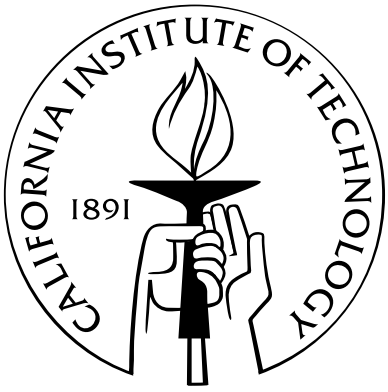

California Institute of Technology

Pasadena, California

2009

(Defended March 11, 2009)

Acknowledgments

I must begin these acknowledgements with my advisor, Dale Pullin, for his support and encouragement through the last five years as this thesis has taken shape. There was little question when I arrived at Caltech that I wanted to work with Dale, and it proved to be a good academic relationship. Next, I must acknowledge Carlos Pantano's role, being almost a coadvisor for the first two years of my research, and continuing his involvement even after moving to UIUC, and taking me under his wing at my first APS conference. On a number of occasions working through the interface problems, he provided the final breakthrough after I had spent many weeks banging my head on my desk. I thank Dale for his patience as we struggled through these problems!

I must also acknowledge Dan Meiron for his advice and direction with the Richtmyer-Meshkov simulations, and for the use of his concept for the linearized form of the Navier-Stokes equations. Thanks also go to Professors Joe Shepherd and Tony Leonard for serving on both my candidacy and thesis committees.

Special thanks must go to Gustavo Wouchuk, for his enthusiastic communications and invaluable assistance in applying his models of the Richtmyer-Meshkov instability to my results. His contribution greatly improved the quality of the conclusions I was able to draw from my simulations.

On a more personal level, there are a number of students at Caltech who have become good friends and made my time here more enjoyable. Shannon Kao, Lydia Ruiz and Sally Bane deserve particular mention. I would also like to thank Derceto Ltd., for letting me leave to pursue my Ph.D, hiring so many of my friends from the University of Auckland (and then my brother too), and then sending them to the US occasionally so I could see them more frequently than I otherwise would have.

I must also thank my family—Ma, Dad, Jason, Granny and Grandpa—for their endless

support from the other side of the Pacific ocean. The same goes to my in-laws, who accepted me right into their family and gave me a home away from home in Albuquerque.

Special acknowledgement has to go to my wife, Sharlotte. She is intertwined with my Caltech experience, right from orientation where we first met as bright-eyed Aeronautics grad students. Her constant love, support, and baking reassure me that I am doing what I was meant to do. In that same respect, I thank God for the insight to study this tiny aspect of His creation, and for the strength I needed to get through all the difficult times. I thank Him also for Christ Church of Pasadena, which added another dimension to my life here in Los Angeles.

Formal thanks must go to the estate of Sir William Pickering, for providing the fellowship for my first year at Caltech. I was fortunate to have met Sir William at a ceremony dedicating a new science building at my high school, Westlake Boys High. His presentation there first brought Caltech to my attention as a possibility for graduate school—and almost exactly one year later, within days of his death, I heard I had been admitted, and with the fellowship bearing his name.

This work was supported by the Advanced Simulation and Computing (ASC) program at Caltech, funded by the Department of Energy, under subcontract no. B341492 of DOE contract W-7405-ENG-48.

Abstract

High-order adaptive mesh refinement offers the potential for accurate and efficient resolution of problems in fluid dynamics and other fields where a wide range of length scales is present. A critical requirement for the interface closures used with these methods is stability in the context of hyperbolic systems of partial differential equations.

In this work, a class of energy-stable high-order finite-difference interface closures is presented for grids with step resolution changes in one dimension. Asymptotic stability in time for these schemes is achieved by imposing a summation-by-parts condition on the interface closure, which is thus also nondissipative. Interface closures compatible with interior fourth- and sixth-order explicit, and fourth-order implicit centered schemes are presented. Validation tests include linear and nonlinear problems in one dimension and in two dimensions with tensor-product grid refinement.

A second class of stable high-order interface closures is presented for two-dimensional cell-centered grids with patch-refinement and step-changes in resolution. For these grids, coarse and fine nodes are not aligned at the mesh interfaces, resulting in hanging nodes. Stability is achieved by again imposing a summation-by-parts condition, resulting in non-dissipative closures, at the cost of accuracy at corner interfaces. Interface stencils for an explicit fourth-order finite-difference scheme are presented for each geometry. Validation tests confirm the stability and accuracy of these closures for linear and nonlinear problems.

The Richtmyer-Meshkov instability is investigated using a novel first-order perturbation of the two-dimensional Navier-Stokes equations about a shock-resolved base flow. The computational domain is efficiently resolved using the one-dimensional fourth-order interface scheme. Results are compared to analytic models of the instability, showing agreement with predicted asymptotic growth rates in the inviscid range, while significant discrepancies are noted in the transient growth phase. Viscous effects are found to be poorly predicted by existing models.

Contents

List of Figures

List of Tables

Chapter 1

Introduction

Adaptive mesh refinement (AMR) methods are increasingly being used to simulate problems in fluid dynamics and other physical systems, as local refinement of the computational grid allows efficient resolution of the wide range of length scales often present in these problems. However, for a given truncation error, it has been shown by Jameson (2003) that high-order uniform methods can be more computationally efficient than standard second-order AMR, due to the greater simplicity of their data structures. High-order AMR methods are therefore sought to combine the efficiency of resolution offered by local mesh refinement with the accuracy of high-order methods, but depend on development of suitable interface closures. This thesis describes such a class of high-order finite-difference interface schemes, suitable for systems of hyperbolic partial differential equations where time stability and numerical dissipation are critical concerns, and demonstrates the potential of high-order AMR by application to the Richtmyer-Meshkov instability.

1.1 Local Mesh Refinement

A challenge for adaptive mesh refinement methods is proper treatment of interfaces at step-changes in grid resolution. For problems sensitive to numerical dissipation, like turbulent flows or wave propagation, stability and accuracy of the interface treatment are critical concerns (Jameson, 2003). Long-time integration of these problems is dependent on the error of the numerical approximation remaining bounded for the duration of the simulation, while avoiding excessive artificial dissipation of important solution features (Carpenter et al., 1994). It is for this reason that centered finite-difference schemes are often preferred for interior regions of the computational domain; the challenge then lies in dealing with boundary

and interface regions where the grid is nonuniform and standard centered schemes cannot be applied.

The standard approach to the interface problem has been to utilize interpolation across grid interfaces, choosing coefficients that satisfy local stability criteria. Recent examples include the second-order method of Choi et al. (2004), which uses quadratic interpolation to avoid wave reflection at interfaces, while the second-order finite-volume method of Lötstedt et al. (2002) and Ferm and Lötstedt (2004) introduces the minimal numerical dissipation necessary for stability of the interfaces. Higher-order interpolation-based schemes, such as those of Gerritsen and Olsson (1998) and Sebastian and Shu (2003), preserve stability at the cost of significant artificial numerical dissipation.

A widely used method for adaptive mesh refinement is that of Berger and Oliger (1984) and Berger and Colella (1989). This method is characterized by a finite-volume–type hierarchical partition of the computational domain, using a recursive patch-based algorithm to iterate across refinement levels. In Berger and Colella, a computationally efficient interpolation/restriction operation transfers information between guard cells at patch boundaries. In the implementation of this algorithm by Pantano et al. (2007), the second-order accurate hybrid centered-difference/weighted essentially nonoscillatory (WENO) method of Hill and Pullin (2004) is used for spatial derivative approximation, relying on the WENO method to provide sufficient dissipation for stability across grid interfaces. The efficiency of the Berger and Colella algorithm notwithstanding, in this work only "flat" refinements of the computational domain are considered, with no sense of an underlying coarse grid remaining in refined regions.

Stability properties of interface stencils are typically analyzed by an eigenvalue analysis using the rigorous GKS theory of Gustafsson et al. (1972), examples of which include Ciment (1971, 1972) and Berger (1985). It was shown by Trefethen (1985) that stability of a single interface does not guarantee stability of a grid composed of multiple interfaces. Interactions between multiple interfaces can lead to algebraic, and possibly even exponential, growth of perturbations even though each individual interface is locally stable. The only rigorous approach to the development of stable multiple-interface treatments is therefore the use of a global stability criteria.

Energy-stable methods are desirable as their global stability can often be proven analytically. Another feature of these methods is their tendency to self-diagnose the resolution

requirement for the problem under consideration, as numerical reflections are generated at interfaces as features that are well supported on the fine grid side propagate to an under-resolved coarse grid. This and other properties of energy-stable methods that are not overly dissipative were identified by Browning et al. (1973); Vichnevetsky (1987); Cathers and Bates (1995). An example of an energy-stable second-order accurate interface scheme is that of Collino et al. (2003).

For ease of analysis, stability is almost invariably discussed in terms of the linear advection equation. Essential to the resulting stability criteria is directional independence; the method of Lötstedt et al. (2002), for example, ensures stability in general only for waves traveling along specific directions, a serious limitation when dealing with systems of partial differential equations like the compressible Euler equations, which support waves traveling in multiple directions simultaneously.

1.2 Summation-by-Parts Operators

As first presented by Kreiss and Scherer (1974), a semidiscrete finite-difference approximation to a partial differential equation (PDE) can be made to satisfy a summation-by-parts (SBP) rule, analogous to integration by parts for the continuous equation. The original context of this method was for boundary stencils, which ensured that energy transfer to and from the computational domain was confined to the boundaries and prohibited energy growth (or decay) elsewhere in the domain. It was also shown that accuracy must drop at the boundary by one order compared to the interior scheme, though this does not affect the convergence rate of the overall scheme as demonstrated by Gustafsson (1975). High-order boundary closures satisfying the SBP criterion were presented by Strand (1994) and Carpenter et al. (1994), with the final component for a stable high-order approximation provided by Carpenter et al. in the simultaneous approximation term (SAT) penalty method for imposing the boundary condition.

Finite-difference approximations that satisfy the summation-by-parts criterion are easily shown to be stable in an energy norm, satisfying both the GKS definition of stability and showing asymptotic stability in time (Carpenter et al., 1994; Abarbanel and Chertock, 2000). Both definitions of stability must be satisfied to prevent nonphysical growth of the numerical solution in hyperbolic problems (Carpenter et al., 1993). The SBP condition is

also a global criterion: since it is only the boundaries that influence the energy balance, if an interface is stable in the summation-by-parts sense, any number of interfaces will also be stable as each makes no contribution to the global energy balance.

The focus of development of SBP operators has been primarily on boundary schemes. At grid interfaces, Nordström and Carpenter (1999) propose a high-order method that uses a penalty-type technique to match the function value and first derivative at a common interface point, analogous to the SAT boundary method. This assumes a vertex-type mesh, compared to the cell-centered finite-volume–type mesh topology considered in this work that avoids overlapping nodes under refinement. The penalty method introduces some numerical dissipation, but has been applied successfully to fluid dynamics and electromagnetic problems where this effect was found to be small (Nordström and Gustafsson, 2003).

In this thesis, customized high-order stencils are designed for the points near grid interfaces such that the summation-by-parts criterion is satisfied across the entire computational domain, thus ensuring stability without introduction of artificial dissipation.

1.3 The Richtmyer-Meshkov Instability

An interesting application of the interface schemes developed in this thesis, demonstrating the power and efficiency of high-order adaptive mesh refinement, is the Richtmyer-Meshkov (RM) instability. This instability, named for the foundational work on this problem by Richtmyer (1960) and Meshkov (1969), occurs when a shock collides with a perturbed interface between fluids of different density. It is similar to the Rayleigh-Taylor instability that occurs at the perturbed interface of two fluids of different densities under acceleration due to gravity. Only the planar reflected-shock case of the RM problem will be considered here, essentially assuming that the incident shock travels from the light fluid into the heavy fluid in a two-dimensional Cartesian geometry.

The initial growth of the interface perturbation is driven by vorticity deposited at the interface by baroclinic torque, a result of the misalignment of the pressure gradient across the shock with the density gradient across the interface. The focus of this work will be on the early-time evolution of the RM instability, which exhibits damped oscillation in the growth rate (e.g., Yang et al., 1994), the result of waves trapped between the reflected and transmitted shocks. At later times, the perturbation grows larger, distorting the interface

and leading to formation of "bubbles" and "spikes" that excite secondary instabilities and eventually result in chaotic mixing of the light and heavy fluids (Zhang and Sohn, 1997; Collins and Jacobs, 2002; Hill et al., 2006; Herrmann et al., 2008).

The simplest model of the Richtmyer-Meshkov instability is the impulsive model of Richtmyer (1960). This models the shock impact on the contact discontinuity as an impulsive acceleration of a sinusoidally perturbed interface of zero thickness between two inviscid incompressible fluids. For small amplitude perturbations, this predicts a linear growth rate in time for the interface amplitude, which was validated by Richtmyer's own simulations. This has been shown to agree at least qualitatively with experimental investigations of the instability, first by Meshkov (1969) and by many authors subsequently for weak shocks (see for example Brouillette and Sturtevant, 1994; Jones and Jacobs, 1997; Collins and Jacobs, 2002), where the linear growth rate is achieved in an asymptotic sense. For stronger shocks, however, the assumptions of the impulsive model break down and the growth rate is no longer accurately predicted.

More advanced models of the instability fall generally into one of two categories. The first covers analytic improvements to the simple impulsive model, where its various assumptions are generalized to improve the growth rate prediction under certain conditions. Those considered in this study include the effect of a distributed initial interface (Mikaelian, 1991; Brouillette and Sturtevant, 1994), viscosity (Mikaelian, 1993; and in more advanced form, Carlès and Popinet, 2001), and finite proximity of the reflected and transmitted shocks (Lombardini, 2008).

Models in the second category are based on linearization of the Euler equations about the 1-D Riemann solution of the shock-interface problem in the small amplitude approximation. These obtain estimates for the asymptotic growth rate either (semi-) analytically by series expansion (Wouchuk and Nishihara, 1997, and Wouchuk, 2001a, are considered here) or by numerical solution (Yang et al., 1994). It is this latter approach that leads into the method used for the simulations presented in this work.

A fundamental challenge encountered with simulation of the Richtmyer-Meshkov instability is the numerical treatment of the shocks in the domain. Since the shock thickness is on the order of the gas mean free path length, which is two to three orders of magnitude smaller than the next smallest scale in the simulation, full resolution of the shock structure has been impossible. Furthermore, because of the weak influence of viscosity in most prob-

lems of interest, an inviscid fluid assumption is often made. In both cases, shock capturing or tracking methods are generally used (e.g., Hill et al., 2006; Herrmann et al., 2008), and so potentially suffer first-order error at the shock (Engquist and Sjögreen, 1998). This is of relatively little concern for these second-order accurate simulations, however.

Examples of high-order simulation of the Richtmyer-Meshkov instability are limited, in part for this reason. The recent work of Yee and Sjögreen (2007) uses a sixth-order filter method in their Navier-Stokes simulation, and as far as the author is aware, no attempt has been made to resolve the full Navier-Stokes shock structure in the context of an RM simulation until this work. This is made possible by the high-order grid-interface closures developed in Chapter 2, which allow efficient resolution of the shock and thin contact region by multiple levels of local refinement.

1.4 Thesis Outline

This thesis is divided into three main chapters, each covering a major topic: Chapter 2 describes the development of the 1-D finite-difference interface schemes, based on Kramer et al. (2007), Chapter 3 describes the 2-D interface schemes for patch-refined grids, and Chapter 4 describes the investigation of the linearized Richtmyer-Meshkov instability conducted using the numerical schemes from Chapter 2.

Chapter 2 introduces the theory of finite-difference schemes and stability, with supplemental material provided in Appendix A. This forms a basis for both the 1-D interface schemes derived in Chapter 2 and for the 2-D theory introduced in Chapter 3. Results of validation tests are given following presentation of the interface schemes in both chapters, using similar test problems. Detailed derivations for these test problems are shown in Appendices E and F. Algorithms for implementation of the interface schemes are described in Appendix C and matrices for the schemes are available in electronic form with this thesis from the Caltech Library. Chapter 4 introduces the theory of the Richtmyer-Meshkov instability and describes the numerical method for its simulation before presenting the results and a discussion of interesting findings in Sections 4.6–4.7. Concluding remarks, including thoughts on future investigations, are presented in Chapter 5. Each chapter is introduced with a brief overview of its content.

Chapter 2

The 1-D Interface Problem

This chapter describes the one-dimensional grid interface problem and its solution. Section 2.1 introduces the spatial finite-difference approximation and the interface problem geometry, which is placed in the context of a hyperbolic partial differential equation in time in Section 2.2. This presents the stability problem for long-time integration, and the conditions the interface scheme must satisfy to be stable. Sections 2.3–2.4 describe the interface solutions, followed in Section 2.5 by a discussion of their properties. Finally, Section 2.6 shows the results from a range of validation problems. Appendix C describes briefly an algorithm for implementation of this scheme.

The content of this chapter largely follows Kramer et al. (2007), but with considerable extension to the stability theory and analysis in Section 2.2. More detailed convergence results are also presented in Section 2.6 than appeared in the original paper. Notation has been updated where necessary for consistency with Chapter 3.

2.1 Domain Discretization

2.1.1 Finite-Difference Schemes

Consider a function $u(x)$, evaluated at discrete points or nodes x_j on a computational domain with $u(x_j) = u_j$. The derivative of this function at a particular point x_i may be approximated to order s by the explicit finite-difference scheme

$$\frac{\mathrm{d}u_i}{\mathrm{d}x} = \frac{1}{\Delta x} \sum_{j=i-k_L}^{i+k_R} q_{ij} u(x_j) + O(\Delta x^s), \tag{2.1.1}$$

where Δx is a discretization scale related to the spacing between the points x_j, q_{ij} are weights for each function value, and the stencil has a width of $k_L + k_R$ points. For a centered difference scheme of order s, the minimum-width stencil has $k_L = k_R = s/2$, giving a total width $s + 1$. Alternatively, the derivative at x_i may be approximated using adjacent derivative values also with the implicit (compact) finite-difference scheme

$$\sum_{j=i-k_L}^{k_R} p_{ij} \frac{\mathrm{d}u_j}{\mathrm{d}x} = \frac{1}{\Delta x} \sum_{j=i-k_L}^{i+k_R} q_{ij} u(x_j) + O(\Delta x^s), \tag{2.1.2}$$

where p_{ij} are additional weights for the derivative values. For the classical centered finite-difference schemes encountered in this work, where nodal spacing is uniform, the simplified form of equation (2.1.2),

$$\begin{aligned} &p_1 \frac{\mathrm{d}u_{i-1}}{\mathrm{d}x} + \frac{\mathrm{d}u_i}{\mathrm{d}x} + p_1 \frac{\mathrm{d}u_{i+1}}{\mathrm{d}x} \\ &\quad = \frac{1}{\Delta x} \Big(q_1(u_{i+1} - u_{i-1}) + q_2(u_{i+2} - u_{i-2}) + q_3(u_{i+3} - u_{i-3}) \Big), \end{aligned} \tag{2.1.3}$$

is used with the coefficient values given in Table 2.1 (Lele, 1992).

Scheme	p_1	q_1	q_2	q_3
Explicit 2nd-order	0	1/2	0	0
Explicit 4th-order	0	2/3	−1/12	0
Implicit 4th-order	1/4	3/4	0	0
Explicit 6th-order	0	3/4	−3/20	1/60

Table 2.1: Coefficients of classical centered finite-difference schemes for equation (2.1.3)

For a domain of N nodes, the function values u_j, $j = 1, \ldots, N$, may be expressed as a vector $\mathbf{u}$ of length N, and equation (2.1.2) may be written in matrix form

$$P \frac{\mathrm{d}\mathbf{u}}{\mathrm{d}x} = \frac{1}{\Delta x} Q\mathbf{u} + O(\Delta x^s), \tag{2.1.4}$$

where $P = \{p_{ij}\}$ and $Q = \{q_{ij}\}$ are $N \times N$ banded matrices. The matrix Q is generally a Toeplitz matrix, except at boundaries and grid interfaces. For an explicit scheme, P can be chosen as the identity matrix.

2.1.2 Grid Interface Description

For a uniform grid discretization, the schemes of Table 2.1 are adequate to define an accurate derivative approximation. We are interested here in grids where there are step changes in resolution, where those schemes cannot be applied.

Consider a spatial domain that has been partitioned into M blocks, each uniformly discretized into N_m node-centered cells of size Δx_m. The interface between adjacent blocks m and $m+1$ is characterized by the ratio

$$r_m = \frac{\Delta x_{m+1}}{\Delta x_m}, \tag{2.1.5}$$

and is identified with the notation 1:r_m for the mth interface. For the 1-D case, there is no restriction for r_m to be an integer ratio. This discretization of the domain yields a total of $N = \sum_{m=1}^{M} N_m$ nodes at locations x_i, with $i = 1, \ldots, N$. Figure 2.1 depicts a portion of such a domain, where nodes have been numbered locally relative to an origin at the interface with positions x_j given by

$$x_j = \begin{cases} \Delta x(\frac{1}{2} + j), & j < 0, \\ r\Delta x(\frac{1}{2} + j), & j \geq 0. \end{cases} \tag{2.1.6}$$

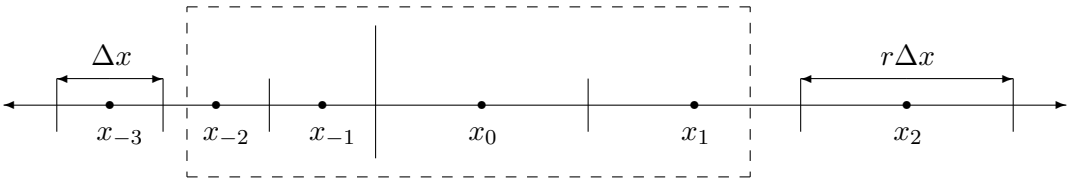

Figure 2.1: Diagram of the 1-D grid interface geometry: the four-point interface region lies inside the dashed box, with the resolution change occurring between nodes x_{-1} and x_0. The node numbering scheme is local relative to the interface region.

The matrix description of the finite difference scheme (2.1.4) may be applied to the block-refined domain, where now Δx refers to the smallest discretization across all blocks,

$$\Delta x = \min_m \Delta x_m. \tag{2.1.7}$$

It is the aim of this work to determine appropriate values of the weights p_{ij} and q_{ij} for the nodes near an interface, such that certain stability criteria to be discussed in Section 2.2 are satsified; away from interfaces, the standard stencils from Table 2.1 may be used because the grid is locally uniform.

2.1.3 Tensor-Product Grids

The one-dimensional interface formulation may also be applied to certain higher-dimensional grids, where refinement is designed in such a way that the grid may be represented as a tensor product of 1-D grids. These grids are essentially one dimensional in character, and are characterized by grid cells of varying aspect ratio. An example of a 2-D tensor-product grid is shown in Figure 2.2, along with a two-dimensional patch-refined grid of the type usually encountered in adaptive mesh refinement schemes. The patch-refined grid is fundamentally different because under refinement, nodes are no longer aligned on Cartesian lines across interfaces, resulting in a nonconforming mesh. This problem is discussed in Chapter 3.

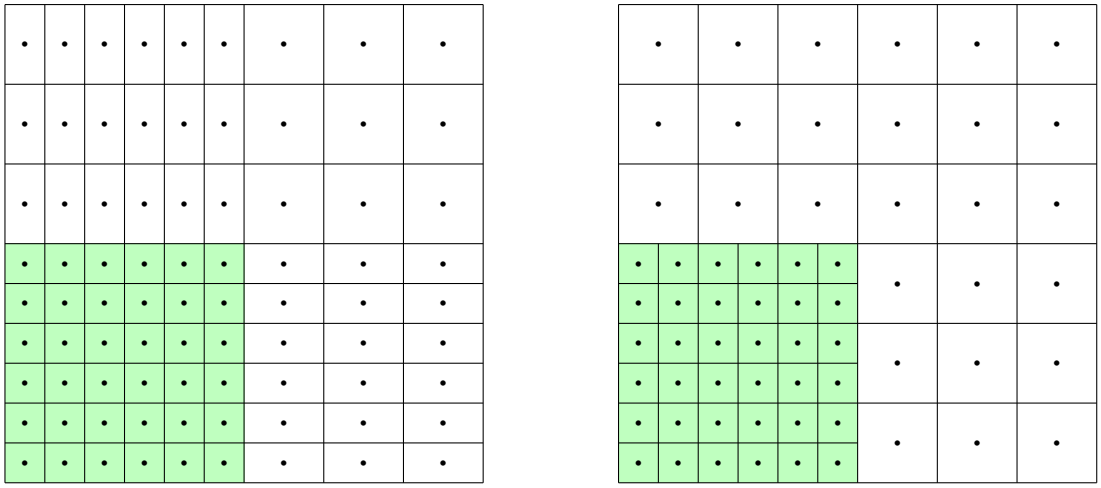

(a) tensor product (b) patch refined

Figure 2.2: Comparison of 2-D grid refinement schemes: for a refined region in the lower-left quadrant, (a) shows the tensor-product grid that remains essentially one dimensional in character in each direction, while (b) shows a true 2-D patch-refinement scheme.

2.1.4 Accuracy Conditions

In general, the weights p_{ij} and q_{ij} may be determined by order conditions derived from Taylor series expansions of the zth-degree polynomial function

$$f_z(x) \equiv x^z, \tag{2.1.8}$$

about the point x_i, in terms of its value at neighbouring points x_j. For a derivative approximation of order s, the elements p_{ij} and q_{ij} are chosen to satisfy equation (2.1.1) or (2.1.2) with $u = f_z(x)$ exactly for $z = 0, \ldots, s$, giving equations

$$z\Delta x \sum_{j=i-k_L}^{i+k_R} p_{ij}(x_j - x_i)^{z-1} = \sum_{j=i-k_L}^{i+k_R} q_{ij}(x_j - x_i)^z. \tag{2.1.9}$$

If a centered finite-difference scheme of order s is chosen for uniform regions of the spatial domain, setting $k_L = k_R$ with the appropriate accuracy in equation (2.1.9) yields the schemes presented in Table 2.1.

In boundary and interface regions of the domain, the same accuracy conditions (2.1.9) apply, but to order $\sigma \leq s$. For reasons of stability discussed in Section 2.2, it is necessary for at least one node in the interface or boundary region to be one order less accurate than the interior scheme, for $\sigma = s - 1$. This does not degrade the global convergence performance of the scheme (Gustafsson, 1975), so if fourth-order convergence is desired, a third-order accurate boundary and/or interface scheme may be used with a fourth-order interior scheme in uniform regions of the domain. The conditions of Gustafsson's proof prevent pollution of the domain by propagation of the lower-order error.

Convergence to the interior order predicted by Gustafsson (1975) is in an asymptotic sense, however; thus it is expected that the presence of many interface regions could degrade the convergence rate when compared to that of a uniform grid because of the presence in the domain of several lower-order points, proportional to the number of interfaces.

2.2 Stability and Summation-by-Parts Formulation

2.2.1 The Advection Equation

Central to this thesis is the concept of numerical stability for finite-difference schemes. The starting point for this discussion is the definition of a Cauchy problem for a hyperbolic PDE, the scalar advection equation:

$$\frac{\partial u}{\partial t} + c\frac{\partial u}{\partial x} = 0, \quad 0 \leq x \leq 1, \quad t \geq 0, \tag{2.2.1}$$

where it is chosen that $c > 0$, with an initial condition

$$u(x, 0) = h(x), \quad 0 \leq x \leq 1, \tag{2.2.2}$$

and the boundary condition at $x = 0$,

$$u(0, t) = g(t), \quad t \geq 0. \tag{2.2.3}$$

The solution to this problem is sought numerically on a grid at nodes x_j on $0 \leq x \leq 1$, where $j = 1, \ldots, N$, and the discretization scale is Δx but is not necessarily uniform throughout. The projection of the exact solution $u(x, t)$ is defined as $\mathbf{v}$ such that $v_j = u(x_j, t)$, while the numerical solution is given by $\mathbf{u}$ with $u_j(t)$ defined at each x_j. A generalized finite-difference scheme is used to approximate the spatial derivative following equation (2.1.4),

$$P\frac{\mathrm{d}\mathbf{u}}{\mathrm{d}x} = \frac{1}{\Delta x}Q\mathbf{u}, \tag{2.2.4}$$

thus giving the semidiscrete form of the advection equation

$$P\frac{\mathrm{d}\mathbf{u}}{\mathrm{d}t} = -\frac{c}{\Delta x}Q\mathbf{u}. \tag{2.2.5}$$

2.2.2 Stability Theory

The importance of stability is rooted in the Lax Equivalence Theorem, which states that a numerical scheme is convergent if it is both consistent and stable (Lomax et al., 2001). Consistency is guaranteed for the schemes described in this work because the numerical

discretizations in space and time are independent. Stability, by the classical Lax definition, requires that the solution error at a fixed time T be bounded as the grid size $\Delta x \to 0$. This is not necessarily true for an arbitrary interface treatment.

On an infinite domain, stability is straightforward to examine by Fourier analysis. The stability problem on a finite domain is considerably more difficult, so more advanced methods are required. GKS stability theory (after Gustafsson et al., 1972) provides conditions for stability based on a normal mode (eigenvalue) analysis of initial-boundary value problems. It is thus a definition of stability in the Lax sense, and therefore permits (exponential) error growth in time, provided that it does not get worse with mesh refinement (Carpenter et al., 1993). Thus for stable long-time integration, asymptotic time stability is also required, which requires that solution error be bounded for fixed Δx as $T \to \infty$.

These concepts are illustrated by the generalized semidiscrete equation

$$\frac{\mathrm{d}\mathbf{u}}{\mathrm{d}t} = A\mathbf{u}, \tag{2.2.6}$$

where A is an arbitrary matrix, and $\mathbf{u}$ is the numerical solution approximating the projection $\mathbf{v}$ of the exact solution modeled by this equation. Asymptotic stability is obvious: if all eigenvalues of A have nonpositive real parts (and A is nondefective), then the error $\mathbf{e} = |\mathbf{v} - \mathbf{u}|$ is bounded with time and the scheme is stable. Naively, this may seem sufficient; but asymptotic stability does not imply GKS stability, because we expect (and by the Lax Equivalence theorem, require) that the error should not grow as the grid is refined, and this is not guaranteed by the eigenvalue restriction alone.

Consider a scheme with multiply degenerate eigenvalues in the left half plane: it is asymptotically stable but experiences transient algebraic growth. GKS stability prohibits growth in this form. On the other hand, positive eigenvalues of A are permitted by the GKS definition, as long as they satisfy certain conditions, because the theory is defined (as is mathematically usual) in terms of the growth estimate it permits. Time stability is mathematically unusual in that it is defined by the solutions it permits: stability requires that no solution have an eigenvalue in the right half of the complex plane. Clearly, then both definitions must be satisfied for a stable and convergent interface scheme (Carpenter et al., 1993). For the interested reader, a more detailed description of GKS stability is presented in Appendix A.1.

2.2.3 Summation-by-Parts Operators

Analogous to integration by parts for continuous PDEs, the semidiscretized equation (2.2.5) can be made to satisfy a summation-by-parts (SBP) rule (Kreiss and Scherer, 1974). Physically, this prevents energy growth (or decay) anywhere in the discrete domain except at the boundaries, where energy is transfered by the boundary conditions. GKS theory is understood in the same context, and it will be shown in Section 2.2.5 that stability is guaranteed for finite-difference schemes that are SBP operators.

A great advantage of designing an interface scheme that satisfies a summation-by-parts condition is that it is a global criterion. This avoids the problem identified by Trefethen (1985), where multiple interfaces may be unstable even if a single interface is locally stable. Here, because each interface satisfies the SBP rule, any number of interfaces will also be stable, as each makes zero contribution to the global energy balance.

Consider a finite-difference approximation of the form (2.2.4), such that the exact solution to (2.2.1), $u(x,t) \in C^m$, has a projection $\mathbf{v}(t)$ onto a grid of N nodes satisfying

$$P\frac{\mathrm{d}\mathbf{v}}{\mathrm{d}x} = \frac{1}{\Delta x}Q\mathbf{v} + P\mathbf{t}, \tag{2.2.7}$$

where $\mathbf{t}$ is the truncation error, with $\|\mathbf{t}\| = O(\Delta x^m)$. This approximation is then a summation-by-parts operator if it satisfies the following conditions (Scherer, 1977; Strand, 1994; Carpenter et al., 1994):

1. There exists a matrix H such that the product HP is symmetric positive definite, i.e., for $\mathbf{u} \in \mathbb{R}$,

$$h_L\|\mathbf{u}\|^2 \leq (\mathbf{u}, HP\mathbf{u}) \leq h_U\|\mathbf{u}\|^2, \tag{2.2.8}$$

   where h_L and h_U are positive constants independent of N. The inner product is defined in the conventional sense,

$$(\mathbf{u}, \mathbf{v}) = \mathbf{u}^T\mathbf{v} = \sum_{i=1}^{N} u_i v_i, \tag{2.2.9}$$

   with the usual identities $(\mathbf{u}, \mathbf{v}) = (\mathbf{v}, \mathbf{u})$, etc.

2. The product $W = HQ$ is antisymmetric except at the corners, such that

$$W + W^T = \text{diag}(2w_{11}, 0, \ldots, 0, 2w_{NN}), \tag{2.2.10}$$

where $w_{11} < 0 < w_{NN}$.

To illustrate the concept of summation-by-parts operators, first consider the continuous equation (2.2.1). From the inner product,

$$(u, u) = \|u\|^2 = \int_0^1 u^2(x, t)\mathrm{d}x,$$

differentiating in time gives the energy estimate

$$\frac{\mathrm{d}}{\mathrm{d}t}\|u\|^2 = -c\left[u^2(1, t) - u^2(0, t)\right]. \tag{2.2.11}$$

For the semidiscrete case (2.2.5), define a norm from the discrete inner product

$$(\mathbf{u}, HP\mathbf{u}) = \|\mathbf{u}\|_H = \mathbf{u}^T HP\mathbf{u}, \tag{2.2.12}$$

and differentiate to obtain the estimate

$$\frac{\mathrm{d}}{\mathrm{d}t}\|\mathbf{u}\|_H^2 = -\frac{c}{\Delta x}\left[\mathbf{u}^T Q^T P^{-T} HP\mathbf{u} + \mathbf{u}^T HQ\mathbf{u}\right].$$

Applying the summation-by-parts conditions, the result analogous to equation (2.2.11) is obtained:

$$\frac{\mathrm{d}}{\mathrm{d}t}\|\mathbf{u}\|_H^2 = -\frac{c}{\Delta x}(2w_{11}u_1^2 + 2w_{NN}u_N^2). \tag{2.2.13}$$

2.2.4 Boundary Conditions

Essential to the stability of the finite-difference approximation is appropriate implementation of the boundary conditions, consistent with the SBP criterion and time stability. The basic injection method for the boundary condition, where $u_1 = g(t)$ is imposed directly, is not necessarily stable in the SBP sense. Instead, we use the simultaneous approximation term (SAT) penalty method proposed by Carpenter et al. (1994), which replaces the

semidiscrete equation (2.2.5) with

$$P\frac{\mathrm{d}\mathbf{u}}{\mathrm{d}t} = -\frac{c}{\Delta x}Q\mathbf{u} + \frac{c}{\Delta x}\tau\mathbf{s}(u_1 - g(t)), \tag{2.2.14}$$

where τ is the SAT parameter, to be defined, and

$$\mathbf{s} = H^{-1}[w_{11}, 0, \ldots, 0]^T = [q_{11}, 0, \ldots, 0]^T. \tag{2.2.15}$$

High-order finite-difference stencils at the boundary that satisfy the SBP conditions have been developed by Strand (1994) and Carpenter et al. (1994) for different interior schemes and with different forms for the norm matrix H. Following similar methods, new boundary stencils have been developed for the interior schemes considered in this work and are presented in Appendix B.

2.2.5 Demonstration of Stability

Having defined the properties of the finite-difference scheme necessary for it to be a summation-by-parts operator, we now demonstrate that it is stable and obtain an estimate for the growth rate of the error norm. This analysis follows that of Carpenter et al. (1994) and Abarbanel and Chertock (2000).

Starting with equation (2.2.14) and setting $g(t) = 0$ for convenience, the energy norm growth rate under the SBP conditions is given by

$$\frac{\mathrm{d}}{\mathrm{d}t}\|\mathbf{u}\|_H^2 = -2\frac{c}{\Delta x}\left[(1-\tau)w_{11}u_1^2 + w_{NN}u_N^2\right]. \tag{2.2.16}$$

Since the norm $\|\mathbf{u}\|_H^2 > 0$, if $\mathrm{d}\|\mathbf{u}\|_H^2/\mathrm{d}t \leq 0$ for all time the scheme will be strictly stable. From the second SBP condition, $w_{11} < 0 < w_{NN}$; therefore for $c > 0$ we require for stability (Carpenter et al., 1994)

$$\tau \geq 1. \tag{2.2.17}$$

Thus with this additional condition (2.2.17), the scheme is strictly stable. The next step is to verify that spatial accuracy is preserved and that the solution error is bounded. To do

so, consider the projection $\mathbf{v}$ of the exact solution in the semidiscrete equation:

$$P\frac{\mathrm{d}\mathbf{v}}{\mathrm{d}t} = -\frac{c}{\Delta x}Q\mathbf{v} + \frac{c}{\Delta x}\tau\mathbf{s}(v_1 - g(t)) + P\mathbf{t} = -\frac{c}{\Delta x}Q\mathbf{v} + P\mathbf{t},$$

since the exact solution has $v_1 = g(t)$. Now define an error $\mathbf{e}(t) = \mathbf{v}(t) - \mathbf{u}(t)$, so

$$P\frac{\mathrm{d}\mathbf{e}}{\mathrm{d}t} = P\frac{\mathrm{d}\mathbf{v}}{\mathrm{d}t} - P\frac{\mathrm{d}\mathbf{u}}{\mathrm{d}t} = -\frac{c}{\Delta x}Q\mathbf{e} + \frac{c}{\Delta x}\tau\mathbf{s}e_1 + P\mathbf{t}.$$

As for the energy norm $\|\mathbf{u}\|_H$, consider an error norm $(\mathbf{e}, HP\mathbf{e})$. Its time rate of change is given by

$$\begin{aligned}\frac{\mathrm{d}}{\mathrm{d}t}(\mathbf{e}, HP\mathbf{e}) &= -\frac{c}{\Delta x}\mathbf{e}^T\left[HQ + (HQ)^T\right]\mathbf{e} + 2\frac{c}{\Delta x}\tau w_{11}e_1^2 + \mathbf{e}^T HP\mathbf{t} + (HP\mathbf{t})^T\mathbf{e} \\ &= -2\frac{c}{\Delta x}\left[(1-\tau)w_{11}e_1^2 + w_{NN}e_N^2\right] + 2(\mathbf{e}, HP\mathbf{t}).\end{aligned}$$

Since the term in the square brackets is greater than zero by construction, we have

$$\frac{\mathrm{d}}{\mathrm{d}t}(\mathbf{e}, HP\mathbf{e}) \leq 2(\mathbf{e}, HP\mathbf{t}). \tag{2.2.18}$$

By the Cauchy-Schwarz inequality,

$$(\mathbf{e}, HP\mathbf{t}) \leq \sqrt{(\mathbf{e}, HP\mathbf{e})}\sqrt{(\mathbf{t}, HP\mathbf{t})}, \tag{2.2.19}$$

thus giving for equation (2.2.18)

$$\frac{\mathrm{d}}{\mathrm{d}t}(\mathbf{e}, HP\mathbf{e}) \leq 2\sqrt{(\mathbf{e}, HP\mathbf{e})}\sqrt{(\mathbf{t}, HP\mathbf{t})},$$

or, more simply,

$$\frac{\mathrm{d}}{\mathrm{d}t}\sqrt{(\mathbf{e}, HP\mathbf{e})} \leq \sqrt{(\mathbf{t}, HP\mathbf{t})}. \tag{2.2.20}$$

Integrating,

$$\sqrt{(\mathbf{e}, HP\mathbf{e})} \leq \sup_{0\leq s\leq t}\|\mathbf{t}(s)\|t, \tag{2.2.21}$$

and then using equation (2.2.12) from the first SBP condition, the error may be bounded

explicitly by

$$\|\mathbf{e}\| \leq \sqrt{\frac{h_U}{h_L}} \sup_{0\leq s\leq t} \|\mathbf{t}(s)\| t. \tag{2.2.22}$$

Growth in the error is therefore at most linear in time, so the error is finite for all $t < \infty$. Thus the scheme is Lax stable and then, by the Lax Equivalence theorem, convergent.

A better estimate of the error rate may be made if the inequality (2.2.17) is sharpened to $\tau > 1$ (Abarbanel and Chertock, 2000). To simplify the following algebra, we set $H = I$ (the identity matrix), and define

$$\tilde{Q} = Q - \tau[\mathbf{s}, \mathbf{0}, \ldots, \mathbf{0}]. \tag{2.2.23}$$

Then the semidiscrete approximation may be rewritten as

$$P\frac{\mathrm{d}\mathbf{u}}{\mathrm{d}t} = -\frac{c}{\Delta x}\tilde{Q}\mathbf{u} - \frac{c}{\Delta x}\tau\mathbf{s}g(t), \tag{2.2.24}$$

and so if we consider $g(t) = 0$, this reduces to

$$\frac{\mathrm{d}\mathbf{u}}{\mathrm{d}t} = -\frac{c}{\Delta x}P^{-1}\tilde{Q}\mathbf{u}, \tag{2.2.25}$$

which has the form of (2.2.6). Immediately it is clear that if all eigenvalues of $-P^{-1}\tilde{Q}$ have negative real parts, the scheme is asymptotically stable. To show that the error is bounded for all time, notice that P is symmetric positive definite, and $\tilde{Q}$ is positive definite, because for any real vector $\mathbf{v}$,

$$(\mathbf{v}, \tilde{Q}\mathbf{v}) = (\mathbf{v}, \frac{1}{2}(\tilde{Q} + \tilde{Q}^T)\mathbf{v}) = (1-\tau)q_{11}v_1^2 + q_{NN}v_N^2 > 0, \tag{2.2.26}$$

since now $\tau > 1$. This guarantees that the real parts of the eigenvalues of $P^{-1}\tilde{Q}$ are positive. To see this, notice that

$$P^{-1}\tilde{Q} = P^{-1/2}\left(P^{-1/2}\tilde{Q}P^{-1/2}\right)P^{1/2}.$$

Since this has the form of a transformation, the eigenvalues of $P^{-1}\tilde{Q}$ and $P^{-1/2}\tilde{Q}P^{-1/2}$ must be similar, and because P is symmetric positive definite, $P^{1/2}$ etc. are well defined.

Now see that

$$\left(\mathbf{v}, (P^{-1/2}\tilde{Q}P^{-1/2})\mathbf{v}\right) = (P^{-1/2}\mathbf{v})^T\tilde{Q}P^{-1/2}\mathbf{v} = \left(P^{-1/2}\mathbf{v}, \tilde{Q}(P^{-1/2}\mathbf{v})\right),$$

which by (2.2.26) is positive. Returning to the semidiscrete equation, consider again the equation for the error $\mathbf{e}$,

$$\frac{\mathrm{d}\mathbf{e}}{\mathrm{d}t} = -\frac{c}{\Delta x}P^{-1}\tilde{Q}\mathbf{e} + \mathbf{t}. \tag{2.2.27}$$

Multiplying by $\mathbf{e}^T$, an equation for the error norm is obtained:

$$\mathbf{e}^T\frac{\mathrm{d}\mathbf{e}}{\mathrm{d}t} = \|\mathbf{e}\|\frac{\mathrm{d}}{\mathrm{d}t}\|\mathbf{e}\| = -\frac{c}{\Delta x}\mathbf{e}^TP^{-1}\tilde{Q}\mathbf{e} + \mathbf{e}^T\mathbf{t} = -\frac{c}{\Delta x}(\mathbf{e}, P^{-1}\tilde{Q}\mathbf{e}) + (\mathbf{e}, \mathbf{t}). \tag{2.2.28}$$

From the eigen decomposition of $P^{-1}\tilde{Q}$, having eigenvalues λ_i and orthonormal eigenvectors $\mathbf{x}_i$, see that

$$(\mathbf{e}, P^{-1}\tilde{Q}\mathbf{e}) = \Re(\mathbf{e}, P^{-1}\tilde{Q}\mathbf{e}) = (e_i\mathbf{x}_i, \sum_i \lambda_i e_i\mathbf{x}_i) = \sum_i e_i^2\Re(\lambda_i).$$

With $\Re(\lambda_i) > 0$ for asymptotic stability of equation (2.2.25),

$$(\mathbf{e}, P^{-1}\tilde{Q}\mathbf{e}) > \lambda_{\min}\sum_i e_i^2 = \lambda_{\min}(\mathbf{e}, \mathbf{e}) = \lambda_{\min}\|\mathbf{e}\|^2,$$

equation (2.2.28) becomes

$$\|\mathbf{e}\|\frac{\mathrm{d}}{\mathrm{d}t}\|\mathbf{e}\| = \lambda_{\min}\|\mathbf{e}\|^2 + (\mathbf{e}, \mathbf{t}). \tag{2.2.29}$$

Again by the Cauchy-Schwartz inequality, $(\mathbf{e}, \mathbf{t}) \leq \|\mathbf{e}\|\|\mathbf{t}\|$, and so we simplify the equation to obtain

$$\frac{\mathrm{d}}{\mathrm{d}t}\|\mathbf{e}\| \leq -\frac{c}{\Delta x}\lambda_{\min}\|\mathbf{e}\| + \|\mathbf{t}\|. \tag{2.2.30}$$

By Gronwall's Lemma, we have the result

$$\|\mathbf{e}\| \leq \sup_{0\leq s\leq t}\|\mathbf{t}(s)\|\frac{\Delta x}{c\lambda_{\min}}\left[1 - \exp\left(-\frac{c\lambda_{\min}t}{\Delta x}\right)\right]. \tag{2.2.31}$$

Thus the error is bounded by the maximum truncation error as $t \to \infty$, and so the scheme is convergent and stable.

2.2.6 Application to the Interface Problem

This theory is now used to develop high-order finite-difference schemes across interfaces where there is a step change in grid resolution. By extension of the SBP property, a scheme that spans the interface will preserve stability of the global scheme if the SBP conditions remain satisfied across the domain and the boundary conditions are implemented appropriately. In the interface region, for the projection $\mathbf{v}(t)$, the local submatrices P' and Q' satisfy

$$P'\frac{\mathrm{d}\mathbf{v}}{\mathrm{d}x} = \frac{1}{\Delta x}Q'\mathbf{v} + P'\mathbf{t}, \tag{2.2.32}$$

where for an interior scheme of order s, $\|\mathbf{t}\| = O(\Delta x^\sigma)$ with $\sigma \leq s$. To preserve the global convergence rate at the interior order, we require $\sigma \geq s - 1$. The general SBP conditions may then be simplified for the finite-difference scheme in the vicinity of a grid interface:

1′. There exists a matrix H' such that the product $H'P'$ is symmetric positive definite.

2′. The product $W' = H'Q'$ is antisymmetric, such that $W' + W'^T = 0$.

2.3 Explicit Interface Closure

We consider first the interface problem for explicit schemes in the interior of the domain, where P is the identity matrix except at boundary and interface regions. Interface closures for both fourth- and sixth-order interior schemes are presented in this section, with the analytic development following focusing on the former scheme with its smaller stencil. It is observed that H can be taken as the identity matrix across the entire domain without consequence in these cases.

2.3.1 Scheme Structure

Consider an n-point interface closure with an explicit centered 5-point interior stencil of the particular form

$$\frac{\mathrm{d}u_i}{\mathrm{d}x} = \frac{1}{\Delta x}\big(-\alpha u_{i-2} - \beta u_{i-1} + \beta u_{i+1} + \alpha u_{i+2}\big), \tag{2.3.1}$$

where the coefficients for a particular scheme from Table 2.1 are given under the mapping $\alpha \to q_2$ and $\beta \to q_1$. In the region of the interface between grids of resolution Δx and $r\Delta x$,

the local parts of the full-domain matrices P and Q have the form

$$P' = \begin{bmatrix} D_p & A_p & 0 \\ A_p^T & \hat{P} & A_p^{\hat{T}} \\ 0 & A_p^{\hat{T}T} & rD_p \end{bmatrix}, \quad Q' = \begin{bmatrix} D_q & A_q & 0 \\ -A_q^T & \hat{Q} & A_q^{\hat{T}} \\ 0 & -A_q^{\hat{T}T} & D_q \end{bmatrix}, \tag{2.3.2}$$

where $\hat{P}$ and $\hat{Q}$ are square $n \times n$ matrices representing the modified interface stencils, $D_p = I$ is the identity matrix of size $k \times k$ (where $k = s/2$), D_q is the block diagonal interior part of Q of the same size as D_p, and for the 5-point interior case,

$$A_q = \begin{bmatrix} 0 & 0 & 0 & \dots \\ \alpha & 0 & 0 & \dots \\ \beta & \alpha & 0 & \dots \end{bmatrix},$$

which is the overlaping part of Q over the interface stencil and is of size $k \times n$. For the explicit case, $A_p = 0$. The superscript $\hat{T}$ denotes the flip-transpose across the antidiagonal, in index notation given by

$$a_{ij}^{\hat{T}} = a_{(n-j+1)(k-i+1)}, \tag{2.3.3}$$

where $A_q = \{a_{ij}\}$.

The accuracy conditions defined by equation (2.1.9) are applied at the interface in terms of the elements of $\hat{P}$, $\hat{Q}$ and A_q to order σ_i for interface nodes $i = -n/2, \dots, n/2-1$ and for each $z = 0, \dots, \sigma_i$. The order to which the accuracy conditions are satisfied for node i, σ_i, is not necessarily the same for all nodes in the interface. The resulting system of equations generated by the accuracy conditions is reduced by the symmetry constraints of $\hat{P}$ and the antisymmetric constraints of $\hat{Q}$, but, depending on the size of the particular scheme, elements may remain unspecified by the accuracy conditions and lead to parametric families of closures. These parameters can be chosen to reduce the bandwidth of the stencil, and/or to modify the eigenvalues of $\hat{P}$.

2.3.2 An Explicit Fourth-Order Interface Closure

A fourth-order closure can be constructed by chosing $\alpha = -1/12$, $\beta = 2/3$, and $n = 4$, such that the matrices $\hat{P}$ and $\hat{Q}$ are given by

$$\hat{P} = \begin{bmatrix} p_{11} & p_{12} & p_{13} & p_{14} \\ p_{12} & p_{22} & p_{23} & p_{24} \\ p_{13} & p_{23} & p_{33} & p_{34} \\ p_{14} & p_{24} & p_{34} & p_{44} \end{bmatrix}, \qquad \hat{Q} = \begin{bmatrix} 0 & q_{12} & q_{13} & q_{14} \\ -q_{12} & 0 & q_{23} & q_{24} \\ -q_{13} & -q_{23} & 0 & q_{34} \\ -q_{14} & -q_{24} & -q_{34} & 0 \end{bmatrix}, \tag{2.3.4}$$

where the symmetry required by the SBP conditions has already been imposed.

Different closure schemes are identified here by the order of accuracy satisfied at each point in the interface region. We denote in compact form the order of accuracy of the interface closure by (σ_{-2})-(σ_{-1})-(σ_0)-(σ_1) for $n = 4$. The ordering is assumed to be from left to right where the left side is the finer grid. Thus, a 4-3-3-4 scheme has four points in the interface closure, the inner two of which satisfy the order conditions to third order, and the outer two satisfy the conditions to fourth order. All interface closures considered here are symmetrically distributed about the grid interface, so a four-point scheme has two points in the coarse block and two in the fine block. The number of points used for a particular closure depends strongly on the size of the interior stencil. For a standard fourth-order interior scheme, a minimum of four points are required in the interface region, because the five-point stencil extends over both blocks for a distance of at least two points on each side. Similarly, for the sixth-order scheme, the interface extends over at least six points.

To maintain the global convergence rate s of the finite difference scheme used in the interior of the domain, the order of accuracy at every point in the interface must be $\sigma \geq s-1$. For a four-point interface scheme with a fourth-order interior scheme, if each point in the interface is third order, there are a total of 16 equations in terms of the 16 independent coefficients of $\hat{P}$ and $\hat{Q}$. However, the set of equations is not linearly independent (this particular system has rank 14); they are insufficient to solve for all 16 variables uniquely. Therefore, to reduce the total truncation error of the scheme, two points can be solved up to fourth-order accuracy, giving 18 equations (in a system of rank 16) in the 16 coefficients, which has a unique solution for each particular arrangement of third- and fourth-order points across the interface. These solutions satisfy the SBP conditions on both $\hat{P}$ and $\hat{Q}$

and are stable for varying ranges of grid ratio, r. It is not possible for a third point in the four-point interface to be fourth order, though, as no more coefficients can be added to the matrices while still maintaining their SBP structure.

For the symmetric 4-3-3-4 interface scheme, applying equation (2.1.9) at each of the four interface nodes yields the four matrix equations (2.3.5)–(2.3.8),

$$\begin{bmatrix} 0 & 0 & 0 & 0 \\ 1 & 1 & 1 & 1 \\ 0 & 2 & 3+r & 3+3r \\ 0 & 3 & \frac{3(3+r)^2}{4} & \frac{27(1+r)^2}{4} \\ 0 & 4 & \frac{(3+r)^2}{2} & \frac{27(1+r)^3}{2} \end{bmatrix} \begin{bmatrix} p_{11} \\ p_{12} \\ p_{13} \\ p_{14} \end{bmatrix} = \begin{bmatrix} 1 & 1 & 1 \\ 1 & \frac{3+r}{2} & \frac{3+3r}{2} \\ 1 & \frac{(3+r)^2}{4} & \frac{9(1+r)^2}{4} \\ 1 & \frac{(3+r)^3}{8} & \frac{27(1+r)^3}{8} \\ 1 & \frac{(3+r)^4}{16} & \frac{81(1+r)^4}{16} \end{bmatrix} \begin{bmatrix} q_{12} \\ q_{13} \\ q_{14} \end{bmatrix} + \begin{bmatrix} -\frac{7}{12} \\ \frac{1}{2} \\ -\frac{1}{3} \\ 0 \\ \frac{2}{3} \end{bmatrix}, \tag{2.3.5}$$

$$\begin{bmatrix} 0 & 0 & 0 & 0 \\ 1 & 1 & 1 & 1 \\ -2 & 0 & 1+r & 1+3r \\ 3 & 0 & \frac{3(1+r)^2}{4} & \frac{3(1+3r)^2}{4} \end{bmatrix} \begin{bmatrix} p_{12} \\ p_{22} \\ p_{23} \\ p_{24} \end{bmatrix} = \begin{bmatrix} 1 & 1 & 1 \\ -1 & \frac{1+r}{2} & \frac{1+3r}{2} \\ 1 & \frac{(1+r)^2}{4} & \frac{(1+3r)^2}{4} \\ -1 & \frac{(1+r)^3}{8} & \frac{(1+3r)^3}{8} \end{bmatrix} \begin{bmatrix} -q_{12} \\ q_{13} \\ q_{14} \end{bmatrix} + \begin{bmatrix} \frac{1}{12} \\ -\frac{1}{6} \\ \frac{1}{3} \\ -\frac{2}{3} \end{bmatrix}, \tag{2.3.6}$$

$$\begin{bmatrix} 0 & 0 & 0 & 0 \\ 1 & 1 & 1 & 1 \\ -3-r & -1-r & 0 & 2r \\ \frac{3(3+r)^2}{4} & \frac{3(1+r)^2}{4} & 0 & 3r^2 \end{bmatrix} \begin{bmatrix} p_{13} \\ p_{23} \\ p_{33} \\ p_{34} \end{bmatrix} = \begin{bmatrix} 1 & 1 & 1 \\ -\frac{3+r}{2} & -\frac{1+r}{2} & r \\ \frac{(3+r)^2}{4} & \frac{(1+r)^2}{4} & r^2 \\ -\frac{(3+r)^3}{8} & -\frac{(1+r)^3}{8} & r^3 \end{bmatrix} \begin{bmatrix} -q_{13} \\ -q_{23} \\ q_{34} \end{bmatrix} - \begin{bmatrix} \frac{1}{12} \\ \frac{r}{6} \\ \frac{r^2}{3} \\ \frac{2r^3}{3} \end{bmatrix}, \tag{2.3.7}$$

$$\begin{bmatrix} 0 & 0 & 0 & 0 \\ 1 & 1 & 1 & 1 \\ -3-3r & -1-3r & -2r & 0 \\ \frac{27(1+r)^2}{4} & \frac{3(1+3r)^2}{4} & 3r^2 & 0 \\ -\frac{27(1+r)^3}{2} & -\frac{(1+3r)^2}{2} & -4r^3 & 0 \end{bmatrix} \begin{bmatrix} p_{14} \\ p_{24} \\ p_{34} \\ p_{44} \end{bmatrix} = - \begin{bmatrix} 1 & 1 & 1 \\ -\frac{3+3r}{2} & -\frac{1+3r}{2} & -r \\ \frac{9(1+r)^2}{4} & \frac{(1+3r)^2}{4} & r^2 \\ -\frac{27(1+r)^3}{8} & -\frac{(1+3r)^3}{8} & -r^3 \\ \frac{81(1+r)^4}{16} & \frac{(1+3r)^4}{16} & r^4 \end{bmatrix} \begin{bmatrix} q_{14} \\ q_{24} \\ q_{34} \end{bmatrix} + \begin{bmatrix} \frac{7}{12} \\ \frac{r}{2} \\ \frac{r^2}{3} \\ 0 \\ -\frac{2r^4}{3} \end{bmatrix}. \tag{2.3.8}$$

Solving this system, the expressions (2.3.9) and (2.3.10) are obtained for the elements of $\hat{P}$

and $\hat{Q}$ in terms of the interface ratio r.

$$
\begin{aligned}
p_{11} &= \frac{1271r^6 - 418r^5 - 479r^4 + 28676r^3 + 214297r^2 + 467870r + 279503}{31104(r+1)(r+3)^2}, \\
p_{22} &= \frac{1271r^6 + 11934r^5 + 9761r^4 + 7812r^3 + 36377r^2 + 12510r + 1743}{3456(r+1)(3r+1)^2}, \\
p_{33} &= \frac{1743r^6 + 12510r^5 + 36377r^4 + 7812r^3 + 9761r^2 + 11934r + 1271}{3456r^2(r+1)(r+3)^2}, \\
p_{44} &= \frac{279503r^6 + 467870r^5 + 214297r^4 + 28676r^3 - 479r^2 - 418r + 1271}{31104r^2(r+1)(3r+1)^2}, \\
p_{12} &= \frac{-1271r^6 - 5758r^5 + 1927r^4 + 5372r^3 + 11095r^2 + 1154r + 1305}{10368\left(3r^3 + 13r^2 + 13r + 3\right)}, \\
p_{13} &= -\frac{819r^6 + 7982r^5 + 4693r^4 + 4388r^3 + 1213r^2 - 16210r + 1723}{10368r(r+1)(r+3)^2}, \\
p_{14} &= -\frac{-1723r^6 + 2642r^5 + 7099r^4 + 7004r^3 + 7099r^2 + 2642r - 1723}{31104r\left(3r^3 + 13r^2 + 13r + 3\right)}, \\
p_{23} &= \frac{819r^6 - 2242r^5 + 1485r^4 + 25988r^3 + 1485r^2 - 2242r + 819}{3456r\left(3r^3 + 13r^2 + 13r + 3\right)}, \\
p_{24} &= -\frac{1723r^6 - 16210r^5 + 1213r^4 + 4388r^3 + 4693r^2 + 7982r + 819}{10368r(r+1)(3r+1)^2}, \\
p_{34} &= \frac{1305r^6 + 1154r^5 + 11095r^4 + 5372r^3 + 1927r^2 - 5758r - 1271}{10368r^2\left(3r^3 + 13r^2 + 13r + 3\right)},
\end{aligned}
\tag{2.3.9}
$$

$$
\begin{aligned}
q_{12} &= \frac{545r^4 - 120r^3 + 2054r^2 + 1368r + 377}{216\left(3r^3 + 13r^2 + 13r + 3\right)}, \\
q_{13} &= \frac{-193r^4 + 261r^3 - 181r^2 + 195r - 34}{216r\left(r^2 + 4r + 3\right)}, \\
q_{14} &= \frac{17r^4 - 63r^3 - 4r^2 - 63r + 17}{108r\left(3r^2 + 10r + 3\right)}, \\
q_{23} &= \frac{193r^4 - 282r^3 + 754r^2 - 282r + 193}{72r\left(3r^2 + 10r + 3\right)}, \\
q_{24} &= \frac{-34r^4 + 195r^3 - 181r^2 + 261r - 193}{216r\left(3r^2 + 4r + 1\right)}, \\
q_{34} &= \frac{377r^4 + 1368r^3 + 2054r^2 - 120r + 545}{216r\left(3r^3 + 13r^2 + 13r + 3\right)}.
\end{aligned}
\tag{2.3.10}
$$

The solution is completed by verifying that these lead to positive definite $\hat{P}$, thus satisfying both SBP conditions at the interface. It has been found numerically for this 4-3-3-4 scheme that the range of values for r over which the minimum eigenvalue of $\hat{P}$ is positive is $1/r_{\max} < r < r_{\max}$, where $r_{\max} \approx 4.551$.

If six points are used with a fourth-order interior scheme, there are now up to 36 independent coefficients of $\hat{P}$ and $\hat{Q}$ available, but no more than 30 equations (6 rows, up to fourth-order accuracy in each). However, the maximum number of fourth-order points in a six-point interface scheme is five, because it is not possible algebraically to enforce the order conditions up to fourth order at all points. Moreover, when comparing four- and six-point fourth-order interface schemes, it is important to note that although formal accuracy of the six-point scheme may be better (with a 4-4-3-4-4-4 scheme, or a truncation error-optimized 4-4-3-3-4-4), both are third order at every point when implemented in an explicit finite-difference method. The formal accuracy at each point in the interface is correct for the original construction of equation (2.2.32), but when this is implemented by inverting P, every point in the block is reduced to third-order accuracy as the lower-order error is spread across the interface by the action of $\hat{P}^{-1}$. This implies that, if the number of points in a block is relatively small compared to the number of interface points, then it is more desirable to minimize the width of the interface than to force fourth-order accuracy at a maximum number of points. It is for this reason that four-point interface closures for fourth-order interior schemes have been presented here.

2.3.3 Inverse Grid Ratios

The grid ratio in the derivation thus far has been arbitrary. For $r > 1$, the solution corresponds to an interface between a fine grid and a coarse grid (moving from left to right), and for $r < 1$ it corresponds to the opposite case. A particular scheme may be solved for any grid ratio, up to the positive definite limit of $\hat{P}$, and, for some closures, it is possible to derive the corresponding reflected stencil, that for $1/r$, directly from the stencil for r. Writing equation (2.2.32) for an interface $\frac{1}{r}$:1, in terms of the matrices $\hat{P}$ and $\hat{Q}$ of the 1:r interface, gives

$$\hat{P}\frac{\mathrm{d}\mathbf{u}}{\mathrm{d}x} = \frac{r}{\Delta x}\hat{Q}\mathbf{u},$$

or, alternatively,

$$\left(\frac{1}{r}\hat{P}\right)\frac{\mathrm{d}\mathbf{u}}{\mathrm{d}x} = \frac{1}{\Delta x}\hat{Q}\mathbf{u}. \tag{2.3.11}$$

The scheme for the inverse ratio interface 1:$\frac{1}{r}$ may then be obtained, in the form of equation (2.2.32), by taking the transpose of the flip-transpose of the original matrices $\hat{P}$ and

$\hat{Q}$ to give

$$\hat{P}^* \frac{\mathrm{d}\mathbf{u}}{\mathrm{d}x} = \frac{1}{\Delta x} \hat{Q}^* \mathbf{u}. \tag{2.3.12}$$

In terms of the elements p_{ij} of the original matrix, the elements of the transformed matrix $\hat{P}^*$ are given by

$$p^*_{ij} = \frac{1}{r} p_{(n+1-i)(n+1-j)}, \tag{2.3.13}$$

and, similarly, the elements of $\hat{Q}^*$ are given by

$$q^*_{ij} = -q_{(n+1-i)(n+1-j)}, \tag{2.3.14}$$

where n is the width of the interface. Note that the negative sign is necessary to preserve the antisymmetry of $\hat{Q}^*$ after the transformation.

Generally, schemes with symmetrically distributed accuracy (like 4-3-3-4 or 4-4-3-3-4-4), are preferable to biased schemes (such as 3-3-4-4 or 4-4-4-3-4-4), as the symmetric schemes behave predictably for both transitions from a fine to a coarse grid, and from a coarse to a fine grid. If the accuracy conditions are applied symmetrically across the interface for a particular grid ratio r, then the stability of the inverse-ratio scheme for a grid ratio $1/r$ follows that of the parent scheme. If not, stability for a particular grid ratio does not imply stability of the inverse ratio. For example, the fourth-order 4-3-3-4 scheme is stable for practical integer grid ratios in the range $1/4 \leq r \leq 4$, but the biased 3-3-4-4 scheme, which is stable for $r = 8$, is unstable for $r = 1/8$. We suspect that this arises because for $r > 1$ the third-order points are in the fine block, where the truncation error is $O(\Delta x^3)$, and the fourth-order points are in the coarse block, with an truncation error of $O((r\Delta x)^4)$. For large r and small Δx, the errors on both sides can be comparable in magnitude depending on $\mathbf{u}$. On the other hand, for a scheme with the third-order points in the coarse block (i.e., for $r < 1$), the truncation error there would be much larger than that in the fine block, adversely affecting stability. Unless a strongly directional refinement is necessary, symmetric interface closures are preferred in general.

2.3.4 An Explicit Sixth-Order Interface Closure

Presented briefly in this section is the interface closure for a six-point sixth-order interface scheme. The derivation follows that shown for the fourth-order scheme in Section 2.3.2,

with correspondingly wider stencils for the sixth-order interior stencil defined in Table 2.1. For a six-point interface scheme, there are now 36 independent coefficients in $\hat{P}$ and $\hat{Q}$ to satisfy at least 36 equations for a minimum of 5th-order accuracy through the interface. Degeneracy of the system (it has rank of 33) allows at least two points to be solved to 6th-order accuracy, for the scheme 6-5-5-5-5-6. One free parameter still remains, so q_{16} was arbitrarily set to zero to close the system.

$$
\begin{aligned}
p_{11} &= \frac{1652211692389}{1639249920000} & p_{12} &= -\frac{31083952147}{415134720000} & p_{13} &= \frac{914794939}{4371333120} \\
p_{14} &= \frac{173389799983}{596090880000} & p_{15} &= \frac{54564029173}{1967099904000} & p_{16} &= -\frac{425297407}{1739612160000} \\
p_{22} &= \frac{162874793821}{105131520000} & p_{23} &= -\frac{3185897141}{2372198400} & p_{24} &= -\frac{126662983969}{150958080000} \\
p_{25} &= -\frac{8141729677}{71165952000} & p_{26} &= -\frac{11386699273}{3083857920000} & p_{33} &= \frac{7485369407}{1873428480} \\
p_{34} &= \frac{5468461423}{23843635200} & p_{35} &= \frac{4104289571}{11240570880} & p_{36} &= -\frac{3905305253}{97418280960} \\
p_{44} &= \frac{181688660341}{216760320000} & p_{45} &= \frac{79567478071}{715309056000} & p_{46} &- \frac{12226504229}{632586240000} \\
p_{55} &= \frac{678741184843}{337217126400} & p_{56} &= -\frac{10527535793}{14612742144000} & p_{66} &= \frac{180918151344709}{90459832320000}
\end{aligned}
$$

Table 2.2: Coefficients of $\hat{P} = \{p_{ij}\}$ for the sixth-order explicit scheme with $r = 2$

$$
\begin{aligned}
q_{12} &= \frac{138050423}{171072000} & q_{13} &= -\frac{38453017}{79833600} & q_{14} &= \frac{48443239}{199584000} \\
q_{15} &= \frac{2912183}{59875200} & q_{16} &= 0 & q_{23} &= \frac{535097839}{283046400} \\
q_{24} &= -\frac{90269753}{80870400} & q_{25} &= -\frac{29644831}{345945600} & q_{26} &= -\frac{6039517}{404352000} \\
q_{34} &= \frac{1895189}{1478400} & q_{35} &= \frac{14623}{106920} & q_{36} &= \frac{1767551}{259459200} \\
q_{45} &= \frac{993971819}{1916006400} & q_{46} &= -\frac{753331379}{5930496000} & q_{56} &= \frac{1702393253}{2264371200}
\end{aligned}
$$

Table 2.3: Coefficients of $\hat{Q} = \{q_{ij}\}$ for the sixth-order explicit scheme with $r = 2$

This solution, shown in Tables 2.2–2.3, was found to have positive definite $\hat{P}$ in the range $1/r_{\max} < r < r_{\max}$ for $r_{\max} \approx 2.085$. A small improvement on these bounds may be possible with different q_{16}, but numerical investigation indicates that there is no stable solution for the 6-5-5-5-5-6 scheme with $r = 4$.

2.4 Implicit Interface Closure

For implicit finite difference schemes (also referred to as compact schemes), the first derivative approximation (2.2.4) leads to a matrix P that is typically tri- or pentadiagonal. This is advantageous computationally, as it can be solved efficiently using a fast algorithm (Ames, 1977). In order to retain this computationally efficient structure and satisfy the SBP constraints in the interface closure, the matrix H must have a nontrivial form and the matrices $V = HP$ and $W = HQ$ are introduced. Note that while the accuracy conditions are applied to P and Q as before, the SBP structure is imposed upon V and W instead.

2.4.1 Scheme Structure

Consider again an n-point interface closure, now with the particular implicit interior stencil of the form

$$a\frac{\mathrm{d}u_{i-1}}{\mathrm{d}x} + b\frac{\mathrm{d}u_i}{\mathrm{d}x} + a\frac{\mathrm{d}u_{i+1}}{\mathrm{d}x} = \frac{1}{\Delta x}\big(-\beta u_{i-1} + \beta u_{i+1}\big). \tag{2.4.1}$$

The matrices in the region of an interface between grids of spacing Δx and $r\Delta x$ have the form of equation (2.3.2) and the local product matrices are given by

$$V' = \begin{bmatrix} D_v & A_v & 0 \\ A_v^T & \hat{V} & rA_v^{\hat{T}} \\ 0 & rA_v^{\hat{T}T} & rD_v \end{bmatrix}, \quad W' = \begin{bmatrix} D_w & A_w & 0 \\ -A_w^T & \hat{W} & A_w^{\hat{T}} \\ 0 & -A_w^{\hat{T}T} & D_w \end{bmatrix}, \tag{2.4.2}$$

where, in terms of the coefficients of the extended stencil in V-W form,

$$A_v = \begin{bmatrix} 0 & 0 & 0 & \dots \\ a' & 0 & 0 & \dots \\ b' & a' & 0 & \dots \end{bmatrix}, \quad \text{and} \quad A_w = \begin{bmatrix} 0 & 0 & 0 & \dots \\ \alpha' & 0 & 0 & \dots \\ \beta' & \alpha' & 0 & \dots \end{bmatrix}.$$

The norm matrix H has the local structure

$$H' = \begin{bmatrix} D_h & A_h & 0 \\ A_h^T & \hat{H} & A_h^{\hat{T}} \\ 0 & A_h^{\hat{T}T} & D_h \end{bmatrix}, \quad \text{with} \quad A_h = \begin{bmatrix} 0 & 0 & 0 & \dots \\ 0 & 0 & 0 & \dots \\ h_1 & 0 & 0 & \dots \end{bmatrix},$$

where D_v, D_w and D_h represent the block-diagonal interior part of each matrix, V, W and H, respectively. The interior part of H, D_h, is a Toeplitz tridiagonal matrix of diagonal h_0 and subdiagonals h_1. The constants h_0 and h_1 are set by the boundary closure (Carpenter et al., 1994), and are considered known a priori. In order to recover P and Q, the matrices that are needed for implementation of the method, we multiply the matrices of (2.3.2) by H' and equate the results to (2.4.2). Introducing the generic A,

$$A = \begin{bmatrix} 0 & 0 & 0 & \dots \\ 0 & 0 & 0 & \dots \\ 1 & 0 & 0 & \dots \end{bmatrix}, \tag{2.4.3}$$

to express $A_p = aA$, $A_q = \beta A$, $A_h = h_1 A$, etc., and applying the SBP constraints on the symmetry of V and W leads to the following relationships

$$\hat{V} = \hat{H}\hat{P} + h_1 a\big(A^T A + r A^{\hat{T}} A^{\hat{T}T}\big), \tag{2.4.4a}$$

$$\hat{W} = \hat{H}\hat{Q} + h_1 \beta\big(A^T A - A^{\hat{T}} A^{\hat{T}T}\big), \tag{2.4.4b}$$

$$0 = A\big(\hat{P} - \frac{1}{r}\hat{P}^{T\hat{T}}\big), \tag{2.4.4c}$$

$$0 = A\big(\hat{H}^T - \hat{H}^{\hat{T}}\big), \tag{2.4.4d}$$

$$0 = A\big(\hat{Q} + \hat{Q}^{T\hat{T}}\big), \tag{2.4.4e}$$

$$a A^T D_h + h_1 \hat{P}^T A^T = h_1 A^T D_p + a\hat{H} A^T, \tag{2.4.4f}$$

$$\beta D_h A + h_1 A\hat{Q} = -h_1 D_q^T A + \beta A \hat{H}^T. \tag{2.4.4g}$$

The last five conditions (c–g) reduce to four equations relating the elements of the first and last rows of $\hat{P}$ and $\hat{Q}$, and the first and last columns of $\hat{H}$:

$$p_{1j} = \frac{1}{h_1}\big((h_1 b - h_0 a)\delta_{1j} + a h_{j1}\big),\ j = 1, \dots, n, \tag{2.4.5a}$$

$$p_{nj} = \frac{r}{h_1}\big((h_1 b - h_0 a)\delta_{nj} + a h_{jn}\big),\ j = 1, \dots, n, \tag{2.4.5b}$$

$$q_{1j} = -\frac{1}{h_1}\big(h_0 \beta \delta_{1j} - \beta h_{j1}\big),\ j = 1, \dots, n, \tag{2.4.5c}$$

$$q_{nj} = \frac{1}{h_1}\big(h_0 \beta \delta_{nj} - \beta h_{jn}\big),\ j = 1, \dots, n, \tag{2.4.5d}$$

where δ_{ij} is the Kronecker Delta. When combined with the accuracy conditions, these equations imply that for an interface region of n points, the first and last rows of $\hat{P}$ and $\hat{Q}$, and the first and last columns of $\hat{H}$, have the same values as the interior rows and columns, respectively, of each matrix. In this way, an n-point interface in $\hat{V}$ and $\hat{W}$ is reduced to a width of $n-2$ points in $\hat{P}$ and $\hat{Q}$.

2.4.2 An Implicit Fourth-Order Interface Closure

The derivation of the implicit scheme follows that of the explicit scheme, and in this case, the problem can be solved in the same manner but now in terms of $\hat{V}$ and $\hat{W}$. For a fourth-order implicit closure, we consider a 6-point wide interface stencil in V and W of the type 4-4-3-3-4-4, according to our notation. The symmetry and antisymmetry of the interface parts $\hat{V}$ and $\hat{W}$, respectively, is built into the structure of the matrices, and the interior region of H takes the values $h_0 = 1$ and $h_1 = -1/8$ (see Appendix B and Carpenter et al., 1994). An equivalent set of equations to (2.3.5)–(2.3.8) is obtained, here in terms of the elements of $\hat{V}$ and $\hat{W}$. Relating these to the elements of $\hat{H}$, $\hat{P}$ and $\hat{Q}$ are an additional 72 equations that arise when the products in equations (2.4.4a) and (2.4.4b) are expanded. The resulting quadratic system for the coefficients of $\hat{V}$, $\hat{W}$, $\hat{H}$, $\hat{P}$ and $\hat{Q}$ appears to be over determined, but can be solved numerically to arbitrary precision.

As noted, starting with a 6-point stencil for $\hat{V}$ and $\hat{W}$ results in a 4-point stencil for $\hat{P}$ and $\hat{Q}$. Moreover, a tridiagonal structure for $\hat{P}$ is imposed to limit the computational cost of an implementation compared to that of the standard compact method. This gives matrices of the following forms:

$$\hat{H} = \begin{bmatrix} h_0 & h_{12} & h_{13} & h_{14} & h_{15} & 0 \\ h_1 & h_0 & h_{23} & h_{24} & h_{25} & 0 \\ 0 & h_{32} & h_0 & h_{34} & h_{35} & 0 \\ 0 & h_{42} & h_{43} & h_0 & h_{45} & 0 \\ 0 & h_{52} & h_{53} & h_{54} & h_0 & h_1 \\ 0 & h_{62} & h_{63} & h_{64} & h_{65} & h_0 \end{bmatrix},$$

$$\hat{P} = \begin{bmatrix} b & a & 0 & 0 & 0 & 0 \\ p_{21} & p_{22} & p_{23} & 0 & 0 & 0 \\ 0 & p_{32} & p_{33} & p_{34} & 0 & 0 \\ 0 & 0 & p_{43} & p_{44} & p_{45} & 0 \\ 0 & 0 & 0 & p_{54} & p_{55} & p_{56} \\ 0 & 0 & 0 & 0 & ra & rb \end{bmatrix}, \quad \hat{Q} = \begin{bmatrix} 0 & \beta & 0 & 0 & 0 & 0 \\ q_{21} & q_{22} & q_{23} & q_{24} & q_{25} & q_{26} \\ q_{31} & q_{32} & q_{33} & q_{34} & q_{35} & q_{36} \\ q_{41} & q_{42} & q_{43} & q_{44} & q_{45} & q_{46} \\ q_{51} & q_{52} & q_{53} & q_{54} & q_{55} & q_{56} \\ 0 & 0 & 0 & 0 & -\beta & 0 \end{bmatrix}. \tag{2.4.6}$$

Reproduced in Tables 2.4–2.6 is a numerical solution for the matrices $\hat{H}$, $\hat{P}$ and $\hat{Q}$ (from which $\hat{V}$ and $\hat{W}$ can be obtained) for a grid ratio of $r = 2$. Evaluation of $\hat{V} = \hat{H}\hat{P}$ confirms that it is positive definite. Note that this solution is not unique, as even similar numerical solutions will vary after some significant figures, depending on the distribution of the error across the solution by the minimization routine.

$$\begin{aligned}
h_{12} &= -0.12324024847848997101643979 16 \\
h_{13} &= -0.03133315275213111324616644 60 \\
h_{14} &= 0.85269971985340694716421239 89 \times 10^{-5} \\
h_{15} &= 0.11860746785502789792431677 28 \times 10^{-3} \\
h_{23} &= 0.06187904919436480596950252 74 \\
h_{24} &= -0.03065823791433004750303446 36 \\
h_{25} &= 0.00408033232237213282647838 22 \\
h_{32} &= -0.14028558242379875813142039 90 \\
h_{34} &= 0.05239255800244507961115328 35 \\
h_{35} &= -0.01296938621920128225701920 23 \\
h_{42} &= 0.01020430657499842054022369 73 \\
h_{43} &= -1.47022529872013555697862272 29 \\
h_{45} &= -0.11575249667458256582304677 57 \\
h_{52} &= 0.00092012345275652849152437 36 \\
h_{53} &= -0.19896595626666399077096291 49 \\
h_{54} &= 0.13595331494923112642912419 20 \\
h_{62} &= 0.24615372487607313952940444 62 \times 10^{-3} \\
h_{63} &= 0.04117523076538650957600046 09 \\
h_{64} &= -0.03068595658037724236968825 72 \\
h_{65} &= -0.12543901701600804235995340 78
\end{aligned}$$

Table 2.4: Coefficients of $\hat{H} = \{h_{ij}\}$ for the fourth-order implicit scheme with $r = 2$

$$
\begin{aligned}
p_{21} &= 0.24249788533015605877893969 58 & p_{22} &= 1.06409044228026781720538998 04\\
p_{23} &= -0.13262867616501410701173634 83 & p_{32} &= 0.04351123458346305481241106 65\\
p_{33} &= 1.60802048028942154848725621 26 & p_{34} &= -0.07834787403622254247062743 05\\
p_{43} &= 2.36932779068267048605543830 99 & p_{44} &= 1.58119431054606984243840388 97\\
p_{45} &= 0.49607173110723153138130189 04 & p_{54} &= 0.05188561370518904416446756 30\\
p_{55} &= 1.84556666821574222599937381 06 & p_{56} &= 0.50327149569999915359504284 43
\end{aligned}
$$

Table 2.5: Coefficients of $\hat{P} = \{p_{ij}\}$ for the fourth-order implicit scheme with $r = 2$

$$
\begin{aligned}
q_{21} &= -0.76125776999234329947115965 50 & q_{22} &= 0.11432577940623282346047532 02\\
q_{23} &= 0.84731715727001746654103511 97 & q_{24} &= -0.23960132522322968364375430 25\\
q_{25} &= 0.04525849663223657410163818 74 & q_{26} &= -0.00604233809291408871143246 81\\
q_{31} &= 0.00216634894056589700674923 37 & q_{32} &= -0.81063929810578478468428100 24\\
q_{33} &= 0.15446170548540313835421816 72 & q_{34} &= 0.77096613579953759971654605 29\\
q_{35} &= -0.12683997178558630092759069 73 & q_{36} &= 0.00988507966586447442518967 19\\
q_{41} &= 0.00588475636453726668381946 35 & q_{42} &= -0.97163625879009501953553619 78\\
q_{43} &= -0.62543594739052595845414433 87 & q_{44} &= 1.05174961440072888328020152 16\\
q_{45} &= 0.52890271505529722707641044 22 & q_{46} &= 0.01053512036005769930575814 72\\
q_{51} &= 0.00195293715296038686855735 64 & q_{52} &= -0.04971310472034828779557907 97\\
q_{53} &= 0.21798529104201816012948307 40 & q_{54} &= -0.72732140303886238891074680 22\\
q_{55} &= -0.19093455708075995569429742 09 & q_{56} &= 0.74803083664499207653500519 48
\end{aligned}
$$

Table 2.6: Coefficients of $\hat{Q} = \{q_{ij}\}$ for the fourth-order implicit scheme with $r = 2$

The interface scheme for the inverse ratio $r = 1/2$ may be obtained from this solution by the same procedure described for the explicit scheme. For higher grid ratios, no solution has been found for $r = 4$ that satisfies the SBP conditions, but it is possible such a solution may exist in an unexplored region of the parameter space.

To demonstrate that the matrices $\hat{P}$ and $\hat{Q}$ as derived here do indeed lead to a stable scheme, Figure 2.3 shows the eigenvalue spectrum of the matrix $-P^{-1}\tilde{Q}$ for a domain of 30 points having two blocks of 15 points each, with an interface between them of a grid ratio $r = 2$. The boundary closure used is that given in Appendix B for the implicit fourth-order scheme. The matrix $\tilde{Q}$ is as defined by equation (2.2.23), representing application of an upstream boundary condition by the SAT method with $\tau = 2$ used for this plot. We observe that the real part of each eigenvalue is indeed negative, so the scheme is asymptotically

stable by equation (2.2.25).

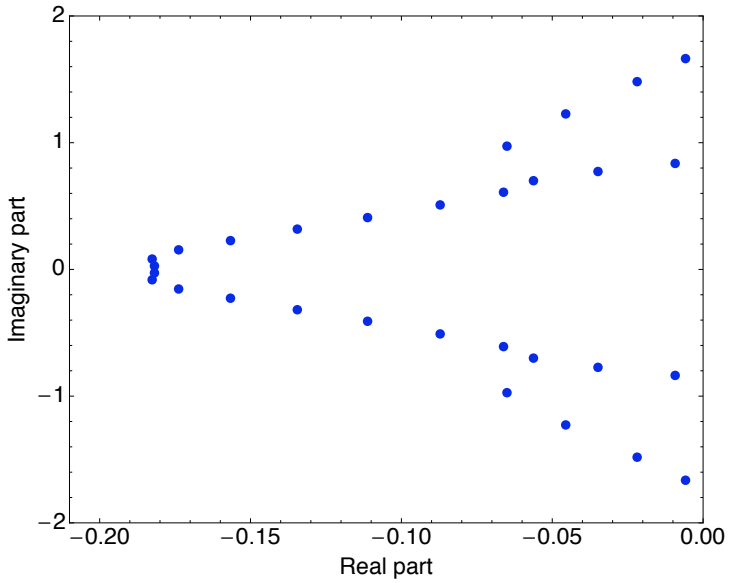

Figure 2.3: Eigenvalues of the matrix $-P^{-1}\tilde{Q}$ for a 30-point domain with an interface of $r = 2$. The grid has two blocks of 15 points each, the first block with discretization Δx and the second with $2\Delta x$. As desired, all eigenvalues lie in the left half of the complex plane.

2.5 Properties of the Interface Schemes

In this section, the spectral and stability properties of the interface schemes derived in Sections 2.3 and 2.4 are examined. We are interested in discovering what effect, if any, the presence of grid interfaces has on the spectral resolution of the grid and its stability when implemented with familiar time-marching schemes.

2.5.1 Spectral Accuracy Estimate

The standard technique for spectral analysis of finite-difference schemes (see Lomax et al., 2001, for example) is difficult to adapt to the interface problem, where the discretization size is nonuniform. A more simple and similarly valuable analysis is provided by Jameson (2003), which estimates the highest mode a given grid may support.

Consider the Fourier series representation of the field, $u(x,t)$,

$$u(x,t) = \sum_k a_k(t) \mathrm{e}^{\mathrm{i}kx}, \tag{2.5.1}$$

defined on $0 \leq x < 2\pi$, where k is the wave number. Its exact derivative is given by

$$\frac{\partial u}{\partial x} = \sum_k a_k(t) \frac{\mathrm{d}}{\mathrm{d}x} \mathrm{e}^{ikx} = \sum_k ika_k(t) \mathrm{e}^{\mathrm{i}kx}, \tag{2.5.2}$$

which is approximated with a general finite difference scheme of order s,

$$\frac{\partial u}{\partial x} \approx \frac{1}{\Delta x} \sum_j q_j f(x_j), \tag{2.5.3}$$

where $\Delta x = 2\pi/N$. The resulting truncation error of the kth mode will be of order $(\Delta x)^{s-1} k^s$. For the test function $u(x) = \mathrm{e}^{\mathrm{i}mx}$, the derivative approximation has the upper bound

$$|\max(\frac{\mathrm{d}u}{\mathrm{d}x})| = \left| \frac{1}{\Delta x} \sum_j q_j \mathrm{e}^{\mathrm{i}mx_j} \right| \leq \frac{1}{\Delta x} \sum_j |q_j| |\mathrm{e}^{imx_j}| = \frac{N}{2\pi} \sum_j |q_j|. \tag{2.5.4}$$

By the Nyquist theorem, the highest discrete Fourier mode that can exist on the interval $0 \leq x < 2\pi$ is $N/2$, so the spectral limit of equation (2.5.4) is $N/2$. (Note that a centered difference scheme will always return zero for this mode.) Table 2.7 shows the maximum derivative value for some typical schemes.

Spectral scheme	2nd-order explicit	4th-order explicit	6th-order explicit
$N/2$	$N/2\pi$	$3N/4\pi$	$11N/12\pi$

Table 2.7: Spectral limits for standard discrete derivative approximations

Since the sum $\sum |q_j|$ is trivial to compute for any explicit scheme, we can investigate the spectral limit of the interface schemes. For the fourth-order explicit interface scheme from Section 2.3.2 with $r = 2$, we find for each of the four interface nodes,

$$\sum_j |\hat{q}_{ij}| = (1.8035, 1.2107, 1.6860, 0.7572).$$

This is based on the fine grid resolution Δx, so the fine grid has a spectral maximum derivative approximation of $\frac{N}{2\pi} \cdot \frac{3}{2}$. The coarse grid has local $\Delta x = 4\pi/N$, so we obtain the bound $\frac{N}{2\pi} \cdot \frac{3}{2} = \frac{N}{2\pi} \cdot \frac{3}{4}$. This gives the spectral maximum derivative that can be supported on the grid: thus we see that the interface does no worse ($0.7572 > 0.75$) than the coarse grid, and the scheme does not degrade the overall spectral accuracy of the domain. The same applies for the inverse refinement ratio.

For the sixth-order explicit scheme from Section 2.3.4,

$$\sum_j |\hat{q}_{ij}| = (4.9114, 12.145, 3.2035, 13.943, 1.1264, 0.97337).$$

By the same argument as for the fourth-order scheme, the limiting coarse grid spectral maximum is $\frac{N}{2\pi} \cdot \frac{11}{12}$, and again the interface is no worse than the coarse grid ($0.97337 > 0.9167$) so the overall spectral accuracy is not degraded.

2.5.2 Truncation Errors

It was made clear in Sections 2.3 and 2.4 that to find an interface closure that satisfies the summation-by-parts conditions, the order of accuracy at the interface points must drop below the interior order of accuracy. Here we examine the truncation errors of each interface scheme to quantify the error that is introduced by the interface closure. Note that Δx is the fine resolution in each of the following examples, as elsewhere in this chapter, and in each case an interface with $r = 2$ is considered.

The truncation error is measured by Taylor series expansion of the difference

$$\frac{\mathrm{d}u_i}{\mathrm{d}x} - \sum_j \hat{d}_{ij} u_j, \tag{2.5.5}$$

for each node i across the interface, where $\hat{d}_{ij}$ are the elements of $\hat{D} = \hat{P}^{-1}\hat{Q}$. For a scheme accurate to order s, the truncation error is proportional to Δx^s.

2.5.2.1 Explicit Fourth-Order Interface Scheme

For the 4-3-3-4 explicit interface scheme, the formal construction of the finite-difference approximation by equation (2.2.4) has the inner two interface points third-order accurate. When evaluating D, however, the third-order truncation error is distributed among the four interface nodes, but this is the more appropriate form in which to evaluate the explicit scheme as this is the form in which the interface closure is implemented. Table 2.8 shows the truncation error for this scheme, with the error of the interior fourth-order explicit scheme shown for comparison.

Point	Truncation error	
Interior (fine)	$\frac{1}{30}\Delta x^5$	$\approx 0.03333\Delta x^5$
Interface $i = 1$	$\frac{4210842691355}{20184098559776}\Delta x^4$	$\approx 0.2086\Delta x^4$
Interface $i = 2$	$\frac{1625251526085}{20184098559776}\Delta x^4$	$\approx 0.08052\Delta x^4$
Interface $i = 3$	$\frac{4031538798845}{5046024639944}\Delta x^4$	$\approx 0.7990\Delta x^4$
Interface $i = 4$	$-\frac{20349849335}{630753079993}\Delta x^4$	$\approx -0.03226\Delta x^4$
Interior (coarse)	$\frac{8}{15}\Delta x^5$	$\approx 0.5333\Delta x^5$

Table 2.8: Truncation errors for each point across the interface with the 4-3-3-4 explicit scheme and $r = 2$

2.5.2.2 Explicit Sixth-Order Interface Scheme

The sixth-order explicit scheme shown in Section 2.3.4 is formally fifth order at the inner four of the six interface points. As for the fourth-order scheme, upon evaluating the matrix D for implementation of the scheme, the fifth-order error is distributed among all six points. The truncation errors at each point of the $r = 2$ interface are presented in Table 2.9. Decimal values for the leading term coefficients are given to simplify comparison; exact rational values may be determined but are too unwieldy to present here.

Point	Truncation error
Interior (fine)	$-\frac{1}{140}\Delta x^7 \approx -0.00714286\Delta x^7$
Interface $i = 1$	$1.25136\Delta x^6$
Interface $i = 2$	$-3.16503\Delta x^6$
Interface $i = 3$	$-1.09049\Delta x^6$
Interface $i = 4$	$-4.38714\Delta x^6$
Interface $i = 5$	$0.21892\Delta x^6$
Interface $i = 6$	$-0.0698666\Delta x^6$
Interior (coarse)	$-\frac{16}{35}\Delta x^7 \approx -0.457143\Delta x^7$

Table 2.9: Truncation errors for each point across the interface with the 6-5-5-5-5-6 explicit scheme and $r = 2$

2.5.2.3 Implicit Fourth-Order Interface Scheme

Truncation errors for the fourth-order implicit scheme are determined from the Taylor expansion of

$$\sum_j \hat{p}_{ij} \frac{\mathrm{d}u_j}{\mathrm{d}x} - \sum_j \hat{q}_{ij} u_j, \tag{2.5.6}$$

because this is the form in which the scheme is implemented. The scheme derived in Section 2.4.2 is formally fourth-order accurate at the outer two points, and since the error is not distributed as in the explicit cases, this is preserved in the truncation error values presented in Table 2.10. Note that these values are subject to some uncertainty due to the numerical solution, so are valid to only three or four significant figures in general. See also that although the accuracy conditions were imposed on $\hat{V}$ and $\hat{W}$ in the derivation of the stencil, $\hat{P}$ and $\hat{Q}$ do properly satisfy the same conditions.

Point	Truncation error
Interior (fine)	$\frac{1}{120}\Delta x^5 \approx 0.008333\Delta x^5$
Interface $i = 1$	$0.07445\Delta x^5$
Interface $i = 2$	$0.2346\Delta x^4$
Interface $i = 3$	$0.5403\Delta x^4$
Interfcae $i = 4$	$0.2482\Delta x^5$
Interior (coarse)	$\frac{4}{15}\Delta x^5 \approx 0.2667\Delta x^5$

Table 2.10: Truncation errors for each point across the interface with the 4-3-3-4 implicit scheme and $r = 2$

2.5.3 Time-Marching Stability

In this section we consider the fully discrete version of equation (2.2.1), having chosen a time-marching scheme for the semidiscrete equation (2.2.25). The stability analysis for explicit Runge-Kutta methods in the uniform grid case is presented in Appendix A.2, but here it is generalized to nonuniform discretizations.

First, the semidiscrete equation is written in terms of a generalized difference matrix $D = P^{-1}Q$,

$$\frac{\mathrm{d}\mathbf{u}}{\mathrm{d}x} = -c\frac{1}{\Delta x} D\mathbf{u} = A\mathbf{u}, \tag{2.5.7}$$

the right-hand side of which is in the form of equation (2.2.6). Following Appendix A.2, the time-marching scheme has the diagonalization of S, where

$$S = X\Lambda^S X^{-1}, \tag{2.5.8}$$

where $\Lambda^S = \text{diag}\left(\lambda^S\right) = \text{diag}\left(\sigma(\lambda^A)\right)$. From equation (2.5.7), the eigenvalues of A are related directly to the eigenvalues of the difference scheme by

$$\lambda^A = -\frac{c}{\Delta x}\lambda^D. \tag{2.5.9}$$

Thus stability is directly dependent on the eigenvalues of the difference matrix D, λ^D. This gives the discrete stability criteria following equation (A2.5),

$$|\sigma(-C\lambda^D)| < 1, \tag{2.5.10}$$

where the time increment has been written in terms of the CFL number

$$C = \frac{c\Delta t}{\Delta x}. \tag{2.5.11}$$

This result gives the discrete stability bound for a given difference matrix D. Note that any change to the grid will change the form of D and potentially its limiting eigenvalue, so care is required when defining the stability bound on the CFL number. Also, for a grid with periodic boundaries and a centered finite-difference scheme, the eigenvalues λ^D are purely imaginary. The following sections investigate the discrete stability bounds for the fourth-order explicit scheme and the corresponding interface solution from Section 2.3.2, with respect to the third-order RK32 Runge-Kutta time-marching scheme from Butcher (2003) used for the results in Section 2.6.

2.5.3.1 Stability for Uniform Grids

To put the stability limits for grids with local refinement in a proper context, we first examine the uniform grid examples shown in Table 2.11. Four grids of 100 points each were considered, this being enough points for the periodic boundary case to closely approach the theoretical CFL limit for an explicit fourth-order finite-difference scheme with a third-order

Runge-Kutta scheme (determined using the spectral analysis presented in Appendix A.2). The results show that finite boundaries do not affect the CFL stability limit, for values of the SAT parameter τ small enough. For the $\tau = 2$ case, the spectrum of which is shown scaled by the limiting CFL in Figure 2.4, all eigenvalues have negative real parts and stability is limited by the eigenvalues with the largest imaginary part. For larger τ, stability becomes constrained by the eigenvalue with the largest negative real part, which significantly reduces the CFL limit compared to the periodic case.

Grid	CFL limit
Theoretical, periodic boundaries	1.2622
Finite matrix, periodic boundaries	1.2627
SAT boundaries, $\tau = 2$	1.2630
SAT boundaries, $\tau = 4$	0.3765
SAT boundaries, $\tau = 6$	0.2193

Table 2.11: Stability bounds for a uniform grid with the fourth-order explicit finite-difference scheme. The theoretical value for a periodic grid is obtained by spectral analysis, and the remaining values from the minimum eigenvalue of a 100-point domain.

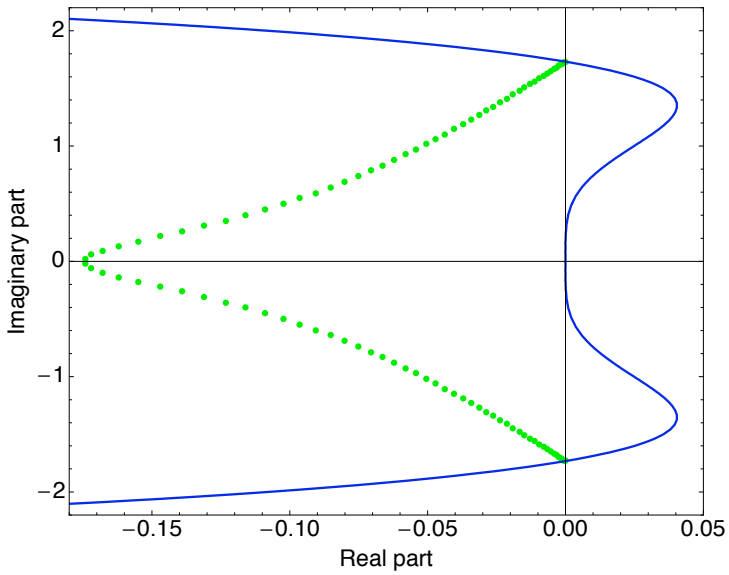

Figure 2.4: Eigenvalue spectrum for a 100-point uniform grid using the fourth-order explicit scheme and SAT boundary conditions with $\tau = 2$. Values are scaled by the limiting CFL to lie within the blue line indicating the stability boundary for the third-order Runge-Kutta scheme.

2.5.3.2 Stability for Nonuniform Grids

Two different grids, each of 100 points, are considered to explore the effect of local refinement on time-marching stability, with results shown in Table 2.12. The first grid has a central refinement region, the domain being split into three blocks of 30, 40 and 30 points each. The central block of 40 points has a discretization of Δx, with the other two blocks having $2\Delta x$, for a refinement scheme 2:1:2. This arrangement permits this grid to have periodic boundary conditions, in which case the eigenvalues are (as expected) purely imaginary and the CFL stability limit is noticeably reduced compared to the uniform grid case. With finite boundaries implemented by the SAT method with $\tau = 2$, shown scaled by the limiting CFL in Figure 2.5, the spectrum has eigenvalues with nonpositive real parts (some have zero real parts), but there is no change to the limiting eigenvalue on the imaginary axis and the stability limit is the same as the periodic case. Using $\tau = 6$ brings a small reduction to the CFL limit, but the limiting eigenvalue is now on the real axis and is, in fact, the same as in the uniform grid case. See that $0.4387/2 \approx 0.2193$, the factor of two resulting from the boundary region having discretization $2\Delta x$ in this case compared to Δx in the uniform grid case.

The second grid considered has two blocks of 50 points each, the first of discretization Δx and the second $2\Delta x$, for a refinement scheme 1:2. This grid cannot have periodic boundary conditions as the boundaries have inconsistent discretizations, so the SAT boundary implementation is used instead. With $\tau = 2$, shown scaled by the limiting CFL in Figure 2.6, there is no stability reduction compared to the uniform case due to the interface, and the eigenvalues have all negative real parts. The interface again has no effect compared to the uniform case with $\tau = 6$.

Grid	CFL limit
Three-block refinement, periodic boundaries	0.4851
Three-block refinement, SAT boundaries, $\tau = 2$	0.4851
Three-block refinement, SAT boundaries, $\tau = 6$	0.4387
Two-block refinement, SAT boundaries, $\tau = 2$	1.2652
Two-block refinement, SAT boundaries, $\tau = 6$	0.2193

Table 2.12: Stability bounds for various nonuniform grids with the fourth-order explicit finite-difference scheme. Each limit is calculated from the minimum eigenvalue of a 100-point domain and based on the smallest discretization. See text for a detailed description of each grid configuration.

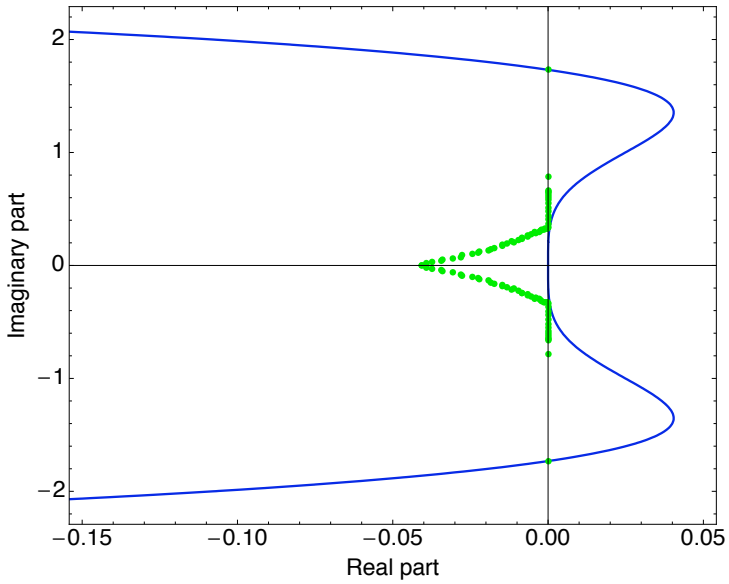

Figure 2.5: Eigenvalue spectrum for the three-block (2:1:2) 100-point grid, using the fourth-order explicit scheme and SAT boundary conditions with $\tau = 2$. Values are scaled by the limiting CFL to lie within the stability boundary of the third-order Runge-Kutta scheme (blue line). Here, $C_{\max} = 0.4851$.

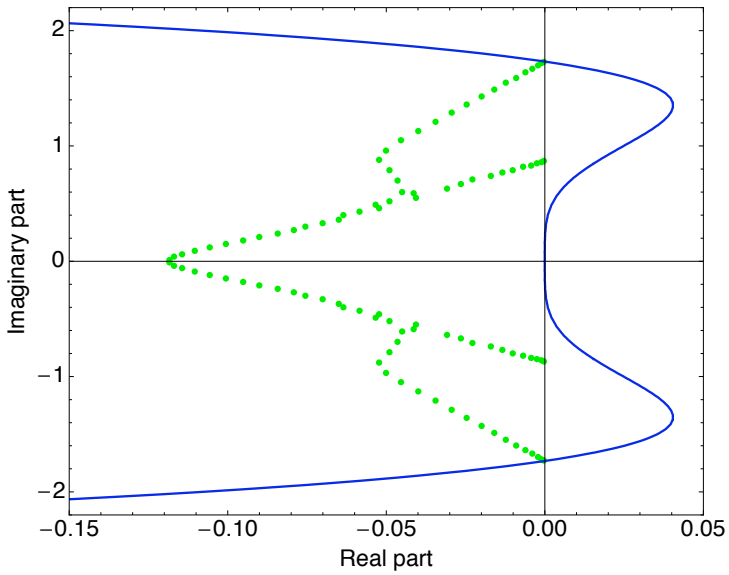

Figure 2.6: Eigenvalue spectrum for the two-block (1:2) 100-point grid, using the fourth-order explicit scheme and SAT boundary conditions with $\tau = 2$. Values are scaled by the limiting CFL to lie within the stability boundary of the third-order Runge-Kutta scheme (blue line). Here, $C_{\max} = 1.2652$.

The conclusion to be drawn from this investigation is that stability of the discrete problem with local refinement is strongly dependent on the form of the grid. The presence of grid interfaces can play a secondary role compared to the implementation of the boundary conditions, but reduction of the CFL limit due to local refinement can be significant for certain schemes. These results are also dependent on the time-marching scheme used; for methods other than Runge-Kutta, the presence of refinement may have a more significant effect or none at all. For the validation problems considered in Section 2.6 and the Richtmyer-Meshkov problem of Chapter 4, a general rule of thumb was that $C \lesssim 0.2$ for stability on most grids. Instability due to the CFL number usually manifested itself at the boundaries first.

2.6 Validation Test Problems

2.6.1 Advecting Wave

For the first validation test, we solve numerically the linear advection equation (2.2.1) to verify that the expected stability and convergence results are obtained. Results are presented for the specific advection problem with boundary and initial conditions

$$u(0,t) = -\sin\frac{2\pi ct}{L}, \qquad t \geq 0, \tag{2.6.1}$$

$$u(x,0) = \sin\frac{2\pi x}{L}, \qquad 0 \leq x \leq L, \tag{2.6.2}$$

having the exact solution

$$u(x,t) = \sin\frac{2\pi}{L}(x-ct),\ 0 \leq x \leq L,\ t \geq 0. \tag{2.6.3}$$

The boundary condition, equation (2.6.1), is applied by the SAT method, with $\tau = 2$, at the first node in the domain. As shown in Figure 2.1, nodes are placed at the center of elements of width Δx, so the first node is located at $\Delta x/2$, and the boundary condition is correspondingly adjusted. Under refinement, the width of each cell (equivalent to the nodal spacing) is reduced and the number of nodes increased by the factor of refinement such that the physical location of the interfaces is fixed in space.

This problem is first solved using an explicit fourth-order finite-difference scheme on a

three-block 1:4:2 grid, with 20 points in the first block and 10 in each of the subsequent blocks for the coarsest case. The first interface has $r_1 = 4$ and the second $r_2 = 1/2$, with closure provided by the four-point 4-3-3-4 interface schemes described in Section 2.3. At the boundary, the four-point 3-3-4-4 boundary closure given in Appendix B is used. Parameter values for the results presented here are $c = 0.25$ and $L = 8$, and the time-marching scheme is the third-order Runge-Kutta RK32 method from Butcher (2003). Five steps of global refinement are performed for the convergence test, the results of which are presented in Table 2.13. The advertised fourth-order convergence rate clearly has been achieved, in both an averaged sense and uniformly, as evidenced by the L_∞ norm. Figure 2.7 presents the solution and error compared to the exact solution for $\Delta x = 1/20$, after two wave transitions through the domain ($T = 2L/c$).

fine Δx	$\log_{10}(L_2)$	rate	$\log_{10}(L_\infty)$	rate
1/10	−2.696		−2.808	
1/20	−3.879	3.93	−4.005	3.98
1/40	−5.074	3.97	−5.212	4.01
1/50	−5.460	3.98	−5.599	3.99
1/80	−6.273	3.99	−6.417	4.01
rate		3.96		4.00

Table 2.13: Convergence results for the explicit scheme solving the 1-D advection equation on a three-block 1:4:2 grid after 10 wave transition times

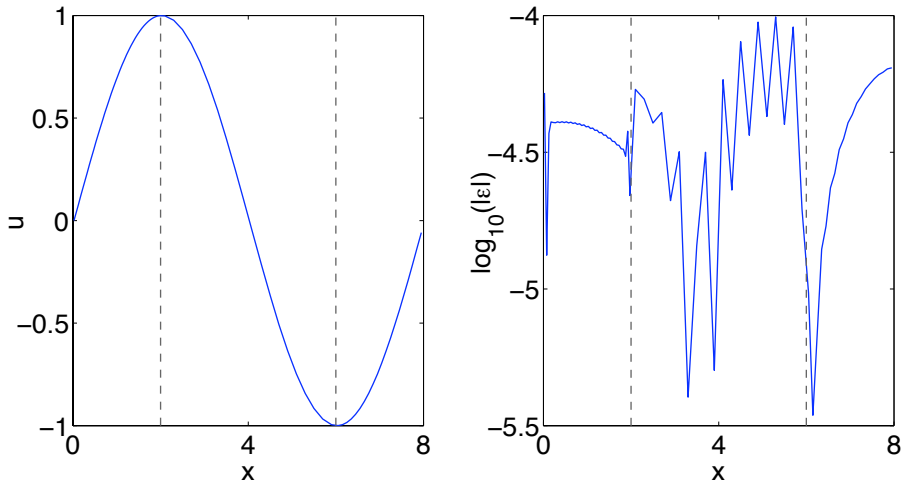

Figure 2.7: Numerical solution and error relative to the exact solution for the 1-D advection equation solved with the fourth-order explicit finite-difference scheme on a three-block 1:4:2 grid, after two wave transitions with $\Delta x = 1/20$. Dashed lines indicate the locations of the grid interfaces.

To test the fourth-order implicit scheme from Section 2.4, a three-block 1:2:1 grid was used, the interfaces having ratios $r_1 = 2$ and $r_2 = 1/2$, respectively. Each block has a minimum of 20 points, with five steps of refinement for the convergence test presented in Table 2.14. Parameter values were as for the explicit test. The advertised fourth-order convergence rate clearly has again been achieved, in both norms. Figure 2.8 shows the solution for the case $\Delta x = 1/20$ with the error relative to the exact solution.

fine Δx	$\log_{10}(L_2)$	rate	$\log_{10}(L_\infty)$	rate
1/10	−4.310		−4.470	
1/20	−5.513	3.99	−5.675	4.00
1/40	−6.713	3.99	−6.892	4.04
1/50	−7.097	3.96	−7.286	4.07
1/80	−7.896	3.91	−8.123	4.10
rate		3.97		4.04

Table 2.14: Convergence results for the implicit scheme solving the 1-D advection equation on a three-block 1:2:1 grid after 10 wave transition times

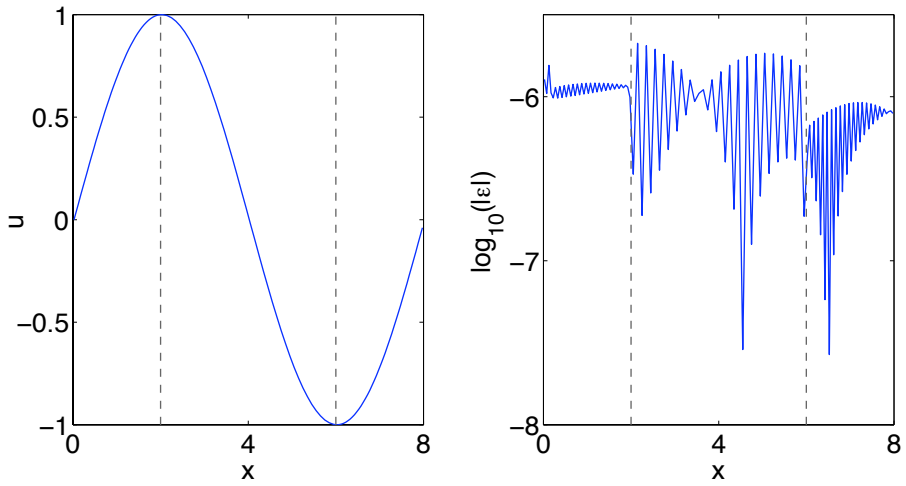

Figure 2.8: Numerical solution and error relative to the exact solution for the 1-D advection equation solved with the fourth-order implicit finite-difference scheme on a three-block 1:2:1 grid, after two wave transitions with $\Delta x = 1/20$. Dashed lines indicate the locations of the grid interfaces.

2.6.2 Navier-Stokes Shock Structure

Having demonstrated stability of the interface schemes with a linear problem, we move on to examine their stability when applied to a nonlinear problem more relevant to practical problems in fluid mechanics. Stability is difficult, if not impossible, to prove in general

for nonlinear problems, but generally follows that of the linear problem. To confirm this, the one-dimensional compressible Navier-Stokes equations are solved for the flow through a fully resolved shock. Although not strictly a hyperbolic system of equations, this problem presents a strong test of stability of the numerical method. To evaluate the viscous terms, the first derivative is applied twice, at the potential risk of (small magnitude) spurious oscillation in the numerical solution. The alternative, to use a specific second-derative stencil, is available only at the boundaries at present (Mattsson and Nordström, 2004); a second-derivative interface scheme in the SBP context is a topic for future research.

A closed-form analytic solution exists to the Navier-Stokes shock problem for the special case of a perfect gas with constant viscosity and Prandtl number $Pr = 3/4$. Applying these simplifications to the 1-D Navier-Stokes equations, following the nondimensionalization in Appendix E.1, we define the reference state as the upstream flow conditions ρ_0, u_0 and p_0, and mean free path length ℓ_0. The resulting equations in terms of dimensionless ρ, u and p are, from (E1.30)–(E1.32),

$$\frac{\partial \rho}{\partial t} + \frac{\partial}{\partial x}(\rho u) = 0, \tag{2.6.4}$$

$$\frac{\partial}{\partial t}(\rho u) + \frac{\partial}{\partial x}\left(\rho u^2 + \frac{p}{\gamma M_0^2} - R'\frac{\partial u}{\partial x}\right) = 0, \tag{2.6.5}$$

$$\frac{\partial}{\partial t}\left(\frac{p}{\gamma M_0^2} + \beta\rho u^2\right) + \frac{\partial}{\partial x}\left(\beta\rho u^3 + \frac{pu}{M_0^2} - R'(\gamma-1)u\frac{\partial u}{\partial x} + \frac{R'}{M_0^2}\frac{\partial}{\partial x}\left(\frac{p}{\rho}\right)\right) = 0, \tag{2.6.6}$$

where $\beta = (\gamma - 1)/2$ and R' is given by

$$R' = \frac{4}{3}\frac{k_2}{\sqrt{\gamma M_0^2}}, \tag{2.6.7}$$

in terms of the constant

$$k_2 = \frac{5}{8}\sqrt{\frac{\pi}{2}}, \tag{2.6.8}$$

which is derived from kinetic theory. This formulation reduces the parameters of the problem to the ratio of specific heats, γ, and the Mach number of the shock, M_0.

For steady flow with $\partial/\partial t \equiv 0$ in the frame of reference where the shock is stationary, and uniform upstream and downstream conditions such that $u = 1$ upstream, we define the shock position coordinate ξ. From Appendix F.1, based on Whitham (1974), the solution

to equations (2.6.4)–(2.6.6) for the velocity profile through a shock is

$$\xi(u) = \frac{1}{k_3(1-\alpha)M_0} \log\left[\left(\frac{\sqrt{\alpha}-\alpha_1}{u-\alpha}\right)^{\alpha} \frac{u-1}{\sqrt{\alpha}-1}\right], \tag{2.6.9}$$

where the velocity ratio $\alpha(M_0, \gamma)$ across the shock is given by the Rankine-Hugoniot relation

$$\alpha = \frac{2+(\gamma-1)M_0^2}{(\gamma+1)M_0^2}, \tag{2.6.10}$$

and k_3 is given by

$$k_3 = \frac{3(\gamma+1)}{8k_1}\sqrt{\frac{\pi}{8\gamma}}. \tag{2.6.11}$$

In obtaining equation (2.6.9), the point $\xi = 0$ is chosen to correspond to the velocity inflection point, $\mathrm{d}^2u/\mathrm{d}\xi^2 = 0$, which fixes the shock in space. For given γ and M_0, (2.6.9) can be solved numerically for u at each position ξ to arbitrary precision; this gives the velocity profile through the shock, and subsequently the density and pressure profiles. We now proceed to solve (2.6.4)–(2.6.6) numerically as an initial-boundary-value problem and consider convergence of the numerical velocity solution to (2.6.9), under the mapping $\xi \to x$.

The numerical problem is solved using a fourth-order finite difference method with the boundary and interface schemes for both explicit and implicit stencils from Sections 2.3.2 or 2.4.2. Implementation of the boundary conditions is by the SAT method, applied to the characteristic form of the equations (detailed in Appendix E.5). The third-order Runge-Kutta time integration scheme from the linear problem is used again, for which, with a CFL number small enough, a stable numerical solution was obtained with $\tau = 2$. Results are presented here for a shock with $M_0 = 2.2$ and $\gamma = 1.4$.

For the explicit scheme, we consider two grids: a reference uniform grid, and a three-block 4:1:4 grid with refinement in the vicinity of the shock. For the three-block grid, the interfaces have grid ratios $r_1 = 4$ and $r_2 = 1/4$, moving from left to right across the domain. The numerical domain extends upstream of the shock to $x = -25$ and downstream to $x = 10$, at which points the difference between the analytic solution and the Rankine-Hugoniot conditions is of the order of machine precision (10^{-16}) for the chosen shock parameters. The initial condition used is the analytic shock solution (2.6.9), evaluated at the nodal positions.

Convergence of the numerical solution error, shown in Tables 2.15–2.16, demonstrates

that the expected fourth-order rate is approached for both grids. Near-fourth-order convergence of the L_∞ norm confirms that convergence is uniform even in the nonlinear case. Figure 2.9 compares the numerical solutions and errors obtained from comparable uniform and three-block grids. In both cases, the smallest discretization is $\Delta x = 1/16$, for a total of 560 points on the uniform grid and 200 on the 4:1:4 three-block grid. With the same time step Δt, the computational cost of the three-block grid is approximately half that of the uniform grid.

Δx	$\log_{10}(L_2)$	rate	$\log_{10}(L_\infty)$	rate
1/4	−3.175		−3.143	
1/5	−3.887	7.35	−3.720	5.95
1/8	−4.717	4.07	−4.538	4.01
1/10	−5.099	3.95	−4.921	3.95
1/16	−5.909	3.97	−5.736	3.99
rate		4.40		4.22

Table 2.15: Convergence results for the Navier-Stokes shock on a uniform grid with the explicit scheme

fine Δx	$\log_{10}(L_2)$	rate	$\log_{10}(L_\infty)$	rate
1/4	−2.651		−2.758	
1/8	−3.652	3.32	−3.776	3.38
1/16	−4.974	4.39	−5.012	4.11
1/20	−5.342	3.80	−5.324	3.21
1/32	−6.143	3.92	−6.029	3.45
rate		3.93		3.68

Table 2.16: Convergence results for the Navier-Stokes shock on a three-block 4:1:4 grid with the explicit scheme

The evolution of numerical error in the equations of motion is shown in Figure 2.10 for the same uniform and three-block grid cases. Plotted are the L_2 norms of the time derivatives from each of equations (2.6.4)–(2.6.6), which in this case are all expected to be zero. Some oscillatory behavior is observed in the solution during the transient phase, but for long times the solution appears to be converging to a stable state.

The shock problem was also solved on a three-block 2:1:2 grid using the implicit finite difference scheme described in Section 2.4.2. Results from this test are shown in Table 2.17, showing again that fourth-order convergence is achieved for the nonlinear problem. Figure 2.11 shows the numerical solution and error at the final time step for a 320-point grid with fine resolution $\Delta x = 1/16$.

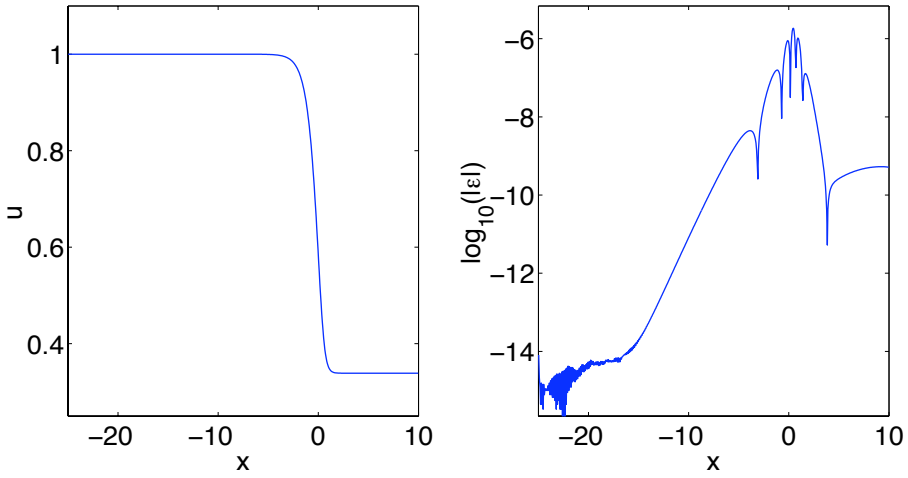

(a) uniform grid

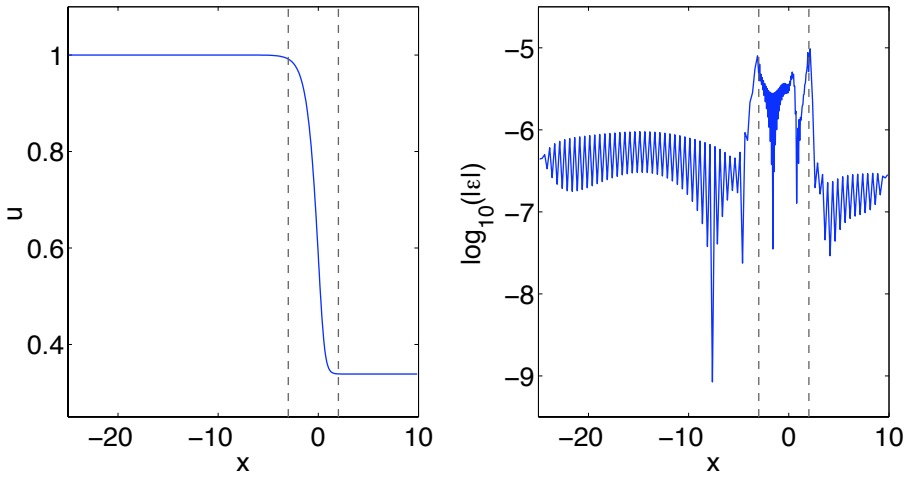

(b) three-block grid

Figure 2.9: Numerical Navier-Stokes shock velocity solution and corresponding point-wise error, for the explicit scheme solved on uniform and three-block 4:1:4 grids. Both solutions shown here have the same minimum discretization, $\Delta x = 1/16$, for a total of 560 points and 200 points respectively. Dashed lines indicate the locations of the grid interfaces.

fine Δx	$\log_{10}(L_2)$	rate	$\log_{10}(L_\infty)$	rate
1/4	−4.004		−3.927	
1/8	−5.359	4.50	−5.202	4.24
1/16	−6.578	4.05	−6.414	4.02
1/20	−6.965	3.99	−6.799	3.97
1/32	−7.800	4.09	−7.666	4.25
rate		4.18		4.12

Table 2.17: Convergence results for the Navier-Stokes shock on a three-block 2:1:2 grid with the implicit scheme

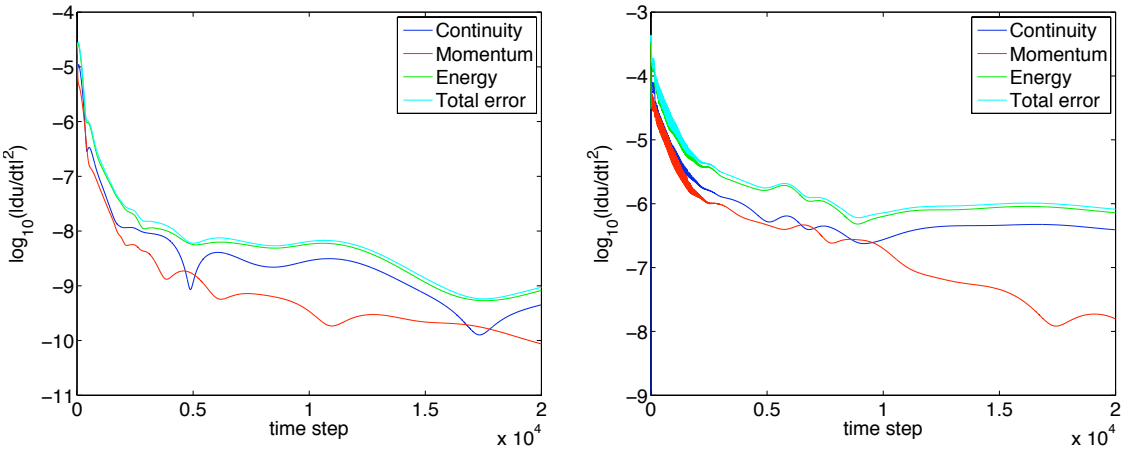

(a) uniform grid (b) three-block grid

Figure 2.10: Behavior of the numerical error in the time derivatives from each equation of motion, for the two grids described in Figure 2.9, over 20,000 time steps.

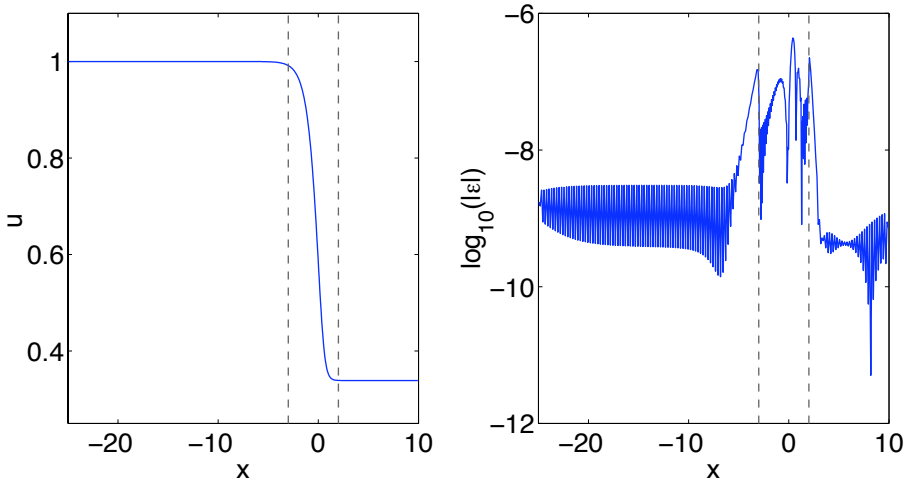

Figure 2.11: Navier-Stokes shock velocity solution and corresponding error plot, for the implicit scheme on a three-block 2:1:2 grid with minimum discretization $\Delta x = 1/16$. Dashed lines indicate the location of the grid interfaces.

2.6.3 Advecting Wave in 2-D

As described in Section 2.1.3, the 1-D interface scheme may be applied to tensor-product–type refinements of higher-dimensional grids. Here we consider the linear problem in 2-D. The two-dimensional scalar advection equation,

$$\begin{aligned} \frac{\partial u}{\partial t} + a\frac{\partial u}{\partial x} + b\frac{\partial u}{\partial y} &= 0, \quad 0 \le x \le 1,\ 0 \le y \le 1,\ t \ge 0, \\ u(0, y, t) &= \sin\left[\omega\left(y/b - 2t\right)\right], \\ u(x, 0, t) &= \sin\left[\omega\left(x/a - 2t\right)\right], \\ u(x, y, 0) &= \sin\left[\omega\left(x/a + y/b\right)\right], \end{aligned} \tag{2.6.12}$$

where a and b represent the advection speeds in the x- and y-directions respectively and ω is a frequency parameter, has the analytic solution

$$u(x, y, t) = \sin\left[\omega\left(x/a + y/b - 2t\right)\right], \tag{2.6.13}$$

and is solved here by a similar implementation as used for the 1-D advection equation. The grid is a unit square with each direction identically divided into five blocks, for a total of 25 blocks, with a factor of 2 refinement between each block for an overall 1:2:4:2:1 scheme ($r = 2$ for the first two interfaces, $r = 1/2$ for the next two) in each direction. The first and last blocks have a minimum of 10 points each, and each of the three remaining blocks has 8 points. The same discretization was used in both x- and y-directions.

Both fourth-order explicit and implicit schemes were tested on this grid. Boundary conditions were implemented by the SAT method, using the same boundary closures as before. The test problem uses parameter values $a = b = 1/4$ and $\omega = \pi/2$, and was run to time $T = 10$. Table 2.18 shows that both average and uniform fourth-order convergence is achieved, for both explicit and implicit schemes.

2.6.4 Inviscid Compressible Vortex in 2-D

For the final example, a nonlinear problem is solved on a similar tensor product-refined two-dimensional grid. Here, the dimensionless compressible Euler equations for a perfect

	Explicit scheme				Implicit scheme			
fine Δx	$\log_{10}(L_2)$	rate	$\log_{10}(L_\infty)$	rate	$\log_{10}(L_2)$	rate	$\log_{10}(L_\infty)$	rate
1/120	−3.604		−3.147		−3.166		−2.751	
1/180	−4.364	4.32	−3.922	4.40	−3.835	3.80	−3.445	3.95
1/240	−4.803	3.51	−4.320	3.19	−4.322	3.90	−3.928	3.87
1/360	−5.507	4.00	−5.017	3.96	−5.018	3.95	−4.625	3.96
rate		3.96		3.87		3.88		3.93

Table 2.18: Convergence results for the 2-D advection equation solved on a grid with tensor-product refinement, for explicit and implicit fourth-order schemes

gas (see Appendix E.2), with parameter $\beta = (\gamma - 1)/2$,

$$\frac{\partial \rho}{\partial t} + \frac{\partial}{\partial x}(\rho u) + \frac{\partial}{\partial y}(\rho v) = 0, \tag{2.6.14}$$

$$\frac{\partial}{\partial t}(\rho u) + \frac{\partial}{\partial x}\left(\rho u^2 + \frac{p}{\gamma M_0^2}\right) + \frac{\partial}{\partial y}(\rho u v) = 0, \tag{2.6.15}$$

$$\frac{\partial}{\partial t}(\rho v) + \frac{\partial}{\partial x}(\rho u v) + \frac{\partial}{\partial y}\left(\rho v^2 + \frac{p}{\gamma M_0^2}\right) = 0, \tag{2.6.16}$$

$$\begin{aligned}&\frac{\partial}{\partial t}\left(\frac{p}{\gamma M_0^2} + \beta\rho\left(u^2+v^2\right)\right)\\ &\quad + \frac{\partial}{\partial x}\left(\frac{pu}{M_0^2} + \beta\rho u\left(u^2+v^2\right)\right) + \frac{\partial}{\partial y}\left(\frac{pv}{M_0^2} + \beta\rho v\left(u^2+v^2\right)\right) = 0,\end{aligned} \tag{2.6.17}$$

are used with a normalization in terms of far-field values, ρ_0 and p_0, and a velocity scale, u_0, which are incorporated into the Mach number parameter, M_0. An analytic solution exists for a constant-entropy vortex with the tangential velocity profile

$$\frac{u_\theta}{u_0} = \frac{r_0}{r}\left(1 - \mathrm{e}^{-\frac{r^2}{r_0^2}}\right), \tag{2.6.18}$$

where $r = \sqrt{x^2+y^2}$, and r_0 is the core radius of the vortex. This is the Lamb-Oseen vortex solution, the details of which are presented in Appendix F.2 along with its density and pressure distribution. Note that for $\gamma = 1.4$, with $M_0 \lesssim 1.35$, the flow is subsonic everywhere (based on local Mach number), and for $M_0 \lesssim 1.9$, there is no evacuation at the core of the vortex. Parameter values of $M_0 = 1.2$ and $r_0 = 4/25$ were used for the results presented here.

The problem is solved numerically with the explicit fourth-order scheme and the third-order Runge-Kutta time-marching scheme on a grid similar to that used for the advection problem of Section 2.6.3, with a domain of side length 4. The same 1:2:4:2:1 refinement

in each direction is used, now with a minimum of 14 points in the coarse blocks, 16 in the intermediate blocks and 24 in the most refined central block for an 84×84–node grid at the largest minimum discretization ($\Delta x = 1/50$). Five steps of global refinement were performed for the convergence test, down to $\Delta x = 1/150$ and a 252×252–node grid. Exact boundary conditions are applied on all edges, using the analytic solution based on equation (2.6.18) to provide solution values as a continuation of the domain, avoiding the need for boundary stencils.

Results are taken at time $t = 2$ for both a static vortex located at the center of the domain and for a vortex convecting across the domain with speed $(0.35, 0.55)$. The initial condition for the convecting vortex is such that at $t = 1$, the core is centered in the domain, and it thus moves from one side of the most refined region to the other during the simulation. This is shown in the vorticity contour plots of Figure 2.12, where the grid interfaces are indicated by dashed lines. Table 2.19 demonstrates that fourth-order convergence is obtained for both examples.

	Static vortex				Convecting vortex			
fine Δx	$\log_{10}(L_2)$	rate	$\log_{10}(L_\infty)$	rate	$\log_{10}(L_2)$	rate	$\log_{10}(L_\infty)$	rate
1/50	−2.567		−2.261		−2.163		−1.581	
1/75	−3.254	3.90	−2.826	3.21	−2.881	4.08	−2.322	4.21
1/100	−3.794	4.32	−3.343	4.15	−3.406	4.20	−2.894	4.58
1/125	−4.215	4.34	−3.760	4.30	−3.791	3.97	−3.192	3.08
1/150	−4.556	4.31	−4.168	5.16	−4.098	3.88	−3.571	4.78
rate		4.18		3.98		4.07		4.14

Table 2.19: Convergence results for the 2-D compressible vortex solved on a grid with tensor-product refinement, for explicit and implicit fourth-order schemes

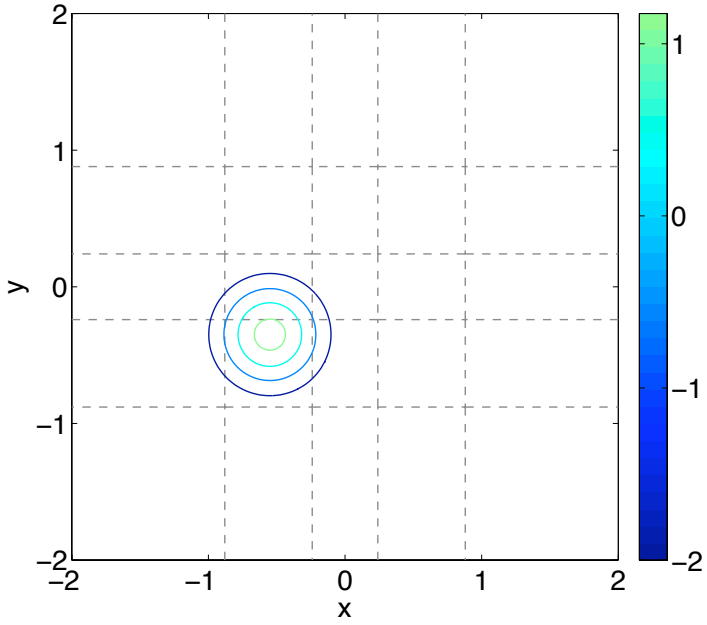

(a) vorticity field at $t = 0$

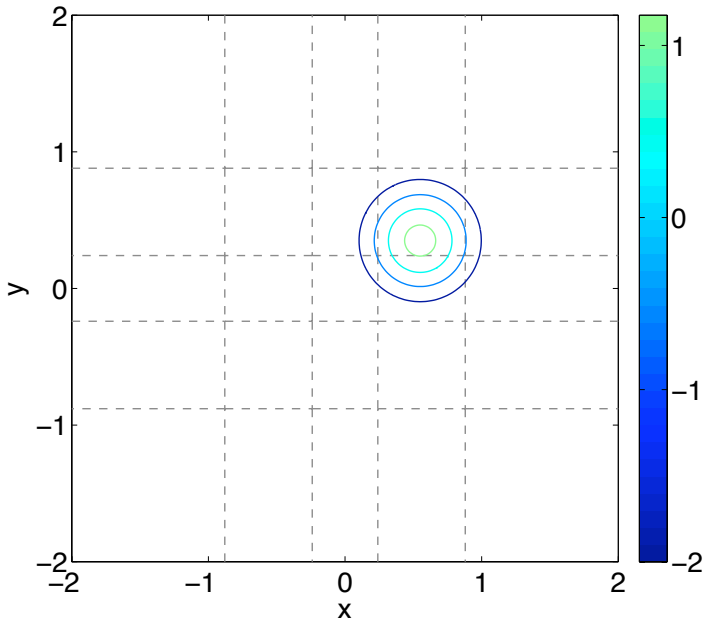

(b) vorticity field at $t = 2$

Figure 2.12: Solution for the convecting inviscid compressible vortex: contours of vorticity showing the initial and final vortex positions. Grid interfaces are indicated by dashed lines and the color scale is $\log_{10}(\omega)$.

Chapter 3

The 2-D Interface Problem

This chapter describes the two-dimensional patch-refined interface problem and its solution, building on the one-dimensional solution presented in Chapter 2. The unique geometries encountered in the 2-D problem are described in Section 3.1, with the 2-D extension to the summation-by-parts theory from Section 2.2 presented in Section 3.2. The interface solutions built on these two components are presented in Section 3.3, and tested in Section 3.4, which shows results from both linear and nonlinear validation problems. An algorithm for implementation of the interface schemes is briefly described in Appendix C.

3.1 Patch Refinement in 2-D

3.1.1 Definition of the Grid

To introduce the two-dimensional problem, consider the scalar advection equation

$$\frac{\partial u}{\partial t} + a\frac{\partial u}{\partial x} + b\frac{\partial u}{\partial y} = 0, \quad (x, y) \in \Omega, \quad t \geq 0, \tag{3.1.1}$$

where a square domain $\Omega = \{(x, y) \in [0, 1] \times [0, 1]\}$ is chosen for simplicity, with initial condition $u(x, y, 0) = u_0(x, y)$ and boundary conditions (for $a > 0$ and $b > 0$),

$$u(0, y, t) = g^x(y, t), \quad t \geq 0, \tag{3.1.2}$$

$$u(x, 0, t) = g^y(x, t), \quad t \geq 0. \tag{3.1.3}$$

The numerical solution to this problem is sought on a node-based finite-volume partition of the domain, chosen over a vertex-based discretization because of its wide use in adaptive

mesh refinement methods (Berger and Colella, 1989; Pantano et al., 2007). Certain regions of this domain are locally refined relative to the original discretization; first, we define the nature of this refinement.

Consider a uniform discretization of the domain Ω into computational cells of size $\Delta x \times \Delta y$, with $\Delta x = 1/N$ and $\Delta y = 1/M$. Under local refinement, Ω is partitioned into two subdomains by $\Omega = \Omega^f \cup \Omega^c$, where the fine region is a block of refined cells defined by

$$\Omega^f \equiv \{(x, y) \in [n_L \Delta x, n_H \Delta x] \times [m_L \Delta y, m_H \Delta y]\},$$

with $0 < n_L < n_H < N$, $0 < m_L < m_H < M$ and $(n_L, n_H, m_L, m_H) \in \mathbb{N}$. The fine region thus occupies an interior part of Ω, with each edge extending over an integer number of coarse cells. Note that in general, Ω^f may include a number of such refined blocks of cells. Within Ω^f, the discretization is refined by ratios r_x and r_y in the x- and y-directions, respectively, for computational cells of size $(\Delta x/r_x) \times (\Delta y/r_y)$, and it is generally required that $1 < r_x, r_y \in \mathbb{N}$. Additional resolution is thus provided for the problem in Ω^f. The remaining coarse region $\Omega^c = \Omega \setminus \Omega^f$, has the original cell dimensions. A sketch of such a partition is shown in Figure 3.1. Dirichlet boundary conditions (3.1.2)–(3.1.3) are imposed on $\Gamma^D = \{(x, y) \in ([0, 1] \times 0) \cup (0 \times [0, 1])\}$, where $\partial\Omega = \Gamma^D + \Gamma^N$. Note that this partitioning of the domain does not affect the equations or boundary conditions.

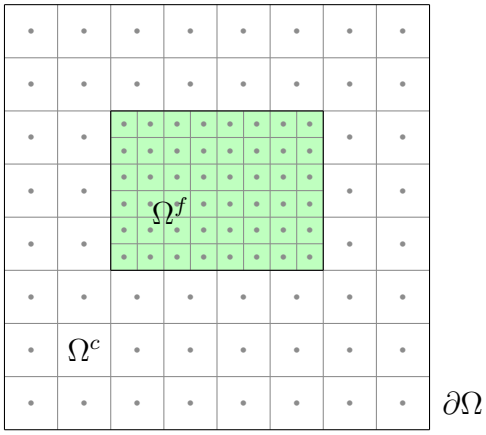

Figure 3.1: Sketch of the partitioning of the domain Ω into the fine region Ω^f (shaded) and coarse region Ω^c.

A numerical method to solve equation (3.1.1) is constructed by approximation of $u(x, y, t) = u^c(x, y, t) + u^f(x, y, t)$, where u^c and u^f are the partitions of u to Ω^c and Ω^f, respec-

tively. Locating nodes at the cell centers in each subdomain, u is discretized such that $u^c(x_I, y_J, t) \approx u^c_{I,J}(t)$, where $x_I = \Delta x(I - 1/2)$ and $y_J = \Delta y(J - 1/2)$, over the index set

$$\mathcal{I}^c = \{(I, J) \in [1, N] \times [1, M] \setminus [n_L + 1, n_H] \times [m_L + 1, m_H]\},$$

and $u^f(x_i, y_j, t) \approx u^f_{i,j}(t)$, where $x_i = \Delta x(n_L + (i-1/2)/r_x)$ and $y_j = \Delta y(m_L + (j-1/2)/r_y)$, over the index set

$$\mathcal{I}^f = \{(i, j) \in [1, (n_H - n_L)r_x] \times [1, (m_H - m_L)r_y]\},$$

where the complete index set $\mathcal{I} = \mathcal{I}^c \cup \mathcal{I}^f$. Let $\mathbf{u} = \{u^c_{I,J}, u^f_{i,j}\} = \{u_\mathcal{I}\}$ denote the discrete approximation to u at the nodes $\mathcal{I}$; no particular ordering of the index set is implied. The resulting approximation of equation (3.1.1) yields a system of ordinary differential equations, which are integrated numerically in time using an appropriate time-integration method, e.g., Runge-Kutta in our case.

3.1.2 Interface Types

The present objective is to develop an explicit finite-difference scheme of the two-dimensional domain with a cell-centered mesh. Approximation of the first derivative at interior cells, away from the interface at $\partial\Omega^f$, is accomplished using standard centered finite-difference techniques. Near $\partial\Omega^f$, there are two prevailing approaches to dealing with the irregular node locations at the interface. The first solves equation (3.1.1) as separate problems on each subdomain Ω^c and Ω^f, using a compatibility condition to transfer information between subdomains. This compatibility condition can be viewed as an addition to the original problem. Examples of this approach include Nordström and Carpenter (1999); Gerritsen and Olsson (1998); Sebastian and Shu (2003). The second approach solves (3.1.1) on the full domain, assuming that a continuous and differentiable function $u(x, y, t)$ exists and is well defined across the grid interfaces. This leaves the problem of the change in resolution to be resolved by the numerical method, where special stencils are required to approximate the spatial derivative in the vicinity of $\partial\Omega^f$. This is the approach considered here.

The historical difficulty encountered with this approach is the appearance of "hanging nodes" at the grid interface, as nodes do not align with Cartesian lines passing through

the cell centers on each side. This problem has made achieving simultaneous high-order accuracy and long-time stability of the interface closure difficult, and is addressed here.

A consequence of the hanging-node geometry is a strong dependence of the interface closure on the refinement ratio. Figure 3.2(a) shows an interface with a refinement factor of 2 in each direction, where an interface stencil for the coarse node would include dependence on four fine nodes, whereas in Figure 3.2(b), with a factor 4 refinement, the same node is now dependent on 16 fine nodes in an equivalent area. In general, this means that an interface stencil cannot have a simple functional dependence on r_x or r_y in the way that the one-dimensional scheme could, cf. Chapter 2. We therefore fix the refinement ratios at $r_x = r_y = 2$ from this point forward, but the discussion presented here may be followed for any integer refinement ratio, though without guarantee that a solution exists.

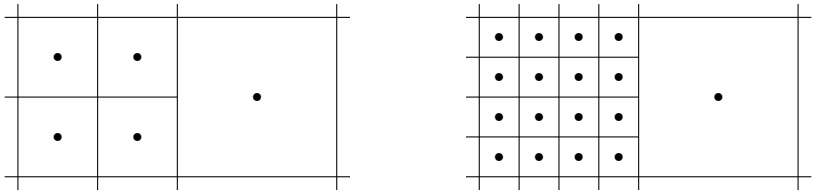

(a) 2× refinement (b) 4× refinement

Figure 3.2: Sketch showing the dependence of the interface topology on the refinement factor: compare (a) refinement factor 2 in each direction, with (b) refinement factor 4 in each direction.

For a general refined region Ω^f, three basic interfaces may be identified, each with a unique topology. These are sketched in Figure 3.3: (a) shows the edge interface, corresponding to the Cartesian edges of $\partial\Omega^f$ where the change in discretization is essentially in one direction only; (b) shows the convex corner interface, where two edges meet at a corner of $\partial\Omega^f$ that is convex relative to Ω^f; and (c) shows the concave corner interface, where the corner is concave relative to the fine region. Other more complex interfaces may be devised, but these three elements are sufficient to build in a domain any arbitrarily refined interior region satisfying simple rules regarding its size such that each interface geometry remains distinct. Multiple levels of refinement, obtained by embedding additionally refined subdomains within Ω^f, present no additional closure problems, as the interface geometries are logically identical to those shown.

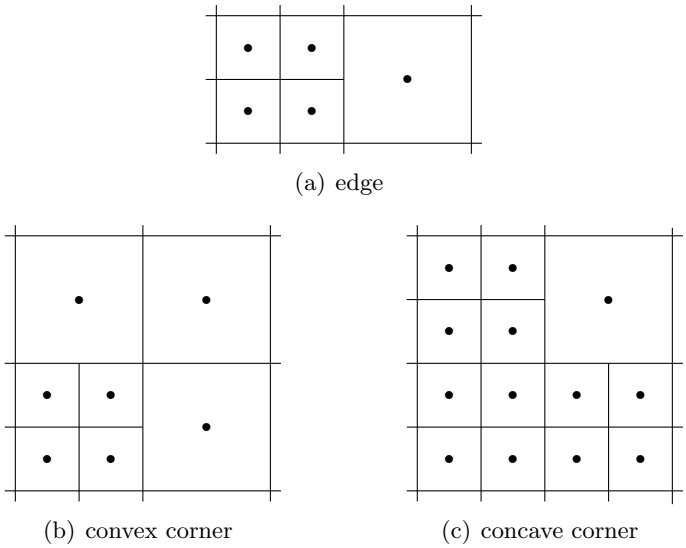

(a) edge

(b) convex corner

(c) concave corner

Figure 3.3: Sketches of the three principal interior interface geometries encountered in 2-D: (a) edge (shown aligned in the x-direction), (b) convex corner, and (c) concave corner (both defined relative to the fine region).

3.2 Formulation and Stability

3.2.1 Summation-by-Parts Formulation in 2-D

For equation (3.1.1), the 1-D theory presented in Section 2.2 is extended in a manner analogous to that described by Abarbanel and Chertock (2000). We define general 2-D finite-difference approximations to the spatial derivatives on the entire domain Ω,

$$\frac{\partial \mathbf{u}}{\partial x} = \frac{1}{\Delta x} D_x \mathbf{u}, \tag{3.2.1}$$

$$\frac{\partial \mathbf{u}}{\partial y} = \frac{1}{\Delta y} D_y \mathbf{u}, \tag{3.2.2}$$

such that a projection $\mathbf{v}$ of the exact solution $u(x, y, t)$ onto the 2-D grid satisfies

$$\frac{\partial \mathbf{v}}{\partial x} = \frac{1}{\Delta x} D_x \mathbf{v} + \mathbf{t}_x, \tag{3.2.3}$$

$$\frac{\partial \mathbf{v}}{\partial y} = \frac{1}{\Delta y} D_y \mathbf{v} + \mathbf{t}_y, \tag{3.2.4}$$

where $\mathbf{t}_x$ and $\mathbf{t}_y$ are the truncation errors in each direction. The discretization spacings Δx and Δy now represent the finest length scale in each direction, following the convention introduced in Chapter 2. In this way, the scaling factor of the discretization for coarse

regions is incorporated into the coefficients of D_x and D_y. These finite-difference approximations, with the 2-D SAT boundary implementation from Abarbanel and Chertock, give a semidiscrete form of equation (3.1.1),

$$\frac{\mathrm{d}\mathbf{u}}{\mathrm{d}t} = -\left(\frac{a}{\Delta x}D_x + \frac{b}{\Delta y}D_y\right)\mathbf{u} - \frac{a}{\Delta x}\mathbf{g}_x - \frac{b}{\Delta y}\mathbf{g}_y, \tag{3.2.5}$$

where the vectors $\mathbf{g}_x$ and $\mathbf{g}_y$ contain the contribution of the boundary conditions. To better understand the structure of the finite-difference matrices in 2-D, see that on a uniform grid ($\Omega^f = \{\}$), the matrices D_x and D_y are block diagonal, and may be written explicitly as

$$D_x = \begin{bmatrix} P^{-1}\tilde{Q} & & & \\ & P^{-1}\tilde{Q} & & \\ & & \ddots & \\ & & & P^{-1}\tilde{Q} \end{bmatrix}, \quad \mathbf{g}_x = \begin{bmatrix} P^{-1}\tau \mathbf{s} g_1^x(t) \\ P^{-1}\tau \mathbf{s} g_2^x(t) \\ \vdots \\ P^{-1}\tau \mathbf{s} g_N^x(t) \end{bmatrix},$$

where P, $\tilde{Q}$, τ and $\mathbf{s}$ are all as defined in 1-D (see Section 2.2), and similarly in the y-direction by the appropriate transformation.

On a patch-refined grid, D_x and D_y will have this block-diagonal structure in uniform regions, but near interfaces a more general form is required. For a grid with a total of $\mathcal{N} = |\mathcal{I}|$ nodes, there will be a subset of nodes, $\mathcal{I}^i \subset \mathcal{I}$, of length $n = |\mathcal{I}^i|$ in the vicinity of $\partial\Omega^f$ that require special interface stencils. These stencils depend on a larger subset of nodes, $\mathcal{I}^d \subset \mathcal{I}$, of length $m = |\mathcal{I}^d| > n$ (which will be different for each derivative). Thus D_x and D_y have potentially dense $n \times m$ submatrices over the interface nodes $\mathcal{I}^i \times \mathcal{I}^d$, which we label $\hat{D}_x$ and $\hat{D}_y$, respectively.

These matrices are defined as general explicit finite difference approximations

$$\frac{\partial u_k}{\partial x} = \frac{1}{\Delta x}\sum_{j \in \mathcal{I}^{dx}} \hat{D}_{x,kj} u_j, \tag{3.2.6}$$

$$\frac{\partial u_k}{\partial y} = \frac{1}{\Delta y}\sum_{j \in \mathcal{I}^{dy}} \hat{D}_{y,kj} u_j, \tag{3.2.7}$$

for all $k \in \mathcal{I}^i$, where Δx and Δy are the discretization scales in the fine region. The formal order of each approximation is determined by Taylor series expansion of the polynomial test

function

$$f_{(z_1,z_2)}(x,y) = x^{z_1} y^{z_2}, \tag{3.2.8}$$

to degree specified by the index pair (z_1, z_2), in the combinations shown in Table 3.1. For either equation (3.2.6) or (3.2.7) to be accurate to a given order, all index pairs up to that order must be satisfied exactly: for a third-order–accurate x-derivative, (3.2.6) must satisfy all ten index pairs up to third order. Both directions must be considered for each derivative because of the off-direction perturbations introduced by the hanging-node geometry of the grid. Simple algebra will show that this does not result in a cross-dependence on the discretizations; therefore, the x-derivative is independent of Δy and vice versa. Note that in order for the discretization to preserve the global convergence rate of an interior scheme of order s, it is expected that the interface schemes must be accurate to at least order $(s-1)$ (Gustafsson, 1975).

Derivative order	Index pairs
0th order	(0,0)
1st order	(1,0); (0,1)
2nd order	(2,0); (0,2); (1,1)
3rd order	(3,0); (0,3); (2,1); (1,2)
4th order	(4,0); (0,4); (3,1); (1,3); (2,2)

Table 3.1: Test polynomial index pairs (z_1, z_2) for given derivative accuracy

3.2.2 Error Bound and Stability Criteria

The stability of equation (3.2.5) is examined in the context of a positive definite norm matrix H, such that for $\mathbf{u} \in \mathbb{R}$,

$$\|\mathbf{u}\|_H^2 = (\mathbf{u}, H\mathbf{u}) = \mathbf{u}^T H \mathbf{u} > 0, \tag{3.2.9}$$

with the equivalence of the norms,

$$h_L \|\mathbf{e}\|^2 \leq \|\mathbf{e}\|_H^2 \leq h_U \|\mathbf{e}\|^2, \tag{3.2.10}$$

where h_L and h_U are positive constants, analogous to the 1-D definition (2.2.8).

The error analysis is similar to that of Section 2.2.5 and follows Abarbanel and Chertock (2000), with some modifications appropriate for the present case. Writing equation (3.2.5)

for the projection of the exact solution, $\mathbf{v}$,

$$\frac{\mathrm{d}\mathbf{v}}{\mathrm{d}t} = -\left(\frac{a}{\Delta x}D_x + \frac{b}{\Delta y}D_y\right)\mathbf{v} - \frac{a}{\Delta x}\mathbf{g}_x - \frac{b}{\Delta y}\mathbf{g}_y - a\mathbf{t}_x - b\mathbf{t}_y, \tag{3.2.11}$$

an equation for the error, $\mathbf{e} = \mathbf{v} - \mathbf{u}$, may be derived according to

$$\frac{\mathrm{d}\mathbf{e}}{\mathrm{d}t} = -\left(\frac{a}{\Delta x}D_x + \frac{b}{\Delta y}D_y\right)\mathbf{e} + \mathbf{t}, \tag{3.2.12}$$

where $\mathbf{t} = -a\mathbf{t}_x - b\mathbf{t}_y$ contains the truncation error contributions from both directions. Taking the norm of this error in the sense just defined gives

$$\frac{\mathrm{d}}{\mathrm{d}t}\|\mathbf{e}\|_H^2 = \mathbf{e}^T\left[\left(-\frac{a}{\Delta x}D_x - \frac{b}{\Delta y}D_y\right)^T H + H\left(-\frac{a}{\Delta x}D_x - \frac{b}{\Delta y}D_y\right)\right]\mathbf{e} + 2(\mathbf{t}, H\mathbf{e}).$$

Writing the term in square brackets as

$$A = \left(\frac{a}{\Delta x}D_x + \frac{b}{\Delta y}D_y\right)^T H + H\left(\frac{a}{\Delta x}D_x + \frac{b}{\Delta y}D_y\right), \tag{3.2.13}$$

leads to

$$\frac{\mathrm{d}}{\mathrm{d}t}\|\mathbf{e}\|_H^2 = -\mathbf{e}^T A\mathbf{e} + 2(\mathbf{t}, H\mathbf{e}). \tag{3.2.14}$$

It is assumed that A can be diagonalized according to $A\mathbf{x}_i = \lambda_i\mathbf{x}_i$, where λ_i and $\mathbf{x}_i$ denote the eigenvalues and normalized eigenvectors of A, respectively. A positive definite matrix A, such that $\mathbf{e}^T A\mathbf{e} > 0$ for all $\mathbf{e} \neq 0$, implies $\mathrm{Re}(\lambda_i) > 0$. Expressing the error in this basis gives $\mathbf{e} = \sum c_i\mathbf{x}_i$, where c_i denote scalar coefficients, and leads to

$$-\mathbf{e}^T A\mathbf{e} = -\sum c_i^2\lambda_i \leq -\lambda_{\min}\|\mathbf{e}\|^2 \leq -\frac{\lambda_{\min}}{h_U}\|\mathbf{e}\|_H^2, \tag{3.2.15}$$

where $\lambda_{\min} = \min(\mathrm{Re}(\lambda_i))$. Using the Cauchy-Schwarz inequality, $(\mathbf{t}, H\mathbf{e}) \leq \|\mathbf{e}\|_H\|\mathbf{t}\|_H$, the error rate

$$\frac{\mathrm{d}}{\mathrm{d}t}\|\mathbf{e}\|_H^2 \leq -\frac{\lambda_{\min}}{h_U}\|\mathbf{e}\|_H^2 + 2\|\mathbf{e}\|_H\|\mathbf{t}\|_H,$$

reduces to

$$\frac{\mathrm{d}}{\mathrm{d}t}\|\mathbf{e}\|_H \leq -\frac{\lambda_{\min}}{2h_U}\|\mathbf{e}\|_H + \|\mathbf{t}\|_H, \tag{3.2.16}$$

which may be integrated to give the error bound (cf. Abarbanel and Chertock, 2000),

$$\|\mathbf{e}\|_H \leq \frac{2h_U}{\lambda_{\min}} \left(\sup_{0 \leq s \leq t} \|\mathbf{t}(s)\|_H \right) \left[1 - \exp\left(-\frac{\lambda_{\min} t}{2h_U} \right) \right]. \tag{3.2.17}$$

In the case where A is only positive semidefinite, such that $\mathbf{e}^T A \mathbf{e} \geq 0$, the error bound is modified to become

$$\|\mathbf{e}\|_H \leq \left(\sup_{0 \leq s \leq t} \|\mathbf{t}(s)\|_H \right) t, \tag{3.2.18}$$

which can be interpreted, with some care, as the limit of equation (3.2.17) when $\lambda_{\min} \to 0$. This shows that the scheme converges for $t < +\infty$ and suffers at most a linear growth in error with time owing to truncation error, thus exhibiting Lax (finite time) stability. To prove asymptotic stability requires a bound on $\|\mathbf{t}(s)\|_H$ for all time, which depends, in general, on the boundary and initial data, as well as on the order of the approximation. A demonstration of asymptotic stability for two particular grids is shown in Section 3.4.

The stability result depends on the condition

$$-\frac{a}{\Delta x}\left(HD_x + D_x^T H \right) - \frac{b}{\Delta y}\left(HD_y + D_y^T H \right) \leq 0. \tag{3.2.19}$$

Notice that the norm H is as yet undefined, except by the fact that it must be a positive definite matrix. For the boundaries, Abarbanel and Chertock propose

$$H_b = P_x^{1/2} P_y P_x^{1/2}, \tag{3.2.20}$$

where H_b spans the set of nodes $\mathcal{I}^b \subset \mathcal{I}^c$ in the vicinity of $\partial\Omega$ and $D_x = P_x^{-1} Q_x$. This can be shown to satisfy equation (3.2.19) with $a > 0$ and $b > 0$. In a patch-refined domain with uniform boundary regions, the 1-D boundary scheme from Section 2.2.4 may be used, with the matrices from Appendix B, and the 2-D matrices P_x and P_y may be formed directly from the known P matrix of the 1-D boundary scheme.

At grid interfaces, stability should be independent of the advection velocities so that the closure may be applied to systems with waves traveling in arbitrary directions. In the case of a uniform domain, the interior makes no contribution to the stability condition (3.2.19), and $\mathbf{e}^T A \mathbf{e}$ is dependent only on the boundary closure. For the patch-refined domain, in order to have the error bound (3.2.17) independent of the interface closure, this should

remain true. This leads to the stronger conditions

$$\hat{H}\hat{D}_x + \hat{D}_x^T\hat{H} = 0, \tag{3.2.21}$$

$$\hat{H}\hat{D}_y + \hat{D}_y^T\hat{H} = 0, \tag{3.2.22}$$

for the interface region, where $\hat{D}_x$ and $\hat{D}_y$ are defined by equations (3.2.6)–(3.2.7). The positive definite matrix $\hat{H}$ spans $\mathcal{I}^i \times \mathcal{I}^i$, and is common to both conditions. It is to be determined along with the elements of $\hat{D}_x$ and $\hat{D}_y$ when constructing the stencil.

We make the following remarks:

1. For symmetric $\hat{H}$, the equations are equivalent to requiring that the products $\hat{H}\hat{D}_x$ and $\hat{H}\hat{D}_y$ be antisymmetric matrices.

2. In the domain interior, away from interfaces and boundaries, $\mathcal{I} \setminus (\mathcal{I}^i \cup \mathcal{I}^b)$, D_x and D_y are naturally antisymmetric by the centered difference scheme, automatically satisfying equations (3.2.21) and (3.2.22).

3. The full-domain matrix H has H_b in boundary regions, $\hat{H}$ in interface regions and is diagonal in interior regions. Since all interior regions, including the interfaces, satisfy the stronger conditions (3.2.21)–(3.2.22), equation (3.2.19) holds throughout the domain and the estimate (3.2.17) is preserved.

4. The criteria (3.2.21)–(3.2.22) are independent of the cell aspect ratio. Although the refinement factor is fixed for a particular interface closure, any combination of Δx and Δy may be used.

5. The norm matrix $\hat{H}$ is not necessary for computational implementation of the scheme, as it does not appear in equation (3.2.5), but it is critical in the derivation of the interface stencils because it links the x- and y-derivatives in a way that ensures stability.

3.3 Interface Closures

3.3.1 Mapping of Interface Schemes

Before considering the individual interface stencils, it is important to understand how the interface elements of Figure 3.3 may be used to construct the interface scheme for an

arbitrary domain. Consider the sketched edge and corner stencils of Figure 3.4, shown in their default orientation (described relative to the fine region). Throughout this section, it is more convenient to map the global index set into a new, locally ordered set, $\mathcal{I} \mapsto \mathcal{I}'$. This local numbering is used to indicate the orientation of the stencil and the relative position of each node. The particular mapping between the global set, $\mathcal{I}$, and these local sets, $\mathcal{I}'$, depends on the global domain and constitutes an implementation issue.

(a) right-hand edge (b) upper-right corner

Figure 3.4: Cartoon representation of interface stencil elements.

Consider now a simple box refinement on a square grid, where the inner box is refined by a factor of two in each direction. To define the complete interface scheme for this grid, the stencils of Figure 3.4 must be mapped to the four edge interfaces and four corner interfaces of this grid. There are two obvious mapping alternatives: reflection or rotation. In the former scheme, the upper edge is mapped from the original right-hand edge by reflection in the line $y = x$, and the remaining edges are obtained by reflection in $y = -x$. Examination of the corners, however, will reveal that the original upper-right corner cannot be simply mapped to the upper-left or the lower-right corners. Using a counterclockwise rotation mapping, though, all the geometries may be obtained from the original pair of Figure 3.4, resulting in the numbering shown in Figure 3.5. The original stencils are shaded and the transformed orientations are boxed.

The final step is to map the particular x- and y-derivatives to the edges and corners. For this purpose, consider 90° rotations of a standard 5-point stencil in Figure 3.6. This sequence generates Table 3.2, which shows how $\hat{D}_x$ and $\hat{D}_y$ in the original orientation are mapped to the x- and y-derivatives in each of the other orientations. With this mapping scheme, one solution for each interface type is sufficient for closure of the interfaces on an arbitrarily refined grid.

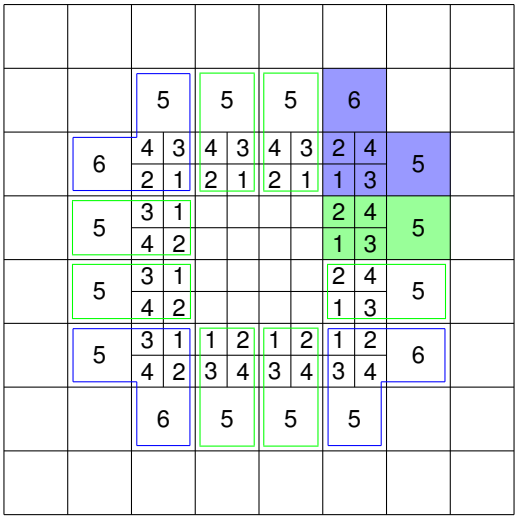

Figure 3.5: Example of a box-refined grid, showing mapping of interface elements to each grid location.

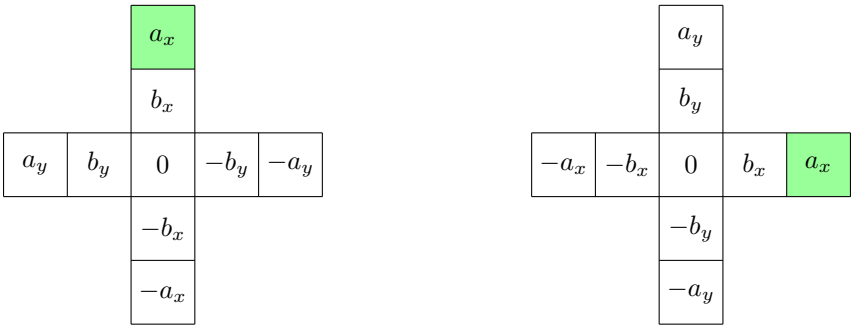

(b) 90° Rotation

(a) Original Orientation

(c) 180° Rotation

(d) 270° Rotation

Figure 3.6: Counterclockwise rotations of a stencil about the origin.

Edge orientation	Corner orientation	x-derivative	y-derivative
Right	Upper right	$\hat{D}_x$	$\hat{D}_y$
Upper	Upper left	$-\hat{D}_y$	$\hat{D}_x$
Left	Lower left	$-\hat{D}_x$	$-\hat{D}_y$
Lower	Lower right	$\hat{D}_y$	$-\hat{D}_x$

Table 3.2: Transformations of the derivative matrices from the default orientation to other orientations by rotation, following Figure 3.6

3.3.2 Interface Scheme Construction

Construction of the interface schemes has four steps:

1. Define interface matrices.

2. Form the accuracy equations from (3.2.6) and (3.2.7).

3. Form the stability equations (3.2.21) and (3.2.22).

4. Solve the resulting system of equations.

The interface matrices are defined from the interface node set $\mathcal{I}^i$ and its dependence set $\mathcal{I}^d$ (which includes the interface nodes, and may not be the same for x- and y-derivatives). Dense $n \times m_x$ matrix $\hat{D}_x$, $n \times m_y$ matrix $\hat{D}_y$, and $n \times n$ matrix $\hat{H}$ are assumed, the latter to contain the influence of the interface within $\mathcal{I}^d$. The accuracy conditions are obtained from equations (3.2.6), (3.2.7) and (3.2.8), resulting in the linear system of equations

$$\frac{\partial f_{(z_1,z_2)}}{\partial x}(x_k, y_k) = \frac{1}{\Delta x} \sum_{j \in \mathcal{I}^{dx}} \hat{D}_{x,kj} f_{(z_1,z_2)}(x_j, y_j), \tag{3.3.1}$$

$$\frac{\partial f_{(z_1,z_2)}}{\partial y}(x_k, y_k) = \frac{1}{\Delta y} \sum_{j \in \mathcal{I}^{dy}} \hat{D}_{y,kj} f_{(z_1,z_2)}(x_j, y_j), \tag{3.3.2}$$

formed for each $k \in \mathcal{I}^i$, where (x_k, y_k) is the location of the node globally indexed by k. For third-order accuracy, Table 3.1 shows that there are ten equations for each k for each derivative. The stability equations are the elements of the $m \times m$ matrices formed by the left-hand sides of equations (3.2.21) and (3.2.22). These are quadratic equations in the unknown elements of $\hat{D}_x$, $\hat{D}_y$ and $\hat{H}$. The resulting system of quadratic equations is solved for the elements of the interface matrices, which is done numerically because of its very large size.

For a solution to exist at an interface, the norm H must have a specific form in the interior regions of the domain, where equation (2.1.3) applies. Let H_c define the part of H that corresponds to coarse interior nodes in $\mathcal{I}^c \setminus (\mathcal{I}^i \cup \mathcal{I}^b)$, and similarly let H_f correspond to the fine interior part $\mathcal{I}^f \setminus \mathcal{I}^i$. Then, we require

$$H_c = \text{diag}(1) = I, \tag{3.3.3a}$$

$$H_f = \text{diag}(\frac{1}{r_x r_y}) = \frac{1}{r_x r_y} I, \tag{3.3.3b}$$

i.e., H has 1 and $1/r_x r_y$ on the diagonal in coarse and fine regions, respectively. A physical intuition exists for this result: the norm, H, is effectively weighting the solution by the area occupied by each cell; for refinement ratios $r_x = r_y = 2$, four fine cells occupy the same area and have the same weight as one coarse cell. The interface solutions presented next also fixed the diagonal of $\hat{H}$ to follow this scheme, although this is not essential to the existence of a solution across the interfaces.

For each of the following interface solutions, the particular difference matrices $\hat{D}_x$ and $\hat{D}_y$ used in Section 3.4 are too large to print but are available online with this thesis from the Caltech Library. These matrices are sufficient for implementation of the interface scheme. Row and column numbering of each matrix follows the local node numbering presented in Sections 3.3.3–3.3.5. Note that each of the following systems involve many degrees of freedom and in some cases these solutions are not unique. Optimization of the solution families may be possible but has not been exhaustively investigated.

3.3.3 Edge Interface

The edge interface is the simplest of the four interface geometries, and the default orientation is considered here to be that shown in Figure 3.3(a). It is clear that a special difference stencil is required for the x-derivative across the interface, but examination of the difference matrix for the y-derivative will show that it cannot satisfy equation (3.2.22) without a special stencil too. With a five-point interior stencil, the interface region for the x-derivative must include at least the first two nodes on either side of the change in discretization. It was found that one additional point in each subrow was also required in the refined region. Figure 3.7 shows the fourth-order interface stencil thus derived, each interface node being formally third-order accurate. The dark-colored nodes (numbered above each node 1–8)

comprise the interface set $\mathcal{I}^i$ for this stencil, and the gray nodes (together with the interface nodes, the full set numbered below each node 1–30 for D_x and 1–24 for D_y) comprise the dependence set, $\mathcal{I}^d$.

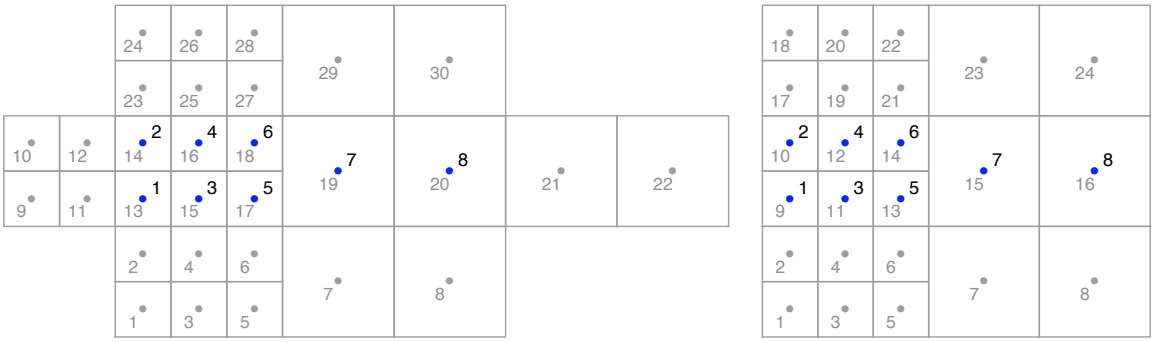

(a) x-derivative (b) y-derivative

Figure 3.7: Edge interface stencils for the fourth-order explicit scheme. Interface nodes are numbered 1–8 on each stencil and the dependence sets 1–30 (x-derivative) and 1–24 (y-derivative).

For the x-derivative, the dependence set includes the natural extensions in the x-direction of the stencils for nodes 1, 2 and 8. These adjacent noninterface nodes (9–12 and 21–22 of $\mathcal{I}^d$) have the interior dependence on nodes 1–4 on the fine side, and nodes 7 and 8 on the coarse side, linking the interface stencil to the interior regions. The y-derivative does not have a natural dependence on those nodes, and since the accuracy conditions at the interface may be resolved entirely within the stencil, its stencil has no need to include them. However, both stencils include dependence on the coarse rows above and below the row of interest, the x-derivative stencil needing the additional nodes to satisfy the accuracy conditions in the y-direction. The y-derivative at nodes 7 and 8 achieves third-order accuracy with essentially a three-point stencil in that direction.

As the most basic of the interface geometries, the edge stencil is expected to tesselate along interface edges and to be compatible with corner interfaces, as was assumed in Section 3.3.1. An arbitrary edge solution may not do either of these things; of all the edge solutions that exist, only a subset will have compatible corner solutions and, therefore, be usable (or useful) in practice. The solution presented here was derived simultaneously with the convex corner and corresponds to one particular member of the family of solutions. An alternative formulation for the edge interface is presented in Appendix D.

Alongside this fourth-order solution, variations with different interior schemes were also

investigated, the critical condition for existence of a solution being that H has the interior form (3.3.3). A second-order edge solution (first-order at the interface) permits a smaller interface set comprising only nodes 3–7 of $\mathcal{I}^i$ from the fourth-order stencil because of the smaller three-point interior stencil. Dependence on the adjacent coarse rows is still required. A rational solution is easily found for this case, as $\hat{H}$ has a particularly simple form. Also, a sixth-order solution exists that is fifth order at the interface, with an appropriately larger stencil.

3.3.4 Convex Corner Interface

The corner interface turns out to be a more challenging problem in the energy-stable SBP context. The trade-off for satisfying the stability equations is a significant loss in the accuracy of the interface stencil compared to the interior accuracy. In lieu of a formal proof, experimentation with stencil sizes and interior schemes yielded the results shown in Table 3.3: with a fourth-order interior scheme, the maximum accuracy achievable at every node in the stencil is just first order, though most nodes can satisfy up to third order.

Interior order	Edge order	Corner order
second	first	zeroth
fourth	third	first
sixth	fifth	second

Table 3.3: Maximum accuracy achievable at every corner interface node with an SBP formulation

Parameterization of the interior difference stencils reveals that it is the order of the interior scheme rather than the particular coefficients that limits accuracy at the corner interface. For a centered five-point stencil from equation (2.3.1) with coefficients $(-\alpha, -\beta, 0, \beta, \alpha)$, there is a family of at least second-order accurate solutions with $\beta = 1/2 - 2\alpha$, and a special case of $\alpha = -1/12$, $\beta = 2/3$ that is fourth order (see Table 2.1). Leaving α as a parameter when solving the accuracy conditions at the corner, the maximum accuracy achievable at all interface nodes is zeroth order, except in the special case of $\alpha = -1/12$, i.e., fourth order. Similarly with a seven-point interior scheme: from the family of fourth-order stencils, only the special case of the sixth-order stencil gave a solution that was at least second order everywhere.

For the fourth-order stencil shown in Figure 3.8, two nodes of $\mathcal{I}^i$ (14 and 15) are first

order, three (8, 12 and 16) are second order, and the remainder are third-order accurate. The dependence set includes the interface nodes (numbered 1–50). The positions of the low-order nodes are not unique, but it is preferable to place them in the fine region where the truncation error is minimized by the smaller Δx. The most serious consequence of this result is that average fourth-order convergence can no longer be expected by Gustafsson (1975); at worst, despite using a fourth-order interior scheme, only second-order convergence could be seen. Note, however, that since there exists no usable second-order solution (a zeroth-order–accurate derivative is meaningless), the fourth-order stencil represents the lowest-order interface solution that satisfies the stability criteria.

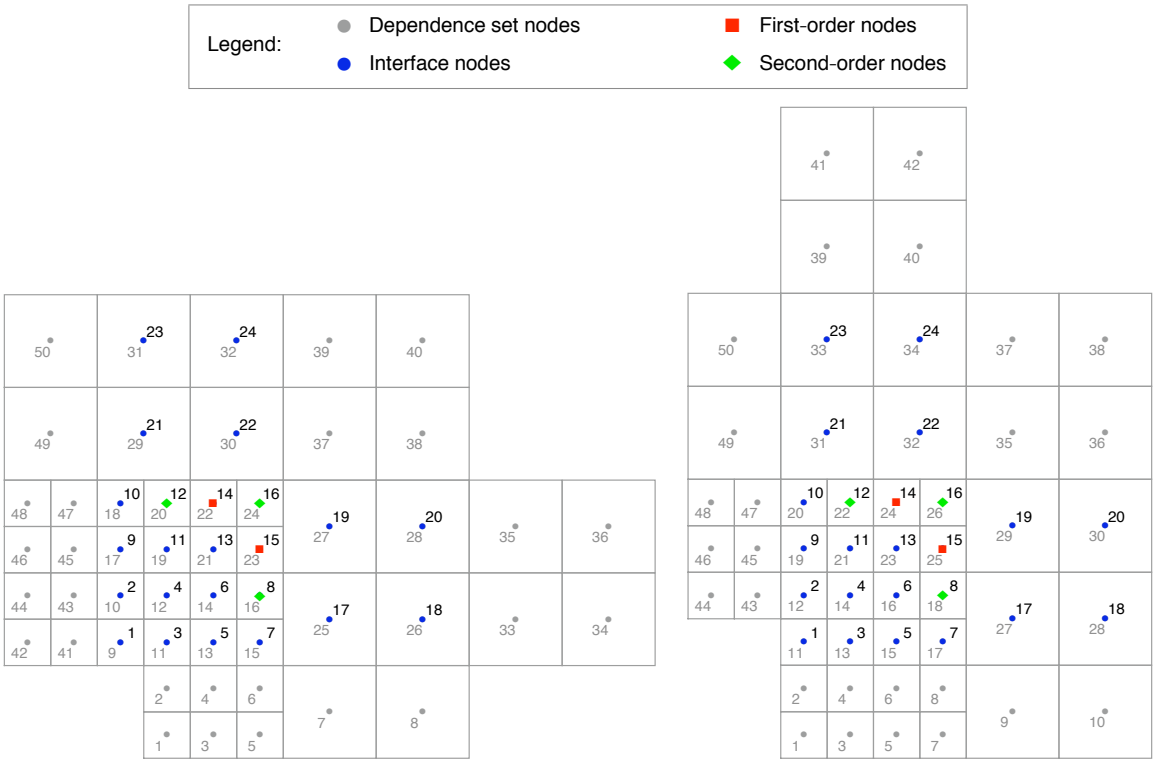

(a) x-derivative (b) y-derivative

Figure 3.8: Convex corner interface stencils for the fourth-order explicit scheme. Interface nodes are numbered 1–24 and the dependence set nodes are numbered 1–50.

The extent of the convex corner interface is determined primarily by the extent of the edge stencil. The inclusion of nodes 1 and 2 in the edge stencil demands that the corner span at least two coarse rows/columns, so nodes 2–16 of the corner must be included to avoid any ambiguity in the stencils at those nodes. The differences between the x- and y-derivatives are limited to extensions of the stencils in the directions of the derivatives.

Both stencils must be dependent on the adjacent edges for compatibility (both below and to the left of the interface, nodes 1–8 and 43–50 of $\mathcal{I}^d$), but node 1 requires another two nodes to its left (x) or below (y). The x-derivative stencil includes the interior nodes to the right of coarse nodes 17–20 on which they are naturally dependent (nodes 33–36); similarly, for the y-derivative, the coarse nodes above 21–24 are included (nodes 39–42).

The corner stencil has dense 24×50 derivative matrices $\hat{D}_x$ and $\hat{D}_y$ with many degrees of freedom, so again a family of solutions exist. With the current edge stencil, the dependence set may be customized so that all nodes need not be dependent on the full set. For example, nodes 17–20 need not be dependent on nodes 41–50, etc. The stencils may also be optimized to reduce the truncation error at the low-order nodes.

It should be noted that there exists a second-order corner interface that is locally first order, which consequently could be used as a meaningful derivative approximation. Unfortunately, this requires a modified stencil in the interior of the fine region: instead of the usual three-point second-order central difference scheme, the five-point second-order stencil with coefficients $(-1/4, 0, 0, 0, 1/4)$ is needed, which has two serious deficiencies. First, the grid resolution is not truly refined, as this modified stencil is equivalent to a staggered grid with the double (coarse) refinement, and second, multiple refinement with this scheme is not possible. Multiple refinement is dependent on any interface appearing locally identical, regardless of its refinement relative to a global scale. If the fine region requires a special stencil, then the same interface scheme cannot be used again in a second refinement of that region, resulting in the loss of proper nesting of the AMR grid hierarchy.

3.3.5 Concave Corner Interface

The concave corner geometry suffers similar difficulties to those of the convex corner. Again, for a fourth-order interior scheme, the maximum accuracy achievable at all nodes at the interface is first order. Figure 3.9 shows the stencil derived here, with four first-order nodes (nodes 5, 6, 17 and 18) and two second-order nodes (11 and 23). Note that for both corners, these first-order nodes do, in fact, satisfy the accuracy conditions for the second-order cross-derivative $\partial^2/\partial x \partial y$ in the Taylor series, as it is the second derivatives ($\partial^2/\partial x^2$ and $\partial^2/\partial y^2$) that present the closure problem. Further, at the concave corner, node 6 is second-order accurate in x in the x-derivative, and node 18 in y in the y-derivative. This arrangement of the low-order nodes was chosen to ensure symmetry of the corner and minimize the error

at these points as far as is possible.

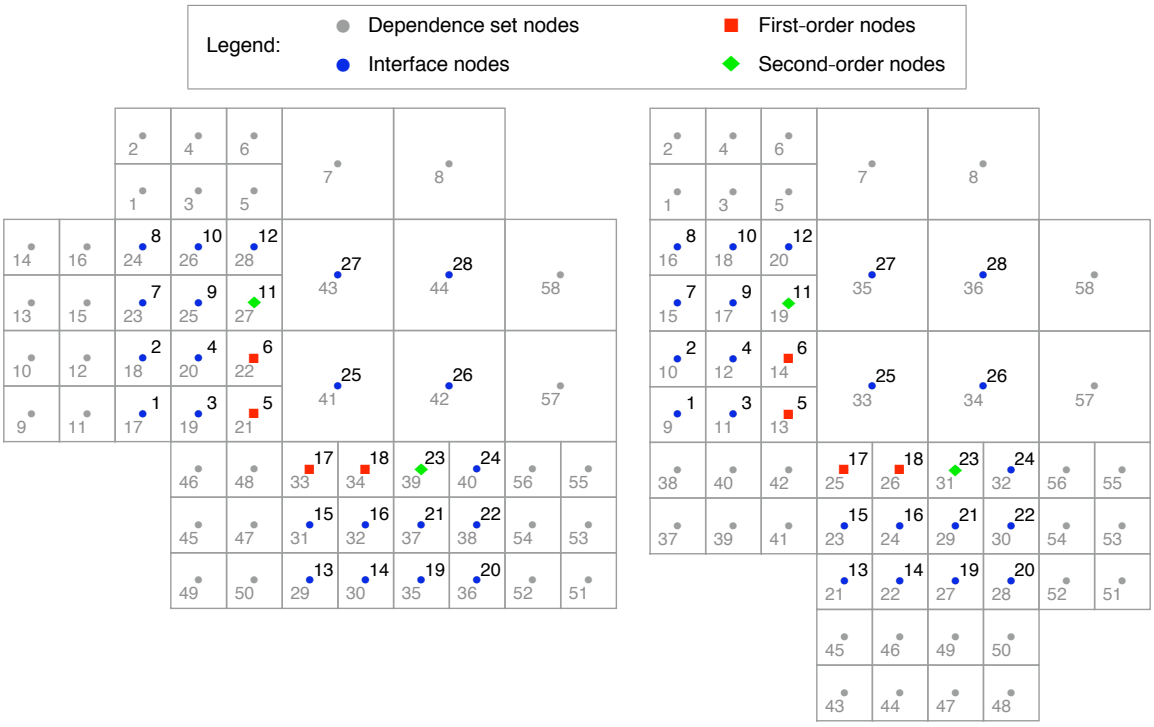

(a) x-derivative (b) y-derivative

Figure 3.9: Concave corner interface stencils for the fourth-order explicit scheme. Interface nodes are numbered 1–28 and the dependence set nodes are numbered 1–58.

Once again, the extent of the concave corner interface is determined by the edge scheme, the potential ambiguity here occurring at the coarse nodes 25–28. The dependence set again includes the adjacent edge row/column (above and to the left of the interface set, nodes 1–8 and 51–58 of $\mathcal{I}^d$) and the natural stencil extensions in the x- and y-directions. The large 28×58 stencil is a consequence of this geometry being dominated by the fine region, but optimization and customization of the dependence sets for each individual node of the stencil can potentially reduce the density of the derivative matrices somewhat.

While the convex corner interface solution was obtained simultaneously with the edge interface to ensure compatibility, it is not necessary to do the same with the concave corner: a solution was found using the previously derived edge solution. This keeps each stencil derivation problem to a size that is feasible to solve on a modern desktop computer.

3.3.6 Truncation Errors

In Table 3.4, the effect of reduced accuracy at the interfaces on the derivative approximations is quantified. Shown are the maximum truncation error terms for each interface scheme, in each derivative direction, and the node in the stencil at which this error occurs. This analysis assumes that $\Delta x = \Delta y$, as different cell aspect ratios will favor certain terms over others. We see that the largest truncation terms for the edge interface are mixed derivatives, whereas at the corners the second-order mixed derivative is specifically set to zero so the greatest error appears in the higher derivatives in the direction of the approximation.

	Edge	Convex corner	Concave corner
Max error, $\partial/\partial x$	$-1.984\Delta x^3\Delta y$	$-1.0183\Delta x^2$	$-3.087\Delta x^2$
Location	node 3	node 15	node 17
Max error, $\partial/\partial y$	$-20.129\Delta x^2\Delta y^2$	$-1.0325\Delta y^2$	$-2.825\Delta y^2$
Location	node 6	node 14	node 5

Table 3.4: Maximum absolute truncation errors, and the node at which this occurs, for each interface geometry assuming $\Delta x = \Delta y$

3.3.7 Refinement Region Topology

Having now defined the full set of interior interface stencils, it is clear that there are a few rules that must be imposed on a refinement scheme such that only these stencils are required to close the interfaces. The basic principle is to avoid interference between corners caused by overlapping dependence sets, such that the elements of $HD + D^T H$ are the same as those in equations (3.2.21) and (3.2.22) from the original definitions of the individual stencils. Thus in a refined region, any two corners must be separated by at least two coarse cells, and since each corner itself occupies two coarse cells in each direction, the minimum length of any side of a refinement region is six coarse cells. Similarly, the minimum separation between two parallel refined regions is eight coarse cells. For multiple levels of refinement, to preserve the independence of each interface, at least seven intermediate cells are required between consecutive refinement interfaces.

Near boundaries, the dependence sets of the interface and boundary closures are permitted to overlap, because the contribution of the boundary stencil to equations (3.2.21)–(3.2.22) will be the same as the interior stencil expected by the interface. For a four-point boundary stencil with a six-point dependence set, the minimum separation between the

domain boundary and an interface is eight cells. With periodic boundary conditions, the interface may extend to the boundary as long as the refinement scheme is periodic also.

3.4 Validation Problems

3.4.1 Advecting Wave

For the first test example, consider the scalar advection equation (3.1.1) with $a = b = 1$, given by

$$\begin{aligned} \frac{\partial u}{\partial t} + \frac{\partial u}{\partial x} + \frac{\partial u}{\partial y} = 0, \quad 0 \le x \le 1,\ 0 \le y \le 1,\ t \ge 0, \\ u(0, y, t) = \sin\left[\omega\left(y - 2t\right)\right], \\ u(x, 0, t) = \sin\left[\omega\left(x - 2t\right)\right], \\ u(x, y, 0) = \sin\left[\omega\left(x + y\right)\right], \end{aligned} \tag{3.4.1}$$

with a frequency parameter $\omega = 2\pi$. This has an analytic solution

$$u(x, y, t) = \sin\left[\omega\left(x + y - 2t\right)\right], \tag{3.4.2}$$

which is used to evaluate the accuracy of the numerical method.

To show that the interface schemes do possess the claimed stability properties, we examine the spectrum of the semidiscrete form of equation (3.4.1),

$$\frac{\mathrm{d}\mathbf{u}}{\mathrm{d}t} = \left(-\frac{1}{\Delta x} D_x - \frac{1}{\Delta y} D_y\right) \mathbf{u} - \frac{\mathbf{g}_x}{\Delta x} - \frac{\mathbf{g}_y}{\Delta y}. \tag{3.4.3}$$

Time stability of this equation (with $\Delta x = \Delta y$) demands that the matrix $(-D_x - D_y)$ have eigenvalues with nonpositive real parts. This matrix has a structure strongly dependent on the grid and its refinement. Two refinement schemes are considered to demonstrate by example that the interface schemes are stable. For the first case of a box refinement, the central third of the domain is refined in each direction by the usual factor of two. The resulting grid has only edge and convex corner interfaces. The second grid of a cross refinement, has a "+"-shaped refined region in the center of the domain, which is three-fifths the width and height of the domain and occupies one-fifth of the total area. It has

eight convex corner interfaces and four concave, with edges in between, providing a test of the three interface solutions together. Both are shown schematically in Figure 3.10.

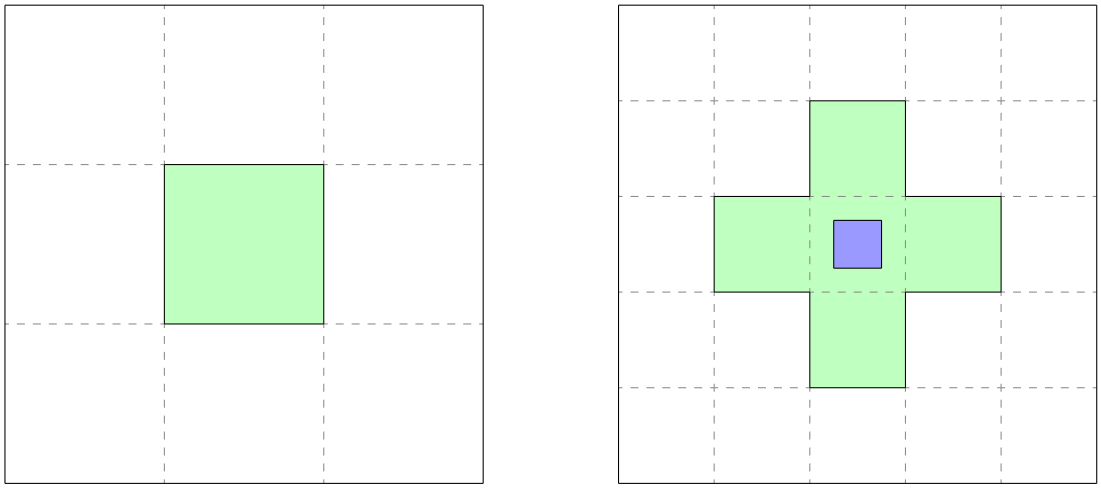

(a) box refinement (b) cross/cross + box refinement

Figure 3.10: Diagrams of the grids used for the validation problems. Shaded regions are refined by a factor of two in each direction compared to the base grid and dashed lines indicate the division of the domain into blocks. The darker shaded region on (b) shows the location of the second level of refinement for the cross + box grid.

For our demonstration, each grid is divided into blocks of eight coarse cells per side. The box refinement has three blocks in each direction, resulting in a 24×24 grid before refinement. The cross refinement has five blocks and a 40×40 coarse grid. With the refinements described, the grids have 768 and 2560 nodes, respectively. Figure 3.11 shows the eigenvalues of $(-D_x - D_y)$ in each case, both using the fourth-order explicit boundary scheme from Appendix E.5 and SAT parameter $\tau = 2$ at the boundary. Note that it is the presence of boundaries alone that results in the spectra having any nonzero real part; the equivalent spectra for domains with periodic boundaries are purely imaginary. This is consistent with the assertion that the interface schemes introduce no additional numerical dissipation.

Two features of Figure 3.11 stand out. First, there appear to be a significant number of eigenvalues on or near the vertical axis. Closer inspection reveals that the maximum real part in each example is very small $O(10^{-13})$ but clearly nonpositive, so the stability criteria is satisfied with all eigenvalues indeed lying in the left half plane. Second, the maximum imaginary part is large relative to the minimum real part, especially compared to the spectrum for a similar uniform grid. This number affects the stability limit of the

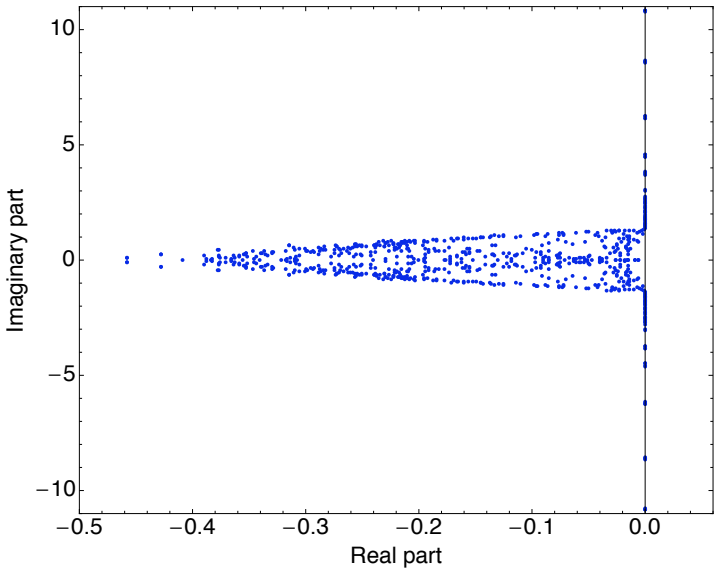

(a) spectrum for box refinement

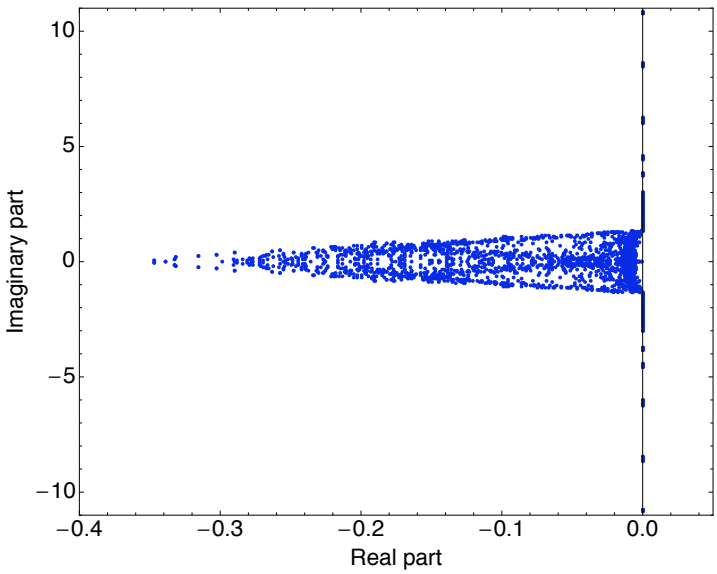

(b) spectrum for cross refinemet

Figure 3.11: Spectra of the matrices $(-D_x - D_y)$ for the test domains, including boundaries by the SAT scheme with $\tau = 2$.

time-marching scheme used to implement equation (3.4.1): for a third-order Runge-Kutta scheme (RK32 from Butcher, 2003) and advection velocities $a = b = 1$, we find the time discretization limit (based on the refined scale Δx)

$$\Delta t \lessapprox 0.16 \Delta x. \tag{3.4.4}$$

This agrees with the stability limit observed in practice. Note that this limit may be extended by using a fourth-order Runge-Kutta scheme, and is dependent on the value of τ at the boundaries.

For the convergence study, a third grid with an additional level of refinement is considered. The cross + box refinement is based on the cross refinement previously described, but with the middle quarters of the subblock at the center of the cross refined in each direction (one quarter of its area), for a total refinement factor of 4 across the grid and demonstrating the interface scheme across multiple levels of refinement (see Figure 3.10). All simulations use the fourth-order interface schemes described in Section 3.3. Table 3.5 shows the results from the convergence study on the cross and cross + box refinements, both run to a time $t = 1$ (two periods) with a CFL number of 1/8. The twice-refined grid is stable at this CFL when based on its finest grid scale.

	Cross refinement				Cross + box refinement			
coarse Δx	$\log_{10}(L_2)$	rate	$\log_{10}(L_\infty)$	rate	$\log_{10}(L_2)$	rate	$\log_{10}(L_\infty)$	rate
1/40	−2.004		−1.173		−2.011		−1.060	
1/60	−2.489	2.75	−1.584	2.34	−2.518	2.88	−1.314	1.44
1/80	−2.817	2.62	−1.791	1.65	−2.819	2.41	−1.609	2.37
1/120	−3.304	2.76	−2.145	2.01	−3.299	2.72	−2.109	2.84
1/160	−3.642	2.71	−2.350	1.64	−3.641	2.74	−2.403	2.36
rate		2.72		1.94		2.69		2.31

Table 3.5: Convergence results for the advection equation on patch-refined grids

It is immediately clear from these results that a fourth-order convergence rate is not achieved. Average convergence (in the L_2-norm) is approximately third order, but the point-wise L_∞-norm converges at closer to a second-order rate. This could be expected with the presence of first-order nodes in the domain, but it appears that in the averaged sense, the rate is a little better. Note that the number of first-order (and second-order) nodes is fixed, a function of the geometry of the refinement rather than the resolution itself. In the convergence study on the cross refinement, there are 32 first-order points; at the

coarse resolution, this represents 1.25% of the grid, while at the finest resolution (coarse $\Delta x = 1/160$) this is just 0.08%.

There is a computational payoff for the ability to refine the grid locally to mitigate the lost convergence rate and accuracy. A simple comparison was made between the cross + box grid and a uniform grid of equivalent resolution. For the twice-refined grid, a coarse discretization of 1/40 gives $\Delta x = 1/160$ in the most refined region and a total of 2752 nodes. The appropriate comparison is therefore to a uniform grid with that resolution having 25,600 nodes. In testing, without optimization of the interface scheme implementation, the uniform grid took 10–13 times longer to reach $t = 1$ with the same time step. This offers some saving beyond the factor of $\sim$9.3 reduction in the problem size with the locally refined grid, despite the cost of the matrix multiplication operations at interfaces.

3.4.2 Inviscid Compressible Vortex

For the second example, a nonlinear problem is considered to demonstrate more generally the stability of the interface schemes. As in Section 2.6.4, the dimensionless compressible Euler equations from Appendix E.2, with parameter $\beta = (\gamma - 1)/2$,

$$\frac{\partial \rho}{\partial t} + \frac{\partial}{\partial x}(\rho u) + \frac{\partial}{\partial y}(\rho v) = 0, \tag{3.4.5}$$

$$\frac{\partial}{\partial t}(\rho u) + \frac{\partial}{\partial x}\left(\rho u^2 + \frac{p}{\gamma M_0^2}\right) + \frac{\partial}{\partial y}(\rho u v) = 0, \tag{3.4.6}$$

$$\frac{\partial}{\partial t}(\rho v) + \frac{\partial}{\partial x}(\rho u v) + \frac{\partial}{\partial y}\left(\rho v^2 + \frac{p}{\gamma M_0^2}\right) = 0, \tag{3.4.7}$$

$$\begin{aligned}&\frac{\partial}{\partial t}\left(\frac{p}{\gamma M_0^2} + \beta\rho\left(u^2 + v^2\right)\right) \\ &\quad + \frac{\partial}{\partial x}\left(\frac{pu}{M_0^2} + \beta\rho u\left(u^2 + v^2\right)\right) + \frac{\partial}{\partial y}\left(\frac{pv}{M_0^2} + \beta\rho v\left(u^2 + v^2\right)\right) = 0,\end{aligned} \tag{3.4.8}$$

are implemented with a normalization in terms of far-field values, ρ_0 and p_0, and a velocity scale, u_0, which are incorporated into the Mach number parameter, M_0. Using again the constant-entropy (Lamb-Oseen) vortex from Appendix F.2 with the tangential velocity profile

$$\frac{u_\theta}{u_0} = \frac{r_0}{r}\left(1 - \mathrm{e}^{-\frac{r^2}{r_0^2}}\right), \tag{3.4.9}$$

and pressure distribution

$$\frac{p}{p_0} = \left(1 - (\gamma - 1)\, M_0^2 \left[\frac{r_0^2}{2r^2}\left(1 - \mathrm{e}^{-\frac{r^2}{r_0^2}}\right)^2 + \mathrm{Ei}\left(-2\frac{r^2}{r_0^2}\right) - \mathrm{Ei}\left(-\frac{r^2}{r_0^2}\right)\right]\right)^{\frac{\gamma}{\gamma-1}}, \quad (3.4.10)$$

where $r = \sqrt{x^2 + y^2}$, and r_0 is the core radius of the vortex, results are presented here for $\gamma = 1.4$, $M_0 = 1.2$ and $r_0 = 4/25$.

The Lamb-Oseen vortex is preferred for this work over the more familiar Taylor vortex, despite having algebraic $(1/r)$ rather than exponential decay of the core strength, because it is stable to axisymmetric perturbation while the Taylor vortex is not. With the lack of numerical dissipation in these interface schemes, numerical error can provide sufficient perturbation to induce this instability. Because of this algebraic decay, in order to keep the domain to a side length of 4, exact boundary conditions are imposed using the analytic solution, as in Section 2.6.

Both stationary and convecting vortex cases are considered, the latter having a convection velocity of (0.2, 0.3) across the domain. In both cases the vortex is initially located at the center of the domain, as shown in Figure 3.12(a). Figure 3.12(b) shows the final location of the convecting vortex at time $t = 1$. Dashed lines indicate the boundaries of the refined region for the box refinement (a) and the cross + box refinement (b). These two grids, along with the cross refinement, are as described for the advection problem, but scaled to the larger domain of this problem.

Table 3.6 shows the results of the convergence study with the convecting vortex. Here, a CFL number of 1/10 was used for the cross grid and 1/12 for the cross + box grid. For the nonlinear problem, the same third-order average (L_2) convergence is seen, while uniform convergence is similar or marginally better than the linear problem, nearing third order in some cases. This confirms the observation that at least one order of convergence is lost from the interior scheme when corner interfaces are present.

A better convergence result is obtained for the case of the vortex on the box refinement grid. As shown in Table 3.7, near–fourth-order convergence is seen, at least in the L_2-norm. For comparison, results for the advection problem on the same grid are shown alongside, where near–third-order L_2 convergence is seen as in Table 3.5. Promisingly for future adaptive use of the interface scheme, the vortex problem on the box refinement grid is the

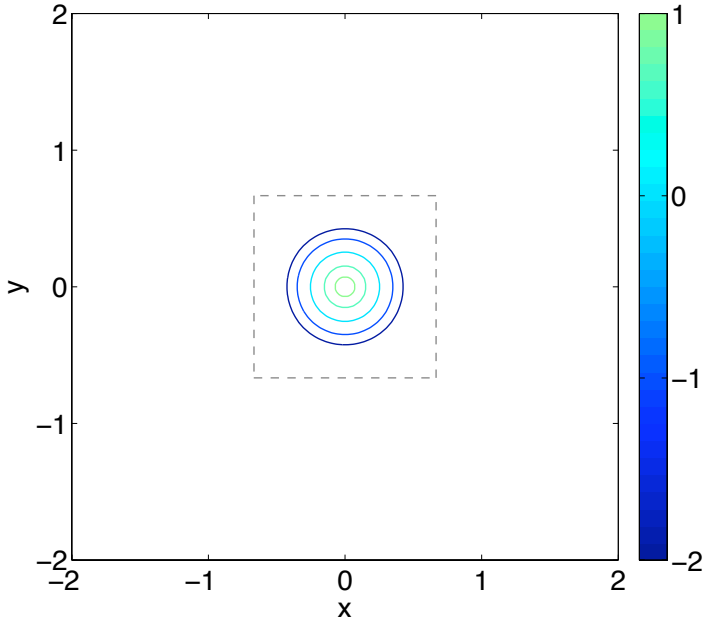

(a) vorticity field at $t = 0$

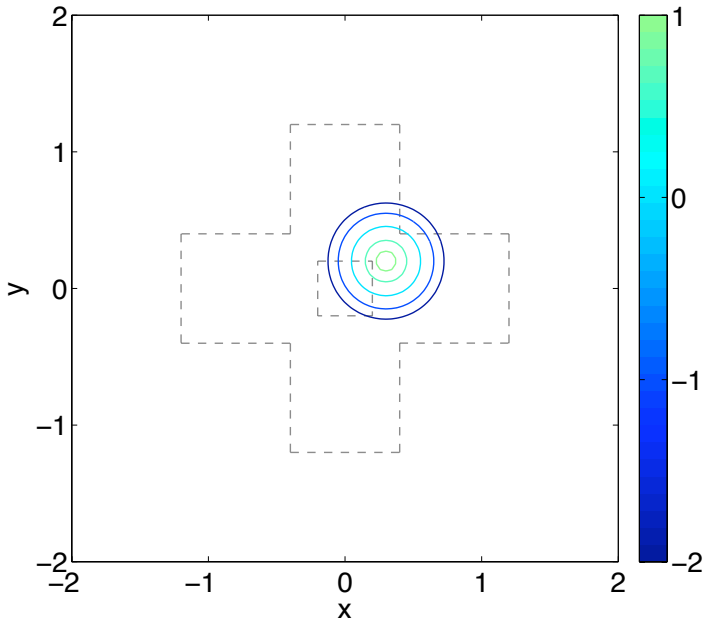

(b) vorticity field at $t = 1$

Figure 3.12: Contours of vorticity for the convecting Lamb-Oseen vortex, showing initial and final positions. Color scale is $\log_{10}(\omega)$. Grid interfaces are indicated by dashed lines, (a) showing box refinement interfaces, (b) showing cross + box refinement.

	Cross refinement				Cross + box refinement			
coarse Δx	$\log_{10}(L_2)$	rate	$\log_{10}(L_\infty)$	rate	$\log_{10}(L_2)$	rate	$\log_{10}(L_\infty)$	rate
1/10	−1.858		−0.934		−1.750		−0.859	
1/15	−2.325	2.65	−1.320	2.19	−2.255	2.87	−1.332	2.69
1/20	−2.680	2.83	−1.678	2.87	−2.618	2.90	−1.678	2.77
1/30	−3.190	2.90	−2.158	2.72	−3.126	2.89	−2.125	2.54
1/40	−3.538	2.78	−2.404	1.97	−3.465	2.72	−2.398	2.18
rate		2.81		2.51		2.86		2.57

Table 3.6: Convergence results for the convecting vortex problem on patch-refined grids

only case where the refinement followed the feature of interest (see the relative positions of the vortex core and the box in Figure 3.12). The advection examples represent something of a worst case, where refinement occurs independently of the discretized field. In practice, regions of refinement would be placed in areas of steepest gradients, thus minimizing the truncation error at the interfaces and leading to convergence performance that should be no worse than that seen in these examples.

	Advection problem				Stationary vortex problem			
N	$\log_{10}(L_2)$	rate	$\log_{10}(L_\infty)$	rate	$\log_{10}(L_2)$	rate	$\log_{10}(L_\infty)$	rate
24	−1.766		−0.957		−1.757		−1.444	
30	−2.006	2.48	−1.102	1.49	−2.179	4.35	−1.895	4.65
48	−2.568	2.75	−1.446	1.69	−3.041	4.22	−2.661	3.75
60	−2.808	2.48	−1.595	1.53	−3.427	3.99	−2.910	2.57
120	−3.605	2.65	−2.226	2.10	−4.418	3.29	−3.403	1.64
rate		2.64		1.81		3.82		2.80

Table 3.7: Convergence results for advection and stationary vortex problems on the box-refined grid

Chapter 4

Navier-Stokes Simulation of the Richtmyer-Meshkov Instability

This chapter presents an investigation of the shock-reflected Richtmyer-Meshkov (RM) instability by a linearized Navier-Stokes simulation utilizing the grid refinement schemes of Chapter 2. Analysis of the instability begins with solution of the Riemann problem for a shock incident on a density interface in Section 4.1. Existing analytic models of the RM instability are presented in Section 4.2, to be used for comparison with the simulation results. The linearized Navier-Stokes equations and the numerical method by which these are implemented are described in Sections 4.3–4.5. Results of the simulation and discussion follow in Sections 4.6–4.7.

Note that throughout this chapter, "interface" will refer to the physical contact region between light and heavy fluids, whether distributed or not. This is not to be confused with the grid interfaces discussed in the previous chapters, which refer to a property of the numerical discretization of a physical domain.

4.1 The Riemann Problem

The generalized Riemann problem may be used as an inviscid one-dimensional model of the base flow for the RM instability. For now, shocks and the density interface are approximated as strict discontinuities. The x-t diagram for the problem of interest for this study is shown in Figure 4.1. We restrict our attention to choices of the initial states such that the Riemann problem for $t > 0$ has a two-shock solution based on states 1 and $0'$. This situation arises when the incident shock travels from the light fluid into the heavy fluid and $\gamma_0 = \gamma_{0'}$. The

alternative situation of a reflected rarefaction and transmitted shock is not considered here (see instead Yang et al., 1994; Wouchuk, 2001b).

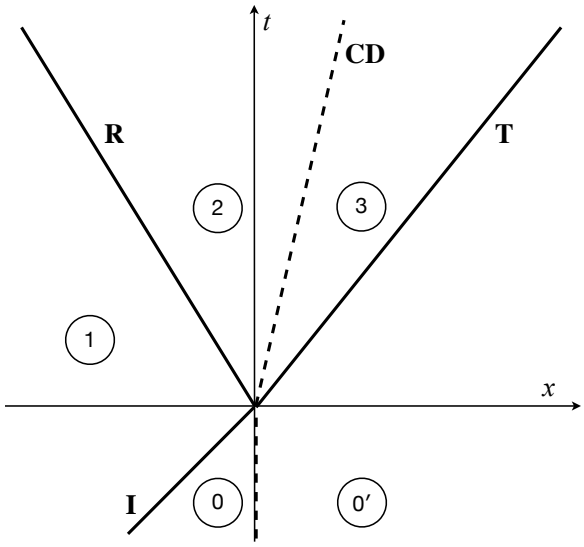

Figure 4.1: The x-t diagram for the Riemann problem in air with $M_{\rm I} = 1.21$, $\rho_{0'}/\rho_0 = 4$. The reference frame is such that the interface is stationary for $t < 0$.

Initially, states 0 and $0'$ are quiescent with $\rho_0 < \rho_{0'}$, and are separated by the contact discontinuity (**CD**). Upon impact of the incident shock (**I**), defined as occurring at time $t = 0$, a shock is transmitted (**T**) and reflected (**R**) and the contact is set in motion with a velocity ΔU. From the initial states, the entire solution may be determined in terms of the incident shock Mach number $M_{\rm I}$ and the isentropic ratios γ_0 and $\gamma_{0'}$ in each fluid by solution of the Riemann problem.

Velocities u_s are defined for each state s in a reference frame such that the interface is stationary for $t < 0$. Thus $u_0 = u_{0'} = 0$, and the impulsive velocity transferred to the interface upon impact, $\Delta U = u_2 = u_3$. Uppercase velocities $U_{\rm I}$, $U_{\rm R}$ and $U_{\rm T}$ refer to the incident, reflected and transmitted shock velocities in this frame, respectively. The shock Mach numbers are defined as the ratio of the shock speed, relative to the unprocessed fluid ahead of the shock, to the sound speed in this fluid:

$$M_{\rm I} = (U_{\rm I} - u_0)/a_0 = U_{\rm I}/a_0, \tag{4.1.1}$$

$$M_{\rm R} = (U_{\rm R} - u_1)/a_1, \tag{4.1.2}$$

$$M_{\rm T} = (U_{\rm T} - u_{0'})/a_{0'} = U_{\rm T}/a_{0'}. \tag{4.1.3}$$

This problem is then solved by applying the Rankine-Hugoniot shock jump conditions across each shock.

4.1.1 Incident Shock Jump Condition

The incident shock is a normal shock moving into a stationary fluid ($u_0 = 0$). Applying the normal shock jump condition, we obtain

$$U_{\mathrm{I}} - u_1 = \frac{2 + (\gamma_0 - 1)M_{\mathrm{I}}^2}{(\gamma_0 + 1)M_{\mathrm{I}}^2} U_{\mathrm{I}},$$

which may be rearranged for the speed in state 1, u_1, to give

$$u_1 = U_{\mathrm{I}} \left(1 - \frac{2 + (\gamma_0 - 1)M_{\mathrm{I}}^2}{(\gamma_0 + 1)M_{\mathrm{I}}^2} \right). \tag{4.1.4}$$

Since $U_{\mathrm{I}} = M_{\mathrm{I}} a_0$, where a_0 is the speed of sound in the fully specified state 0, this equation may be evaluated directly for u_1. Density and pressure in state 1 follow simply from the normal-shock relations:

$$\rho_1 = \rho_0 \frac{(\gamma_0 + 1)M_{\mathrm{I}}^2}{2 + (\gamma_0 - 1)M_{\mathrm{I}}^2}, \tag{4.1.5}$$

$$p_1 = p_0 \frac{2\gamma_0 M_{\mathrm{I}}^2 - \gamma_0 + 1}{\gamma_0 + 1}. \tag{4.1.6}$$

4.1.2 Transmitted Shock Jump Condition

Like the incident shock, the transmitted shock is moving into a stationary fluid ($u_{0'} = 0$), so $U_{\mathrm{T}} = M_{\mathrm{T}} a_{0'}$, where $a_{0'}$ is the known speed of sound in the heavy fluid. Applying the normal shock jump condition,

$$U_{\mathrm{T}} - u_3 = \frac{2 + (\gamma_{0'} - 1)M_{\mathrm{T}}^2}{(\gamma_{0'} + 1)M_{\mathrm{T}}^2} U_{\mathrm{T}},$$

from which we obtain

$$u_3 = U_{\mathrm{T}} \left(1 - \frac{2 + (\gamma_{0'} - 1)M_{\mathrm{T}}^2}{(\gamma_{0'} + 1)M_{\mathrm{T}}^2} \right), \tag{4.1.7}$$

$$\rho_3 = \rho_{0'} \frac{(\gamma_{0'}+1)M_{\mathrm{T}}^2}{2+(\gamma_{0'}-1)M_{\mathrm{T}}^2}, \tag{4.1.8}$$

$$p_3 = p_0 \frac{2\gamma_{0'}M_{\mathrm{T}}^2 - \gamma_{0'} + 1}{\gamma_{0'}+1}. \tag{4.1.9}$$

Note that from continuity of pressure across the initial (stationary) interface, $p_{0'} = p_0$, and in the heavy fluid, the ratio of specific heats is given by $\gamma_{0'}$.

4.1.3 Reflected Shock Jump Condition

For the reflected shock, care is required when applying the jump conditions because the shock propagates into a moving fluid. In this case,

$$U_{\mathrm{R}} - u_2 = \frac{2+(\gamma_0-1)M_{\mathrm{R}}^2}{(\gamma_0+1)M_{\mathrm{R}}^2}(U_{\mathrm{R}} - u_1),$$

which gives the expression for the velocity in state 2

$$u_2 = U_{\mathrm{R}} + (u_1 - U_{\mathrm{R}})\frac{2+(\gamma_0-1)M_{\mathrm{R}}^2}{(\gamma_0+1)M_{\mathrm{R}}^2}. \tag{4.1.10}$$

A more useful form, in terms of the unknowns u_2 and M_{R} alone, is given by

$$u_2 = u_1 + a_1 M_{\mathrm{R}}\left(1 - \frac{2+(\gamma_0-1)M_{\mathrm{R}}^2}{(\gamma_0+1)M_{\mathrm{R}}^2}\right). \tag{4.1.11}$$

The density and pressure in region 2 are given by the familiar relations, in terms of the as-yet unknown reflected shock Mach number M_{R}:

$$\rho_2 = \rho_1 \frac{(\gamma_0+1)M_{\mathrm{R}}^2}{2+(\gamma_0-1)M_{\mathrm{R}}^2}, \tag{4.1.12}$$

$$p_2 = p_1 \frac{2\gamma_0 M_{\mathrm{R}}^2 - \gamma_0 + 1}{\gamma_0+1}. \tag{4.1.13}$$

The solution follows by noting that velocity and pressure are continuous across the interface (**CD**): i.e., $u_2 = u_3$, and $p_2 = p_3$. Equating (4.1.11) to (4.1.7) and (4.1.13) to (4.1.9) with the appropriate substitutions, the following two equations are obtained in terms of the unknown Mach numbers M_{R} and M_{T}, with only the incident Mach number

M_{I} as a parameter:

$$a_{0'} M_{\mathrm{T}} \left(\frac{2(M_{\mathrm{T}}^2 - 1)}{(\gamma_{0'} + 1) M_{\mathrm{T}}^2} \right) = a_0 M_{\mathrm{I}} \left(\frac{2(M_{\mathrm{I}}^2 - 1)}{(\gamma_0 + 1) M_{\mathrm{I}}^2} \right) + a_1 M_{\mathrm{R}} \left(\frac{2(M_{\mathrm{R}}^2 - 1)}{(\gamma_0 + 1) M_{\mathrm{R}}^2} \right), \tag{4.1.14}$$

$$\frac{2\gamma_{0'} M_{\mathrm{T}}^2 - \gamma_{0'} + 1}{\gamma_{0'} + 1} = \left(\frac{2\gamma_0 M_{\mathrm{I}}^2 - \gamma_0 + 1}{\gamma_0 + 1} \right) \left(\frac{2\gamma_0 M_{\mathrm{R}}^2 - \gamma_0 + 1}{\gamma_0 + 1} \right), \tag{4.1.15}$$

where $a_1 = \sqrt{\gamma_0 p_1 / \rho_1} = a_1(\gamma_0, M_{\mathrm{I}})$. This system is straightforward to solve numerically, and from this solution the entire flow field can be built up.

Solutions for the parameter values chosen for simulation are shown in Table 4.1. The pre-shock Atwood number, A, and post-shock Atwood number, A^+ are defined in terms of the density solution by

$$\mathrm{A} = \frac{\rho_{0'} - \rho_0}{\rho_{0'} + \rho_0}, \quad \text{and} \quad \mathrm{A}^+ = \frac{\rho_3 - \rho_2}{\rho_3 + \rho_2}.$$

In all cases, both light and heavy gases are air with $\gamma_0 = \gamma_{0'} = 1.4$. State 0 (the reference state) is at standard atmospheric conditions having density $\rho_0 = 1.205$ kg/m^3 and pressure $p_0 = p_{0'} = 101.3$ kPa. Velocities are normalized relative to the incident shock velocity U_{I}.

M_{I}	1.05	1.05	1.21	1.21	2.20	2.20
M_{T}	1.0552	1.0672	1.2333	1.2884	2.3570	2.7493
U_{T}	0.8205	0.5082	0.8322	0.5324	0.8748	0.6248
M_{R}	1.0049	1.0161	1.0183	1.0616	1.0633	1.2232
U_{R}	−0.8951	−0.9060	−0.6321	−0.6703	0.002562	−0.09645
$\rho_{0'}$	1.5	4.0	1.5	4.0	1.5	4.0
u_1	0.07748	0.07748	0.2642	0.2642	0.6612	0.6612
ρ_1	1.0840	1.0840	1.3590	1.3590	2.9512	2.9512
p_1	1.1196	1.1196	1.5415	1.5415	5.4800	5.4800
ΔU	0.06965	0.05166	0.2376	0.1764	0.5978	0.4518
ρ_2	1.0928	1.1132	1.4005	1.4999	3.2655	4.0781
p_2	1.1323	1.1621	1.6079	1.7699	6.3149	8.6517
ρ_3	1.63914	4.4526	2.0992	5.9818	4.7369	14.445
p_3	1.1323	1.1621	1.6079	1.7699	6.3149	8.6517
A	0.2	0.6	0.2	0.6	0.2	0.6
A^+	0.19999	0.59998	0.1996	0.5991	0.1839	0.5597

Table 4.1: Riemann solutions for the parameter sets used in the simulations of the Richtmyer-Meshkov instability. Values shown are normalized by ρ_0, p_0 and U_{I}, as appropriate.

4.2 Models of the Instability

4.2.1 Impulsive Model

The simplest model for the Richtmyer-Meshkov instability, proposed originally by Richtmyer (1960), approximates the problem by an impulsively accelerated perturbed interface of zero thickness between two inviscid and incompressible fluids. If the interface is assumed to have small amplitude, the velocity perturbations in each fluid are also small and the problem may be linearized. From this model, as shown in detail in Appendix G, we obtain the familiar linear growth in time for the interface perturbation amplitude:

$$h(t) = h(0)\left[1 + \mathrm{A}\Delta U k t\right], \tag{4.2.1}$$

where A is the Atwood number, ΔU is the post-shock speed of the interface, and k is the wave number of the perturbation. Closer analysis of the impulsive problem and the experiments of Meshkov (1969) indicate that post-shock values should be used for the initial amplitude $h(0)$ and the Atwood number. This gives a more precise definition of the perturbation growth rate as

$$h(t) = h(0^+)\left[1 + \mathrm{A}^+\Delta U k t\right], \tag{4.2.2}$$

where $h(0^+)$ is the initial post-shock amplitude of the perturbation (taking into account compression of the interface by the shock), and A^+ is the post-shock Atwood number.

The post-linear regime is beyond this study, but nonlinear models do exist (e.g., Zhang and Sohn, 1997; Herrmann et al., 2008), and experimental evidence points to the growth becoming nonlinear at late times (Collins and Jacobs, 2002). At this point, the interface has transitioned from sinusoidal through the appearance of "bubbles and spikes" to the onset of turbulence. In this work, the focus is on the start-up and early-time linear behavior of the interface perturbation.

4.2.2 Viscous Model Corrections

Viscous effects on the RM instability have generally been ignored, due to the flow regime in which the problem is usually studied, with the exception of models by Mikaelian (1993)

and Carlès and Popinet (2001). In each case, viscosity damps the growth of the instability, though the models disagree strongly as to the extent of the attenuation. Both models begin with a linearization of the incompressible viscous Navier-Stokes equations, but use different approaches to solve the resulting equations. The Mikaelian model assumes the same x-velocity profile in each fluid as the impulsive model, thus ignoring any contribution from viscosity in the x-direction, while Carlès and Popinet approximate viscous effects at the interface analogous to a boundary layer and use matched asymptotic expansions to extend the solution to the outer inviscid region.

The resulting solutions give the following perturbation amplitude models: for Mikaelian,

$$h(t) = h(0)\left[1 + \mathrm{A}\Delta U \frac{1}{2k\nu}\left(1 - \mathrm{e}^{-2k^2\nu t}\right)\right], \tag{4.2.3}$$

where the kinematic viscosity is an averaged value

$$\nu = (\mu_2 + \mu_3)/(\rho_2 + \rho_3), \tag{4.2.4}$$

and for Carlès and Popinet,

$$h(t) = h(0)\left[(1 + \mathrm{A}\Delta U k t) - \frac{16}{3\sqrt{\pi}} \frac{\sqrt{\rho_1\mu_1}\sqrt{\rho_2\mu_2}}{(\rho_1 + \rho_2)(\sqrt{\rho_1\mu_1} + \sqrt{\rho_2\mu_2})} \mathrm{A}\Delta U k^2 t^{3/2}\right], \tag{4.2.5}$$

where an additional higher-order factor of the second mode (e^{2iky}) has been neglected, as this cannot be expressed in the linear formulation used in this work. The neglected term is of order k^3t^2, so is vanishingly small in the cases considered here. Following the impulsive model, for both models the initial amplitude $h(0)$ and Atwood number A are taken as the post-shock values.

Simulations of the impulsive problem with viscous incompressible fluids, performed by Carlès and Popinet, show that their model predicts the viscous effect significantly better. This fact notwithstanding, both models are used to compare against the simulations shown in Section 4.6.

4.2.3 Distributed Interface Effect

Most models of the RM instability assume that the interface is a strict discontinuity, but the amplitude growth rate may be significantly altered by finite density gradients. Experi-

mentally, significant attenuation has been seen where the interface thickness is on the order of 10% of the perturbation wavelength (Jones and Jacobs, 1997; Collins and Jacobs, 2002). Analytic models for this effect exist, beginning with Mikaelian (1991), where both hyperbolic tangent and error function interface approximations were considered, the effect being similar for profiles of similar thickness. In Brouillette and Sturtevant (1994), a modified growth rate

$$\frac{\mathrm{d}h(t)}{\mathrm{d}t} = \frac{\mathrm{A}\Delta U k}{\psi} h(0^+), \tag{4.2.6}$$

is proposed, where ψ is an eigenvalue of the Sturm-Liouville boundary value problem

$$\frac{1}{\rho}\left(\rho \frac{\mathrm{d}f}{\mathrm{d}y}\right) - \left(1 - \frac{\psi}{k\mathrm{A}}\frac{1}{\rho}\frac{\mathrm{d}\rho}{\mathrm{d}y}\right) k^2 f = 0, \quad f \to 0 \text{ as } y \to \pm\infty. \tag{4.2.7}$$

The Jacobs experiments show good agreement with this result.

For the simulations performed here, where $k\Delta_C < 0.02$ so thickness is no more than 0.3% of the perturbation wavelength, there is no noticeable effect due to the distributed interface. The Mikaelian (1991) model predicts a growth rate indistinguishable from the impulsive model, so this effect may be safely neglected in this study.

4.2.4 Characteristic Start-Up Time

In Lombardini (2008), a modified version of the impulsive theory is used to characterize the start-up process of the RM instability, leaving the asymptotic growth rate, $\dot{h}_\infty$, as a parameter of the model. The key extension of this model is the imposition of moving plane boundaries at the trailing edges of each shock, recognizing that in the early growth phase of the instability, the proximity of the reflected and transmitted shocks will trap waves in the interface region and alter the initial growth rate. At later times, the effect of these finite boundaries diminishes as the shocks move further away, and so the model approaches the infinite-boundary state of the impulsive theory.

The key result is a characteristic time scale τ, during which the proximity of the shocks affects the interface growth rate. This is defined by

$$\tau = \frac{1}{2k}\left(\frac{1-\mathrm{A}^+}{-(U_\mathrm{R} - u_2)} + \frac{1+\mathrm{A}^+}{U_\mathrm{T} - u_3}\right), \tag{4.2.8}$$

where A^+ is the post-shock Atwood number, U_R is the reflected shock speed, U_T is the

transmitted shock speed, and $u_2 = u_3$ is the speed of the interface, all defined as in Section 4.1. Note that $(U_R - u_2) < 0$ and $(U_T - u_3) > 0$ are the shock speeds in the post-impact frame in which the interface is stationary for $t > 0$. For time $t \gg \tau$, the linear asymptotic growth rate is recovered.

4.2.5 Asymptotic Linear Theory

The final model that will be compared to our numerical results is that of Wouchuk (2001a). This is an inviscid model that uses a truncated series expansion of the linearized RM problem, and captures the main physical phenomena driving the instability: the initial deposition of vorticity on the interface by the incident shock, bulk vorticity generated behind the reflected and transmitted shocks, and reverberation of sound waves between the shock fronts. It has been shown to accurately predict asymptotic growth rates (Wouchuk, 2001a; Herrmann et al., 2008; Lombardini, 2008).

From Wouchuk and Nishihara (1997), the asymptotic growth rate of the perturbation amplitude is given exactly (in the linear theory) by

$$\dot{h}_\infty = \frac{-\rho_3 v_3(0^+) + \rho_2 v_2(0^+)}{\rho_3 + \rho_2} + \frac{\rho_3 F_3 + \rho_2 F_2}{\rho_3 + \rho_2}, \tag{4.2.9}$$

where the state numbering follows Section 4.1, and $v_2(0^+)$ and $v_3(0^+)$ are the tangential velocities at the interface in each fluid immediately after impact. The functions F_2 and F_3 are central to the improved prediction of this model, as they represent the sonic interactions between the shocks and the interface. These functions cannot be calculated analytically, so are approximated by a truncated series expression.

For weak shocks, the first term of equation (4.2.9) is dominant, the model giving results similar to the impulsive model (4.2.2). The second term becomes more important as shock strength increases (or for highly compressible fluids), adding a correction for the vorticity generated by the shocks upon impact.

To summarize this section, presented in Table 4.2 is a comparison of the asymptotic growth rate predictions $\dot{h}_\infty / kh(0^-)$ by equations (4.2.2) and (4.2.9) for each of the parameter cases defined in Table 4.1. Also shown is the start-up time scale τ, scaled by wave number, defined by equation (4.2.8).

Incident shock M_{I}	1.05	1.05	1.21	1.21	2.20	2.20
Pre-shock A	0.2	0.6	0.2	0.6	0.2	0.6
Post-shock A^+	0.19999	0.59998	0.1996	0.5991	0.1839	0.5597
Impulsive model $\dot{h}_\infty$	0.01295	0.02934	0.03616	0.08703	0.04421	0.1386
Wouchuk model $\dot{h}_\infty$	0.01341	0.03010	0.04058	0.09303	0.06030	0.1556
$k\tau$ from (4.2.8)	1.2137	1.9612	1.4688	2.4826	2.8224	4.9086

Table 4.2: Predictions for the asymptotic growth rate $\dot{h}_\infty/kh(0^-)$, using the impulsive model and Wouchuk (2001a) model, and the characteristic start-up time proposed by Lombardini (2008), for each case from Table 4.1.

4.3 Linearized Navier-Stokes Equations

For this investigation of the Richtmyer-Meshkov instability, we solve the Navier-Stokes equations in 2-D, linearized about a fully resolved numerical solution for the base flow, in a frame of reference in which the interface is stationary for $t < 0$. Shocks and the interface are treated as continuous features, and it is assumed that the perturbation amplitude remains small throughout the simulation. The problem is also simplified to consider a single fluid, such that $\gamma_0 = \gamma_{0'} = \gamma$.

Starting with the general compressible Navier-Stokes equations for a Newtonian fluid with zero bulk viscosity and Fourier heat conduction, we define two-dimensional Cartesian axes (x, y) where the shocks propagate in the direction parallel to the x-axis. Following the derivation presented in Appendix E.3, these assumptions yield the system

$$\frac{\partial \rho}{\partial t} + \frac{\partial(\rho u)}{\partial x} + \frac{\partial(\rho v)}{\partial y} = 0, \tag{4.3.1}$$

$$\frac{\partial(\rho u)}{\partial t} + \frac{\partial(\rho u^2)}{\partial x} + \frac{\partial(\rho uv)}{\partial y} = -\frac{\partial p}{\partial x} + \mu\left(\frac{4}{3}\frac{\partial^2 u}{\partial x^2} + \frac{\partial^2 v}{\partial x \partial y} + \frac{\partial^2 u}{\partial y^2}\right), \tag{4.3.2}$$

$$\frac{\partial(\rho v)}{\partial t} + \frac{\partial(\rho uv)}{\partial x} + \frac{\partial(\rho v^2)}{\partial y} = -\frac{\partial p}{\partial y} + \mu\left(\frac{\partial^2 v}{\partial x^2} + \frac{\partial^2 u}{\partial x \partial y} + \frac{4}{3}\frac{\partial^2 v}{\partial y^2}\right), \tag{4.3.3}$$

$$\begin{aligned}
&\frac{\partial}{\partial t}\big(\rho e + \frac{1}{2}\rho(u^2+v^2)\big) + \frac{\partial}{\partial x}\big(\rho ue + \frac{1}{2}\rho u(u^2+v^2)\big) + \frac{\partial}{\partial y}\big(\rho ve + \frac{1}{2}\rho v(u^2+v^2)\big) \\
&\quad = -\frac{\partial(pu)}{\partial x} - \frac{\partial(pv)}{\partial y} + \kappa\big(\frac{\partial^2 T}{\partial x^2} + \frac{\partial^2 T}{\partial y^2}\big) \\
&\quad + \mu\left[\frac{4}{3}\frac{\partial}{\partial x}\big(u\frac{\partial u}{\partial x}\big) + \frac{\partial}{\partial x}\big(v\frac{\partial v}{\partial x} + v\frac{\partial u}{\partial y}\big) + \frac{\partial}{\partial y}\big(u\frac{\partial v}{\partial x} + u\frac{\partial u}{\partial y}\big) + \frac{4}{3}\frac{\partial}{\partial y}\big(v\frac{\partial v}{\partial y}\big)\right].
\end{aligned} \tag{4.3.4}$$

It is assumed that μ and κ are constant, an acceptable approximation for weaker shocks where the change in temperature is small. For the strongest shock considered here, $M_{\mathrm{I}} = 2.20$, the difference in the velocity profiles due to this assumption is no greater than 10%

(see Figure F.1 for a comparison).

For the equation of state, a perfect gas is specified such that

$$p = \rho RT, \tag{4.3.5}$$

$$e = C_V T = \frac{1}{\gamma - 1}\frac{p}{\rho}. \tag{4.3.6}$$

The latter result allows e to be eliminated from the energy equation. The resulting equations are then nondimensionalized, as in Appendix E.1, where the reference parameters ρ_0 and p_0 are defined at state 0, and the velocity scale is the incident shock velocity, U_I, defined in Section 4.1. A length scale is provided by the mean free path in state 0, ℓ_0, given by

$$\ell_0 = \nu_0 \frac{8}{5}\sqrt{\frac{2}{\pi RT_0}}, \tag{4.3.7}$$

where ν_0 is the kinematic viscosity of the fluid in state 0. This is then clearly a viscous length scale. For the parameter values used in these simulations, with state 0 the same for all cases (Table 4.1), $\ell_0 = 6.65 \times 10^{-8}$ m. Note that physical time is scaled by ℓ_0/U_I, so one nondimensional time unit corresponds to $O(10^{-10})$ seconds, depending on the value of U_I. For expediency, from this point onward throughout this chapter, all variables refer to nondimensional values, without change in notation, unless otherwise noted.

We now propose a form for the solution to equations (4.3.1)–(4.3.4) that represents a small sinusoidal perturbation in the y-direction of a 1-D base flow:

$$u = \bar{u}(x,t) + \epsilon u'(x,t)\mathrm{e}^{\mathrm{i}ky}, \tag{4.3.8}$$

$$v = \epsilon v'(x,t)\mathrm{e}^{\mathrm{i}ky}, \tag{4.3.9}$$

$$\rho = \bar{\rho}(x,t) + \epsilon \rho'(x,t)\mathrm{e}^{\mathrm{i}ky}, \tag{4.3.10}$$

$$p = \bar{p}(x,t) + \epsilon p'(x,t)\mathrm{e}^{\mathrm{i}ky}, \tag{4.3.11}$$

where the small parameter $\epsilon \ll 1$, the overbar indicates the base flow variables that are one dimensional but generally unsteady, and prime quantities are the first-order perturbation variables. The wave number k is generally complex. Substituting equations (4.3.8)–(4.3.11) into the nondimensional form of equations (4.3.1)–(4.3.4), and expanding in powers of ϵ, at

order ϵ^0 we obtain for the base flow

$$\frac{\partial \bar{\rho}}{\partial t} = -\frac{\partial(\bar{\rho}\bar{u})}{\partial x}, \tag{4.3.12}$$

$$\frac{\partial(\bar{\rho}\bar{u})}{\partial t} = -\frac{\partial}{\partial x}\left(\frac{\bar{p}}{\gamma M_{\mathrm{I}}^2} + \bar{\rho}\bar{u}^2 - \frac{4}{3}\frac{1}{\mathrm{Re}}\frac{\partial \bar{u}}{\partial x}\right), \tag{4.3.13}$$

$$\frac{\partial}{\partial t}\left(\frac{\bar{p}}{\gamma M_{\mathrm{I}}^2} + \beta\bar{\rho}\bar{u}^2\right) = -\frac{\partial}{\partial x}\left(\frac{\bar{p}\bar{u}}{M_{\mathrm{I}}^2} + \beta\bar{\rho}\bar{u}^3 - \frac{1}{\mathrm{PrRe}M_{\mathrm{I}}^2}\frac{\partial \bar{T}}{\partial x} - \frac{4}{3}\frac{\gamma-1}{\mathrm{Re}}\bar{u}\frac{\partial \bar{u}}{\partial x}\right), \tag{4.3.14}$$

where $\beta = (\gamma-1)/2$. These are the familiar (nonlinear) 1-D compressible Navier-Stokes equations. At order ϵ, we have

$$\frac{\partial \rho'}{\partial t} = -\frac{\partial}{\partial x}\left[\bar{\rho}u' + \rho'\bar{u}\right] - \mathrm{i}k\bar{\rho}v', \tag{4.3.15}$$

$$\begin{aligned}\frac{\partial}{\partial t}\left(\bar{\rho}u' + \rho'\bar{u}\right) = &-\frac{\partial}{\partial x}\left[\frac{p'}{\gamma M_{\mathrm{I}}^2} + \rho'\bar{u}^2 + 2\bar{\rho}\bar{u}u' - \frac{1}{\mathrm{Re}}\left(\frac{4}{3}\frac{\partial u'}{\partial x} + \mathrm{i}kv'\right)\right] \\ &- \mathrm{i}k\bar{\rho}\bar{u}v' - \frac{1}{\mathrm{Re}}k^2u',\end{aligned} \tag{4.3.16}$$

$$\frac{\partial}{\partial t}\left(\bar{\rho}v'\right) = -\frac{\partial}{\partial x}\left[\bar{\rho}\bar{u}v' - \frac{1}{\mathrm{Re}}\left(\frac{\partial v'}{\partial x} + \mathrm{i}ku'\right)\right] - \mathrm{i}k\frac{p'}{\gamma M_{\mathrm{I}}^2} - \frac{1}{\mathrm{Re}}\frac{4}{3}k^2v', \tag{4.3.17}$$

$$\begin{aligned}&\frac{\partial}{\partial t}\left(\frac{p'}{\gamma M_{\mathrm{I}}^2} + \beta\left(\rho'\bar{u}^2 + 2\bar{\rho}\bar{u}u'\right)\right) \\ &\quad= -\frac{\partial}{\partial x}\left[\frac{p'\bar{u} + \bar{p}u'}{M_{\mathrm{I}}^2} + \beta\left(\rho'\bar{u}^3 + 3\bar{\rho}\bar{u}^2u'\right) - \frac{1}{\mathrm{PrRe}M_{\mathrm{I}}^2}\frac{\partial T'}{\partial x} - \frac{4}{3}\frac{\gamma-1}{\mathrm{Re}}\left(\bar{u}\frac{\partial u'}{\partial x} + u'\frac{\partial \bar{u}}{\partial x}\right)\right] \\ &\qquad- \mathrm{i}kv'\left(\frac{\bar{p}}{M_{\mathrm{I}}^2} + \beta\bar{\rho}\bar{u}^2\right) - \frac{1}{\mathrm{PrRe}}k^2\frac{T'}{M_{\mathrm{I}}^2} + \frac{\gamma-1}{\mathrm{Re}}\bar{u}\left(\mathrm{i}k\frac{\partial v'}{\partial x} - k^2u'\right).\end{aligned} \tag{4.3.18}$$

These equations (4.3.15)–(4.3.18) for the first-order perturbations form a linear system of partial differential equations with variable coefficients. A detailed description of the linearization and nondimensionalization of the full system of equations is provided in Appendix E.3.

This system is expressed in terms of four parameters: the incident shock Mach number M_{I}, γ, and the Reynolds and Prandtl numbers, Re and Pr. For consistency with the Navier-Stokes shock solution, the Reynolds number for these equations is based on the molecular viscosity derived from kinetic theory (see Appendices E.1 and E.3), such that

$$\mathrm{Re} = \frac{\sqrt{\gamma M_{\mathrm{I}}^2}}{k_2}, \quad \text{where} \quad k_2 = \frac{5}{8}\sqrt{\frac{\pi}{2}}. \tag{4.3.19}$$

Similarly, for the Prandtl number we require $\mathrm{Pr} = 3/4$.

Note that for a real wave number k, provided that the initial perturbed fields ρ', u' and p' are real and v' has zero real part, it can be shown that the solution to equations (4.3.12)–(4.3.18) will evolve to have v' purely imaginary, and all other fields purely real.

4.4 Implementation

4.4.1 Numerical Method

The implementation of the Navier-Stokes equations (4.3.12)–(4.3.18) to simulate the linearized Richtmyer-Meshkov instability was developed from the original 1-D Navier-Stokes shock test problem described in Appendix F.1 and is now extended to include the 2-D perturbed system. The solution strategy is to solve the base flow equations (4.3.12)–(4.3.14) and the first-order perturbation equations (4.3.15)–(4.3.18) simultaneously. The numerical solution obtained for equations (4.3.12)–(4.3.14) is the unsteady 1-D base flow, corresponding to the viscous version of the shock-interface impact problem described in Section 4.1. The solution to equations (4.3.15)–(4.3.18) proceeds using the (x, t)-dependent coefficients from the base flow, and describes the first-order perturbation of the RM instability.

The basic numerical method uses a fourth-order explicit finite-difference scheme to approximate the spatial derivatives, with local refinement (described in detail in Section 4.4.4) using the 1-D interface schemes from Chapter 2. Interpolation to shift the refined region(s) of the grid between time steps uses the sixth-order scheme of Fornberg (1988), the higher-order interpolation minimizing its contribution to the truncation error. Second derivatives are evaluated by applying the first derivative scheme twice. Time integration is by the third-order RK32 Runge-Kutta scheme from Butcher (2003), with uniform time stepping.

For generality, the perturbed flow is permitted to be complex, allowing for variation of the phase of the initial perturbation. This facility has not been utilized in the results presented here, so as noted previously, with a purely real initial condition, the perturbed flow will remain real for all time (except v', which will always be purely imaginary). The additional computational cost of this provision was found to be negligible.

A full set of validation tests was performed on the implementation of the 2-D system. The details of these tests, together with comprehensive convergence results verifying that fourth-order convergence is achieved, are presented in Appendix H.

4.4.2 Boundary Conditions

Characteristic boundary conditions are implemented using the simultaneous approximation term (SAT) method (originally from Carpenter et al., 1994 and described in Chapter 2). The method for the 1-D base-flow equations follows somewhat the method proposed by Svärd et al. (2007) for the Navier-Stokes equations, while the 2-D first-order equations are linear with nonconstant coefficients so the implementation of characteristic boundary conditions is somewhat simpler. Details of the derivation of the boundary conditions for both nonlinear 1-D and linearized 2-D equation sets are shown in Appendix E.5. For all time, the boundary state at the left (upstream) end is state 1, and at the right (downstream) end, state $0'$. The computational domain is chosen to be large enough to contain the reflected and transmitted shocks (including tails) until the end of the simulation. This simplifies the boundary conditions, as both states are constant throughout the simulation.

In cases where the left-hand boundary is a supersonic inlet, all three characteristics $\bar{u}$, $(\bar{u} - \bar{a}^*)$ and $(\bar{u} + \bar{a}^*)$ are inward facing and should be specified (see Appendix E.4 for variable definitions). Characteristic speeds for the linearized system are the same, with the addition of a second variable on $\bar{u}$, so at the left-hand boundary all four linearized perturbed characteristic variables should be specified. If the left-hand boundary is subsonic, the $(\bar{u}-\bar{a}^*)$ characteristic points out of the domain, so an additional boundary condition is required. This is provided by the temperature gradient, for which $\partial\bar{T}/\partial x$ is set to zero in the base flow and $\partial T'/\partial x$ is set to zero in the perturbed flow.

On the right-hand boundary, the choice of boundary condition is ambiguous since state 0' has $\bar{u} = 0$ and hence the $\bar{u}$ characteristic is parallel to the boundary in (x, t)-space. While the $(\bar{u}-\bar{a}^*)$-characteristic points into the domain and must be specified, there is a choice for the second boundary condition. If the $\bar{u}$-characteristic is specified, the system is closed, but if it is not, the additional boundary condition is provided by setting the velocity gradient $\partial\bar{u}/\partial x$ to zero. For the perturbed flow, two additional boundary conditions are required if the $\bar{u}$-characteristic is not specified, and these are $\partial u'/\partial x = 0$ and $\partial v'/\partial x = 0$, as the outflow is assumed to be quiescent. In practice, it was found that small perturbations could tip $\bar{u}$ slightly negative at the right-hand boundary, of order 10^{-12} or less, so the choice of boundary condition was determined by a real-time switching based on the sign of $\bar{u}$.

Stability of the boundary conditions is dependent on the SAT parameter, τ_{SAT} (Ap-

pendix E.5). By Carpenter's original derivation (Carpenter et al., 1994), the stability criteria is $\tau_{\text{SAT}} > 1$, which is supported by numerical experiments conducted with this system. For the results presented, values for τ_{SAT} of between 2 and 6 were used. Note from Chapter 2 the resulting stability limits on the CFL number; in practice, typical values for the CFL (based on the smallest Δx in the domain) were 0.16–0.18, depending on the discretization.

4.4.3 Initial Condition

Conceptually, the initial condition for the Richtmyer-Meshkov problem is an interface in the density field with some spatial perturbation of amplitude h_0, as shown in the schematic Figure 4.2. For this analysis, by convention, $\rho_{0'} > \rho_0$, so the incident shock is moving into a heavier fluid, with the result that a shock will be reflected upon impact.

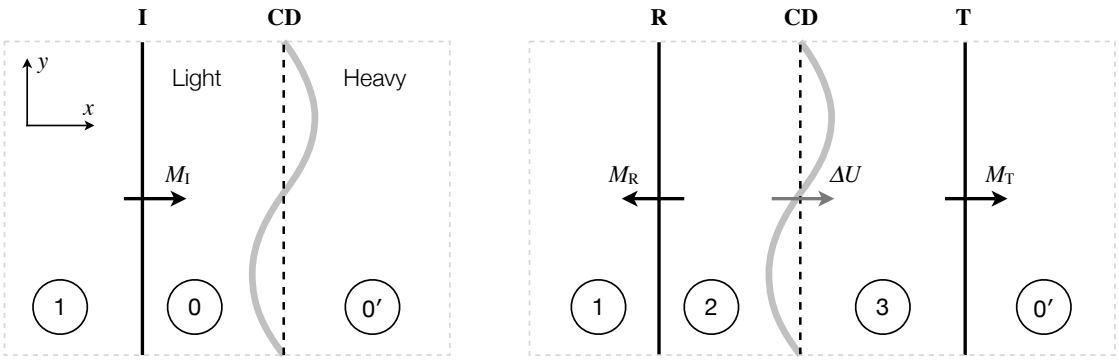

(a) $t < 0$ (b) $t > 0$

Figure 4.2: Schematic of the reflected-shock Richtmyer-Meshkov problem. The incident shock hits the interface centerline at $t = 0$.

The classic form of a discontinuous density interface with a sinusoidal perturbation is given in terms of an initial amplitude h_0 by

$$\rho(x, y, t = 0) = \begin{cases} \rho_0, & x < h_0 \sin(ky), \\ \rho_{0'}, & x > h_0 \sin(ky), \end{cases} \tag{4.4.1}$$

where the interface is centered at $x = 0$. Such an initial condition was found to be unstable in this numerical implementation, as implementation of the step-function discontinuity introduces Gibbs-type oscillation that cannot be dissipated by the numerical method and grows with time. The alternative is to model the contact surface more realistically with a

statically diffusing density interface, using the solution given by Duff et al. (1962),

$$\rho(x, y, t = 0) = \frac{\rho_{0'} + \rho_0}{2} + \frac{\rho_{0'} - \rho_0}{2} \operatorname{erf}(x + h_0 \sin(ky)). \tag{4.4.2}$$

Closely related is the alternative profile

$$\rho(x, y, t = 0) = \frac{\rho_{0'} + \rho_0}{2} + \frac{\rho_{0'} - \rho_0}{2} \tanh(x + h_0 \sin(ky)), \tag{4.4.3}$$

which is easier to analyze, and under the appropriate scaling, differs from the error function profile by less than 3.5% (Mikaelian, 1991).

For our problem described by equations (4.3.12)–(4.3.18), we approximate the perturbed interface given in equation (4.4.2) within the constraints of the form of the linearization. Clearly, (4.4.2) is not of the form $\bar{\rho} + \rho'(x, t)\mathrm{e}^{\mathrm{i}ky}$. If it is recast slightly more generally as

$$\rho(x, y, t = 0) = \frac{\rho_{0'} + \rho_0}{2} + \frac{\rho_{0'} - \rho_0}{2} \operatorname{erf}(x + h_0 \mathrm{e}^{\mathrm{i}ky}), \tag{4.4.4}$$

however, we see that the desired form may be approximated by a Taylor expansion about x for small amplitude h_0:

$$\rho(x, y, t = 0) \approx \left[\frac{\rho_{0'} + \rho_0}{2} + \frac{\rho_{0'} - \rho_0}{2} \operatorname{erf}(x)\right] + \left[\frac{\rho_{0'} - \rho_0}{2} \frac{2}{\sqrt{\pi}} \mathrm{e}^{-x^2}\right] h_0 \mathrm{e}^{\mathrm{i}ky} + \ldots. \tag{4.4.5}$$

Generalizing this result for an initial profile of thickness Δ_C, we obtain the initial condition

$$\bar{\rho}(x, t = 0) = \frac{\rho_{0'} + \rho_0}{2} + \frac{\rho_{0'} - \rho_0}{2} \operatorname{erf}(2x/\Delta_\mathrm{C}), \tag{4.4.6}$$

$$\rho'(x, t = 0) = \frac{\rho_{0'} - \rho_0}{2} \frac{4h_0}{\Delta_\mathrm{C}\sqrt{\pi}} \mathrm{e}^{-(2x/\Delta_\mathrm{C})^2}, \tag{4.4.7}$$

or, alternatively, for a tanh profile,

$$\bar{\rho}(x, t = 0) = \frac{\rho_{0'} + \rho_0}{2} + \frac{\rho_{0'} - \rho_0}{2} \tanh(2x/\Delta_\mathrm{C}), \tag{4.4.8}$$

$$\rho'(x, t = 0) = \frac{\rho_{0'} - \rho_0}{2} \frac{2h_0}{\Delta_\mathrm{C}} \operatorname{sech}^2(2x/\Delta_\mathrm{C}). \tag{4.4.9}$$

All other fields are initialized to be constant across the interface region. The thickness Δ_C is treated as a constant parameter here, but is, in fact, a time-varying quantity that will be

discussed in detail in Section 4.5.

The choice between the error function and hyperbolic tangent initial conditions turns out to have little consequence on the solution. The computational initial condition is designed such that the head of the incident shock and the tail of the interface are indistinguishable from the base state (0) to computational accuracy, so once the simulation begins the shock moves towards the interface as it begins diffusing. Neither profile (4.4.6) nor (4.4.8) is an exact steady solution to the Navier-Stokes equations with a zero velocity field, so small waves are sent out in the velocity and pressure fields once the simulation begins, which are visible as small ripples in each field but decay quickly. Comparison of solutions started with each initial condition (Figure 4.3) show that this has little influence on the shocked interface shape or position (the maximum difference is on the order of 0.1%), so the choice of equation (4.4.6) or (4.4.8) is of little consequence. Nevertheless, results presented here use the tanh initial condition, unless otherwise noted.

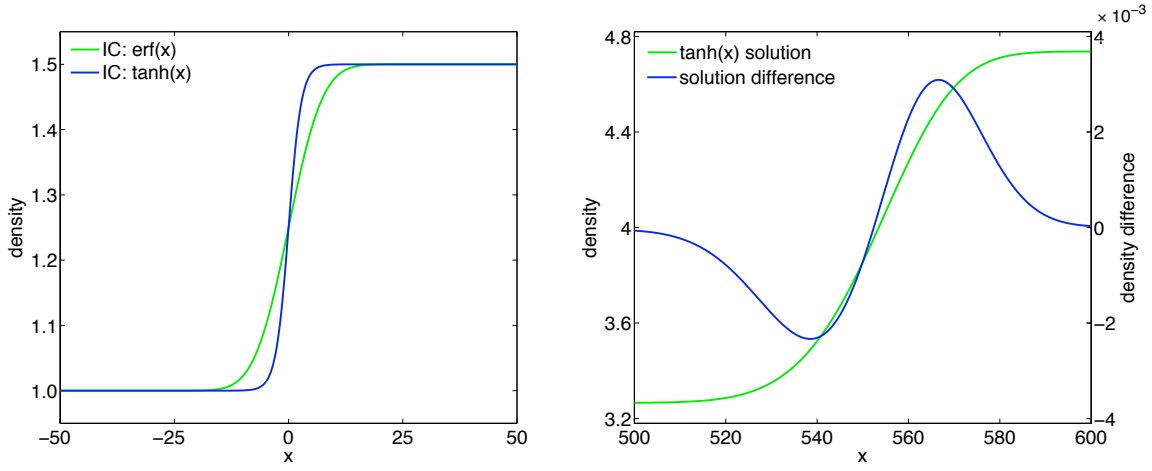

(a) initial condition

(b) solution at $t = 1000$

Figure 4.3: Demonstration of the weak dependence of the post-impact interface profile on the initial condition: post-impact, solutions are almost identical despite different initial approximation functions and thicknesses. Plotted in (b) is the solution for the $\tanh(x)$ initial condition, with the difference (tanh solution − erf solution) (blue line) plotted on the right-hand y-axis. Note the relative scales; the difference is on the order of 0.1%.

The incident shock is initialized using the Navier-Stokes shock solution (presented in Appendix F.1) for the given incident Mach number M_{I}. The domain upstream of the shock, state 1, is uniform and initialized to the Rankine-Hugoniot conditions based on the incident shock. For the remainder of the computational domain, downstream of the interface and

shock, the initial condition is the quiescent state $0'$.

4.4.4 Refinement Tracking

Local refinement of the computational domain is desirable in the vicinity of the shocks and the interface to efficiently resolve the full solution. Because one or more flow features are necessarily in motion relative to the solution reference frame, the local refinement scheme for the RM problem must be designed to track each feature of interest with time, i.e., an adaptive mesh refinement scheme is necessary. In the general case, AMR requires complicated solution gradient detection algorithms to ensure that adequate refinement occurs where it is needed. For the RM problem, however, we adopt a simpler approach, using the 1-D Riemann solution described in Section 4.1 to give an a priori indication of where refinement of the solution will be required. Thus the inviscid Euler solution may be used to design a refinement scheme that tracks the solution features of interest, with a relatively simple algorithm that shifts the refinement regions based on the known locations of the shocks and interface. This is demonstrated by Figure 4.4, which shows the refinement scheme in (x, t)-space, overlaying the x-t diagram of the Riemann solution. The extent of the refinement relative to the continuous solution is shown in Figure 4.5.

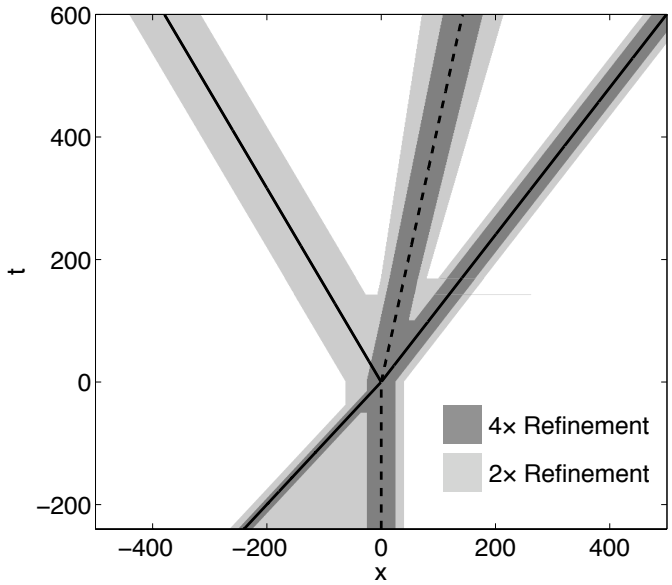

Figure 4.4: A two-level grid refinement scheme for $M_I = 1.21$ and A $= 0.2$, overlaying the x-t diagram for this problem. The shaded regions show how the refined regions follow the flow features based on the Riemann solution.

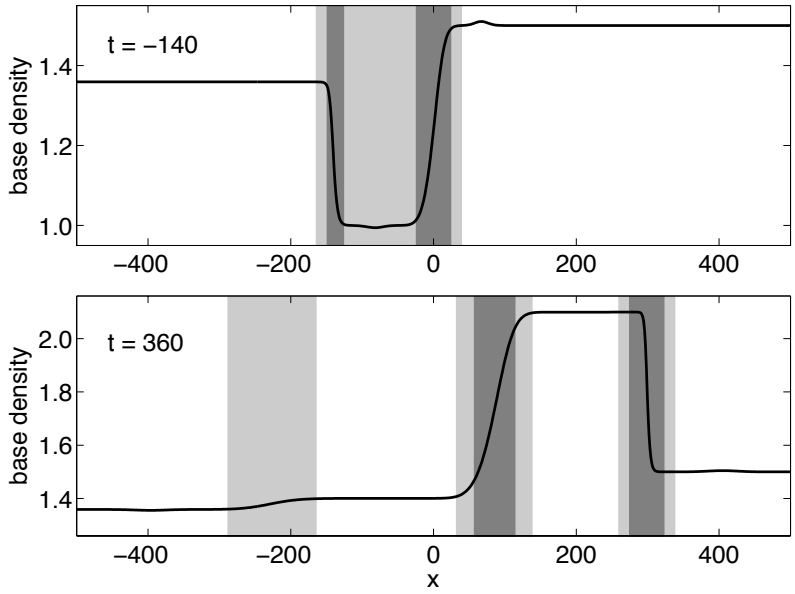

Figure 4.5: The refinement scheme from Figure 4.4 shown relative to the continuous solution, at times $t = -140$ and $t = 360$. Refined regions extend across the majority of the width of each feature, the solution being relatively flat elsewhere.

In general, two levels of refinement were used, each of factor two for an overall refinement of four times between the finest and coarsest discretizations. This was done both at the transmitted shock and interface, as these exhibit the steepest gradients, while the much-weaker reflected shock was often refined just once. Grid shifting occurred at a rate specified by the speed of each feature as given by the Riemann solution. To preserve the integrity of the grid, a shift was performed only once the feature had travelled a distance equivalent to at least one coarse cell, so the refinement advanced in appropriate multiples of the coarse grid spacing.

For the case of $M_{\mathrm{I}} = 2.20$ and $\mathrm{A} = 0.6$ an additional level of refinement was required to resolve a very steep gradient that appears during impact of the incident shock with the interface. If left underresolved, this sharp peak resulted in nonphysical oscillation at the trailing corner of the transmitted shock for the remainder of the simulation. With a small region of additional refinement at the transmitted shock, this oscillation disappeared and the solution remained smooth for all time.

More sophisticated controls on the refinement scheme are imposed once the flow features have separated fully after impact. For the interface, to ensure that the perturbation remains properly refined, the refinement region gradually extends while it convects to follow the

slow diffusion of the interface. Also, to ensure that each feature remains centered in its refinement region, a check is imposed to stop advancement of the refinement if the feature drifts too far off-center. This particular problem is due to the round-off error involved in the approximation of its speed as an integer ratio of time steps to grid cells, and only becomes apparent at late times in the simulations.

4.5 Amplitude Measurement

4.5.1 Definition

The fundamental quantity of interest for investigation of the Richtmyer-Meshkov instability is the amplitude of the perturbation on the density interface, $h(t)$. This is relatively easy to define physically in the discontinuous case from the recovered 2-D density field, as shown in Figure 4.6.

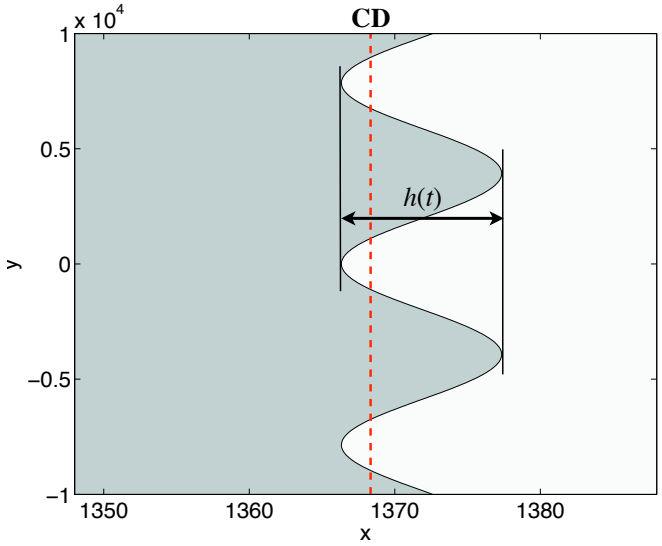

Figure 4.6: Definition of the perturbation amplitude $h(t)$ in physical 2-D space. Shown is the 50% contour between states 2 and 3 at $t = 5760$, with the dashed line showing the location of the interface based on the Riemann solution, for $M_{\mathrm{I}} = 1.21$, $A = 0.2$.

To describe the amplitude of the perturbation in the linearized distributed-interface problem, we start with the definition used by Lombardini (2008). The position of the centerline of the perturbation is defined as

$$x_{\mathrm{C}}(y,t) \equiv \frac{\int_{-\infty}^{\infty} x\psi(1-\psi)\mathrm{d}x}{\int_{-\infty}^{\infty} \psi(1-\psi)\mathrm{d}x}, \tag{4.5.1}$$

where ψ is a normalized density function with $\psi \in [0,1]$, which may be defined by

$$\psi(x,y,t) = \frac{\rho(x,y,t) - \rho_1}{\rho_2 - \rho_1}. \tag{4.5.2}$$

The perturbation amplitude is given by

$$h(t) = \frac{1}{2}|x_{\mathrm{C}}^{\mathrm{bubble}} - x_{\mathrm{C}}^{\mathrm{spike}}|, \tag{4.5.3}$$

where $x_{\mathrm{C}}^{\mathrm{bubble}}$ and $x_{\mathrm{C}}^{\mathrm{spike}}$ are the maximum and minimum values of x_{C} in a wavelength.

We will first demonstrate this definition with a tanh interface profile of the form

$$\psi(x,y,t) = \frac{1}{2}\left[1 + \tanh\left(\frac{2(x - x_{\mathrm{C}}(y,t))}{\Delta_{\mathrm{C}}(t)}\right)\right], \tag{4.5.4}$$

where $\Delta_{\mathrm{C}}(t)$ is the thickness of the interface. Note that this thickness is consistent with the tangent thickness definition for tanh, the same definition used to estimate the shock thickness. Evaluating the denominator of equation (4.5.1), we see that

$$\begin{aligned}\int_{-\infty}^{\infty} \psi(1-\psi)\mathrm{d}x &= \frac{1}{4}\int_{-\infty}^{\infty}\left[1 - \tanh^2\left(\frac{2(x-xc)}{\Delta_{\mathrm{C}}}\right)\right]\mathrm{d}x \\ &= \frac{1}{4}\int_{-\infty}^{\infty}\operatorname{sech}^2\left(\frac{2(x-xc)}{\Delta_{\mathrm{C}}}\right)\mathrm{d}x \\ &= \frac{1}{4}\Delta_{\mathrm{C}},\end{aligned}$$

which we will use to define the interface thickness by

$$\Delta_{\mathrm{C}}(t) = 4\int_{-\infty}^{\infty}\psi(1-\psi)\mathrm{d}x. \tag{4.5.5}$$

Evaluating the numerator of (4.5.1),

$$\begin{aligned}\int_{-\infty}^{\infty} x\psi(1-\psi)\mathrm{d}x &= \frac{1}{4}\int_{-\infty}^{\infty} x\left[1 - \tanh^2\left(\frac{2(x-xc)}{\Delta_{\mathrm{C}}}\right)\right]\mathrm{d}x \\ &= \frac{1}{4}\int_{-\infty}^{\infty} x\operatorname{sech}^2\left(\frac{2(x-xc)}{\Delta_{\mathrm{C}}}\right)\mathrm{d}x \\ &= \frac{1}{4}x_{\mathrm{C}}\Delta_{\mathrm{C}},\end{aligned}$$

we recover x_{C}.

For the linearized problem, we consider a linearization of equation (4.5.4), such that

$$\psi(x,y,t) = \frac{1}{2}\left[1 + \tanh\left(\frac{2x}{\Delta_C}\right) - \frac{2x_C}{\Delta_C}\operatorname{sech}^2\left(\frac{2x}{\Delta_C}\right)\right]. \tag{4.5.6}$$

In this case, we find that the denominator of (4.5.1) gives

$$\begin{aligned}\frac{1}{4}\int_{-\infty}^{\infty}&\left[\operatorname{sech}^2\left(\frac{2x}{\Delta_C}\right) + \frac{4x_C}{\Delta_C}\tanh\left(\frac{2x}{\Delta_C}\right)\operatorname{sech}^2\left(\frac{2x}{\Delta_C}\right) - \left(\frac{2x_C}{\Delta_C}\right)^2\operatorname{sech}^4\left(\frac{2x}{\Delta_C}\right)\right]\mathrm{d}x \\ &= \frac{1}{4}\Delta_C - \frac{2}{3}\frac{x_C^2}{\Delta_C},\end{aligned}$$

and the numerator,

$$\begin{aligned}\frac{1}{4}\int_{-\infty}^{\infty}&x\left[\operatorname{sech}^2\left(\frac{2x}{\Delta_C}\right) + \frac{4x_C}{\Delta_C}\tanh\left(\frac{2x}{\Delta_C}\right)\operatorname{sech}^2\left(\frac{2x}{\Delta_C}\right) - \left(\frac{2x_C}{\Delta_C}\right)^2\operatorname{sech}^4\left(\frac{2x}{\Delta_C}\right)\right]\mathrm{d}x \\ &= \frac{1}{4}x_C\Delta_C.\end{aligned}$$

Notice that the thickness estimate defined by equation (4.5.5) is no longer exact in the linearized case, but may be corrected if x_C is known.

The definition of x_C by equation (4.5.1) therefore suffers from a significant error in the linearized case. The linearized perturbation lends itself to a better definition of the interface amplitude, however. First notice the linearization of ψ from equation (4.5.6),

$$\psi(x,y,t) = \bar{\psi}(x,t) - \psi'(x,y,t), \tag{4.5.7}$$

for which the tanh profile gives

$$\bar{\psi} = \frac{1}{2}\left[1 + \tanh\left(\frac{2x}{\Delta_C}\right)\right], \tag{4.5.8}$$

$$\psi' = \frac{x_C}{\Delta_C}\operatorname{sech}^2\left(\frac{2x}{\Delta_C}\right). \tag{4.5.9}$$

Now notice that the integral

$$\int_{-\infty}^{\infty}\psi'\mathrm{d}x = \int_{-\infty}^{\infty}\frac{x_C}{\Delta_C}\operatorname{sech}^2\left(\frac{2x}{\Delta_C}\right)\mathrm{d}x = x_C,$$

without any error contribution from the linearization. Thus, for the linearized problem,

this definition of the centerline position is preferred.

An important test of the amplitude definition is the limit as $\Delta_C \to 0$, i.e., in the limit of a discontinuous interface. We do so by applying this limit to equation (4.5.4), for

$$\psi_0(x, y, t) = H\left(x - x_C(y, t)\right), \tag{4.5.10}$$

where $H(x)$ is the Heaviside step function. First, see that equation (4.5.5) returns the correct result, since

$$\int_{-\infty}^{\infty} x\psi(1-\psi)\mathrm{d}x = \int_{-\infty}^{\infty} xH(x - x_C)\left[1 - H(x - x_C)\right]\mathrm{d}x = 0.$$

In the limit $\Delta_C \to 0$, the original definition (4.5.1) returns x_C, as required. To test the linearized case, consider

$$\psi = \bar{\psi} - \psi' = H(x) + x_C\delta(x), \tag{4.5.11}$$

where $\delta(x)$ is the Dirac delta function. Then

$$\int_{-\infty}^{\infty} \psi'\mathrm{d}x = x_C \int_{-\infty}^{\infty} \delta(x)\mathrm{d}x = x_C,$$

so the linearized definition recovers the correct centerline position.

To relate the centerline position to the perturbation amplitude, note that by the linearization used,

$$x_C = -h(t)\mathrm{e}^{\mathrm{i}ky}, \tag{4.5.12}$$

so in each case $h(t)$ may be directly recovered from the integral measure, since

$$\frac{1}{2}|-h(t)\mathrm{e}^{\mathrm{i}\pi/2} + h(t)\mathrm{e}^{-\mathrm{i}\pi/2}| = h(t),$$

as the maximum and minimum locations are known explicitly from the arbitrary phase term. This gives the definitions of the perturbation amplitude and interface thickness

$$h(t) = |x_C| = \left|\int_{-\infty}^{\infty} \psi'\mathrm{d}x\right|, \tag{4.5.13}$$

$$\Delta_C = 2I_\Delta + 2\sqrt{I_\Delta^2 + \frac{2}{3}x_C^2}, \tag{4.5.14}$$

where

$$I_\Delta = 4\int_{-\infty}^{\infty} \psi(1-\psi)\mathrm{d}x, \tag{4.5.15}$$

correcting the thickness measure for the linearization effect.

Finally, a comment should be made regarding the limits of integration. Although defined here as $(-\infty, \infty)$, in practice these definitions are applied on finite integration windows, primarily to avoid influence from the perturbations on the shocks. These windows are chosen to be large enough such that the perturbed solution is zero (or approximately zero) at the window ends, and the feature of interest is wholly contained.

4.5.2 Initial Amplitude Ambiguity

The definition of amplitude by equation (4.5.13) causes some difficulty near $t = 0$, during interaction of the shock with the interface, when the interface becomes indistinguishable from the shock(s). This issue is illustrated in Figure 4.7. Shock-interface interaction in the viscous problem is a distributed process, beginning when the head of the incident shock reaches the tail of the interface, and continuing until the tails of both reflected and transmitted shocks separate from the interface. Through this time, an integration window for equation (4.5.13) cannot be defined that does not also include the shock; thus $h(t)$ is undetermined near $t = 0$.

This poses an analytic difficulty when comparing the results from these simulations to the models of the RM instability described in Section 4.2. The impulsive model, and other models derived under similar assumptions, base the growth rate estimate on the initial post-shock perturbation amplitude, $h(0^+)$. Because the interface perturbation cannot be properly calculated until the shock perturbation has separated from it (as in the later time plots of Figure 4.7), $h(0^+)$ cannot be identified until some time after impact.

One possibility is to estimate $h(0^+)$ from a simulation with $k = 0$, which models a planar perturbation of the interface. This is predicted (and found, in the inviscid limit) to have zero growth, as the instability is not excited. Figure 4.8 shows $h(t)$ for a zero–wave number simulation, with the shaded region indicating where the presence of a shock corrupts the amplitude calculation. Also shown on this plot are external approximations of pre- and post-shock amplitudes. Diffusion effects are small enough to make the reasonable approximation $h(0^-) = h_0 = 1$, where h_0 is the small parameter in the linearization of the

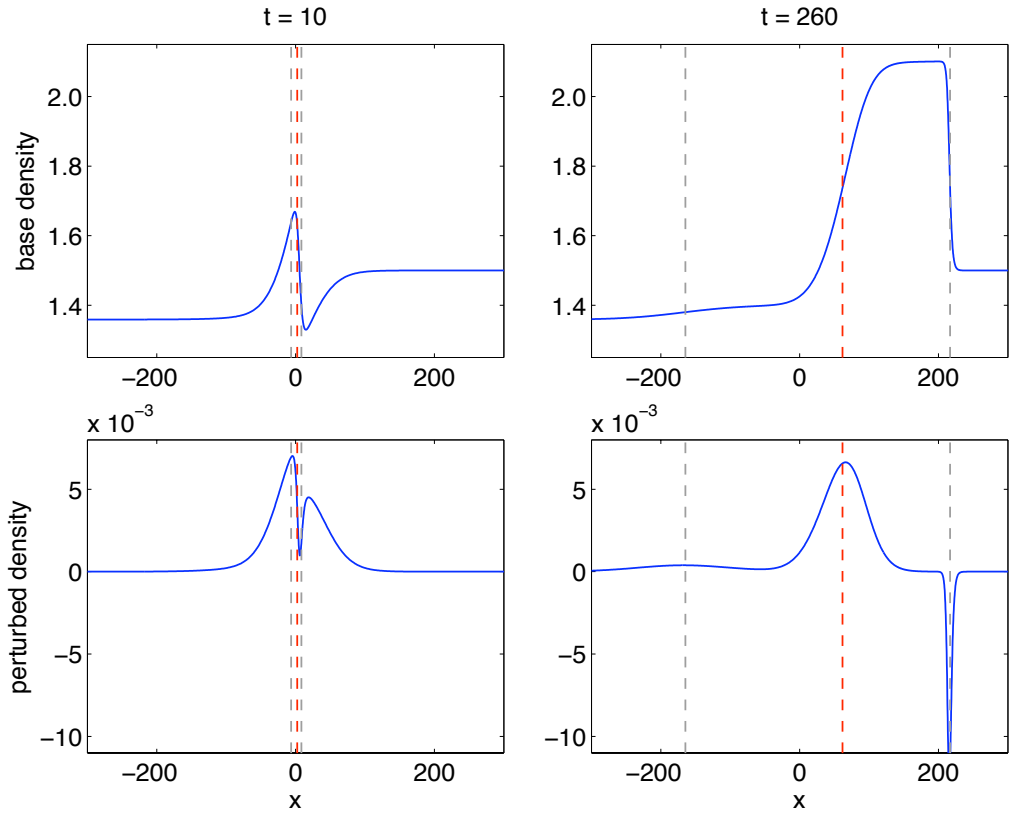

Figure 4.7: Demonstration of the initial amplitude ambiguity: (left) solution at small time, where interface and shock are indistinguishable; (right) at later time, where interface and shocks have separated. The Euler interface location is shown by the red dashed line, shocks by the grey dashed lines.

perturbed field. Note that the small deviation from this value in Figure 4.8 as the incident shock enters the integration window is due to the small wavelike perturbations from the initial condition approximation of the interface washing out of the window.

An estimate for the post-shock amplitude is given by Meshkov (1969), which models the compression of the perturbation by the incident shock:

$$h(0^+) = \left(1 - \frac{\Delta U}{U_\mathrm{I}}\right) h(0^-), \tag{4.5.16}$$

where $\Delta U = u_2 = u_3$, the post-impact speed of the interface, and U_I is the incident shock speed (both dimensional values). This is in excellent agreement with the asymptotic value for $h(t)$ obtained from $k = 0$ simulations with each parameter set, as demonstrated by Table 4.3 and Figure 4.8. Equation (4.5.16) is used to estimate $h(0^+)$ for all results presented in the following sections.

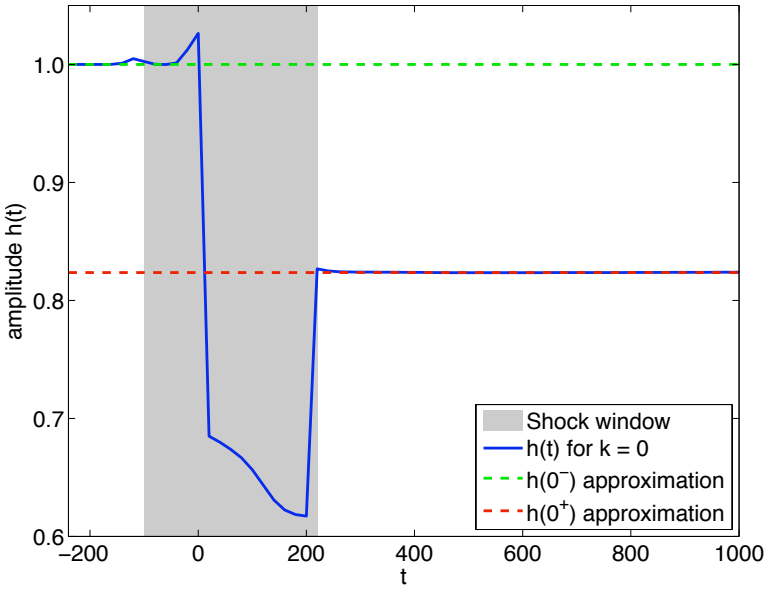

Figure 4.8: Plot of perturbation amplitude for $k = 0$ ($M_{\mathrm{I}} = 1.21$, $\mathrm{A} = 0.6$). The shaded region indicates the time range in which either the incident or transmitted shock is contained within the integration window. Once the transmitted shock has passed out of the window, the amplitude is in agreement with the estimate for $h(0^+)$ given by equation (4.5.16).

Parameters	$h(0^+)$ by (4.5.16)	Simulation $h(0^+)$
$M_{\mathrm{I}} = 1.05$, $\mathrm{A} = 0.2$	0.930350	0.930343
$M_{\mathrm{I}} = 1.05$, $\mathrm{A} = 0.6$	0.948345	0.948290
$M_{\mathrm{I}} = 1.21$, $\mathrm{A} = 0.2$	0.762441	0.762353
$M_{\mathrm{I}} = 1.21$, $\mathrm{A} = 0.6$	0.823618	0.823527
$M_{\mathrm{I}} = 2.20$, $\mathrm{A} = 0.2$	0.402234	0.402303
$M_{\mathrm{I}} = 2.20$, $\mathrm{A} = 0.6$	0.548190	0.548037

Table 4.3: Comparison of estimates for $h(0^+)$ obtained from $k = 0$ simulations and the approximation (4.5.16). To three or four significant figures, the measures are identical.

4.6 Simulation Results

Throughout this section, results are presented with the perturbation amplitude normalized by $h(0^-) = h_0$, as this is an arbitrary factor of the linearization and is set to unity for convenience. The time origin $t = 0$ is defined as the impact time from the inviscid 1-D Riemann problem, and shock and interface positions are defined likewise where shown. The interface initial condition is the hyperbolic tangent function defined by equation (4.4.8), although as shown in Section 4.4.3, this is of little consequence post-impact. Simulation results are based on the six parameter combinations defined in Table 4.1.

4.6.1 Form of the Solution

Before analyzing the simulation results, it is instructive to consider briefly the full numerical solution. An example of this is shown in Figure 4.9. Before impact, the unperturbed incident shock is seen approaching the interface, which is slowly diffusing. Small ripples visible on either side of the interface are due to the initial condition not being an exact solution to the Navier-Stokes equations. Some time post-impact, the reflected and transmitted shocks have separated from the interface, and each now carries a perturbation of its own. The peak magnitude of the interface perturbation is in fact smaller post-impact in this case, due to the compressive effect of the incident shock. Note also the relative steepness of each shocks: predictions of the shock thickness are 12, 20 and 130 mean free path lengths for the incident, transmitted and reflected shocks, respectively.

4.6.2 Approaching the Inviscid Limit

To characterize the viscous RM problem, we identify relevant length scales as the incident shock thickness Δ_{I}, the interface thickness Δ_{C}, the interface wavelength $\lambda = 2\pi/k'$ (in terms of the dimensional wave number k'), and the mean free path in the state-0 fluid $\ell_0 = \nu/\tilde{a}$, where ν is the averaged kinematic viscosity as defined in equation (4.2.4), and $\tilde{a}$ is a characteristic sound speed. Note that $\Delta_{\mathrm{I}} \sim \ell_0$, and is a known function of the incident shock Mach number. The interface thickness Δ_{C} is a controllable parameter of the initial condition.

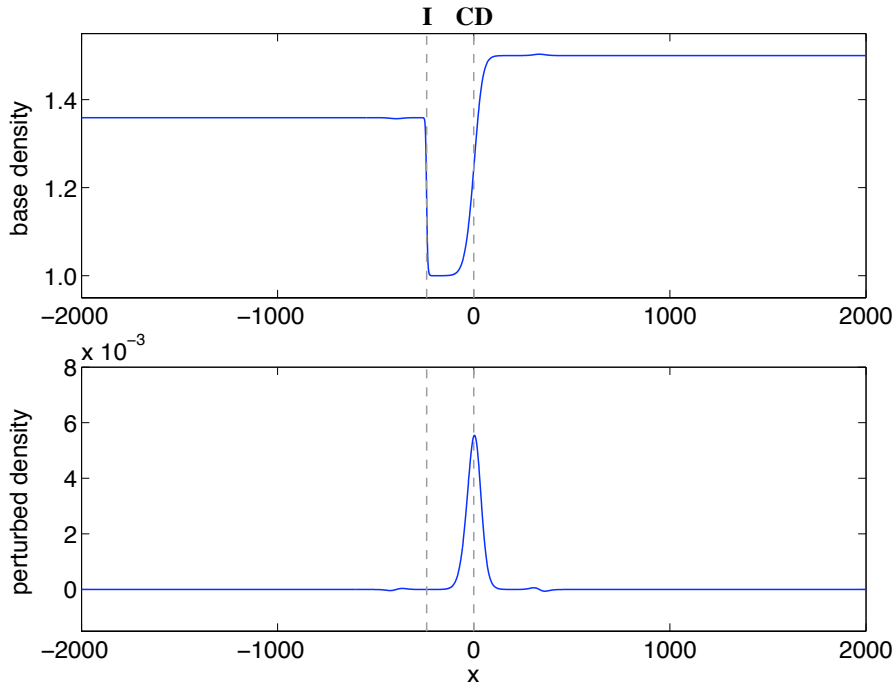

(a) base and perturbed density solutions at $t = -240$

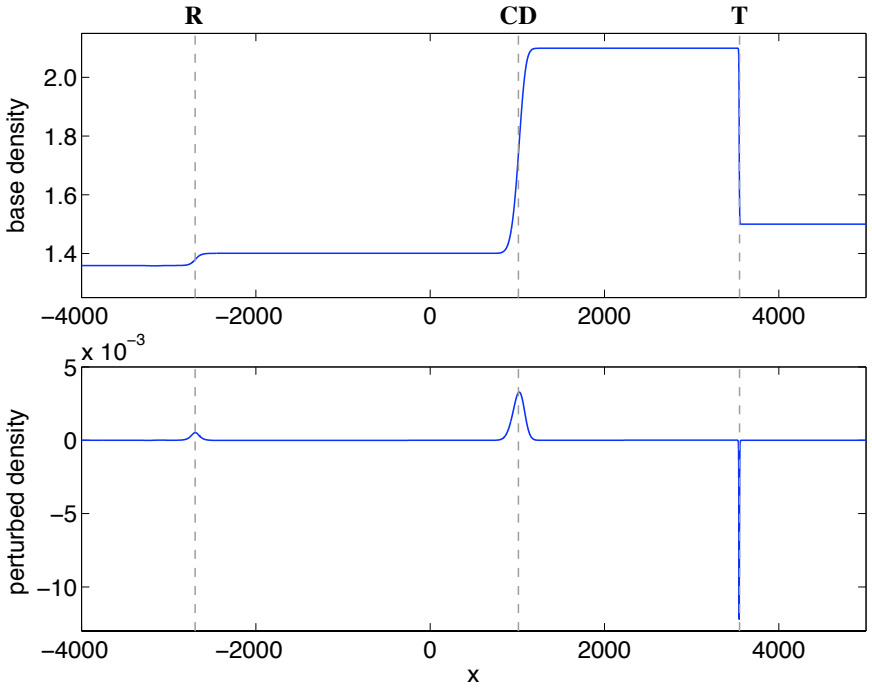

(b) base and perturbed density solutions at $t = 4260$

Figure 4.9: Form of the numerical solution, before and after shock impact with the interface. Case for $M_{\mathrm{I}} = 1.21$, $\mathrm{A} = 0.2$ shown, with dashed lines indicating positions of interface and shocks determined from the Riemann solution (Figure 4.1).

A Reynolds number at the interface is defined (in terms of dimensional quantities) by

$$\mathrm{Re_I} \equiv \frac{\Delta U \lambda}{\nu}, \tag{4.6.1}$$

where ΔU is the interface velocity, defined in Section 4.1. By this definition, we expect that as $\mathrm{Re_I}$ increases, we approach the inviscid limit and the simulation results will approach the inviscid model predictions. Noting that from equation (4.3.7) we may write $\nu = \tilde{a}\ell_0$ for a characteristic sound speed $\tilde{a}$, see that

$$\mathrm{Re_I} = \left(\frac{\Delta U}{\tilde{a}}\right)\frac{2\pi}{k}, \tag{4.6.2}$$

where k is now the nondimensional wave number. The term of equation (4.6.2) in parentheses is determined by the initial conditions of the incident shock, while the second term is a free parameter of the simulation and controlled by the choice of nondimensional wave number k for a given initial condition. We also define the dimensionless length scales

$$\eta \equiv k\Delta_\mathrm{C}, \quad \text{and} \quad \zeta \equiv \Delta_\mathrm{C}/\Delta_\mathrm{I}.$$

The first of these controls the relative diffusiveness of the interface, so is held constant as the Reynolds number is varied. Thus for each parameter case from Table 4.1, a sequence of simulations is performed of decreasing k and increasing Δ_C such that η is held constant, which corresponds to increasing $\mathrm{Re_I}$. This necessarily means that ζ then increases with $\mathrm{Re_I}$ in each sequence of simulations. Note that decreasing k also increases the timescale for the start-up of the instability by equation (4.2.8), so simulations with smaller k must be run to longer times to ensure that the linear regime has been reached. In the following results, plots are labelled by $\mathrm{Re_I}$.

4.6.3 Weak Shock, $M_\mathrm{I} = 1.05$

We consider first the weak shock case, where the impulsive model is expected to accurately predict the growth rate of the perturbation. The following results have $\eta = k\Delta_\mathrm{C} = 0.01$, and correspond to a range of wave numbers from $k = 0.0032$ to $k = 0.0005$. Not all cases are shown on all plots, for clarity. Figure 4.10 shows the growth profiles for pre-shock Atwood numbers of 0.2 and 0.6 for a range of Reynolds numbers, plotted against nondimensional

time t (defined in Section 4.3 and independent of k). The primary feature of these plots is the decrease in growth rate with decreasing k (increasing $\mathrm{Re_I}$). Some oscillation in the growth of the lowest-$\mathrm{Re_I}$ cases is also visible.

The effect of wave number is scaled out in Figure 4.11, where the normalized amplitude $h(t)/h(0^+)-1$ is plotted against a time axis scaled by $\mathrm{A}^+\Delta U k$. Here, collapse of the curves for most wave numbers is observed, to the extent that the wavelength and amplitude of oscillations in the growth are similar. Growth also tends to asymptote toward the slope predicted by the impulsive model. The lowest Reynolds number cases, $\mathrm{Re_I} = 296$ for $\mathrm{A} = 0.2$ and $\mathrm{Re_I} = 445$ for $\mathrm{A} = 0.6$, however, do not collapse in the same way, displaying significantly different behavior. Growth appears to be significantly attenuated by viscosity for these cases.

The oscillatory effects are shown more clearly in Figure 4.12, where growth rate, scaled by k, is plotted against scaled time kt. At both Atwood numbers, the higher two $\mathrm{Re_I}$ cases have similar growth rate profiles over the available history, and oscillate about an average growth rate near the impulsive model prediction. Lower $\mathrm{Re_I}$ cases show larger amplitude oscillations, centered about lower average growth rates. Note that Wouchuk (2001a) predicts a higher growth rate in the inviscid limit compared to the impulsive model.

The start-up time prediction given in equation (4.2.8) is examined in Figure 4.13. Here, the perturbation growth is plotted against time scaled by the characteristic time τ. Collapse of the curves is expected again as τ scales directly with k, but of interest here is that τ appears to be a good estimate of the time before growth enters the linear phase. For $t > \tau$, growth follows the impulsive model rate prediction very closely.

4.6.4 Intermediate Shock, $M_\mathrm{I} = 1.21$

Results for the intermediate-strength shock are broadly similar to those for the weak shock case. Results are presented for Atwood numbers $\mathrm{A} = 0.2$ and $\mathrm{A} = 0.6$, with $\eta = 0.01$ covering a range of wave numbers from $k = 0.0064$ to $k = 0.0004$. Figure 4.14 shows amplitude histories for varying k for each Atwood number. Again, ripples in the growth curves are evident, particularly for the lower-$\mathrm{Re_I}$ cases. Plotting normalized amplitude $h(t)/h(0^+)-1$ against scaled time $\mathrm{A}^+\Delta U k$ in Figure 4.15 shows collapse of the amplitude histories for Reynolds numbers in the inviscid range. At lower $\mathrm{Re_I}$, and the case $\mathrm{Re_I} = 746$ with $\mathrm{A} = 0.2$ in particular, collapse is less convincing as there is noticeable attenuation of

the growth rate compared to the impulsive model prediction.

Similar collapse is seen for Figure 4.16, with the time axis scaled by the start-up time scale τ of equation (4.2.8). As in the weak shock case, the growth rate asymptotes closely toward the impulsive model for $t > \tau$. Plots of the amplitude growth rates, shown in Figure 4.17, indicate that for both Atwood numbers considered, the impulsive model makes a better prediction of the asymptotic growth rate than Wouchuk (2001a), as oscillation appears to be centered closer to the impulsive rate. Behavior is otherwise similar to that observed in the weak shock case, with the lower-$\mathrm{Re_I}$ cases having larger-amplitude oscillation. In the case of $\mathrm{Re_I} = 1492$, $\mathrm{A} = 0.2$, gradual decay of the growth rate is also apparent.

For the $\mathrm{A} = 0.2$ cases with $\mathrm{Re_I} = 746$ and $\mathrm{Re_I} = 1492$, attenuation of the growth rate by viscosity is clear from Figure 4.18. Comparison of the growth rates with the viscous model of Carlès and Popinet (2001) show that the decay envelope is captured with reasonable accuracy, particularly for $\mathrm{Re_I} = 1492$ where the oscillation in the growth rate is quite closely centered on the model's prediction. Note that since the model makes no attempt to estimate effects due to proximity of the shocks, it cannot be expected to capture oscillation in the growth rate.

Figure 4.19 shows results for $M_\mathrm{I} = 1.21$, $\mathrm{A} = 0.2$ and $\eta = 0.02$, with particular focus on the low-$\mathrm{Re_I}$ cases. These show significant viscous attenuation of the perturbation amplitude growth, to the extent that the lowest case shown decays (and so is, in fact, stable). Also plotted are the amplitude predictions by the Carlès and Popinet model with equation (4.2.5) for each case. Because this model is based on similar assumptions to the impulsive model, it should be considered more as an asymptotic growth prediction than as a time-accurate growth prediction. Nevertheless, it predicts the decay of the $\mathrm{Re_I} = 239$ case within a similar time frame, notable as the Mikaelian (1993) model (not shown) does not.

4.6.5 Strong Shock, $M_\mathrm{I} = 2.20$

For the final sequence of simulations, we consider a stronger shock of $M_\mathrm{I} = 2.20$, with $\eta = 0.01$ and over a range of wave numbers $k = 1/100$ to $k = 1/1600$. At this Mach number, the impulsive model is expected to not predict the asymptotic growth rate as successfully as it had at the lower-M_I examples. Figure 4.20 shows the perturbation amplitude histories for Atwood numbers $\mathrm{A} = 0.2$ and $\mathrm{A} = 0.6$. Also plotted are the asymptotic growth rates predicted by the Wouchuk (2001a) model (dashed lines), offset from the time origin to

partially account for the start-up process of the instability. The case $\mathrm{Re_I} = 4994$, $\mathrm{A} = 0.2$ shows similar behavior to low-$\mathrm{Re_I}$ cases at lower Mach numbers, with noticeable oscillations in amplitude growth and a reduced asymptotic growth rate compared to higher-$\mathrm{Re_I}$ cases.

Examination of the growth rates in Figure 4.21 supports this, showing the greater amplitude of oscillation and slight downward trend of the $\mathrm{Re_I} = 4994$ case. In general, the amplitude of oscillation in the scaled growth rate $\dot{h}(t)/kh(0^+)$ is seen to decrease with k. Other features of the growth rate profile are relatively consistent, with the frequency of oscillation in particular scaling well by kt. Excepting again the case with $\mathrm{Re_I} = 4994$, for both Atwood numbers asymptotic growth appears to be better predicted by Wouchuk's model than the impulsive model.

Figure 4.22 confirms that the start-up timescale τ is still a useful measure in the strong-shock case. For $\mathrm{A} = 0.6$, however, growth appears to have entered the linear phase before $t = \tau$, so the characteristic time may be slightly overestimated in this case. Collapse of the growth curves is still observed, as with the weaker shock cases, though here growth asymptotes toward the prediction of Wouchuk's model instead of the impulsive model.

4.6.6 Interface Thickness

To complete this investigation of the Richtmyer-Meshkov instability, we consider the time evolution of the interface thickness and, in the following section, the perturbations on the reflected and transmitted shocks. The interface thickness, defined by equation (4.5.14), evolves along with the amplitude as a description of the perturbed density field. The interface diffuses slowly before impact, is compressed by the shock, then continues diffusing with time as the interface between the post-shock states. Plots of interface thickness for a selection of the cases described in the previous section are shown in Figure 4.23. Of note in these plots is the very weak influence of initial (pre-shock) interface thickness (proportional to $1/k$ in each case) on the subsequent thickness history: the thickness histories collapse for all but the thickest initial condition, particularly for stronger shocks. The origin of this phenomenon is difficult to identify as the thickness also suffers from the perturbation ambiguity during impact, but it is clear that compression by the shock has a dominant effect on the post-shock interface thickness.

Since evolution of the interface is primarily a diffusive process, we expect

$$\Delta_C \sim \sqrt{\nu t}. \tag{4.6.3}$$

Figure 4.24 shows that this is indeed the case, showing agreement of the measured interface thickness with a profile $\sqrt{\nu t}$, and linear growth in Δ_C^2 with time.

4.6.7 Shock Perturbations

Upon interaction with the interface perturbation, the reflected and transmitted shocks develop perturbations of their own. These perturbations are stable (Landau and Lifshitz, 1959; Erpenbeck, 1962), unlike the interface perturbation, and are expected to decay with time. This is confirmed by the simulation results, which show that the perturbation amplitude oscillates within a decaying envelope at both the reflected and transmitted shocks. Also notable is that the amplitude perturbation passes through zero multiple times as it decays, and that the reflected shock amplitude is initially of opposite sign to the transmitted shock amplitude.

The collapse of the interface perturbation amplitude curves when plotted against time scaled by the perturbation wave number (kt) suggests that a similar scaling may apply to the shock perturbations. For the transmitted shock perturbation, this is generally true, illustrated by the examples in Figure 4.25, where collapse is very good except for some of the lowest Reynolds number cases. On the other hand, the reflected shock perturbation does not appear to collapse at all when plotted against kt (Figure 4.26). The spatial frequency of the reflected shock perturbation is necessarily k by the form of the linearization, so it is speculated that collapse may occur for a different scaling of the form $k^\alpha t^\beta$. The reason for a higher-order dependence on k and/or t for the reflected shock and not the transmitted shock is unclear.

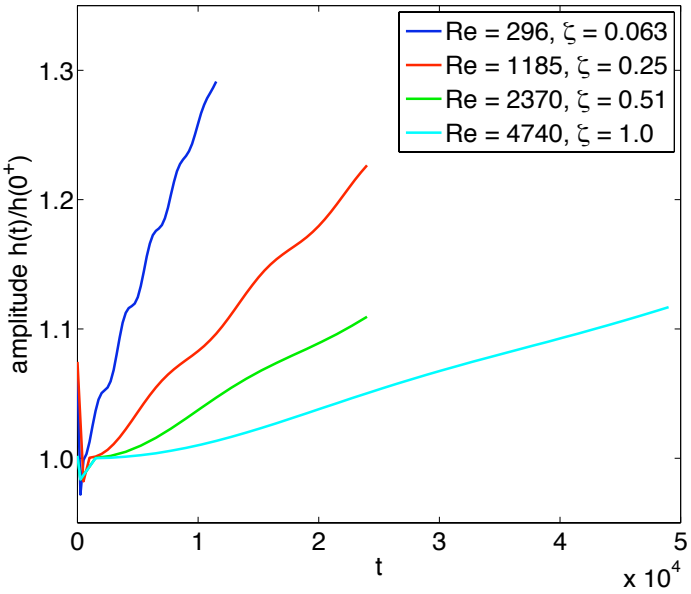

(a) A = 0.2

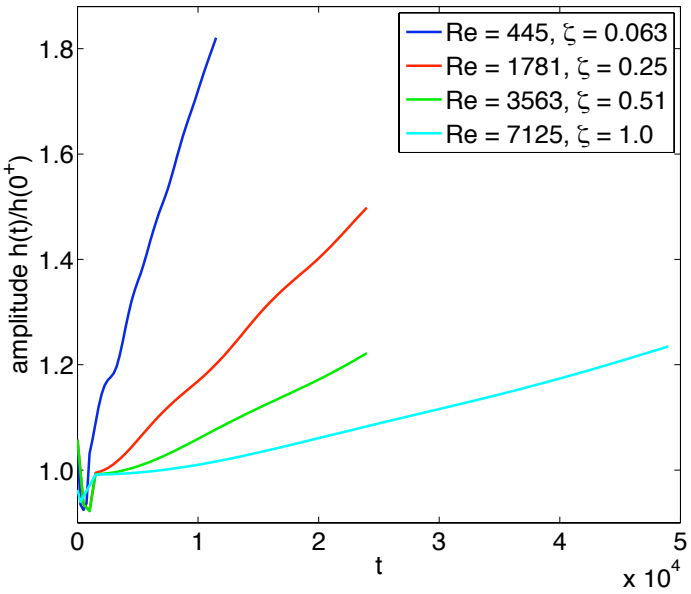

(b) A = 0.6

Figure 4.10: Plots of perturbation amplitude $h(t)/h(0^+)$ for $M_{\mathrm{I}} = 1.05$ with varying wave number.

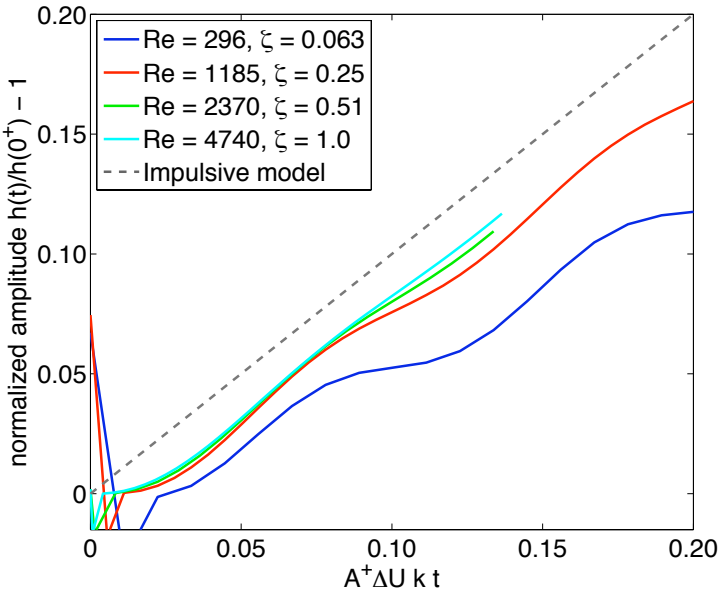

(a) A = 0.2

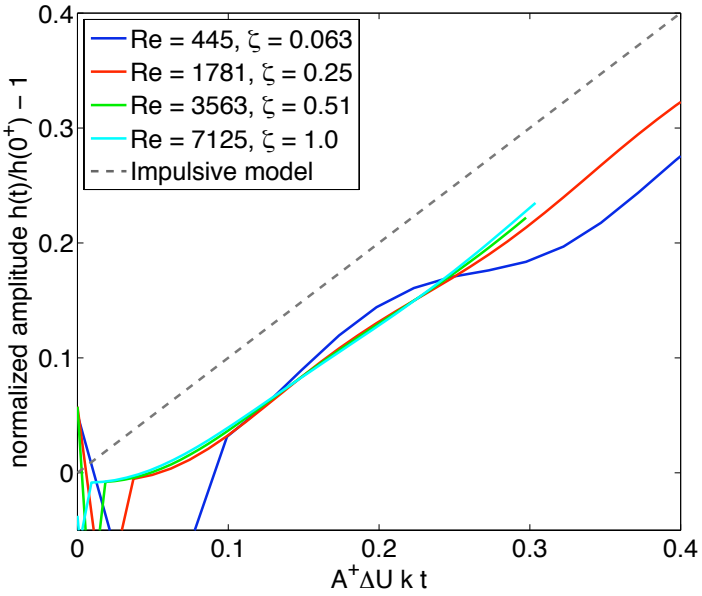

(b) A = 0.6

Figure 4.11: Plots of normalized perturbation amplitude $h(t)/h(0^+) - 1$ against scaled time $\mathrm{A}^+\Delta U k t$ for $M_\mathrm{I} = 1.05$, with the dashed line showing asymptotic impulsive model growth. The time axis scaling is chosen such that the impulsive model has unity slope.

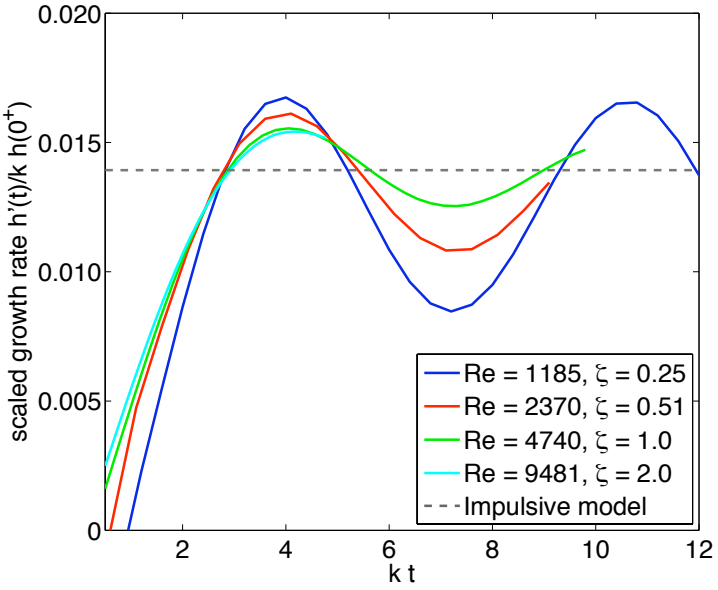

(a) A = 0.2

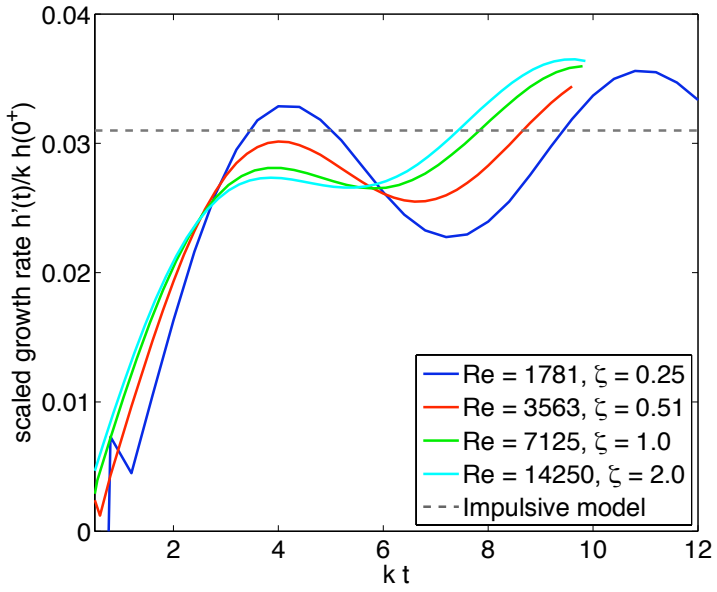

(b) A = 0.6

Figure 4.12: Plots of perturbation amplitude growth rate $\dot{h}(t)/kh(0^+)$ against scaled time kt for $M_{\mathrm{I}} = 1.05$, with the dashed line showing asymptotic impulsive model growth in each case. Very early time values ($kt < 1$) are erratic due to the initial ampltiude ambiguity discussed in Section 4.5.2.

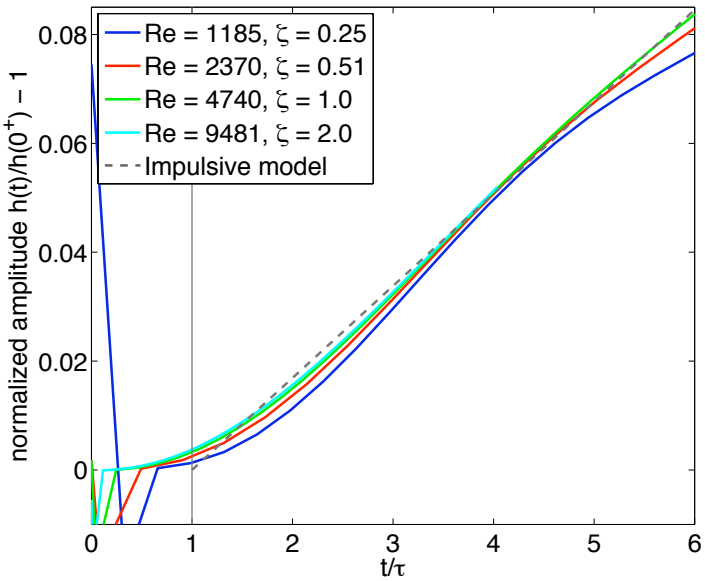

(a) A = 0.2

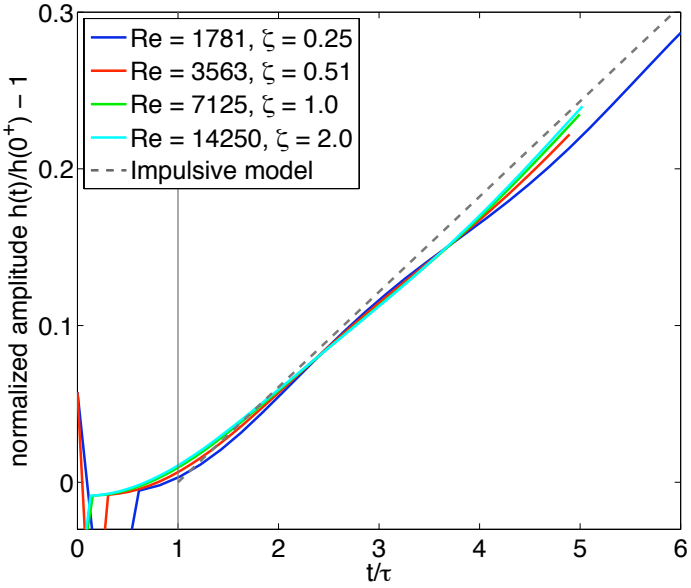

(b) A = 0.6

Figure 4.13: Plots of normalized perturbation amplitude $h(t)/h(0^+) - 1$ against time scaled by the start-up time τ from Lombardini (2008), for $M_\mathrm{I} = 1.05$. The dashed line shows asymptotic impulsive model growth shifted to begin at $t = \tau$.

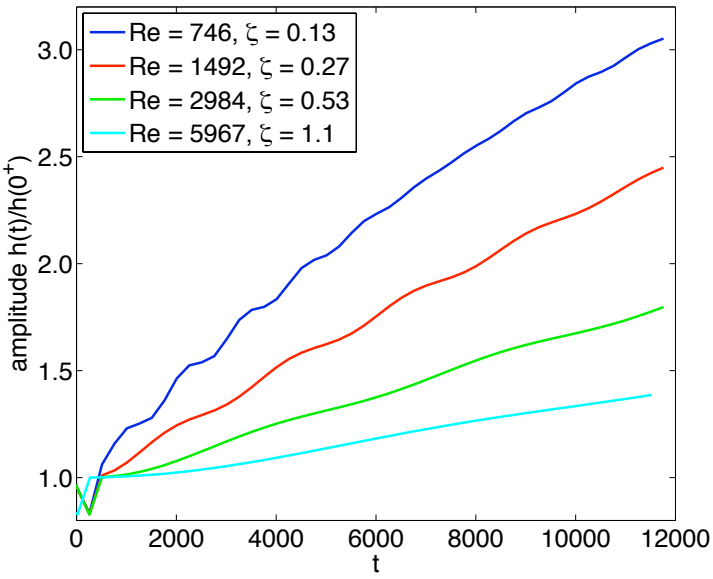

(a) A = 0.2

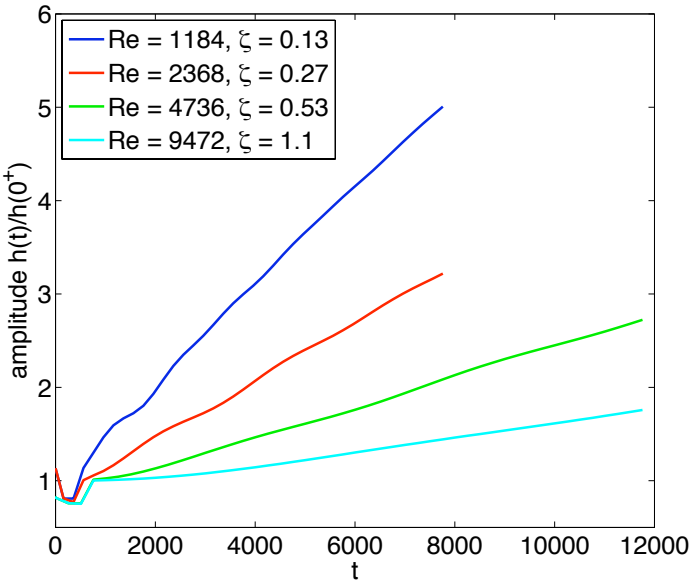

(b) A = 0.6

Figure 4.14: Plots of perturbation amplitude $h(t)/h(0^+)$ for $M_{\mathrm{I}} = 1.21$ with varying wave number.

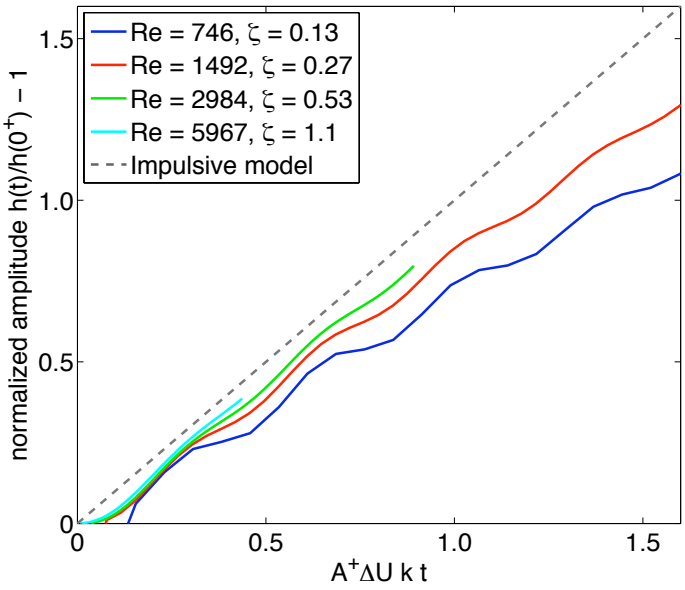

(a) A = 0.2

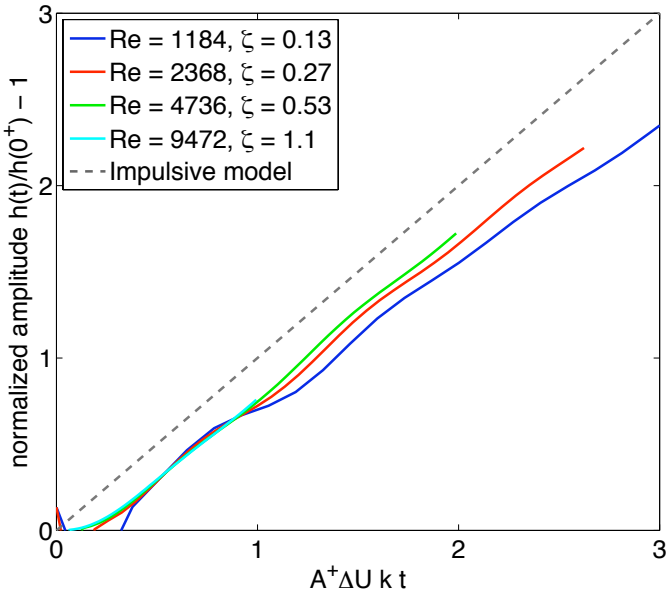

(b) A = 0.6

Figure 4.15: Plots of normalized perturbation amplitude $h(t)/h(0^+) - 1$ against scaled time $\mathrm{A}^+\Delta U k t$ for $M_\mathrm{I} = 1.21$, with the dashed line showing asymptotic impulsive model growth.

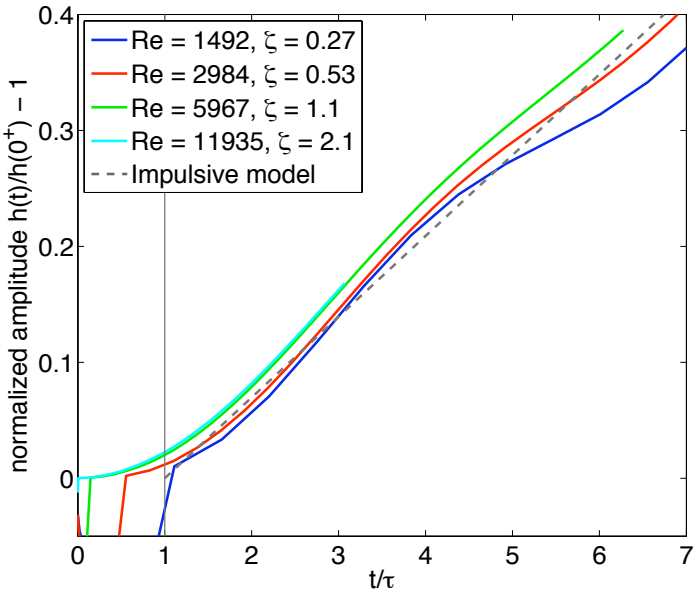

(a) A = 0.2

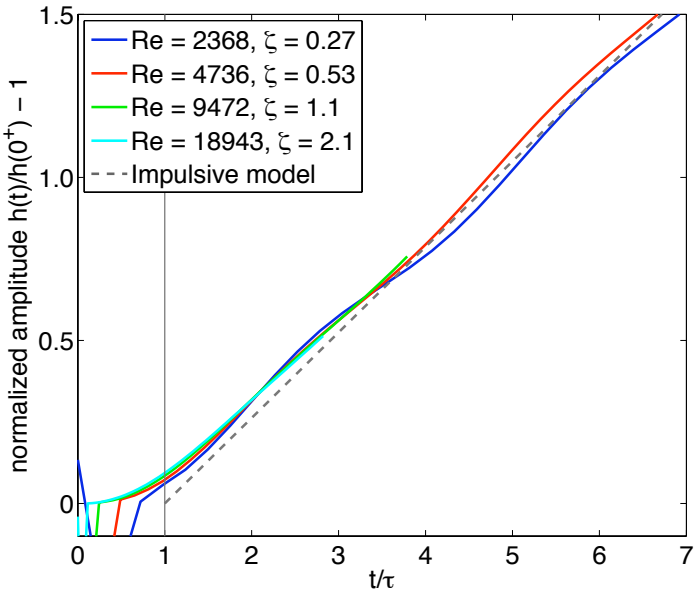

(b) A = 0.6

Figure 4.16: Plots of normalized perturbation amplitude $h(t)/h(0^+) - 1$ against time scaled by the start-up time τ from Lombardini (2008), for $M_{\mathrm{I}} = 1.21$. The dashed line shows asymptotic impulsive model growth shifted to begin at $t = \tau$.

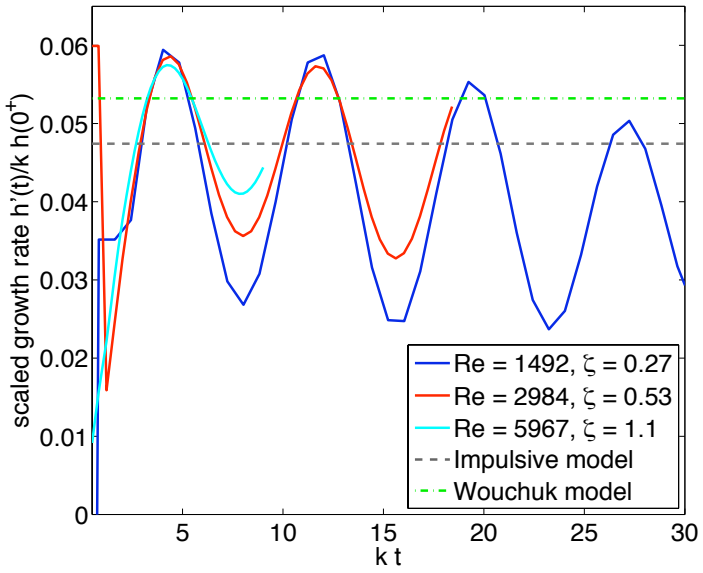

(a) A = 0.2

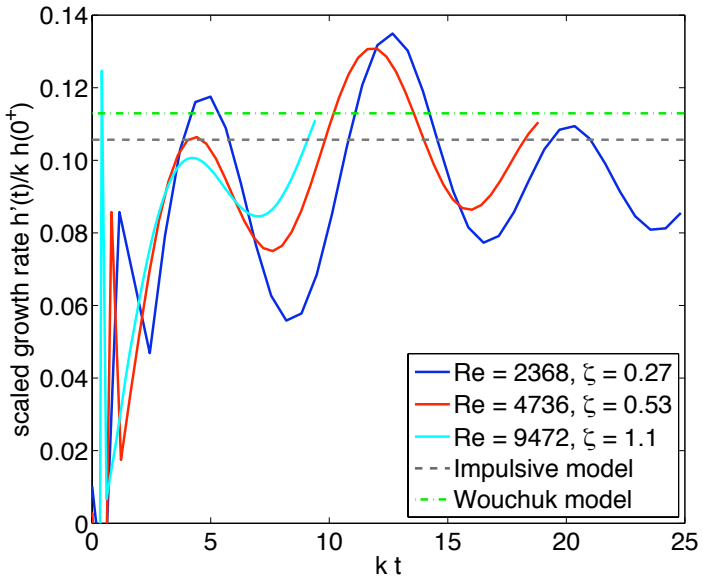

(b) A = 0.6

Figure 4.17: Plots of perturbation amplitude growth rate $\dot{h}(t)/kh(0^+)$ against scaled time kt for $M_{\mathrm{I}} = 1.21$. The dashed and dot-dashed lines show asymptotic growth rates predicted by the impulsive and Wouchuk (2001a) models, respectively.

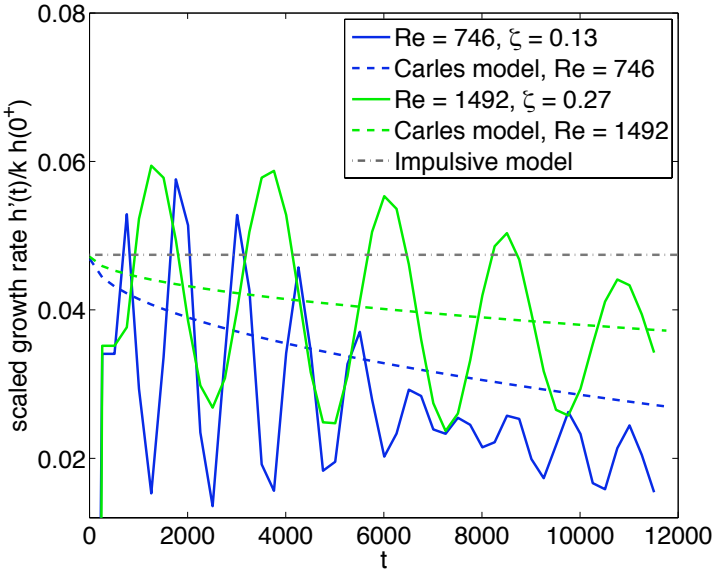

Figure 4.18: Plots of perturbation amplitude growth rate $\dot{h}(t)/kh(0^+)$ against scaled time kt for $M_\mathrm{I} = 1.21$ and A $= 0.2$, for low-$\mathrm{Re_I}$ cases affected by viscosity. Dashed lines show the growth rate predictions of the Carlès and Popinet (2001) model, and the dot-dashed line shows the impulsive model prediction for reference.

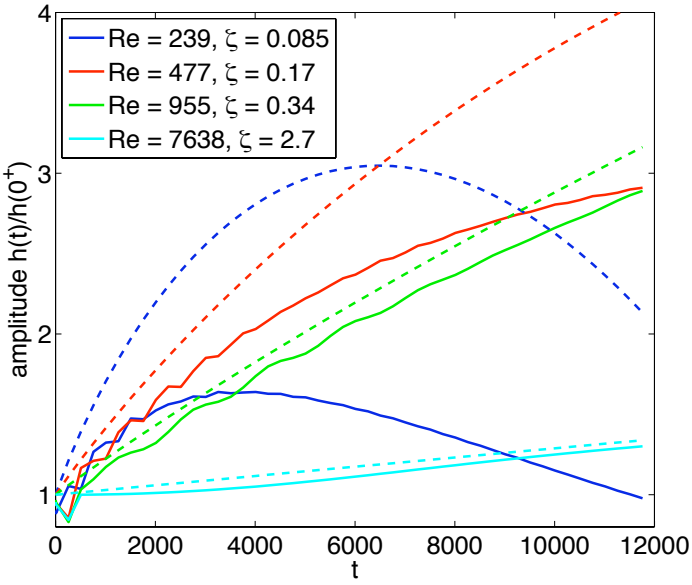

Figure 4.19: Plots of perturbation amplitude for $M_\mathrm{I} = 1.21$ and $\eta = 0.02$, showing Reynolds number effects. Dashed lines show the predictions of the Carlès and Popinet (2001) model for each case. At low $\mathrm{Re_I}$, viscosity attenuates growth significantly compared to the impulsive model.

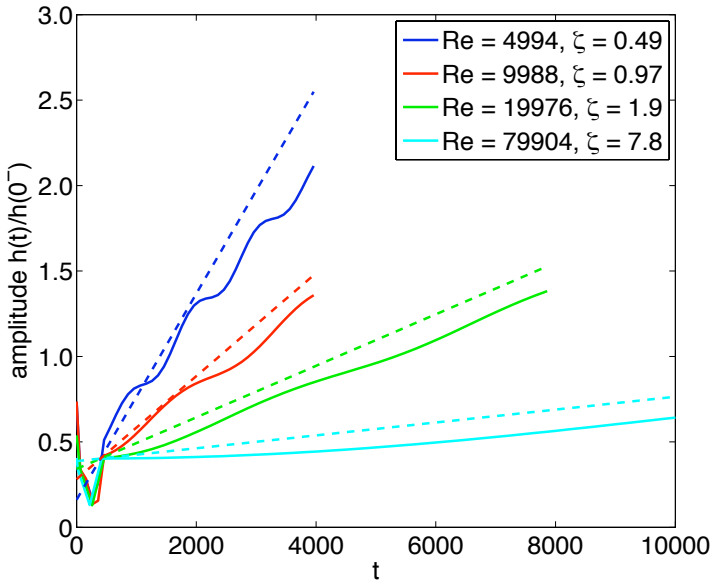

(a) A = 0.2

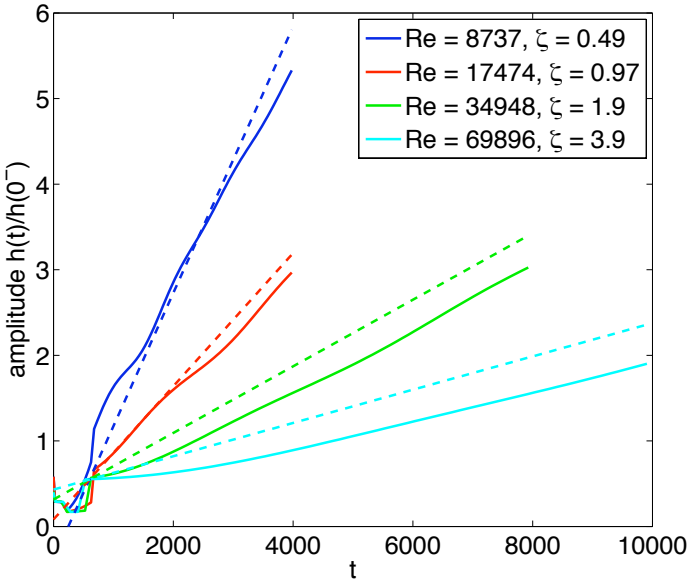

(b) A = 0.6

Figure 4.20: Plots of perturbation amplitude $h(t)/h(0^+)$ for $M_{\mathrm{I}} = 2.20$ with varying wave number. Dashed lines show the asymptotic growth predicted by the asymptotic model of Wouchuk (2001a) for each case.

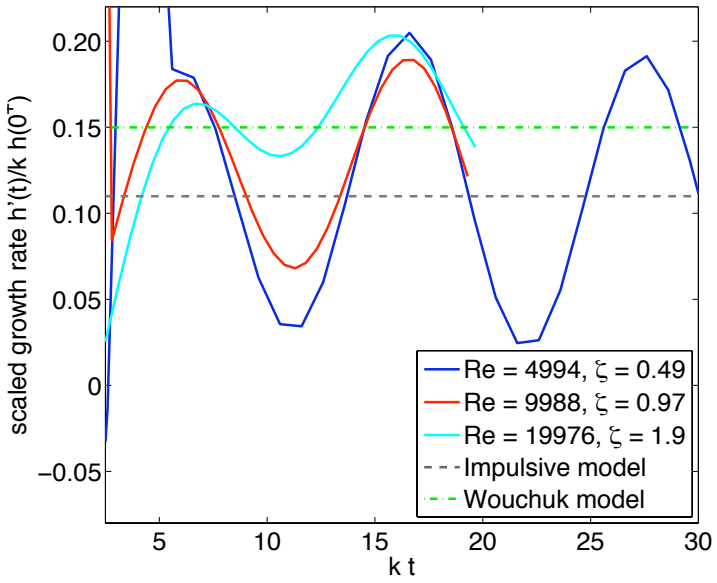

(a) A = 0.2

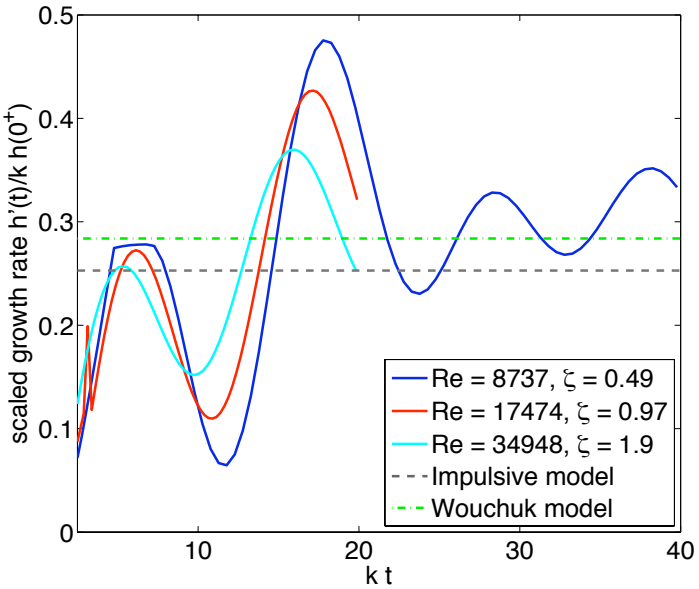

(b) A = 0.6

Figure 4.21: Plots of perturbation amplitude growth rate $\dot{h}(t)/kh(0^+)$ against scaled time kt for $M_{\mathrm{I}} = 2.20$, with the dashed and dot-dashed lines showing asymptotic growth rates for the impulsive and Wouchuk (2001a) models in each case, respectively.

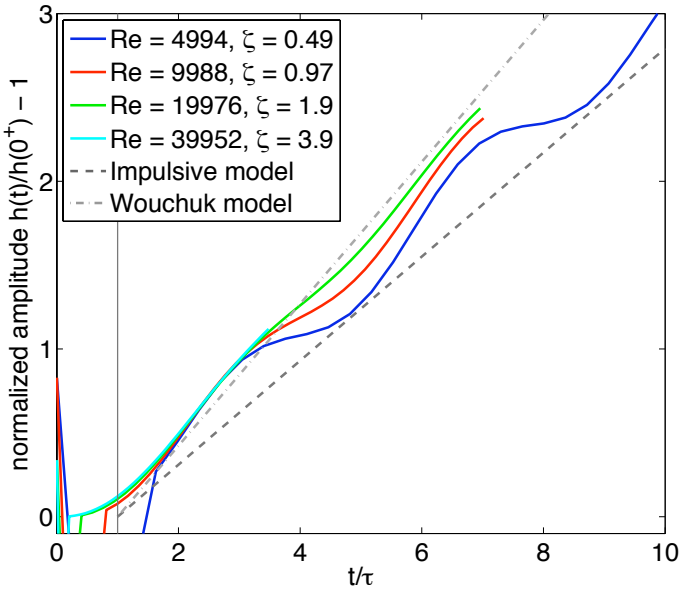

(a) A = 0.2

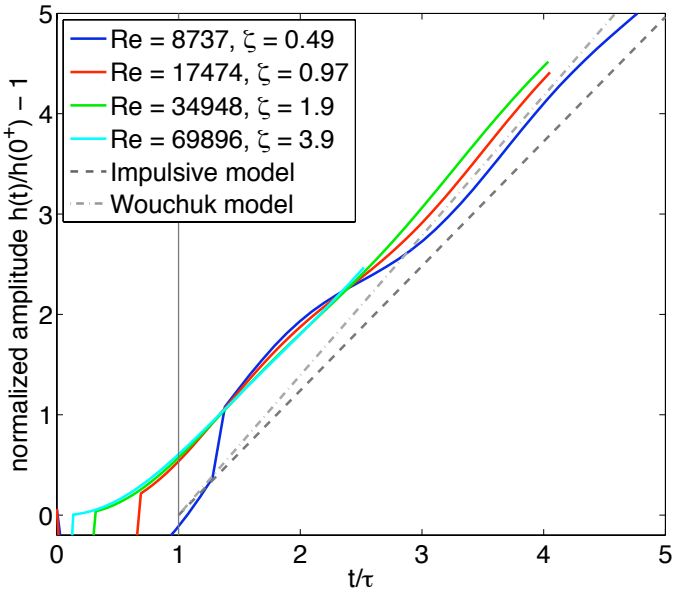

(b) A = 0.6

Figure 4.22: Plots of normalized perturbation amplitude $h(t)/h(0^+) - 1$ against time scaled by the start-up time τ from Lombardini (2008), for $M_{\mathrm{I}} = 2.20$. The dashed line shows asymptotic impulsive model growth shifted to begin at $t = \tau$, and the dot-dashed line the asymptotic prediction of Wouchuk (2001a).

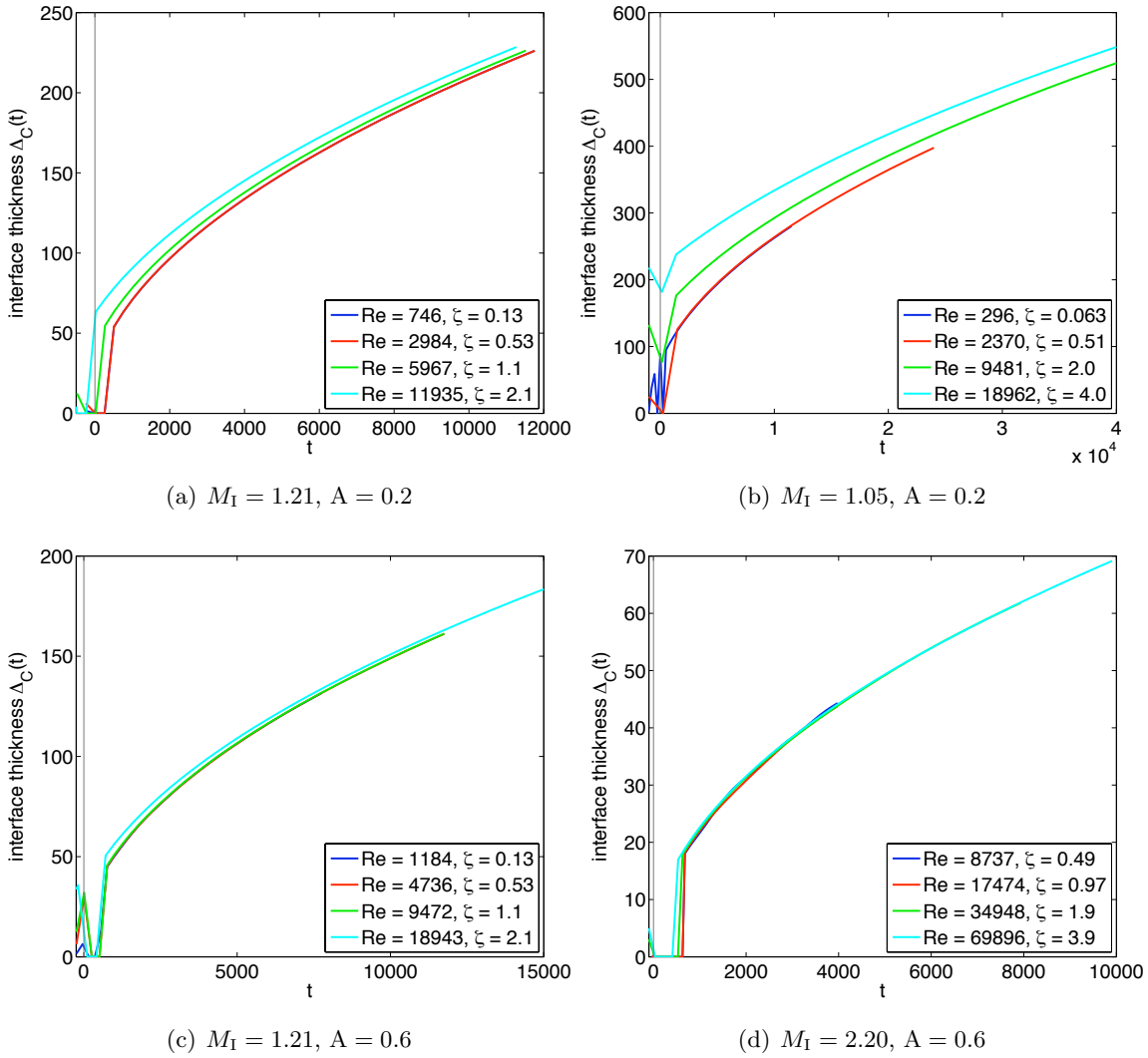

(a) $M_{\mathrm{I}} = 1.21$, A $= 0.2$

(b) $M_{\mathrm{I}} = 1.05$, A $= 0.2$

(c) $M_{\mathrm{I}} = 1.21$, A $= 0.6$

(d) $M_{\mathrm{I}} = 2.20$, A $= 0.6$

Figure 4.23: Plots of interface perturbation thickness for a range of initial problem parameters. The weak influence of pre-shock thickness (indicated by ζ) is clear for all cases; note for plot (b) that the ratio of thickest to thinnest initial thickness is 64.

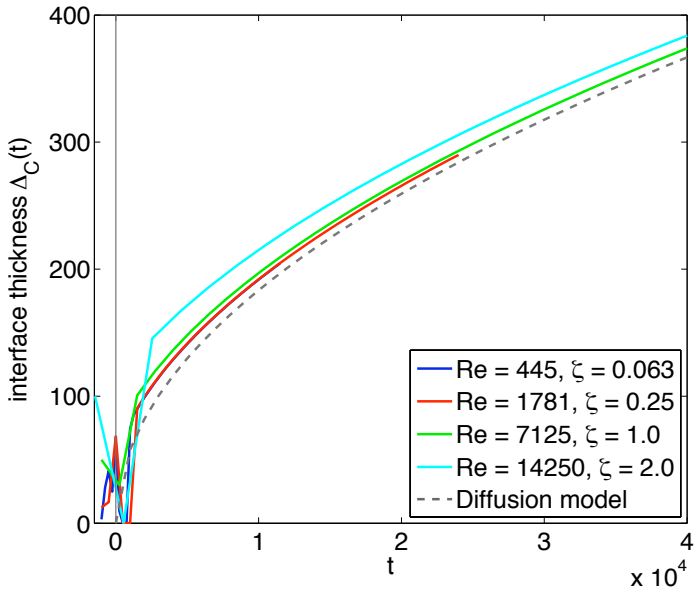

(a) $\Delta_C(t)$

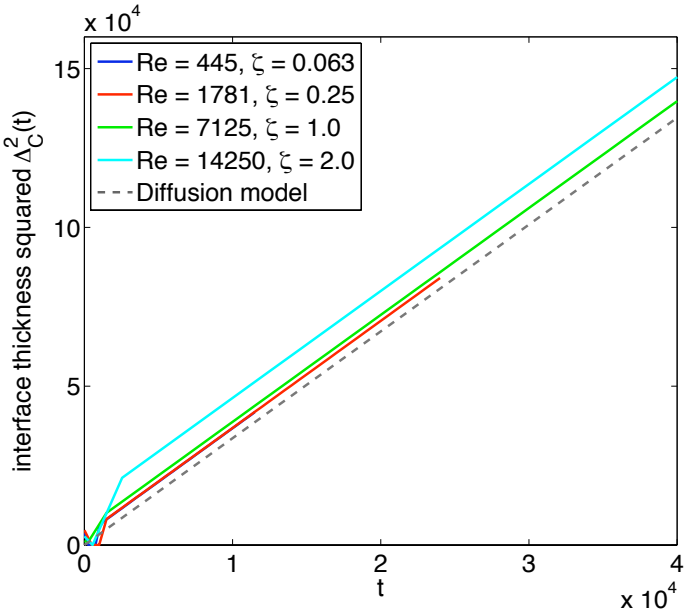

(b) $\Delta_C^2(t)$

Figure 4.24: Plots of interface thickness for the case $M_I = 1.05$, A $= 0.6$ with the diffusion model for comparison. A linear fit for Δ_C^2 plotted against time indicates that the diffusive model is appropriate.

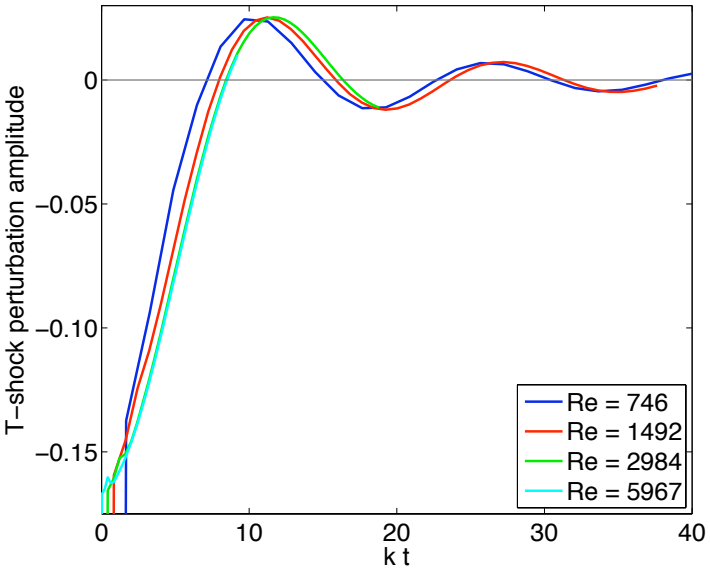

(a) $M_{\mathrm{I}} = 1.21$, A $= 0.2$

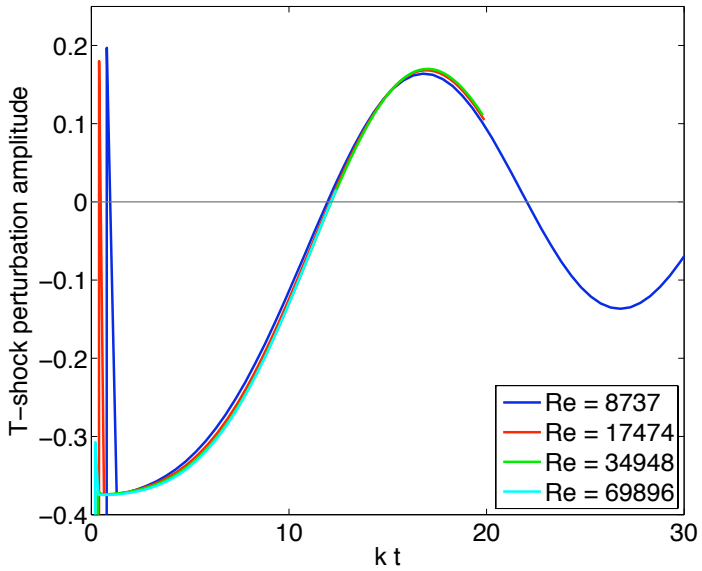

(b) $M_{\mathrm{I}} = 2.20$, A $= 0.6$

Figure 4.25: Transmitted shock perturbation amplitude plotted against scaled time kt, showing collapse of the curves across Reynolds number.

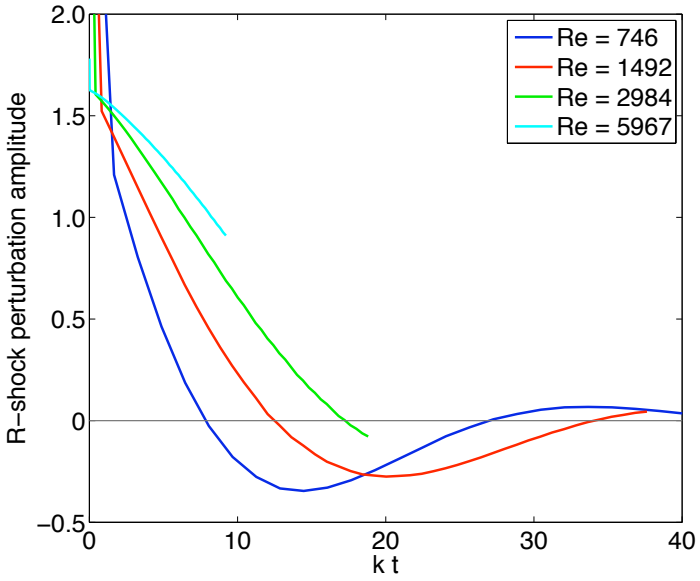

(a) $M_{\mathrm{I}} = 1.21$, A $= 0.2$

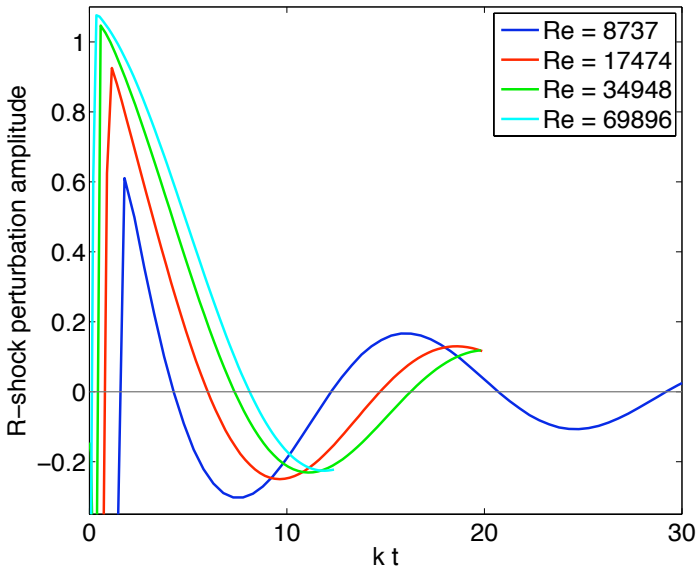

(b) $M_{\mathrm{I}} = 2.20$, A $= 0.6$

Figure 4.26: Reflected shock perturbation amplitude plotted against scaled time kt, showing that collapse does not occur with this scaling.

4.7 Discussion of the Results

We conclude this chapter with a closer analysis of the results obtained in the simulations presented in the previous section. The focus is on three cases: the weak shock $M_{\mathrm{I}} = 1.05$ with $\mathrm{A} = 0.6$, the intermediate shock $M_{\mathrm{I}} = 1.21$ with $\mathrm{A} = 0.6$, and the strong shock $M_{\mathrm{I}} = 2.20$ and $\mathrm{A} = 0.2$. Plots of interface perturbation amplitude growth rate $\dot{h}(t)/h(0^+)$ are shown for three particular Reynolds numbers in Figures 4.27–4.29. Wave numbers quoted are nondimensional values.

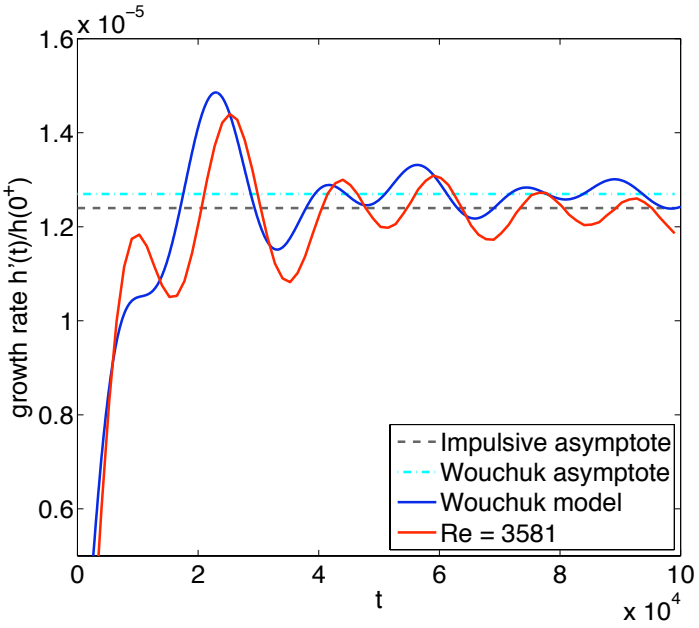

Figure 4.27: Plot of amplitude growth rate $\dot{h}(t)/h(0^+)$, for $M_{\mathrm{I}} = 1.05$, $\mathrm{A} = 0.6$, $k = 0.0004$, with asymptotic growth rate predictions shown for impulsive and Wouchuk (2001a) models. Overlaid also is the time history predicted by Wouchuk's theory.

The intermediate-strength shock case with pre-shock Atwood number $\mathrm{A} = 0.6$ is intended to approximate the experiments of Collins and Jacobs (2002) of similar parameters. The two principal differences between those experiments and these simulations are that the physical case was achieved with an air/SF_6 interface and that the pre-shock interface is considerably more diffuse in the experimental setup. The effect on the perturbation growth rate of the two-fluid physical problem compared to the single-fluid simulation is to reduce the interface speed (ΔU), though this change is of a similar order of magnitude to the difference between the predicted and measured speeds in the shock tube. The diffuse interface attenuates the growth rate in the manner described in Section 4.2.3; Collins and Jacobs use

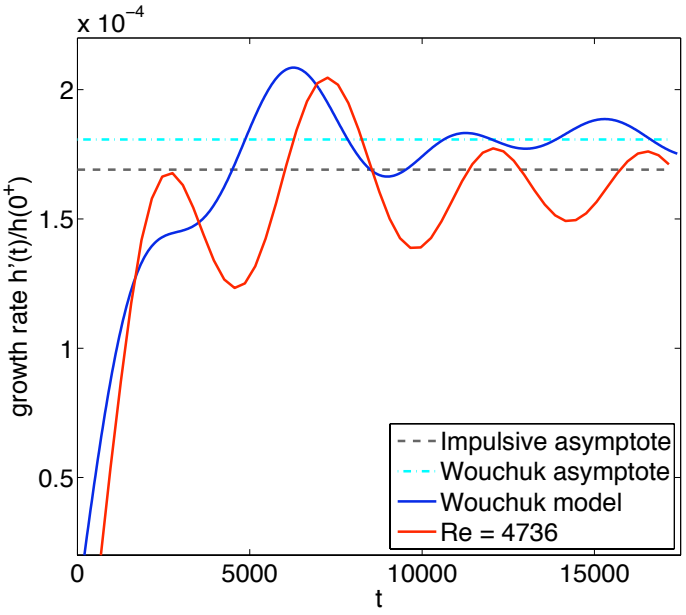

Figure 4.28: Plot of amplitude growth rate $\dot{h}(t)/h(0^+)$, for $M_{\mathrm{I}} = 1.21$, A $= 0.6$, $k = 0.0016$, with asymptotic growth rate predictions shown for impulsive and Wouchuk (2001a) models. Overlaid also is the time history predicted by Wouchuk's theory.

the correction from Brouillette and Sturtevant (1994) with $\psi = 1.07$ (post-shock), while the interface thickness in the simulated case is so small (on the order of the shock thickness) that it has no measurable effect.

4.7.1 Comparisons with Analytic Models

Beginning with the weak shock case, Figures 4.12–4.13 suggest that the impulsive model is a good approximation of the asymptotic growth rate of the instability under these conditions. Figure 4.27, plotting a longer time history, confirms this. The average nondimensional growth rate from the simulation, after the initial transient, is 1.244×10^{-5}, compared to 1.240×10^{-5} for the impulsive model prediction. The simulation agrees quite well with the Wouchuk (2001a) model, sharing many of the features of the time history. Asymptotically, however, the simulation tracks a little lower than the model; it is possible that this is due to a small attenuating viscous effect.

For the intermediate case shown in Figure 4.28(b), the long-term growth rate is centered very closely on the impulsive model prediction, a conclusion supported by the good agreement shown by this model in Figures 4.16–4.17 for all but the lowest Reynolds number cases. Upon correcting for diffuse interface effects, the experiments of Collins and Jacobs

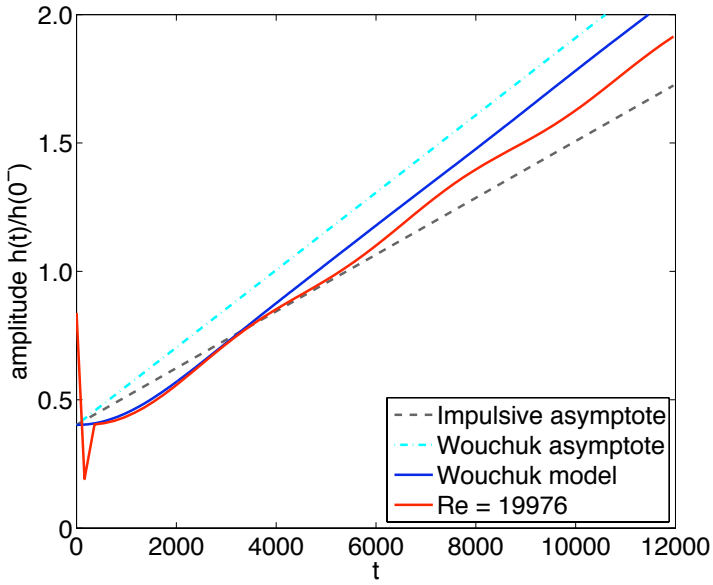

(a) Amplitude $h(t)/h(0^-)$

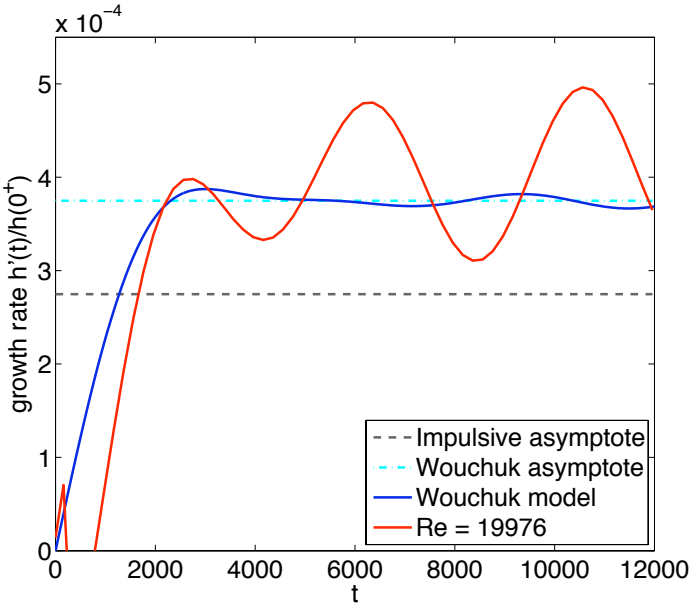

(b) Rate $\dot{h}(t)/h(0^+)$

Figure 4.29: Amplitude and growth rate plots for $M_{\mathrm{I}} = 2.20$, $\mathrm{A} = 0.2$, $k = 0.0025$, compared to the Wouchuk (2001a) model prediction. Also shown for reference are asymptotic growth rate predictions from this and the impulsive model.

(2002) come to a similar conclusion (for the linear regime). In this case, Wouchuk's model appears to slightly overestimate the asymptotic growth rate. It is notable also that the model underpredicts the amplitude of the first peak in the growth rate calculated from the simulation, for both this case and $M_I = 1.05$. Further, after this peak, there appears to be a phase difference between our results and the model, which we speculate may be due to very early start-up effects detected only with full resolution of the shock and interface.

Some evidence for this theory may come from the simulations of Herrmann et al. (2008), Figure 4 in particular. This compares the result of a 2-D Navier-Stokes simulation of the instability at $M_{\mathrm{I}} = 1.21$ (at a Reynolds number in the inviscid range) with Wouchuk's model, to excellent agreement. Their simulation uses a shock capturing/tracking method and treats the interface as a level set scalar, so it is discontinuous for all time and does not suffer from the amplitude measurement difficulties we encounter. This implies that the fundamental assumptions of the Herrmann et al. simulations are more similar to Wouchuk's inviscid model than these results at the early growth stages of the instability, so neither can capture the early time effects observed in the present simulations.

Returning to the asymptotic behavior of the instability, based on Figures 4.13 and 4.16 for the weak and intermediate shock cases, a simple model for amplitude growth rate that accounts for start-up of the instability is proposed:

$$\frac{\dot{h}(t)}{h(0^+)} = \begin{cases} 0, & t \leq \tau, \\ \mathrm{A}^+ \Delta U k, & t > \tau. \end{cases} \tag{4.7.1}$$

This has the form of a shifted time origin for the impulsive model, and appears to closely approximate the simulated growth profiles in the inviscid limit. For stronger shocks, the impulsive model growth rate assumption may be inappropriate (compare Figure 4.22), but it is clearly demonstrated that the start-up process for the instability is well characterized by τ. In general, this result also supports the scaling of oscillations in the instability growth by kt, as τ is directly related to $1/k$ (4.2.8). Note that for most physical problems, the start-up time scale is very small; here $\tau \sim 10^{-7}$ seconds.

For the strong shock, results from the simulations point unambiguously to Wouchuk's model being the best estimate of the asymptotic growth rate. Figure 4.29 confirms this, with the plot of growth rate showing oscillation about the Wouchuk prediction, well clear

of the impulsive model. However, comparison of the time histories shows that the model considerably underpredicts the magnitude of oscillation in the growth rate. This implies that the amount of acoustic energy trapped between the shocks in the interface region is underestimated by the model, caused by the numerical difficulty involved with calculating the contribution from the transmitted shock. The simulation results confirm that this is a significant effect under these conditions: comparison of the amplitude curves shows that although early-time agreement is good, the effect of the oscillations in growth rate contribute to an overprediction of the amplitude by the model at later times.

4.7.2 Influence of Viscosity

Based on these results, we can conclude that contact with the inviscid limit has been made. The primary Reynolds number effect that has been observed is due simply to the dependence of $\mathrm{Re_I}$ on the wave number k; this is confirmed by the majority of results and the collapse of amplitude histories when the effect of k has been scaled out. In the cases where viscous effects are seen, the result is attenuation of the growth rate compared to the inviscid models and transient oscillation of greater amplitude. In the most extreme cases, the attenuation is large enough to cause decay of the interface perturbation, in which case the instability is suppressed. Existing viscous models do not model the observed growth very well, though the Carlès and Popinet (2001) model does display similar gross behavior in those cases where viscous effects are significant. It does not, however, predict very well which those cases are.

Comparison of the viscosity-influenced cases suggests some bounds on the Reynolds numbers at which viscous effects are significant. Based on these simulations, for $\mathrm{Re_I} < 1000$, viscosity has a significant attenuating influence on the amplitude growth rate. In the range $1000 < \mathrm{Re_I} < 5000$, there may be a small effect due to viscosity, but attenuation is small enough that the inviscid models are an acceptable approximation. Beyond this, the asymptotic behavior of the interface amplitude is essentially indistinguishable from the inviscid approximation.

Chapter 5

Conclusion

This thesis has presented stable high-order finite-difference interface schemes for both one-dimensional refinement and two-dimensional patch-refined grids with step changes in resolution. By satisfying the summation-by-parts criterion at the interface for each geometry, numerical stability of the interface schemes was enforced without resort to numerical dissipation. Demonstrating the value of high-order mesh refinement using these interface schemes, the Richtmyer-Meshkov instability was investigated with a shock-resolved Navier-Stokes simulation.

5.1 The 1-D Interface Scheme

Extending the concepts of stability and summation-by-parts operators to generalized stencils at a step-change in grid resolution, a class of stable high-order finite-difference interface closures has been developed. Stability has been demonstrated analytically for the linear advection problem. Further, the interface treatment is numerically nondissipative as the summation-by-parts formulation ensures no contribution is made to the energy norm. The global convergence rate of the interior scheme, s, is maintained by enforcing accuracy at the interface to order $\sigma \geq s - 1$. Interface closures have been presented for fourth- and sixth-order explicit and fourth-order implicit interior schemes. Explicit closures are available for arbitrary refinement ratios, within limits for stability. The implicit closure maintains the efficient tridiagonal structure of the interior scheme through the interface.

Numerical tests of these schemes have verified the claims of stability and convergence rate with refinement of the spatial discretization, for both the linear advection problem and the nonlinear one-dimensional Navier-Stokes shock structure problem. The one-dimensional

interface scheme may also be applied on two-dimensional grids with local refinement such that the grid may be represented as the tensor product of 1-D grids. Stability and convergence on grids of this type were confirmed by numerical testing with the linear 2-D advection problem and the nonlinear Euler equations solving a compressible vortex problem.

5.2 The 2-D Interface Scheme for Patch Refinement

Patch refinement on two-dimensional grids results in hanging nodes across grid interfaces, with three distinct geometries identified at the edges and corners of the refined regions. Extension of the summation-by-parts criterion in two dimensions has been used to design stable high-order finite-difference closures for these interfaces. This has been shown to guarantee stability of the semidiscrete form of the partial differential equation in the linear case, without introducing numerical dissipation at the interfaces. The cost of achieving this stability is the presence of first- and second-order–accurate nodes in the corner interface stencils with an explicit fourth-order finite-difference interior scheme, reducing the formal convergence rate of the spatial discretization. In the course of this investigation it was also found that there exists no second-order scheme that satisfies the summation-by-parts conditions, as these demand zeroth-order–accurate nodes at the corners that render the derivative approximation meaningless.

Validation testing of the interface closure on three different grids has shown that the presence of low-order interface points reduces the convergence rate by at least one order compared to the truncation error of the interior scheme. The numerical tests were conducted using the same linear advection and nonlinear Euler vortex problems as for the one-dimensional interface scheme. The latter test also demonstrates that careful design of the refinement scheme relative to regions of interest in the solution may mitigate the effects of reduced accuracy at the interfaces.

5.3 Comments on Future Interface Schemes

The schemes described in this thesis represent an attempt at resolving an important and long-standing problem in the field of computational physics, and there remains room for extension and development of these interface treatments to widen their applicability and

improve their computational efficiency. Thus far, only Cartesian grids have been considered, but there is scope for similar interface schemes to be developed for cylindrical or polar geometries. The focus of these schemes has also been limited to hyperbolic problems, and thus compressible flows. For incompressible problems, the system of equations is parabolic and involves solution of a Poisson equation, where the numerical stability problem is quite different and a new formulation of the stability criteria is required.

Regarding implementation of these interface schemes, the 2-D problem in particular is complex and difficult to implement for a general grid refinement geometry. Though beyond the scope of this work, there is potential for improvement in this regard with advanced computational data structures that deal efficiently with the flat grid topology of this scheme. Alternatively, high-order nondissipative interface schemes for hierarchical grids (like those efficiently implemented by the method of Berger and Colella, 1989) could be investigated.

The ultimate goal of this effort is to develop a stable interface treatment for fully three-dimensional patch-refined grids. On one hand, the conceptual leap from 2-D to 3-D is considerably smaller than that from 1-D to 2-D, as the hanging-node problem has already been solved. The 3-D patch-refined grid is topologically similar to that in 2-D, and may be approached in a similar manner: in place of the edge and corner interfaces identified in 2-D, there will be three-dimensional faces, edges and corners. The same principles of accuracy, stability and consistency with neighboring interfaces will continue to apply. On the other hand, the 3-D problem will be computationally demanding, involving likely hundreds of nodes in the vicinity of each interface, and may even be too cumbersome and inefficient to be usefully implemented. Also, we speculate that additional reductions in the maximum order of accuracy achievable at 3-D edges and corners may result, further increasing the computational cost and complexity of the method. Ultimately, a solution to the 3-D problem may exist, but it may be so unwieldy as to be of only academic interest.

5.4 The Richtmyer-Meshkov Instability

The start-up and linear growth phases of the Richtmyer-Meshkov instability have been investigated using a novel shock-resolved Navier-Stokes simulation. By assuming a linearized form for the solution with a perturbed interface, where the base flow is the solution to the nonlinear 1-D Navier-Stokes equations for a shock incident on a density interface, the

problem could be reduced to a 1-D computational domain. To efficiently resolve the full structure of the shocks, the interface closures of Chapter 2 were employed in a refinement scheme that tracked the solution features based on the inviscid Riemann solution. A full set of validation tests for the explicit fourth-order code has shown that the method is time stable and converges at the expected fourth-order rate.

Results from the simulations show that for weak and intermediate strength shocks, the impulsive model is adequate for prediction of the asymptotic growth rate of the perturbation. For strong shocks, the model from Wouchuk (2001a) accurately predicts the asymptotic growth rate. Transient growth shows general agreement with Wouchuk's model for weaker shocks, while for stronger shocks the same model significantly underestimates the amplitude of oscillation in the growth rate. The characteristic start-up time proposed by Lombardini (2008) is verified as a good estimate of the time for the instability to enter the linear growth regime. The extent of the influence of viscosity is predicted by a Reynolds number based on the perturbation wave number. Existing models of viscous attenuation are found to poorly predict the growth rate of the instability in most cases.

Further investigation within the current formulation may begin with a broader exploration of the parameter space, primarily in M_{I} and Atwood number. Of great interest would be fully resolved simulations of high-M_{I} shocks, as the existing theory and body of simulation results is somewhat limited in this area. The greatest hurdle for these problems is the resolution requirements, as discovered for the $M_{\mathrm{I}} = 2.20$, $\mathrm{A} = 0.6$ case, where successively greater refinements are required to resolve the very steep gradients encountered during impact of the shock with the interface. Computational cost may also be reduced with more sophisticated time-stepping routines, where the stability boundaries permit larger CFL numbers for the locally refined grids.

Extension of the present approach should begin with an implementation of the two-species gas mixture case, which is of interest because the relative values of γ_0 and $\gamma_{0'}$ have a strong influence on the transient growth of the solution. Comparison to experimental results would be improved, as each fluid could be modeled more accurately. Further work may also be done to progressively weaken the approximations made in the current formulation, depending on the particular focus of the future investigation.

Appendix A

Analysis of Finite-Difference Schemes

A.1 GKS Stability Theory

Stability of a discrete approximation to a linear hyperbolic partial differential equation may be analyzed for the Cauchy problem on an infinite domain using standard Fourier techniques (e.g., Lomax et al., 2001, §7.7), but on finite domains with imposed boundary values, this analysis is not appropriate and GKS stability theory, after Gustafsson et al. (1972), must be used. This discussion largely follows that of Carpenter et al. (1993), and is presented here as the precursor to the introduction of summation-by-parts operators, which are themselves shown to be GKS stable in Section 2.2.5.

The power of the GKS theory is that it allows separation of the stability problem into an infinite-domain Cauchy problem and two boundary problems. A necessary and sufficient condition for stability then requires that each problem have no eigensolution. This is formulated for the discrete problem (here following Berger, 1985) by assuming a normal mode form for the solution vector

$$u(j\Delta x, n\Delta t) \approx u_j^n = z^n \phi_j, \tag{A1.1}$$

where ϕ_j is the solution to the resolvent equation for the finite difference scheme (this form comes from a discrete Laplace transform in time that underpins the GKS analysis). Upon assuming a form $\phi_j = \phi_0 \kappa^j$, the resolvent equation will give a polynomial in κ^j that has

multiple roots κ_k^j, so we can write down the general form

$$\phi_j = \sum_{|\kappa_s| \leq 1} p(j,s)\kappa_s^j(z), \tag{A1.2}$$

where p is the polynomial coefficient in j of order one less than the multiplicity of the root κ_s. Stability, in the sense that the solution (A1.1) is bounded, then requires that there be no solutions for ϕ_j with

1. $|z| > 1$ and $|\kappa| < 1$, or
2. $|z| = 1$ and $|\kappa| \leq 1$.

These conditions bound ϕ_j by excluding terms from the summation equation (A1.2) that could cause growth: (1), where $|z| > 1$, or (2), in the degenerate case where $|z| = 1$. The remaining combinations of $|z|$ and $|\kappa|$ leave equation (A1.1) bounded in space and time.

The GKS theory may also be extended to the semidiscrete problem if a Runge-Kutta time-marching scheme is used with a discretization that is inside the stability region. The results look similar, but it is useful to cast the problem in the semidiscrete form to compare the resulting stability conditions to those required for asymptotic stability. Following Carpenter et al. (1993), we assume a normal-mode solution to the semidiscrete problem described by (2.2.6)

$$u_j(t) = \mathrm{e}^{Gt}\phi_j, \tag{A1.3}$$

where $G = \mathrm{diag}(\lambda^A)$ are the eigenvalues of A. Again we assume a form for ϕ_j

$$\phi_j = \phi_0 \kappa^j. \tag{A1.4}$$

An eigensolution to the initial-boundary value problem (2.2.6) is then defined as a nontrivial function with $\Re(G) \geq 0$ that satisfies

1. for $\Re(G) > 0$, $|\kappa| < 1$ (so a GKS-eigenvalue exists), or
2. for $\Re(G) = 0$ and $|\kappa| = 1$, a perturbation to $|\kappa| = 1 - \epsilon$ with $\epsilon > 0$ generates an eigenvalue $\Re(G) > \delta$, where $\delta > 0$ (i.e., a generalized GKS eigenvalue exists).

The condition for stability is then that there exists no such eigensolution; see that (1) allows a solution bounded in x that would grow exponentially in time, and that (2) covers

the limiting case. For a given scheme, stability is determined by assuming a solution of the normal mode form (A1.3) and showing that the resulting κ is not a GKS eigenvalue.

To demonstrate the resolvent condition and the form of the roots κ, we use an example from Carpenter et al. (1993) and start with the generalized eigenvalue equation derived from equation (2.2.6):

$$Gu_j = Au_j. \tag{A1.5}$$

The resolvent equation follows upon substitution of equation (A1.3); for the fourth-order implicit scheme, this has the form

$$\left(\frac{1}{4}\phi_{j-1} + \phi_j + \frac{1}{4}\phi_{j+1}\right) G = \frac{3}{4}\left(\phi_{j+1} - \phi_{j-1}\right). \tag{A1.6}$$

Substituting for ϕ_j by (A1.4), we obtain a quadratic equation in κ

$$\left(\frac{1}{\kappa} + 4 + \kappa\right) G = 3\left(\kappa - \frac{1}{\kappa}\right). \tag{A1.7}$$

The first root ($\kappa_1 = \kappa$) is obvious, but to find the second, substitute a function $f(\kappa)$ such that

$$\left(f^2 + 4f + 1\right) G = 3(f^2 - 1), \tag{A1.8}$$

where $f^2 + 4f + 1 = (\kappa^2 + 4\kappa + 1)g(\kappa)$ and $f^2 - 1 = (\kappa^2 - 1)g(\kappa)$, for some amplitude function $g(\kappa)$. Doing the algebra, we find a quadratic in $f(\kappa)$ with the two roots we seek,

$$\kappa_1 = \kappa \quad \text{and} \quad \kappa_2 = \frac{-\kappa - 2}{2\kappa + 1},$$

so ϕ_j has the general form

$$\phi_j = C_1\kappa_1^j + C_2\kappa_2^j, \tag{A1.9}$$

where C_1 and C_2 are constants determined from the boundary treatment. Note that $|\kappa_1| \geq 1$ implies $|\kappa_2| \leq 1$ here; Gustafsson et al. (1972) shows that in the discrete case with $|z| > 1$, there will be Nl linearly independent solutions with $|\kappa| < 1$ and Nr with $|\kappa| > 1$ for a difference stencil with l points to the left and r to the right (N is the size of the system, which is clearly assumed to be uniform).

A final quirk of Lax/GKS stability is that the eigenvalues of the spatial finite-difference

scheme must satisfy

$$\Re(\lambda_j) \leq \omega, \quad \omega \geq 0$$

as a necessary condition. This means that the eigenvalues asymptotically approach a bound in the right-hand complex plane as $N \to \infty$. This may appear somewhat alarming at first glance for time stability, but notice that the eigenvalues of a centered difference scheme on an infinite domain (as approached in the limit $N \to \infty$) have zero real part; the key is to keep $\omega = 0$ as the limit when finite boundaries are present.

Regarding GKS stability at the interfaces, it is prohibitively difficult to perform this analysis directly on stencils as large and complex as those used in the interface schemes, so instead we rely on the summation-by-parts property to guarantee GKS stability.

A.2 Time-Marching Stability Theory

Having demonstrated stability for the semidiscrete problem, further analysis is necessary to ensure that a given time discretization preserves those stability properties. Our primary interest here is in one-step explicit time-marching methods like Runge-Kutta, but the analysis may be adapted to investigate other schemes.

For a one-step time-marching method, equation (2.2.6) is discretized to obtain for the solution at time step n,

$$\mathbf{u}^{n+1} = S\mathbf{u}^n = S^{n+1}\mathbf{u}^0, \tag{A2.1}$$

where S is a function of the general matrix A. Diagonalizing the discrete system, this may be written in terms of the eigenvalues of S,

$$w_j^{n+1} = \sigma(\lambda_j^A \Delta t) w_j^n = [\sigma(\lambda_j^A \Delta t)]^n w_j^0, \tag{A2.2}$$

where $\mathbf{w} = X^{-1}\mathbf{u}$, expressed in terms of the right eigenvectors X and eigenvalues λ_j^A of A. For an sth-order Runge-Kutta scheme, S and its eigenvalues may be expressed directly in terms of A and λ_j^A:

$$S = I + \Delta t A + \frac{\Delta t^2}{2} A^2 + \cdots + \frac{\Delta t^s}{s!} A^s, \tag{A2.3}$$

$$\sigma(z) = 1 + z + \frac{1}{2} z^2 + \cdots + \frac{1}{s!} z^s, \tag{A2.4}$$

where $z = \lambda_j^A \Delta t$. For the solution (A2.2) to be asymptotically stable, we simply require

$$\max_j |\sigma(\lambda_j^A \Delta t)| < 1. \tag{A2.5}$$

This is the von Neumann stability condition. For general A, the eigenvalues λ_j^A may be complex, so $\sigma(z)$ is in general a complex-valued function. The stability boundaries are visualized by plotting contours of $|\sigma(z)| = 1$, shown in Figure A.1 for the third- and fourth-order Runge-Kutta schemes (with coefficients from Butcher, 2003).

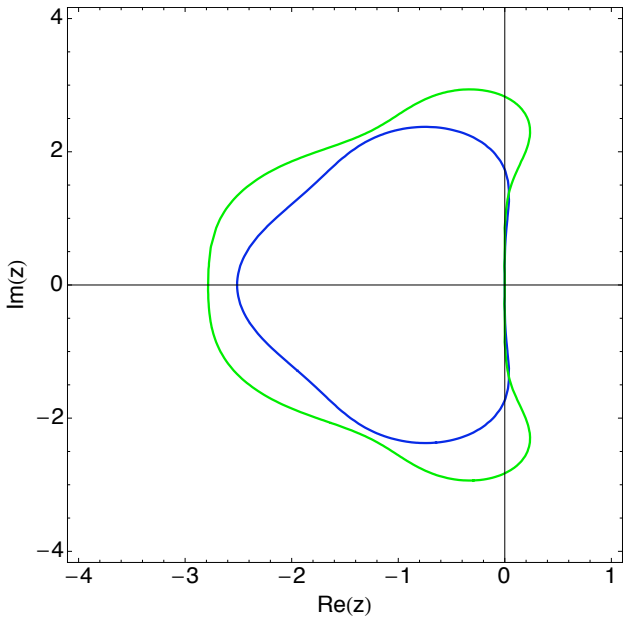

Figure A.1: Stability boundaries of the third-order (blue) and fourth-order (green) Runge-Kutta time-marching schemes, defined by $|\sigma(z)| < 1$. Values of $z = \lambda_j^A \Delta t$ inside each contour are stable.

For the advection equation (2.2.1) solved on a uniform grid with periodic boundary conditions, spectral analysis of the finite-difference scheme allows precise bounds for discrete stability to be defined. In this case, the eigenvalues of A may be represented in terms of the modified wave number, k':

$$\lambda^A = -\mathrm{i}ck', \tag{A2.6}$$

where k' is determined by Fourier analysis of the finite-difference scheme used (e.g., Lomax et al., 2001, §3.5). Defining the CFL number as $C = c\Delta t/\Delta x$, substituting equation (A2.6) into (A2.5), we have

$$|\sigma(-iCk'\Delta x)| < 1. \tag{A2.7}$$

Thus the stability limit on C can be found directly from the spectrum of the finite difference scheme (which defines k') and the spectrum of the time-marching scheme (which defines the function $\sigma(z)$). From this follows some observations:

1. For centered finite difference schemes, k' is real so $z = -iCk'\Delta x$ is purely imaginary. Thus stability is limited by the intersection of the contour $|\sigma(z)| = 1$ with the imaginary axis.

2. Generally, for a centered scheme with $c_1 = \max(k'\Delta x)$ and a time-marching scheme having an intersection of $|\sigma(z)| = 1$ with the imaginary axis at $\lambda^A \Delta t = c_2$, the bound on stability is given by

$$C < c_1/c_2. \tag{A2.8}$$

   For the centered fourth-order explicit finite-difference scheme with a third-order Runge-Kutta time-marching scheme, $c_1 = 1.732$ and $c_2 = 1.372$, giving the stability criterion $C < 1.262$.

Appendix B

Stable Boundary Schemes

B.1 Explicit Fourth-Order Boundary Closure

The boundary closure derivation follows the theory of Strand (1994), but is applied here in a form analogous to that used for the interface schemes. Four points are sufficient to close the boundary problem to third order at the outer two points and fourth order at the inner two points in the fourth-order explicit case, without free parameters. The scheme is described here as 3-3-4-4, following the naming convention given to the interface schemes, where the numbers refer to the order of accuracy at each point, and the domain end being at the left-hand side. Given here in equations (B.1)–(B.2) are the first six rows and columns of the P and Q matrices of this boundary scheme.

$$P = \begin{bmatrix} \frac{2429}{10368} & \frac{469}{3456} & -\frac{113}{1152} & \frac{277}{10368} & 0 & 0 \\ \frac{469}{3456} & \frac{4871}{3456} & -\frac{721}{3456} & \frac{205}{3456} & 0 & 0 \\ -\frac{113}{1152} & -\frac{721}{3456} & \frac{3623}{3456} & -\frac{43}{3456} & 0 & 0 \\ \frac{277}{10368} & \frac{205}{3456} & -\frac{43}{3456} & \frac{10397}{10368} & 0 & 0 \\ 0 & 0 & 0 & 0 & 1 & 0 \\ 0 & 0 & 0 & 0 & 0 & 1 \end{bmatrix} \tag{B.1}$$

$$Q = \begin{bmatrix} -\frac{1}{2} & \frac{167}{216} & -\frac{149}{432} & \frac{31}{432} & 0 & 0 \\ -\frac{167}{216} & 0 & \frac{133}{144} & -\frac{65}{432} & 0 & 0 \\ \frac{149}{432} & -\frac{133}{144} & 0 & \frac{143}{216} & -\frac{1}{12} & 0 \\ -\frac{31}{432} & \frac{65}{432} & -\frac{143}{216} & 0 & \frac{2}{3} & -\frac{1}{12} \\ 0 & 0 & \frac{1}{12} & -\frac{2}{3} & 0 & \frac{2}{3} \\ 0 & 0 & 0 & \frac{1}{12} & -\frac{2}{3} & 0 \end{bmatrix} \tag{B.2}$$

The right-hand boundary is obtained from the left by the transpose/flip-transpose transformation. The summation-by-parts constraints are met by the boundary closure when combined with the SAT method for application of the boundary conditions.

B.2 Explicit Sixth-Order Boundary Closure

The sixth-order explicit boundary closure is derived similarly to the fourth-order explicit scheme. Six points are sufficient to close the boundary problem to at least fifth-order accuracy, the scheme shown here in equations (B.3)–(B.4) being 5-5-5-6-6-6. Shown here are the left-hand boundary regions of P and Q. The right-hand boundary is obtained by the same transformation described for the fourth-order case.

$$P = \begin{bmatrix} \frac{53464067}{279936000} & \frac{13030159}{55987200} & -\frac{1016513}{5598720} & \frac{3695851}{27993600} & -\frac{2695189}{55987200} & \frac{2072623}{279936000} \\ \frac{13030159}{55987200} & \frac{78554551}{55987200} & -\frac{14216029}{27993600} & \frac{275275}{1119744} & -\frac{916649}{11197440} & \frac{612203}{55987200} \\ -\frac{1016513}{5598720} & -\frac{14216029}{27993600} & \frac{24866869}{13996800} & -\frac{6005707}{13996800} & \frac{972023}{5598720} & -\frac{163537}{5598720} \\ \frac{3695851}{27993600} & \frac{275275}{1119744} & -\frac{6005707}{13996800} & \frac{16373749}{13996800} & -\frac{1774429}{27993600} & \frac{288059}{27993600} \\ -\frac{2695189}{55987200} & -\frac{916649}{11197440} & \frac{972023}{5598720} & -\frac{1774429}{27993600} & \frac{57248311}{55987200} & -\frac{199409}{55987200} \\ \frac{2072623}{279936000} & \frac{612203}{55987200} & -\frac{163537}{5598720} & \frac{288059}{27993600} & -\frac{199409}{55987200} & \frac{280091267}{279936000} \end{bmatrix} \tag{B.3}$$

$$Q = \begin{bmatrix} -\frac{1}{2} & \frac{20701}{24300} & -\frac{985667}{1555200} & \frac{621509}{1555200} & -\frac{216053}{1555200} & \frac{32947}{1555200} \\ -\frac{20701}{24300} & 0 & \frac{2251333}{1555200} & -\frac{144251}{172800} & \frac{440579}{1555200} & -\frac{68789}{1555200} \\ \frac{985667}{1555200} & -\frac{2251333}{1555200} & 0 & \frac{33791}{32400} & -\frac{138353}{518400} & \frac{58757}{1555200} \\ -\frac{621509}{1555200} & \frac{144251}{172800} & -\frac{33791}{32400} & 0 & \frac{1149253}{1555200} & -\frac{45991}{311040} \\ \frac{216053}{1555200} & -\frac{440579}{1555200} & \frac{138353}{518400} & -\frac{1149253}{1555200} & 0 & \frac{911}{1215} \\ -\frac{32947}{1555200} & \frac{68789}{1555200} & -\frac{58757}{1555200} & \frac{45991}{311040} & -\frac{911}{1215} & 0 \end{bmatrix} \tag{B.4}$$

B.3 Implicit Fourth-Order Boundary Closure

The four-point implicit boundary closure used in this work is that developed in Carpenter et al. (1994), and is presented here for completeness. This scheme has third-order accuracy at each of the four points of the boundary region, and has P tridiagonal, so preserves the efficient structure of the interior scheme. Reproduced in equations (B.5)–(B.6) are the four rows and columns of the boundary part of the matrices H, P and Q from Carpenter et al. (1994).

$$H = \begin{bmatrix} \frac{70282007653}{7658388480} & -\frac{9426299}{2268480} & -\frac{192913}{1067520} & 0 \\ -\frac{55530689643}{2552796160} & \frac{8051589}{756160} & \frac{149823}{355840} & 0 \\ \frac{63842626133}{2552796160} & -\frac{9153739}{756160} & -\frac{4433}{355840} & -\frac{1}{8} \\ -\frac{71498870443}{7658388480} & \frac{10110149}{2268480} & \frac{102703}{1067520} & 1 \end{bmatrix}, \tag{B.5}$$

$$P = \begin{bmatrix} \frac{211}{429} & 1 & 0 & 0 \\ 1 & \frac{3563}{1688} & -\frac{1}{8} & 0 \\ 0 & \frac{43}{17} & \frac{1893}{1054} & \frac{139}{186} \\ 0 & 0 & \frac{1}{4} & 1 \end{bmatrix}, \quad Q = \begin{bmatrix} -\frac{289}{234} & \frac{279}{286} & \frac{75}{286} & -\frac{7}{2574} \\ -\frac{8635}{3376} & \frac{6987}{3376} & \frac{1851}{3376} & -\frac{203}{3376} \\ -\frac{15043}{18972} & -\frac{4089}{2108} & \frac{147}{124} & \frac{29353}{18972} \\ 0 & 0 & -\frac{3}{4} & 0 \end{bmatrix}. \tag{B.6}$$

As for the explicit schemes, the right-hand boundary scheme is obtained by transformation of the above left-hand side matrices.

Appendix C

Interface Scheme Implementation

This section briefly describes the implementation of the 1-D and 2-D interface schemes used for the validation tests and the Richtmyer-Meshkov instability study. This implementation is by no means unique, nor necessarily the most efficient computationally, but it illustrates a potential methodology for using these schemes in a practical computation.

C.1 Implementation of the 1-D Scheme

A domain is defined by a discretization Δx and two vectors, each of length M for a domain of M blocks (as defined in Section 2.1): $\mathbf{n} = \{n_m\}$, containing the number of nodes in each block, and $\mathbf{r} = \{r_m\}$, containing the multiple of Δx that defines the discretization of that block, $r_m \Delta x$. The following algorithm calculates the derivative approximation $D\mathbf{u}$ of a discrete vector $\mathbf{u}$:

```
for m = 1,..., M:
    if m = M,
        calculate the derivative at the RH boundary
    else
        calculate the derivative across the interface
    end
    for each interior node of the block, calculate the derivative
    if m = 1, calculate the derivative at the LH boundary
```

In this way, the derivatives for the nodes on both sides of the interface between blocks m and $m+1$ are calculated in a single matrix multiplication using $D = \hat{P}^{-1}Q$, where for the

fourth-order explicit scheme,

$$Q = \begin{bmatrix} -\alpha & -\beta & 0 & q_{12} & q_{13} & q_{14} & 0 & 0 \\ 0 & -\alpha & -q_{12} & 0 & q_{23} & q_{24} & 0 & 0 \\ 0 & 0 & -q_{13} & -q_{23} & 0 & q_{34} & \alpha & 0 \\ 0 & 0 & -q_{14} & -q_{24} & -q_{34} & 0 & \beta & \alpha \end{bmatrix},$$

so the full dependence set of the interface nodes is included. All quantities are as defined in Section 2.3. The same applies for the boundaries, such that both ends of each block are calculated by these matrix operations. Derivative values for the remaining interior elements of the block are calculated using the standard stencil.

This algorithm was implemented for the validation problems described in Section 2.6. For the 2-D tensor-product grids, the same algorithm was applied in each direction to calculate the respective derivatives, now with separate block description vectors $\mathbf{n}$ and $\mathbf{r}$ for the x and y directions. The algorithm was used again for the investigation of the Richtmyer-Meshkov stability in Chapter 4, but where $\mathbf{n}$ and $\mathbf{r}$ are now time-varying quantities (in both value and length, as the number of blocks can change).

For the implicit scheme, the P and Q matrices were built up in a similar way for the entire domain, then inverted to calculate the derivative. Due to the tridiagonal structure of P, maintained through the interface regions, this is a relatively fast operation. Note that H is not required to calculate any derivatives.

C.2 Implementation of the 2-D Scheme

The implementation in 2-D for patch refinement follows a similar algorithm to the 1-D scheme, though the details are an order magnitude more complicated. The domain is now divided into rectangular blocks, so the vectors $\mathbf{n}$ and $\mathbf{r}$ become matrices. The algorithm calculates the right-hand and upper ends of each block, using the 1-D boundary matrix for each row or column or the appropriate interface matrix. Determining the appropriate interface matrix requires detailed logic based on the refinement in the current and neighboring blocks. Once the interface type is identified, the interface node sets $\mathcal{I}^i$ and $\mathcal{I}^d$ are collected and ordered to follow the numbering of Section 3.3. A single matrix multiplication using the difference matrix $\hat{D}_x$ or $\hat{D}_y$ calculates the derivative for the interface nodes of each set.

This complexity notwithstanding, the method can be broken down to three steps to be performed for each block:

1. if the block has a boundary, calculate the derivatives using the boundary stencil,
2. if the block has an interface on its right or upper edge,
   (a) identify the interface node set(s), $\mathcal{I}^i$ and $\mathcal{I}^d$,
   (b) calculate the derivatives for the full interface set(s),
3. calculate the derivatives for the remaining interior nodes using the standard stencil.

Here, the most difficult steps are the those needed to identify the interface sets, which must be properly ordered in each of the four orientations possible for each interface, and for both derivatives. Note that not all blocks have interfaces with a change in resolution, in which case data values from the adjacent block are required. A companion data structure for the solution vector may be an efficient way to identify interface nodes more quickly, and certain node-numbering/ordering schemes may prove more efficient than others.

The six derivative matrices ($\hat{D}_x$ and $\hat{D}_y$ for each of the three interface geometries) provided online with this thesis are for the default orientations defined in Section 3.3. These are transformed to the other possible orientations following Table 3.2.

Appendix D

Alternative 2-D Edge Interface Formulation

For the edge interface, an alternative formulation to that shown in Section 3.3.3 is available. Consider solving equation (3.1.1) now on a grid of infinite extent with an interface at $x = 0$, such that the left half plane is refined by ratios r_x and r_y in the x- and y-directions, respectively, relative to the right half plane. Thus $\Omega^f = \{(x, y) \in x < 0\}$, and $\Omega^c = \{(x, y) \in x > 0\}$, and a grid is obtained that contains only the edge interface geometry from Figure 3.3. Note that each cell row of the grid is identical in this case, so nodes may be identified by a global index pair (i, j), where $i \in \mathbb{N}$ identifies the node position in the coarse row j, with the indexing chosen such that $(0, j)$ is the coarse node closest to the interface at $x = 0$. A convenient choice for the numbering within the fine part of each row is the "N"-counting scheme, shown in Figure D.1. With the familiar refinement ratios $r_x = r_y = 2$, the node locations $(x, y)_{i,j}$ are given by

$$(x, y)_{i,j} = \begin{cases} ([i/2]\Delta x, [2j + 1/2]\Delta y), & \text{if } i < 0 \text{ and odd,} \\ ([i/2 + 1/2]\Delta x, [2j - 1/2]\Delta y), & \text{if } i < 0 \text{ and even,} \\ ([2i + 1]\Delta x, 2j\Delta y), & i \geq 0, \end{cases} \tag{D.1}$$

where Δx and Δy are the refined grid discretizations.

This node-numbering scheme leads naturally to a formulation of the interface problem in terms of fourth-order tensors. Here, using the difference tensor $\mathbf{D}_{x,ijkl}$ as an example, the first pair of indices relate to the rows of the matrix D_x (the independent indices), and the second pair to the columns of D_x (the dependent indices). Within each index pair, the

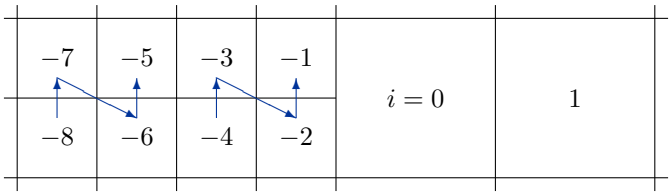

Figure D.1: The "N"-counting scheme for refined regions of an infinite grid with an interface at $x = 0$, for a row j.

first index refers to the node number (i) and the second to the row (j). This can be done only because each row of this grid is identical; for any refinement where $\partial\Omega^f$ has corners, there is implicitly a change in the form of the rows and this formulation cannot be used.

For the interface scheme from Section 3.3.3, for a given grid row j of the edge-interface grid, the dependence set extends only to rows $\{j-1, j, j+1\}$. Consequently, the matrices for the interface stencil may be written as

$$\hat{\mathbf{D}}_{x,ijkl} = \hat{D}^{-1}_{x,ik}\delta_{j-1,l} + \hat{D}^{0}_{x,ik}\delta_{j,l} + \hat{D}^{+1}_{x,ik}\delta_{j+1,l}, \tag{D.2}$$

$$\hat{\mathbf{D}}_{y,ijkl} = \hat{D}^{-1}_{y,ik}\delta_{j-1,l} + \hat{D}^{0}_{y,ik}\delta_{j,l} + \hat{D}^{+1}_{y,ik}\delta_{j+1,l}, \tag{D.3}$$

$$\hat{\mathbf{H}}_{ijkl} = \hat{H}^{0}_{ik}\delta_{j,l}, \tag{D.4}$$

where $\delta_{j,l}$ is the Kronecker delta, and each of $\hat{D}^{-1}_x$, $\hat{D}^0_x$, $\hat{D}^{+1}_x$, $\hat{D}^{-1}_y$, $\hat{D}^0_y$, $\hat{D}^{+1}_y$ and $\hat{H}^0$ are second-order matrices of finite extent. In the case of the stencil from Figure 3.7, all are 8×8 matrices, except $\hat{D}^0_x$, which is 8×14. The accuracy conditions (3.3.1)–(3.3.2) are constructed as before, in this case over the full matrices $\hat{\mathbf{D}}_x$ and $\hat{\mathbf{D}}_y$, and the stability conditions (3.2.21)–(3.2.22) expand to

$$\hat{H}^0_{im}\hat{D}^{-1}_{x,mk} + \hat{H}^0_{mk}\hat{D}^{+1}_{x,mi} = 0, \tag{D.5}$$

$$\hat{H}^0_{im}\hat{D}^{0}_{x,mk} + \hat{H}^0_{mk}\hat{D}^{0}_{x,mi} = 0, \tag{D.6}$$

$$\hat{H}^0_{im}\hat{D}^{+1}_{x,mk} + \hat{H}^0_{mk}\hat{D}^{-1}_{x,mi} = 0, \tag{D.7}$$

in x, and similarly in y. The resulting edge solution is identical to that of Section 3.3.3. The advantage of this formulation is that the matrices $\hat{D}^{-1}$, $\hat{D}^0$ and $\hat{D}^{+1}$ have a particularly simple structure, but this formulation cannot be applied at the corners where the grid changes structure in two directions.

Appendix E

Manipulations of the Navier-Stokes Equations

E.1 Nondimensional Form

The Navier-Stokes equations for a general compressible fluid are

$$\frac{\partial \rho}{\partial t} + u_j \frac{\partial \rho}{\partial x_j} + \rho \frac{\partial u_j}{\partial x_j} = 0, \tag{E1.1}$$

$$\rho \frac{\partial u_i}{\partial t} + \rho u_j \frac{\partial u_i}{\partial x_j} = -\frac{\partial p}{\partial x_i} + \frac{\partial \tau_{ij}}{\partial x_j}, \tag{E1.2}$$

$$\rho \frac{\partial}{\partial t}\left(e + \frac{1}{2}u_k u_k\right) + \rho u_j \frac{\partial}{\partial x_j}\left(e + \frac{1}{2}u_k u_k\right) = -\frac{\partial (p u_j)}{\partial x_j} + \frac{\partial (u_k \tau_{kj})}{\partial x_j} - \frac{\partial q_j}{\partial x_j}, \tag{E1.3}$$

where τ_{ij} is the deviatoric stress tensor and q_j is the heat transfer vector (which is zero if the flow is adiabatic). For a general Newtonian fluid, the deviatoric stress is given by

$$\tau_{ij} = \lambda S_{kk} \delta_{ij} + 2\mu S_{ij}, \tag{E1.4}$$

where

$$S_{ij} = \frac{1}{2}\left(\frac{\partial u_i}{\partial x_j} + \frac{\partial u_j}{\partial x_i}\right).$$

For the problems considered in this thesis, we assume zero bulk viscosity,

$$\mu_v = \lambda + \frac{2}{3}\mu = 0, \tag{E1.5}$$

so the deviatoric stress may be expressed in terms of the dynamic viscosity alone to obtain

$$\tau_{ij} = -\frac{2}{3}\mu S_{kk} + 2\mu S_{ij}. \tag{E1.6}$$

Further assuming Fourier heat conduction,

$$q_i = -\kappa \frac{\partial T}{\partial x_i}. \tag{E1.7}$$

At this point, we confine the analysis to the 1-D Navier-Stokes equations, reducing the system (E1.1)–(E1.3) to

$$\begin{aligned}
&\frac{\partial \rho}{\partial t} + \frac{\partial (\rho u)}{\partial x} = 0, \\
&\rho \frac{\partial u}{\partial t} + \rho u \frac{\partial u}{\partial x} = -\frac{\partial p}{\partial x} + \frac{\partial \tau}{\partial x}, \\
&\rho \frac{\partial}{\partial t}\left(e + \frac{1}{2}u^2\right) + \rho u \frac{\partial}{\partial x}\left(e + \frac{1}{2}u^2\right) = -\frac{\partial (pu)}{\partial x} + \frac{\partial (\tau u)}{\partial x} - \frac{\partial q}{\partial x}.
\end{aligned}$$

Applying the stress and heat conduction assumptions, and writing the system in conservative form, we have

$$\frac{\partial \rho}{\partial t} + \frac{\partial (\rho u)}{\partial x} = 0, \tag{E1.8}$$

$$\frac{\partial (\rho u)}{\partial t} + \frac{\partial (\rho u^2)}{\partial x} = -\frac{\partial p}{\partial x} + \frac{4}{3}\frac{\partial}{\partial x}\left(\mu \frac{\partial u}{\partial x}\right), \tag{E1.9}$$

$$\frac{\partial}{\partial t}\left(\rho e + \frac{1}{2}\rho u^2\right) + \frac{\partial}{\partial x}\left(\rho e u + \frac{1}{2}\rho u^3\right) = -\frac{\partial (pu)}{\partial x} + \frac{4}{3}\frac{\partial}{\partial x}\left(\mu u \frac{\partial u}{\partial x}\right) + \frac{\partial}{\partial x}\left(\kappa \frac{\partial T}{\partial x}\right). \tag{E1.10}$$

In general, viscosity and heat conduction are functions of x and t, but in this work we will assume constant μ and κ for

$$\frac{\partial \rho}{\partial t} + \frac{\partial (\rho u)}{\partial x} = 0, \tag{E1.11}$$

$$\frac{\partial (\rho u)}{\partial t} + \frac{\partial (\rho u^2)}{\partial x} = -\frac{\partial p}{\partial x} + \frac{4}{3}\mu \frac{\partial^2 u}{\partial x^2}, \tag{E1.12}$$

$$\frac{\partial}{\partial t}\left(\rho e + \frac{1}{2}\rho u^2\right) + \frac{\partial}{\partial x}\left(\rho e u + \frac{1}{2}\rho u^3\right) = -\frac{\partial (pu)}{\partial x} + \frac{4}{3}\mu \frac{\partial}{\partial x}\left(u \frac{\partial u}{\partial x}\right) + \kappa \frac{\partial^2 T}{\partial x^2}. \tag{E1.13}$$

We now specify a perfect gas, so $p = \rho R T$ and $e = C_v T$, where R is the specific gas constant and C_v is the specific heat capacity at constant volume. This allows both

temperature and internal energy to be expressed in terms of pressure and density:

$$T = \frac{1}{R}\frac{p}{\rho}, \tag{E1.14}$$

$$e = C_v T = \frac{C_v}{R}\frac{p}{\rho} = \frac{1}{\gamma - 1}\frac{p}{\rho}, \tag{E1.15}$$

which gives a conserved energy term

$$\rho e + \frac{1}{2}\rho u^2 = \frac{p}{\gamma - 1} + \frac{1}{2}\rho u^2. \tag{E1.16}$$

Applying this to the system, after a little simplification we have the system

$$\frac{\partial \rho}{\partial t} = -\frac{\partial(\rho u)}{\partial x}, \tag{E1.17}$$

$$\frac{\partial(\rho u)}{\partial t} = -\frac{\partial}{\partial x}\left(\rho u^2 + p - \frac{4}{3}\mu\frac{\partial u}{\partial x}\right), \tag{E1.18}$$

$$\frac{\partial}{\partial t}\left(\frac{p}{\gamma - 1} + \frac{1}{2}\rho u^2\right) = -\frac{\partial}{\partial x}\left(\frac{\gamma}{\gamma - 1}pu + \frac{1}{2}\rho u^3 - \frac{4}{3}\mu u\frac{\partial u}{\partial x} - \frac{\kappa}{R}\frac{\partial}{\partial x}\left(\frac{p}{\rho}\right)\right). \tag{E1.19}$$

To nondimensionalize these equations, we define reference states ρ_0, u_0 and p_0. Further, since we are interested in problems at the scale of thickness of a shock, the length scale is a reference mean free path length, ℓ_0. Thus we define the dimensionless variables, denoted by a hat,

$$\hat{x} = \frac{x}{\ell_0}, \quad \hat{\rho} = \frac{\rho}{\rho_0}, \quad \hat{u} = \frac{u}{u_0}, \quad \hat{p} = \frac{p}{p_0}, \quad \hat{t} = \frac{t u_0}{\ell_0}.$$

For the derived quantities, note that $\hat{T} = \hat{e} = \hat{p}/\hat{\rho}$. Thus we obtain the nondimensional version of (E1.17)–(E1.19),

$$\frac{\partial \hat{\rho}}{\partial \hat{t}} = -\frac{\partial}{\partial \hat{x}}\left(\hat{\rho}\hat{u}\right),$$

$$\frac{\partial(\hat{\rho}\hat{u})}{\partial \hat{t}} = -\frac{\partial}{\partial \hat{x}}\left(\hat{\rho}\hat{u}^2 + \frac{p_0}{\rho_0 u_0^2}\hat{p} - \frac{4}{3}\frac{\mu}{\rho_0 u_0 \ell_0}\frac{\partial \hat{u}}{\partial \hat{x}}\right),$$

$$\frac{\partial}{\partial \hat{t}}\left(\frac{p_0}{\rho_0 u_0^2}\frac{\hat{p}}{\gamma - 1} + \frac{1}{2}\hat{\rho}\hat{u}^2\right) = -\frac{\partial}{\partial \hat{x}}\left(\frac{\gamma}{\gamma - 1}\frac{p_0}{\rho_0 u_0^2}\hat{p}\hat{u} + \frac{1}{2}\hat{\rho}\hat{u}^3 - \frac{4}{3}\frac{\mu}{\rho_0 u_0 \ell_0}\hat{u}\frac{\partial \hat{u}}{\partial \hat{x}} - \frac{\kappa p_0}{\rho_0^2 u_0^3 \ell_0 R}\frac{\partial \hat{T}}{\partial \hat{x}}\right).$$

Three dimensionless groups are common to these equations:

$$\frac{p_0}{\rho_0 u_0^2} = \frac{1}{\gamma}\frac{1}{u_0^2}\frac{\gamma p_0}{\rho_0} = \frac{1}{\gamma M_0^2}, \tag{E1.20}$$

$$\frac{\mu_0}{\rho_0 u_0 \ell_0} = \frac{1}{\mathrm{Re}}, \tag{E1.21}$$

$$\frac{\kappa p_0}{\rho_0^2 u_0^3 \ell_0 R} = \frac{C_p}{R}\frac{\kappa}{\mu C_p}\frac{\mu}{\rho_0 u_0 \ell_0}\frac{p_0}{\rho_0 u_0^2} = \frac{1}{(\gamma-1)\mathrm{PrRe}M_0^2}. \tag{E1.22}$$

where the Mach number $M_0 = u_0/a_0$ is defined with respect to the reference sound speed, and we have defined a Reynolds number, Re, and a Prandtl number, $\mathrm{Pr} = \mu C_p/\kappa$, in terms of the reference states. This reduces the problem to four nondimensional parameters: γ, M_0, Re and Pr, giving

$$\frac{\partial \hat{\rho}}{\partial \hat{t}} = -\frac{\partial}{\partial \hat{x}}\left(\hat{\rho}\hat{u}\right), \tag{E1.23}$$

$$\frac{\partial(\hat{\rho}\hat{u})}{\partial \hat{t}} = -\frac{\partial}{\partial \hat{x}}\left(\hat{\rho}\hat{u}^2 + \frac{\hat{p}}{\gamma M_0^2} - \frac{4}{3}\frac{1}{\mathrm{Re}}\frac{\partial \hat{u}}{\partial \hat{x}}\right), \tag{E1.24}$$

$$\frac{\partial}{\partial \hat{t}}\left(\frac{\hat{p}}{\gamma M_0^2} + \beta\hat{\rho}\hat{u}^2\right) = -\frac{\partial}{\partial \hat{x}}\left(\frac{\hat{p}\hat{u}}{M_0^2} + \beta\hat{\rho}\hat{u}^3 - \frac{4}{3}\frac{\gamma-1}{\mathrm{Re}}\hat{u}\frac{\partial \hat{u}}{\partial \hat{x}} - \frac{1}{\mathrm{PrRe}M_0^2}\frac{\partial \hat{T}}{\partial \hat{x}}\right), \tag{E1.25}$$

where $\beta = (\gamma-1)/2$.

For the Navier-Stokes shock solution, two further simplifications are made. First, the Prandtl number is set to $\mathrm{Pr} = 3/4$ for analytic expediency (see Appendix F.1), though this is only a small deviation from the standard value for air ($\mathrm{Pr} = 0.72$). Second, since we have used the mean free path ℓ_0 as our length scale, we use kinetic theory to define the Reynolds number in terms of γ and M_0. Dynamic viscosity, based on a hard-sphere molecular model, is given by

$$\mu = \rho_0 k_1 \ell_0 \bar{v}, \tag{E1.26}$$

where the constant $k_1 = 5\pi/32$, and the mean molecular speed $\bar{v}$ is given by

$$\bar{v} = \sqrt{\frac{8RT_0}{\pi}} = \sqrt{\frac{8p_0}{\pi\rho_0}} = a_0\sqrt{\frac{8}{\pi\gamma}}. \tag{E1.27}$$

Substituting this result into the expression for the Reynolds number,

$$\mathrm{Re} = \frac{\rho_0 u_0 \ell_0}{\mu} = \frac{u_0}{a_0}\frac{1}{k_1}\sqrt{\frac{\pi\gamma}{8}} = \frac{\sqrt{\gamma M_0^2}}{k_2}, \tag{E1.28}$$

where

$$k_2 = \frac{5}{8}\sqrt{\frac{\pi}{2}}. \tag{E1.29}$$

Thus we have the nondimensional system of equations

$$\frac{\partial \hat{\rho}}{\partial \hat{t}} = -\frac{\partial}{\partial \hat{x}}\left(\hat{\rho}\hat{u}\right), \tag{E1.30}$$

$$\frac{\partial(\hat{\rho}\hat{u})}{\partial \hat{t}} = -\frac{\partial}{\partial \hat{x}}\left(\hat{\rho}\hat{u}^2 + \frac{\hat{p}}{\gamma M_0^2} - R'\frac{\partial \hat{u}}{\partial \hat{x}}\right), \tag{E1.31}$$

$$\frac{\partial}{\partial \hat{t}}\left(\frac{\hat{p}}{\gamma M_0^2} + \beta\hat{\rho}\hat{u}^2\right) = -\frac{\partial}{\partial \hat{x}}\left(\frac{\hat{p}\hat{u}}{M_0^2} + \beta\hat{\rho}\hat{u}^3 - R'(\gamma-1)\hat{u}\frac{\partial \hat{u}}{\partial \hat{x}} - \frac{R'}{M_0^2}\frac{\partial \hat{T}}{\partial \hat{x}}\right), \tag{E1.32}$$

where

$$R' = \frac{4}{3}\frac{k_2}{\sqrt{\gamma M_0^2}}, \tag{E1.33}$$

the system now defined entirely by the two parameters γ and M_0.

E.2 Nondimensional Form of the Euler Equations

The general compressible Euler equations, expressed in conservative form, are

$$\frac{\partial \rho}{\partial t} + \frac{\partial(\rho u_j)}{\partial x_j} = 0, \tag{E2.1}$$

$$\frac{\partial(\rho u_i)}{\partial t} + \frac{\partial(\rho u_i u_j)}{\partial x_j} + \frac{\partial p}{\partial x_i} = 0, \tag{E2.2}$$

$$\frac{\partial}{\partial t}\left(\rho e + \frac{1}{2}\rho u_k u_k\right) + \frac{\partial}{\partial x_j}\left(\rho e u_j + \frac{1}{2}\rho u_k u_k u_j\right) + \frac{\partial(p u_j)}{\partial x_j} = 0. \tag{E2.3}$$

In 2-D, these reduce to the continuity, x- and y-momentum and energy equations

$$\frac{\partial \rho}{\partial t} + \frac{\partial(\rho u)}{\partial x} + \frac{\partial(\rho v)}{\partial y} = 0, \tag{E2.4}$$

$$\frac{\partial(\rho u)}{\partial t} + \frac{\partial(\rho u^2)}{\partial x} + \frac{\partial(\rho u v)}{\partial y} + \frac{\partial p}{\partial x} = 0, \tag{E2.5}$$

$$\frac{\partial(\rho v)}{\partial t} + \frac{\partial(\rho u v)}{\partial x} + \frac{\partial(\rho v^2)}{\partial y} + \frac{\partial p}{\partial y} = 0, \tag{E2.6}$$

$$\begin{aligned}&\frac{\partial}{\partial t}\left(\rho e + \frac{1}{2}\rho(u^2+v^2)\right)\\ &+ \frac{\partial}{\partial x}\left(\rho u e + \frac{1}{2}\rho u(u^2+v^2) + pu\right) + \frac{\partial}{\partial y}\left(\rho v e + \frac{1}{2}\rho v(u^2+v^2) + pv\right) = 0.\end{aligned} \tag{E2.7}$$

Assuming a perfect gas, so $p = \rho RT$ and $e = C_v T$, the internal energy may be expressed in terms of pressure, simplifying the conserved energy term by

$$\rho e + \frac{1}{2}\rho(u^2 + v^2) = \frac{p}{\gamma - 1} + \frac{1}{2}\rho(u^2 + v^2). \tag{E2.8}$$

Nondimensionalizing the equations, we define reference far-field density, velocity and pressure values ρ_0, u_0 and p_0, to give dimensionless variables

$$\hat{\rho} = \frac{\rho}{\rho_0}, \quad \hat{u} = \frac{u}{u_0}, \quad \hat{p} = \frac{p}{p_0}.$$

The length scale is not important in this scaling of the Euler equations, so may be defined arbitrarily. Upon substitution of the dimensionless variables, as with the 1-D Navier-Stokes equations in Appendix E.1, the pressure terms are scaled by the parameter group

$$\frac{\rho_0 u_0^2}{p_0} = \gamma \frac{\rho_0}{\gamma p_0} u_0^2 = \gamma \frac{u_0^2}{a_0^2} = \gamma M_0^2, \tag{E2.9}$$

and the system may therefore be written in terms of the two parameters, γ and Mach number M_0. Thus we obtain the nondimensional equations

$$\frac{\partial \hat{\rho}}{\partial \hat{t}} + \frac{\partial}{\partial \hat{x}}\left(\hat{\rho}\hat{u}\right) + \frac{\partial}{\partial \hat{y}}\left(\hat{\rho}\hat{v}\right) = 0, \tag{E2.10}$$

$$\frac{\partial}{\partial \hat{t}}\left(\hat{\rho}\hat{u}\right) + \frac{\partial}{\partial \hat{x}}\left(\hat{\rho}\hat{u}^2 + \frac{\hat{p}}{\gamma M_0^2}\right) + \frac{\partial}{\partial \hat{y}}\left(\hat{\rho}\hat{u}\hat{v}\right) = 0, \tag{E2.11}$$

$$\frac{\partial}{\partial \hat{t}}\left(\hat{\rho}\hat{v}\right) + \frac{\partial}{\partial \hat{x}}\left(\hat{\rho}\hat{u}\hat{v}\right) + \frac{\partial}{\partial \hat{y}}\left(\hat{\rho}\hat{v}^2 + \frac{\hat{p}}{\gamma M_0^2}\right) = 0, \tag{E2.12}$$

$$\begin{aligned}\frac{\partial}{\partial \hat{t}}&\left(\frac{\hat{p}}{\gamma M_0^2} + \beta\hat{\rho}\left(\hat{u}^2 + \hat{v}^2\right)\right) \\ &+ \frac{\partial}{\partial \hat{x}}\left(\frac{\hat{p}\hat{u}}{M_0^2} + \beta\hat{\rho}\hat{u}\left(\hat{u}^2 + \hat{v}^2\right)\right) + \frac{\partial}{\partial \hat{y}}\left(\frac{\hat{p}\hat{v}}{M_0^2} + \beta\hat{\rho}\hat{v}\left(\hat{u}^2 + \hat{v}^2\right)\right) = 0,\end{aligned} \tag{E2.13}$$

where $\beta = (\gamma - 1)/2$.

To preserve numerical stability, we now write these equations in the skew-symmetric form suggested by Honein and Moin (2004). This replaces the convective terms in the general dimensional form of the momentum and energy equations with

$$\frac{\partial}{\partial x_j}\left(\rho u_i u_j\right) \mapsto \frac{1}{2}\frac{\partial}{\partial x_j}\left(\rho u_i u_j\right) + \frac{1}{2}\rho u_j \frac{\partial u_i}{\partial x_j} + \frac{1}{2}u_i \frac{\partial(\rho u_j)}{\partial x_j}, \tag{E2.14}$$

$$\frac{\partial}{\partial x_j}\left(\rho e u_j + \frac{1}{2}\rho u_k u_k u_j + p u_j\right) \mapsto \frac{1}{2}\frac{\partial(\rho e u_j)}{\partial x_j} + \frac{1}{2}\rho u_j \frac{\partial e}{\partial x_j} + \frac{1}{2} e \frac{\partial(\rho u_j)}{\partial x_j} + \frac{1}{2} u_k \frac{\partial(\rho u_j u_k)}{\partial x_j} + \frac{1}{2}\rho u_j u_k \frac{\partial u_k}{\partial x_j} + p\frac{\partial u_j}{\partial x_j} + u_j \frac{\partial p}{\partial x_j}. \tag{E2.15}$$

(from Hill et al., 2006). Applying the perfect gas assumption and the nondimensionalization, we obtain the full skew-symmetric form of the equations (the hats have been dropped from the variables in these nondimensional equations for simplicity):

$$\frac{\partial \rho}{\partial t} + \frac{\partial(\rho u)}{\partial x} + \frac{\partial(\rho v)}{\partial y} = 0, \tag{E2.16}$$

$$\frac{\partial(\rho u)}{\partial t} + \frac{1}{2}\left[\frac{\partial}{\partial x}\left(\rho u^2 + \frac{2p}{\gamma M_0^2}\right) + \frac{\partial(\rho u v)}{\partial y} + \rho u \frac{\partial u}{\partial x} + \rho v \frac{\partial u}{\partial y} + u\frac{\partial(\rho u)}{\partial x} + u\frac{\partial(\rho v)}{\partial y}\right] = 0, \tag{E2.17}$$

$$\frac{\partial(\rho v)}{\partial t} + \frac{1}{2}\left[\frac{\partial(\rho u v)}{\partial x} + \frac{\partial}{\partial y}\left(\rho v^2 + \frac{2p}{\gamma M_0^2}\right) + \rho u \frac{\partial v}{\partial x} + \rho v \frac{\partial v}{\partial y} + v\frac{\partial(\rho u)}{\partial x} + v\frac{\partial(\rho v)}{\partial y}\right] = 0, \tag{E2.18}$$

$$\begin{aligned}
&\frac{\partial}{\partial t}\left(\frac{p}{\gamma M_0^2} + \beta\rho(u^2+v^2)\right) \\
&+ \beta\left[u\frac{\partial(\rho u^2)}{\partial x} + u\frac{\partial(\rho u v)}{\partial y} + v\frac{\partial(\rho u v)}{\partial x} + v\frac{\partial(\rho v^2)}{\partial y} + \rho u^2\frac{\partial u}{\partial x} + \rho u v\frac{\partial u}{\partial y} + \rho u v\frac{\partial v}{\partial x} + \rho v^2\frac{\partial v}{\partial y}\right] \\
&+ \frac{1}{2\gamma M_0^2}\left[\frac{\partial(pu)}{\partial x} + \frac{\partial(pv)}{\partial y} + \rho u\frac{\partial}{\partial x}\left(\frac{p}{\rho}\right) + \rho v\frac{\partial}{\partial y}\left(\frac{p}{\rho}\right) + \frac{p}{\rho}\frac{\partial(\rho u)}{\partial x} + \frac{p}{\rho}\frac{\partial(\rho v)}{\partial y}\right] \\
&+ \frac{(\gamma-1)}{\gamma M_0^2}\left[p\frac{\partial u}{\partial x} + p\frac{\partial v}{\partial y} + u\frac{\partial p}{\partial x} + v\frac{\partial p}{\partial y}\right] = 0.
\end{aligned} \tag{E2.19}$$

E.3 The Linearized Navier-Stokes Equations

Starting once again with the Navier-Stokes equations for a general compressible fluid,

$$\frac{\partial \rho}{\partial t} + u_j\frac{\partial \rho}{\partial x_j} + \rho\frac{\partial u_j}{\partial x_j} = 0, \tag{E3.1}$$

$$\rho\frac{\partial u_i}{\partial t} + \rho u_j\frac{\partial u_i}{\partial x_j} = -\frac{\partial p}{\partial x_i} + \frac{\partial \tau_{ij}}{\partial x_j}, \tag{E3.2}$$

$$\rho\frac{\partial}{\partial t}\left(e + \frac{1}{2}u_k u_k\right) + \rho u_j\frac{\partial}{\partial x_j}\left(e + \frac{1}{2}u_k u_k\right) = -\frac{\partial(p u_j)}{\partial x_j} + \frac{\partial(u_k \tau_{kj})}{\partial x_j} - \frac{\partial q_j}{\partial x_j}, \tag{E3.3}$$

where for a Newtonian fluid with zero bulk viscosity the deviatoric stress tensor is given by

$$\tau_{ij} = \mu\left(\frac{\partial u_i}{\partial x_j} + \frac{\partial u_j}{\partial x_i} - \frac{2}{3}\frac{\partial u_k}{\partial x_k}\delta_{ij}\right), \tag{E3.4}$$

and with Fourier heat conduction,

$$q_i = -\kappa\frac{\partial T}{\partial x_i}. \tag{E3.5}$$

As in Section 4.3, we will assume constant μ and κ.

For the Richtmyer-Meshkov problem, we begin by reducing the general system to 2-D. Evaluating the stress tensor, for the case of constant viscosity, we have for the momentum equations

$$\frac{\partial \tau_{ij}}{\partial x_j} = \mu\begin{bmatrix} \frac{4}{3}\frac{\partial^2 u}{\partial x^2} + \frac{\partial^2 v}{\partial x \partial y} + \frac{\partial^2 u}{\partial y^2} \\ \frac{\partial^2 v}{\partial x^2} + \frac{\partial^2 u}{\partial x \partial y} + \frac{4}{3}\frac{\partial^2 v}{\partial y^2} \end{bmatrix},$$

and for the energy equation

$$\frac{\partial(u_k\tau_{kj})}{\partial x_j} = \mu\left[\frac{4}{3}\frac{\partial}{\partial x}\big(u\frac{\partial u}{\partial x}\big) + \frac{\partial}{\partial x}\big(v\frac{\partial v}{\partial x} + v\frac{\partial u}{\partial y}\big) + \frac{\partial}{\partial y}\big(u\frac{\partial v}{\partial x} + u\frac{\partial u}{\partial y}\big) + \frac{4}{3}\frac{\partial}{\partial y}\big(v\frac{\partial v}{\partial y}\big)\right].$$

Substituting these, and making the other simplifications, we have the system

$$\frac{\partial \rho}{\partial t} + \frac{\partial(\rho u)}{\partial x} + \frac{\partial(\rho v)}{\partial y} = 0, \tag{E3.6}$$

$$\frac{\partial(\rho u)}{\partial t} + \frac{\partial(\rho u^2)}{\partial x} + \frac{\partial(\rho uv)}{\partial y} = -\frac{\partial p}{\partial x} + \mu\left(\frac{4}{3}\frac{\partial^2 u}{\partial x^2} + \frac{\partial^2 v}{\partial x \partial y} + \frac{\partial^2 u}{\partial y^2}\right), \tag{E3.7}$$

$$\frac{\partial(\rho v)}{\partial t} + \frac{\partial(\rho uv)}{\partial x} + \frac{\partial(\rho v^2)}{\partial y} = -\frac{\partial p}{\partial y} + \mu\left(\frac{\partial^2 v}{\partial x^2} + \frac{\partial^2 u}{\partial x \partial y} + \frac{4}{3}\frac{\partial^2 v}{\partial y^2}\right), \tag{E3.8}$$

$$\begin{aligned} &\frac{\partial}{\partial t}\big(\rho e + \frac{1}{2}\rho(u^2+v^2)\big) + \frac{\partial}{\partial x}\big(\rho ue + \frac{1}{2}\rho u(u^2+v^2)\big) + \frac{\partial}{\partial y}\big(\rho ve + \frac{1}{2}\rho v(u^2+v^2)\big) \\ &\quad = -\frac{\partial(pu)}{\partial x} - \frac{\partial(pv)}{\partial y} + \kappa\big(\frac{\partial^2 T}{\partial x^2} + \frac{\partial^2 T}{\partial y^2}\big) \\ &\quad + \mu\left[\frac{4}{3}\frac{\partial}{\partial x}\big(u\frac{\partial u}{\partial x}\big) + \frac{\partial}{\partial x}\big(v\frac{\partial v}{\partial x} + v\frac{\partial u}{\partial y}\big) + \frac{\partial}{\partial y}\big(u\frac{\partial v}{\partial x} + u\frac{\partial u}{\partial y}\big) + \frac{4}{3}\frac{\partial}{\partial y}\big(v\frac{\partial v}{\partial y}\big)\right]. \end{aligned} \tag{E3.9}$$

We propose a form for the solution to this system that represents a small sinusoidal perturbation in the y-direction of a 1-D base flow in (x,t),

$$u = \bar{u}(x,t) + \epsilon u'(x,t)\mathrm{e}^{\mathrm{i}ky}, \tag{E3.10}$$

$$v = \bar{v}(x,t) + \epsilon v'(x,t)\mathrm{e}^{\mathrm{i}ky}, \tag{E3.11}$$

$$\rho = \bar{\rho}(x,t) + \epsilon\rho'(x,t)\mathrm{e}^{\mathrm{i}ky}, \tag{E3.12}$$

$$p = \bar{p}(x,t) + \epsilon p'(x,t)\mathrm{e}^{\mathrm{i}ky}. \tag{E3.13}$$

where we specify $\bar{v} = 0$ so the averaged flow is one-dimensional. Substituting the linear forms (E3.10)–(E3.13) into each equation, we find for continuity

$$\frac{\partial\rho}{\partial t} + \frac{\partial(\rho u)}{\partial x} + \frac{\partial(\rho v)}{\partial y} \mapsto \left[\frac{\partial\bar{\rho}}{\partial t} + \frac{\partial(\bar{\rho}\bar{u})}{\partial x}\right] + \epsilon\left[\frac{\partial\rho'}{\partial t} + \frac{\partial}{\partial x}\left(\bar{\rho}u' + \rho'\bar{u}\right) + \mathrm{i}k\bar{\rho}v'\right]\mathrm{e}^{\mathrm{i}ky} + O(\epsilon^2),$$

for x-momentum,

$$\begin{aligned}
&\frac{\partial(\rho u)}{\partial t} + \frac{\partial}{\partial x}\left(p + \rho u^2\right) + \frac{\partial(\rho uv)}{\partial y} - \mu\left(\frac{4}{3}\frac{\partial^2 u}{\partial x^2} + \frac{\partial^2 v}{\partial x\partial y} + \frac{\partial^2 u}{\partial y^2}\right)\\
&\quad\mapsto \left[\frac{\partial(\bar{\rho}\bar{u})}{\partial t} + \frac{\partial}{\partial x}\left(\bar{p} + \bar{\rho}\bar{u}^2\right) - \frac{4}{3}\mu\frac{\partial^2\bar{u}}{\partial x^2}\right] + \epsilon\left[\frac{\partial}{\partial t}\left(\bar{\rho}u' + rho'\bar{u}\right) + \mathrm{i}k\bar{\rho}\bar{u}v'\right.\\
&\qquad\qquad \left. + \frac{\partial}{\partial x}\left(p' + 2\bar{\rho}\bar{u}u' + \rho'\bar{u}^2\right) - \mu\left(\frac{4}{3}\frac{\partial^2 u'}{\partial x^2} + \mathrm{i}k\frac{\partial v'}{\partial x} - k^2u'\right)\right]\mathrm{e}^{\mathrm{i}ky} + O(\epsilon^2),
\end{aligned}$$

for y-momentum,

$$\begin{aligned}
&\frac{\partial(\rho v)}{\partial t} + \frac{\partial(\rho uv)}{\partial x} + \frac{\partial}{\partial y}\left(p + \rho v^2\right) - \mu\left(\frac{\partial^2 v}{\partial x^2} + \frac{\partial^2 u}{\partial x\partial y} + \frac{4}{3}\frac{\partial^2 v}{\partial y^2}\right)\\
&\qquad\mapsto \epsilon\left[\frac{\partial}{\partial t}\left(\bar{\rho}v'\right) + \frac{\partial}{\partial x}\left(\bar{\rho}\bar{u}v'\right) + \mathrm{i}kp' - \mu\left(\frac{\partial^2 v'}{\partial x^2} + \mathrm{i}k\frac{\partial u'}{\partial x} - \frac{4}{3}k^2v'\right)\right]\mathrm{e}^{\mathrm{i}ky} + O(\epsilon^2),
\end{aligned}$$

and energy, first for the convective terms,

$$\begin{aligned}
&\frac{\partial}{\partial t}\left(\rho e + \frac{1}{2}\rho(u^2+v^2)\right) + \frac{\partial}{\partial x}\left(\rho ue + \frac{1}{2}\rho u(u^2+v^2) + pu\right) + \frac{\partial}{\partial y}\left(\rho ve + \frac{1}{2}\rho v(u^2+v^2) + pv\right)\\
&\quad\mapsto \left[\frac{\partial}{\partial t}\left(\bar{\rho}\bar{e} + \frac{1}{2}\bar{\rho}\bar{u}^2\right) + \frac{\partial}{\partial x}\left(\bar{\rho}\bar{u}\bar{e} + \frac{1}{2}\bar{\rho}\bar{u}^3 + \bar{p}\bar{u}\right)\right]\\
&\qquad + \epsilon\left[\frac{\partial}{\partial t}\left(\bar{\rho}e' + \rho'\bar{e} + \bar{\rho}\bar{u}u' + \frac{1}{2}\rho'\bar{u}^2\right) + \mathrm{i}k\left(\bar{\rho}\bar{e}v' + \frac{1}{2}\bar{\rho}\bar{u}^2v' + \bar{p}v'\right)\right.\\
&\qquad\quad \left. + \frac{\partial}{\partial x}\left(\bar{\rho}\bar{u}e' + \bar{\rho}u'\bar{e} + \rho'\bar{u}\bar{e} + \frac{3}{2}\bar{\rho}\bar{u}^2u' + \frac{1}{2}\rho'\bar{u}^3 + \bar{p}u' + p'\bar{u}\right)\right]\mathrm{e}^{\mathrm{i}ky} + O(\epsilon^2),
\end{aligned}$$

for the heat conduction terms,

$$\kappa\left(\frac{\partial^2 T}{\partial x^2} + \frac{\partial^2 T}{\partial y^2}\right) \mapsto \left[\kappa\frac{\partial^2\bar{T}}{\partial x^2}\right] + \epsilon\left[\kappa\left(\frac{\partial^2 T'}{\partial x^2} - k^2T'\right)\right]\mathrm{e}^{\mathrm{i}ky} + O(\epsilon^2),$$

and finally for the dissipative terms

$$\frac{4}{3}\frac{\partial}{\partial x}\big(u\frac{\partial u}{\partial x}\big)+\frac{\partial}{\partial x}\big(v\frac{\partial v}{\partial x}+v\frac{\partial u}{\partial y}\big)+\frac{\partial}{\partial y}\big(u\frac{\partial v}{\partial x}+u\frac{\partial u}{\partial y}\big)+\frac{4}{3}\frac{\partial}{\partial y}\big(v\frac{\partial v}{\partial y}\big)$$
$$\mapsto\left[\frac{4}{3}\frac{\partial}{\partial x}\left(\bar{u}\frac{\partial\bar{u}}{\partial x}\right)\right]+\epsilon\left[\frac{4}{3}\frac{\partial}{\partial x}\left(\bar{u}\frac{\partial u'}{\partial x}+u'\frac{\partial\bar{u}}{\partial x}\right)+\mathrm{i}k\bar{u}\frac{\partial v'}{\partial x}-k^2\bar{u}u'\right]\mathrm{e}^{\mathrm{i}ky}+O(\epsilon^2).$$

Putting the pieces together, we recover from the order ϵ^0 terms the familiar 1-D Navier-Stokes equations for the base flow:

$$\frac{\partial\bar{\rho}}{\partial t}+\frac{\partial(\bar{\rho}\bar{u})}{\partial x}=0, \tag{E3.14}$$
$$\frac{\partial(\bar{\rho}\bar{u})}{\partial t}+\frac{\partial}{\partial x}\left(\bar{\rho}\bar{u}^2+\bar{p}-\frac{4}{3}\bar{\mu}\frac{\partial\bar{u}}{\partial x}\right)=0, \tag{E3.15}$$
$$\frac{\partial}{\partial t}\big(\bar{\rho}\bar{e}+\frac{1}{2}\bar{\rho}\bar{u}^2\big)+\frac{\partial}{\partial x}\left(\bar{\rho}\bar{u}\bar{e}+\frac{1}{2}\bar{\rho}\bar{u}^3+\bar{p}\bar{u}-\kappa\frac{\partial\bar{T}}{\partial x}-\frac{4}{3}\mu\bar{u}\frac{\partial\bar{u}}{\partial x}\right)=0. \tag{E3.16}$$

From the order ϵ terms, we obtain

$$\frac{\partial\rho'}{\partial t}+\frac{\partial}{\partial x}\left(\rho'\bar{u}+\bar{\rho}u'\right)+\mathrm{i}k\bar{\rho}v'=0, \tag{E3.17}$$
$$\frac{\partial}{\partial t}\left(\bar{\rho}u'+\rho'\bar{u}\right)+\frac{\partial}{\partial x}\left(p'+\rho'\bar{u}^2+2\bar{\rho}\bar{u}u'\right)+\mathrm{i}k\bar{\rho}\bar{u}v'$$
$$=\mu\left(\frac{4}{3}\frac{\partial^2u'}{\partial x^2}+\mathrm{i}k\frac{\partial v'}{\partial x}-k^2u'\right), \tag{E3.18}$$
$$\frac{\partial}{\partial t}\left(\bar{\rho}v'\right)+\frac{\partial}{\partial x}\left(\bar{\rho}\bar{u}v'\right)+\mathrm{i}kp'=\mu\left(\frac{\partial^2v'}{\partial x^2}+\mathrm{i}k\frac{\partial u'}{\partial x}-\frac{4}{3}k^2v'\right), \tag{E3.19}$$
$$\frac{\partial}{\partial t}\left(\bar{\rho}e'+\rho'\bar{e}+\bar{\rho}\bar{u}u'+\frac{1}{2}\rho'\bar{u}^2\right)+\frac{\partial}{\partial x}\left(\bar{\rho}\bar{u}e'+\bar{\rho}u'\bar{e}+\rho'\bar{u}\bar{e}+\frac{3}{2}\bar{\rho}\bar{u}^2u'+\frac{1}{2}\rho'\bar{u}^3\right)$$
$$+\frac{\partial}{\partial x}\big(\bar{p}u'+p'\bar{u}\big)+\mathrm{i}k\left(\bar{\rho}\bar{e}v'+\frac{1}{2}\bar{\rho}\bar{u}^2v'+\bar{p}v'\right)=\kappa\left(\frac{\partial^2T'}{\partial x^2}-k^2T'\right)$$
$$+\mu\left[\frac{4}{3}\frac{\partial}{\partial x}\left(\bar{u}\frac{\partial u'}{\partial x}+u'\frac{\partial\bar{u}}{\partial x}\right)+\mathrm{i}k\bar{u}\frac{\partial v'}{\partial x}-k^2\bar{u}u'\right]. \tag{E3.20}$$

To make further progress, we specify a perfect gas, where

$$e=C_VT=\frac{1}{\gamma-1}\frac{p}{\rho}. \tag{E3.21}$$

This allows e to be eliminated from the energy equation, simplifying the convective term to

$$\begin{aligned}
&\frac{\partial}{\partial t}\left(p+\beta\rho(u^2+v^2)\right)+\frac{\partial}{\partial x}\left(\gamma pu+\beta\rho u(u^2+v^2)\right)+\frac{\partial}{\partial y}\left(\gamma pv+\beta\rho v(u^2+v^2)\right)\\
&\quad\mapsto\left[\frac{\partial}{\partial t}\left(\bar{p}+\beta\bar{\rho}\bar{u}^2\right)+\frac{\partial}{\partial x}\left(\gamma\bar{p}\bar{u}+\beta\bar{\rho}\bar{u}^3\right)\right]+\epsilon\left[\frac{\partial}{\partial t}\left(p'+2\beta\bar{\rho}\bar{u}u'+\beta\rho'\bar{u}^2\right)\right.\\
&\qquad\left.+\frac{\partial}{\partial x}\left(\gamma(\bar{p}u'+p'\bar{u})+3\beta\bar{\rho}\bar{u}^2u'+\beta\rho'\bar{u}^3\right)+\mathrm{i}k\left(\gamma\bar{p}v'+\beta\bar{\rho}\bar{u}^2v'\right)\right]\mathrm{e}^{\mathrm{i}ky}+O(\epsilon^2),
\end{aligned}$$

where $\beta=(\gamma-1)/2$. Nondimensionalization of the equations follows Appendix E.1, using reference parameters ρ_0, p_0 and U_I and the mean free path ℓ_0 for the length scale. For the Richtmyer-Meshkov problem, these correspond to state 0 and the incident shock speed, so the resulting Mach number is therefore that of the incident shock, M_I. Since the Navier-Stokes shock solution from Appendix F.1 is used, for consistency we define $\mathrm{Pr}=3/4$ and the Reynolds number from kinetic theory

$$\mathrm{Re}=\frac{\sqrt{\gamma M_\mathrm{I}^2}}{k_2},\quad\text{where}\quad k_2=\frac{5}{8}\sqrt{\frac{\pi}{2}}. \tag{E3.22}$$

We write the nondimensional equations using the same variables as before to avoid a proliferation of symbols, noting from the context that the variables are now in dimensionless form. For the base flow, we have

$$\frac{\partial\bar{\rho}}{\partial t}+\frac{\partial(\bar{\rho}\bar{u})}{\partial x}=0, \tag{E3.23}$$

$$\frac{\partial(\bar{\rho}\bar{u})}{\partial t}+\frac{\partial}{\partial x}\left(\frac{\bar{p}}{\gamma M_\mathrm{I}^2}+\bar{\rho}\bar{u}^2\right)=\frac{4}{3}\frac{1}{\mathrm{Re}}\frac{\partial^2\bar{u}}{\partial x^2}, \tag{E3.24}$$

$$\frac{\partial}{\partial t}\left(\frac{\bar{p}}{\gamma M_\mathrm{I}^2}+\beta\bar{\rho}\bar{u}^2\right)+\frac{\partial}{\partial x}\left(\frac{\bar{p}\bar{u}}{M_\mathrm{I}^2}+\beta\bar{\rho}\bar{u}^3\right)=\frac{1}{\mathrm{PrRe}M_\mathrm{I}^2}\frac{\partial^2\bar{T}}{\partial x^2}+\frac{4}{3}\frac{\gamma-1}{\mathrm{Re}}\frac{\partial}{\partial x}\left(\bar{u}\frac{\partial\bar{u}}{\partial x}\right), \tag{E3.25}$$

and for the first-order perturbation equations,

$$\frac{\partial\rho'}{\partial t}+\frac{\partial}{\partial x}\left(\bar{\rho}u'+\rho'\bar{u}\right)+\mathrm{i}k\bar{\rho}v'=0, \tag{E3.26}$$

$$\begin{aligned}
&\frac{\partial}{\partial t}\left(\bar{\rho}u'+\rho'\bar{u}\right)+\frac{\partial}{\partial x}\left(\frac{p'}{\gamma M_\mathrm{I}^2}+\rho'\bar{u}^2+2\bar{\rho}\bar{u}u'\right)+\mathrm{i}k\bar{\rho}\bar{u}v'\\
&\qquad=\frac{1}{\mathrm{Re}}\left(\frac{4}{3}\frac{\partial^2u'}{\partial x^2}+\mathrm{i}k\frac{\partial v'}{\partial x}-k^2u'\right),
\end{aligned} \tag{E3.27}$$

$$\frac{\partial}{\partial t}\left(\bar{\rho}v'\right)+\frac{\partial}{\partial x}\left(\bar{\rho}\bar{u}v'\right)+\mathrm{i}k\frac{p'}{\gamma M_\mathrm{I}^2}=\frac{1}{\mathrm{Re}}\left(\frac{\partial^2v'}{\partial x^2}+\mathrm{i}k\frac{\partial u'}{\partial x}-\frac{4}{3}k^2v'\right), \tag{E3.28}$$

$$\frac{\partial}{\partial t}\left(\frac{p'}{\gamma M_{\mathrm{I}}^2}+\beta\left(\rho'\bar{u}^2+2\bar{\rho}\bar{u}u'\right)\right)$$
$$+\frac{\partial}{\partial x}\left(\frac{p'\bar{u}+\bar{p}u'}{M_{\mathrm{I}}^2}+\beta\left(\rho'\bar{u}^3+3\bar{\rho}\bar{u}^2u'\right)\right)+\mathrm{i}k\left(\frac{\bar{p}v'}{M_{\mathrm{I}}^2}+\beta\bar{\rho}\bar{u}^2v'\right)$$
$$=\frac{1}{\mathrm{PrRe}M_{\mathrm{I}}^2}\left(\frac{\partial^2T'}{\partial x^2}-k^2T'\right)+\frac{\gamma-1}{\mathrm{Re}}\left[\frac{4}{3}\frac{\partial}{\partial x}\left(\bar{u}\frac{\partial u'}{\partial x}+u'\frac{\partial\bar{u}}{\partial x}\right)+\mathrm{i}k\bar{u}\frac{\partial v'}{\partial x}-k^2\bar{u}u'\right]. \tag{E3.29}$$

Finally, note that to evaluate the (nondimensional) temperature variables $\bar{T}$ and T', we refer to the Taylor expansion

$$T(p,\rho)=\frac{p}{\rho}=\frac{\bar{p}}{\bar{\rho}}+\epsilon\frac{p'}{\bar{\rho}}-\epsilon\frac{\bar{p}\rho'}{\bar{\rho}^2}+O(\epsilon^2), \tag{E3.30}$$

thus clearly

$$\bar{T}=\frac{\bar{p}}{\bar{\rho}},\quad T'=\bar{T}\left(\frac{p'}{\bar{p}}-\frac{\rho'}{\bar{\rho}}\right).$$

E.4 Characteristic Form

For compressible flows, boundary conditions for the Navier-Stokes equations are usually implemented in characteristic form. This is to ensure that the problem is well posed, so information is specified only on those characteristics that point into the computational domain. For the types of problems considered in this work, the flow is typically smooth near the boundary with minimal contribution from the viscous terms, so the characteristic analysis may be performed on the Euler equations. We begin with the 1-D equations in nondimensional form from equations (E1.30)–(E1.32), and consider the first-order perturbation equations (E3.26)–(E3.29) separately.

E.4.1 Characteristic Form of the 1-D Equations

Starting with equations (E1.30)–(E1.32), we discard the viscous terms and write the system in the form

$$\frac{\partial U}{\partial t}+\frac{\partial F(U)}{\partial x}=0, \tag{E4.1}$$

in terms of the conserved variable vector and flux vector given by

$$U = \begin{bmatrix} \rho \\ \rho u \\ \frac{\gamma-1}{2}\rho u^2 + \frac{p}{\gamma M_0^2} \end{bmatrix}, \quad \text{and} \quad F(U) = \begin{bmatrix} \rho u \\ \rho u^2 + \frac{p}{\gamma M_0^2} \\ \frac{\gamma-1}{2}\rho u^3 + \frac{pu}{M_0^2} \end{bmatrix}.$$

By the chain rule,

$$\frac{\partial F}{\partial x} = \frac{\partial F}{\partial U}\frac{\partial U}{\partial x} = A\frac{\partial U}{\partial x},$$

which gives the linearized equation

$$\frac{\partial U}{\partial t} + A\frac{\partial U}{\partial x} = 0. \tag{E4.2}$$

This equation is transformed to the primitive variable vector $V = [\rho, u, p]^T$ by defining

$$M = \frac{\partial U}{\partial V}, \tag{E4.3}$$

to give the primitive equation

$$\frac{\partial V}{\partial t} + \tilde{A}\frac{\partial V}{\partial x} = 0, \tag{E4.4}$$

where

$$\tilde{A} = M^{-1}AM = \begin{bmatrix} u & \rho & 0 \\ 0 & u & \frac{1}{\gamma M_0^2 \rho} \\ 0 & \gamma p & u \end{bmatrix}.$$

To obtain the final characteristic form of the equations, we diagonalize the matrix $\tilde{A} = \tilde{R}\Lambda\tilde{R}^{-1}$, where Λ is the matrix of characteristic speeds

$$\Lambda = \begin{bmatrix} u & 0 & 0 \\ 0 & u - \frac{a}{M_0} & 0 \\ 0 & 0 & u + \frac{a}{M_0} \end{bmatrix}, \tag{E4.5}$$

in terms of the nondimensional speed of sound defined by $a \equiv \sqrt{p/\rho}$, such that

$$\frac{\partial C}{\partial t} + \Lambda\frac{\partial C}{\partial x} = 0. \tag{E4.6}$$

The characteristic variables are defined by the transformation $\mathrm{d}C = \tilde{R}^{-1}\mathrm{d}V$, so we choose a particular scaling of the eigenvector matrices such that

$$\tilde{R} = \begin{bmatrix} -\frac{\rho^\gamma}{\gamma a^2} & -\frac{\rho}{2a^*} & \frac{\rho}{2a^*} \\ 0 & \frac{1}{2} & \frac{1}{2} \\ 0 & -\frac{1}{2}a\gamma\rho & \frac{1}{2}a\gamma\rho \end{bmatrix}, \quad \text{and} \quad \tilde{R}^{-1} = \begin{bmatrix} -\gamma a^2\rho^{-\gamma} & 0 & \rho^{-\gamma} \\ 0 & 1 & -\frac{1}{a\gamma M_0\rho} \\ 0 & 1 & \frac{1}{a\gamma M_0\rho} \end{bmatrix},$$

where the scaled sound speed is $a^* = a/M_0$, to give

$$\mathrm{d}C = \begin{bmatrix} -\gamma a^2\rho^{-\gamma}\mathrm{d}\rho + \rho^{-\gamma}\mathrm{d}p \\ \mathrm{d}u - \frac{1}{a\gamma M_0\rho}\mathrm{d}p \\ \mathrm{d}u + \frac{1}{a\gamma M_0\rho}\mathrm{d}p \end{bmatrix}. \tag{E4.7}$$

The first characteristic variable may be obtained directly by integration; thus $p\rho^{-\gamma} = \text{const}$ on the characteristics $\mathrm{d}x/\mathrm{d}t = u$. To make further progress, we must assume that $p\rho^{-\gamma}$ is constant *everywhere* (i.e., the flow is isentropic), in which case the characteristic variable vector

$$C = \begin{bmatrix} p\rho^{-\gamma} \\ u - \frac{2}{\gamma-1}a^* \\ u + \frac{2}{\gamma-1}a^* \end{bmatrix}, \tag{E4.8}$$

is obtained. Note that differentiating C gives $\mathrm{d}C$ as defined in equation (E4.7) directly. Also, a similar result may be obtained by direct diagonalization of the matrix A, such that $A = R\Lambda R^{-1}$, but it is far more convenient to work in terms of the primitive variables, as above, and obtain $R = M\tilde{R}$. For Chapter 4, the results shown apply to the 1-D base-flow equations, where all variables are the base flow quantities.

E.4.2 Characteristic Form of the 2-D Linearized Equations

Starting with the first-order perturbation equations (E3.26)–(E3.29), we again discard the viscous terms and write the system in the form

$$\frac{\partial U'}{\partial t} + \frac{\partial F(U')}{\partial x} = 0, \tag{E4.9}$$

where the conserved vector and flux vector are given by

$$U' = \begin{bmatrix} \rho' \\ \bar{\rho}u' + \rho'\bar{u} \\ \bar{\rho}v' \\ \frac{p'}{\gamma M_0^2} + \frac{\gamma-1}{2}\left(\rho'\bar{u}^2 + 2\bar{\rho}\bar{u}u'\right) \end{bmatrix}, \text{ and } F(U') = \begin{bmatrix} \bar{\rho}u' + \rho'\bar{u} \\ \frac{p'}{\gamma M_0^2} + \rho'\bar{u}^2 + 2\bar{\rho}\bar{u}u' \\ \bar{\rho}\bar{u}v' \\ \frac{\bar{p}u' + p'\bar{u}}{M_0^2} + \frac{\gamma-1}{2}\left(\rho'\bar{u}^3 + 3\bar{\rho}\bar{u}^2u'\right) \end{bmatrix}.$$

Note that the reference Mach number M_0 is the incident shock Mach number in the Richtmyer-Meshkov problem. The corresponding primitive vector is

$$V' = \left[\rho', u', v', p'\right]^T. \tag{E4.10}$$

Note that this system, unlike that of the 1-D equations, is linear in the primitive variables.

Performing the diagonalization as in the previous section, we find the matrix of characteristic speeds

$$\Lambda' = \begin{bmatrix} \bar{u} & 0 & 0 & 0 \\ 0 & \bar{u} & 0 & 0 \\ 0 & 0 & \bar{u} - \bar{a}^* & 0 \\ 0 & 0 & 0 & \bar{u} + \bar{a}^* \end{bmatrix}, \tag{E4.11}$$

where $\bar{a} = \sqrt{\bar{p}/\bar{\rho}}$ and $\bar{a}^* = \bar{a}/M_0$, and the characteristic vector differential

$$\mathrm{d}C' = \begin{bmatrix} -\gamma\bar{a}^2\bar{\rho}^{-\gamma}\mathrm{d}v' \\ -\gamma\bar{a}^2\bar{\rho}^{-\gamma}\mathrm{d}\rho' + \bar{\rho}^{-\gamma}\mathrm{d}p' \\ \mathrm{d}u' - \frac{1}{\bar{a}^*\gamma M_0^2\bar{\rho}}\mathrm{d}p' \\ \mathrm{d}u' + \frac{1}{\bar{a}^*\gamma M_0^2\bar{\rho}}\mathrm{d}p' \end{bmatrix}. \tag{E4.12}$$

Integration in this case is straightforward, because each differential is linear in terms of the perturbed quantity, giving

$$C' = \begin{bmatrix} -\gamma\bar{a}^2\bar{\rho}^{-\gamma}v' \\ \bar{\rho}^{-\gamma}(p' - \gamma\bar{a}^2\rho') \\ u' - \frac{p'}{\gamma M_0^2}\frac{1}{\bar{\rho}\bar{a}^*} \\ u' + \frac{p'}{\gamma M_0^2}\frac{1}{\bar{\rho}\bar{a}^*} \end{bmatrix}, \tag{E4.13}$$

where each is constant on its respective characteristic.

E.5 Implementation of Boundary Conditions

Implementation of characteristic boundary conditions for linear systems of equations by the simultaneous approximation term (SAT) method is straightforward, and demonstrated in the original paper by Carpenter et al. (1994). For the nonlinear Navier-Stokes equations, however, care must be taken to properly formulate the boundary terms. The recent work by Svärd et al. (2007) provides a formulation of the far-field Navier-Stokes boundary conditions using the SAT method, and demonstrates stability under certain (quite strict) assumptions. It is not necessary to delve into the details of this proof here, but the following 1-D formulation, used for both the Navier-Stokes shock in Section 2.6.2 and the Richtmyer-Meshkov problem in Chapter 4, appears to be consistent with this proof and was found to be stable in practice.

E.5.1 SAT Boundary Terms

Following Appendix E.4, we may write for the characteristic form of the 1-D Navier-Stokes equations (E1.30)–(E1.32), excluding the viscous terms,

$$\frac{\partial C}{\partial t} + \Lambda \frac{\partial C}{\partial x} = 0. \tag{E5.1}$$

To define boundary conditions for this equation, we consider only the components that point into the domain and so split $\Lambda = \Lambda^+ + \Lambda^-$ into positive and negative eigenvalues at each boundary. The boundary conditions are then,

$$\text{at } x = L, \quad \alpha(\Lambda^+ + \Lambda'_L)C = g_L(t), \tag{E5.2}$$

$$\text{at } x = R, \quad \alpha(\Lambda^- + \Lambda'_R)C = g_R(t), \tag{E5.3}$$

where the additional matrices Λ'_L and Λ'_R are zero except for the case of a subsonic outflow, in which case $(\Lambda'_L)_{3,2} = -(u+a^*)$ (if at the left-hand boundary) and $(\Lambda'_R)_{2,3} = -(u-a^*)$ (at the right-hand boundary). Implementing these by the SAT method, we have the following semidiscrete approximation to equation (E5.1):

$$\frac{\mathrm{d}\mathbf{C}}{\mathrm{d}t} = -D\Lambda\mathbf{C} + \mathbf{s}_L\tau\Big[(\Lambda^+ + \Lambda'_L)(\mathbf{C}_L - \mathbf{g}_L)\Big] + \mathbf{s}_R\tau\Big[(\Lambda^- + \Lambda'_R)(\mathbf{C}_R - \mathbf{g}_R)\Big], \tag{E5.4}$$

where D is the usual finite-difference approximation of the first derivative, τ is the SAT parameter, and

$$\mathbf{s}_L = P^{-1}[q_{11}, 0, \ldots, 0]^T, \tag{E5.5}$$

$$\mathbf{s}_R = P^{-1}[0, \ldots, 0, q_{NN}]^T. \tag{E5.6}$$

Multiplying this equation by R and transforming from $\mathbf{C}$ back to the conserved vector $\mathbf{U}$ except for the boundary terms, we obtain

$$\frac{\mathrm{d}\mathbf{U}}{\mathrm{d}t} = -DA\mathbf{U} + \mathbf{s}_L \tau B_L(\mathbf{C}_L - \mathbf{g}_L) + \mathbf{s}_R \tau B_R(\mathbf{C}_R - \mathbf{g}_R). \tag{E5.7}$$

We thus define the boundary matrices $B_L = R(\Lambda^+ + \Lambda'_L)$ and $B_R = R(\Lambda^- + \Lambda'_R)$, whose structure depends on the signs of the characteristic speeds at each boundary. Note that for stability, we still require $\tau > 1$ (Svärd et al., 2007).

Finally, the viscous terms may be reintroduced. Defining a splitting of the flux vector $F = F^I + F^V = AU + F^V$, for

$$F^V = -\left[0,\ \frac{1}{\mathrm{Re}}\frac{\partial^2 u}{\partial x^2},\ \frac{\gamma - 1}{\mathrm{Re}}\frac{\partial}{\partial x}\left(u\frac{\partial u}{\partial x}\right) + \frac{1}{\mathrm{RePr}M_0^2}\frac{\partial^2 T}{\partial x^2}\right]^T, \tag{E5.8}$$

we have for the semidiscrete form of the 1-D Navier-Stokes equations,

$$\frac{\mathrm{d}\mathbf{U}}{\mathrm{d}t} = -D\mathbf{F} + \mathbf{s}_L \tau B_L(\mathbf{C}_L - \mathbf{g}_L) + \mathbf{s}_R \tau B_R(\mathbf{C}_R - \mathbf{g}_R) - 2\mathbf{s}_L(\mathbf{F}_L^V - \mathbf{g}_L^V) - 2\mathbf{s}_R(\mathbf{F}_R^V - \mathbf{g}_R^V). \tag{E5.9}$$

The factor of -2 in front of the viscous boundary terms is required for stability (Svärd et al., 2007). For the 2-D first-order perturbation equations, a very similar result is obtained:

$$\frac{\mathrm{d}\mathbf{U}'}{\mathrm{d}t} = -D\mathbf{F}' + \mathbf{s}_L \tau B'_L(\mathbf{C}'_L - \mathbf{g}'_L) + \mathbf{s}_R \tau B'_R(\mathbf{C}'_R - \mathbf{g}'_R) - 2\mathbf{s}_L(\mathbf{F}'^V_L - \mathbf{g}'^V_L) - 2\mathbf{s}_R(\mathbf{F}'^V_R - \mathbf{g}'^V_R). \tag{E5.10}$$

In each case, the flow conditions at the boundary (supersonic/subsonic, inlet/outlet) determine which of the boundary terms are implemented. For the 1-D Navier-Stokes equations, a total of five boundary conditions are required for a well-posed problem, while seven are

required for the 2-D first-order perturbation equations.

E.5.2 Boundary Matrices for the 1-D Equations

At a supersonic inlet, $u - a^* > 0$, so all three characteristics point into the domain. Thus three independent boundary conditions are specified and no viscous boundary condition is required. The matrix B_L for this case is given by

$$B_L = \begin{bmatrix} -\frac{\rho^\gamma u}{\gamma a^2} & -\frac{\rho}{2a^*}(u-a^*) & \frac{\rho}{2a^*}(u+a^*) \\ -\frac{\rho^\gamma u^2}{\gamma a^2} & -\frac{\rho}{2a^*}(u-a^*)^2 & \frac{\rho}{2a^*}(u+a^*)^2 \\ -\beta\frac{\rho^\gamma u^3}{\gamma a^2} & -\frac{\rho}{2a^*}(u-a^*)\big(a^{*2}+\beta u(u-2a^*)\big) & \frac{\rho}{2a^*}(u+a^*)\big(a^{*2}+\beta u(u+2a^*)\big) \end{bmatrix}.$$

For a subsonic inlet, $u > 0$ but $u - a^* < 0$, so two characteristics point into the domain. This gives for B_L

$$B_L = \begin{bmatrix} -\frac{\rho^\gamma u}{\gamma a^2} & 0 & \frac{\rho}{2a^*}(u+a^*) \\ -\frac{\rho^\gamma u^2}{\gamma a^2} & 0 & \frac{\rho}{2a^*}(u+a^*)^2 \\ -\beta\frac{\rho^\gamma u^3}{\gamma a^2} & 0 & \frac{\rho}{2a^*}(u+a^*)\big(a^{*2}+\beta u(u+2a^*)\big) \end{bmatrix}.$$

An additional boundary condition for this case is provided by imposing $\partial T/\partial x = 0$. For a subsonic outlet with $u < 0$, two characteristics point into the domain, for

$$B_R = \begin{bmatrix} -\frac{\rho^\gamma}{\gamma a^2}u & -\frac{\rho}{a^*}(u-a^*) & 0 \\ -\frac{\rho^\gamma}{\gamma a^2}u^2 & -\frac{\rho}{a^*}u(u-a^*) & 0 \\ -\frac{\rho^\gamma}{\gamma a^2}\beta u^3 & -\frac{\rho}{a^*}(u-a^*)(a^{*2}+\beta u^2) & 0 \end{bmatrix}.$$

These two conditions are sufficient for an outlet boundary. For a subsonic outlet with $u > 0$, the first column of B_R is zero, and the final boundary condition is given by imposing $\partial u/\partial x = 0$. For all these results, as elsewhere, $\beta = (\gamma - 1)/2$ and $a^* = a/M_0$, where M_0 is the reference Mach number. For the base flow of the Richtmyer-Meshkov problem in Chapter 4, all quantities in these matrices have an overbar and $M_0 \to M_\mathrm{I}$.

E.5.3 Boundary Matrices for the 2-D Linearized Equations

The characteristics for the first-order perturbation equations are functions of the base flow, so the boundary coefficient matrices follow a very similar form. For a supersonic inlet, all

four characteristics point into the domain, giving

$$B'_L = \begin{bmatrix} 0 & -\frac{\bar{\rho}^\gamma \bar{u}}{\gamma \bar{a}^2} & -\frac{\bar{\rho}}{2\bar{a}^*}(\bar{u}-\bar{a}^*) & \frac{\bar{\rho}}{2\bar{a}^*}(\bar{u}+\bar{a}^*) \\ 0 & -\frac{\bar{\rho}^\gamma \bar{u}^2}{\gamma \bar{a}^2} & -\frac{\bar{\rho}}{2\bar{a}^*}(\bar{u}-\bar{a}^*)^2 & \frac{\bar{\rho}}{2\bar{a}^*}(\bar{u}+\bar{a}^*)^2 \\ -\frac{\bar{\rho}^{\gamma+1}\bar{u}}{\gamma \bar{a}^2} & 0 & 0 & 0 \\ 0 & -\frac{\beta \bar{\rho}^\gamma \bar{u}^3}{\gamma \bar{a}^2} & -\frac{\bar{\rho}(\bar{u}-\bar{a}^*)}{2\bar{a}^*}\left(\bar{a}^{*2}+\beta\bar{u}(\bar{u}-2\bar{a}^*)\right) & \frac{\bar{\rho}(\bar{u}+\bar{a}^*)}{2\bar{a}^*}\left(\bar{a}^{*2}+\beta\bar{u}(\bar{u}+2\bar{a}^*)\right) \end{bmatrix}.$$

For a subsonic inlet, $\bar{u}-\bar{a}^* < 0$, so boundary conditions on three characteristics are specified:

$$B'_L = \begin{bmatrix} 0 & -\frac{\bar{\rho}^\gamma \bar{u}}{\gamma \bar{a}^2} & 0 & \frac{\bar{\rho}}{2\bar{a}^*}(\bar{u}+\bar{a}^*) \\ 0 & -\frac{\bar{\rho}^\gamma \bar{u}^2}{\gamma \bar{a}^2} & 0 & \frac{\bar{\rho}}{2\bar{a}^*}(\bar{u}+\bar{a}^*)^2 \\ -\frac{\bar{\rho}^{\gamma+1}\bar{u}}{\gamma \bar{a}^2} & 0 & 0 & 0 \\ 0 & -\frac{\beta \bar{\rho}^\gamma \bar{u}^3}{\gamma \bar{a}^2} & 0 & \frac{\bar{\rho}}{2\bar{a}^*}(\bar{u}+\bar{a}^*)\left(\bar{a}^{*2}+\beta\bar{u}(\bar{u}+2\bar{a}^*)\right) \end{bmatrix}.$$

The additional boundary condition is given by imposing $\partial T'/\partial x = 0$. For a subsonic outlet with $\bar{u} < 0$, three characteristics point into the domain, for

$$B'_R = \begin{bmatrix} 0 & -\frac{\bar{\rho}^\gamma}{\gamma \bar{a}^2}\bar{u} & -\frac{\bar{\rho}}{\bar{a}^*}(\bar{u}-\bar{a}^*) & 0 \\ 0 & -\frac{\bar{\rho}^\gamma}{\gamma \bar{a}^2}\bar{u}^2 & -\frac{\bar{\rho}}{\bar{a}^*}\bar{u}(\bar{u}-\bar{a}^*) & 0 \\ -\frac{\bar{\rho}^{\gamma+1}\bar{u}}{\gamma \bar{a}^2} & 0 & 0 & 0 \\ 0 & -\frac{\bar{\rho}^\gamma}{\gamma \bar{a}^2}\beta\bar{u}^3 & -\frac{\bar{\rho}}{\bar{a}^*}(\bar{u}-\bar{a}^*)(\bar{a}^{*2}+\beta\bar{u}^2) & 0 \end{bmatrix}.$$

These three conditions are sufficient, but if $\bar{u} > 0$, only the $\bar{u}-\bar{a}^*$ characteristic points into the domain so the first two columns of B'_R are zero. The additional two boundary conditions are then given by $\partial u'/\partial x = 0$ and $\partial v'/\partial x = 0$.

Appendix F

Solutions of the Navier-Stokes Equations

F.1 Navier-Stokes Shock Solution

F.1.1 Shock Solution Derivation

Under a specific set of assumptions, the 1-D Navier-Stokes equations may be solved analytically for the flow through a (continuous) shock, following the analysis of Whitham (1974). Starting with the 1-D equations with zero bulk viscosity, from (E1.8)–(E1.10), we assume steady flow ($\partial/\partial t \equiv 0$) and a perfect gas to obtain the system

$$\frac{\mathrm{d}(\rho u)}{\mathrm{d}x} = 0, \tag{F1.1}$$

$$\rho u \frac{\mathrm{d}u}{\mathrm{d}x} + \frac{\mathrm{d}p}{\mathrm{d}x} - \frac{4}{3}\frac{\mathrm{d}}{\mathrm{d}x}\left(\mu \frac{\mathrm{d}u}{\mathrm{d}x}\right) = 0, \tag{F1.2}$$

$$\rho u \frac{\mathrm{d}e}{\mathrm{d}x} + p\frac{\mathrm{d}u}{\mathrm{d}x} - \frac{4}{3}\mu\left(\frac{\mathrm{d}u}{\mathrm{d}x}\right)^2 - \frac{\mathrm{d}}{\mathrm{d}x}\left(\kappa \frac{\mathrm{d}T}{\mathrm{d}x}\right) = 0, \tag{F1.3}$$

$$p = \rho R T. \tag{F1.4}$$

Immediately, the continuity equation may be integrated to find

$$\rho u = \rho_0 u_0, \tag{F1.5}$$

where ρ_0 and u_0 are the upstream density and velocity. Next, substituting this result into the gas law

$$p = \frac{\rho_0 u_0}{u} R T, \tag{F1.6}$$

and differentiating with respect to x, an expression for $\mathrm{d}p/\mathrm{d}x$ is obtained:

$$\frac{\mathrm{d}p}{\mathrm{d}x} = \frac{\rho_0 u_0}{u} R \frac{\mathrm{d}T}{\mathrm{d}x} - \frac{p}{u}\frac{\mathrm{d}u}{\mathrm{d}x}. \tag{F1.7}$$

Now substituting this result into the momentum and energy equations, and using $e = C_v T$ and $R = C_p - C_v$, where C_v and C_p are the specific heat capacities of the gas, we have

$$\frac{p}{\rho_0 u_0}\frac{\mathrm{d}u}{\mathrm{d}x} = u\frac{\mathrm{d}u}{\mathrm{d}x} + R\frac{\mathrm{d}T}{\mathrm{d}x} - \frac{4}{3}\frac{\mu}{\rho_0 u_0}\frac{\mathrm{d}}{\mathrm{d}x}\left(\mu\frac{\mathrm{d}u}{\mathrm{d}x}\right), \tag{F1.8}$$

$$C_p\frac{\mathrm{d}T}{\mathrm{d}x} + u\frac{\mathrm{d}u}{\mathrm{d}x} - \frac{4}{3}\frac{1}{\rho_0 u_0}\frac{\mathrm{d}}{\mathrm{d}x}\left(\mu u\frac{\mathrm{d}u}{\mathrm{d}x}\right) - \frac{1}{\rho_0 u_0}\frac{\mathrm{d}}{\mathrm{d}x}\left(\kappa\frac{\mathrm{d}T}{\mathrm{d}x}\right) = 0. \tag{F1.9}$$

The energy equation (F1.9) may be immediately integrated, to obtain

$$C_p T + \frac{1}{2}u^2 - \frac{\kappa}{C_p\rho_0 u_0}\left(\frac{4}{3}\frac{\mu C_p}{\kappa}u\frac{\mathrm{d}u}{\mathrm{d}x} + C_p\frac{\mathrm{d}T}{\mathrm{d}x}\right) = C_1 = \text{const.}$$

The Prandtl number $\mathrm{Pr} = \mu C_p/\kappa$ has the value 0.72 in air, but to make further progress, we approximate it as 3/4 to obtain from the last result

$$\frac{1}{2}u^2 + C_p T - \frac{\kappa}{C_p\rho_0 u_0}\frac{\mathrm{d}}{\mathrm{d}x}\left(\frac{1}{2}u^2 + C_p T\right) = C_1. \tag{F1.10}$$

Integrating again,

$$\frac{1}{2}u^2 + C_p T = C_1 + C_2 \exp\left(C_p\rho_0 u_0 \int \frac{\mathrm{d}x}{\kappa(T(x))}\right). \tag{F1.11}$$

Since the flow is uniform at $x \to \infty$, $C_2 = 0$, giving

$$\frac{1}{2}u^2 + C_p T = C_1. \tag{F1.12}$$

Now integrating the momentum equation (F1.9),

$$\rho_0 u_0 u + p - \frac{4}{3}\mu\frac{\mathrm{d}u}{\mathrm{d}x} = C_3. \tag{F1.13}$$

From the boundary condition that $\mathrm{d}u/\mathrm{d}x \to 0$ at $x \to -\infty$, clearly $C_3 = \rho_0 u_0^2 + p_0$. Then combining this with the result from the energy equation, we can write down an ODE in

terms of u alone:

$$\frac{4}{3}\frac{\mu}{\rho_0 u_0}u\frac{\mathrm{d}u}{\mathrm{d}x} - \frac{\gamma+1}{2\gamma}u^2 + \frac{C_3}{\rho_0 u_0}u = \frac{\gamma-1}{\gamma}C_1. \tag{F1.14}$$

To complete the analysis, we nondimensionalize the equation using the upstream mean free path and velocity, defining dimensionless variables

$$\xi = \frac{x}{\ell_0} \quad \text{and} \quad V = \frac{u}{u_0}.$$

From kinetic theory, viscosity can be written as a function of temperature by

$$\frac{\mu}{\mu_0} = \left(\frac{T}{T_0}\right)^n, \tag{F1.15}$$

where for air, $n = 0.76$. Thus we have

$$\left(\frac{T}{T_0}\right)^n V\frac{\mathrm{d}V}{\mathrm{d}\xi} - k_3 M_0(V-1)(V-\alpha) = 0, \tag{F1.16}$$

where the constants k_3, and α are given by

$$k_3 = \frac{3}{8k_1}(\gamma+1)\sqrt{\frac{\pi}{8\gamma}}, \quad \text{with } k_1 = \frac{5\pi}{32},$$
$$\alpha = \frac{\gamma-1}{\gamma+1} + \frac{2}{\gamma+1}\frac{1}{M_0^2}.$$

Note that α is the velocity ratio across a normal shock as given by the Rankine-Hugoniot relations. From

$$C_1 = \frac{1}{2}u^2 + C_pT = \frac{1}{2}u_0^2 + C_pT_0, \tag{F1.17}$$

temperature may be expressed in terms of velocity by

$$\frac{T}{T_0} = 1 + \frac{\gamma-1}{2}M_0^2(1-V^2), \tag{F1.18}$$

and so an ODE for $V(\xi)$ is obtained:

$$V\left[1 + \frac{\gamma-1}{2}M_0^2(1-V^2)\right]^n \frac{\mathrm{d}V}{\mathrm{d}\xi} - k_3 M_0(V-1)(V-\alpha) = 0. \tag{F1.19}$$

At this point, if $n = 0.76$ is to be used, the equation must be integrated numerically. If the viscosity is assumed constant with $n = 0$, however, the ODE may be integrated directly

to obtain an implicit equation for V:

$$\xi(V) = \frac{1}{(1-\alpha)k_3 M_0} \log\left[\left(\frac{\sqrt{\alpha}-\alpha}{V-\alpha}\right)^{\alpha} \frac{1-V}{1-\sqrt{\alpha}}\right], \tag{F1.20}$$

where the constant of integration has been chosen such that the origin is at the inflection point of the shock, i.e., such that $\xi = 0$ at $\mathrm{d}^2V/\mathrm{d}\xi^2 = 0$. From this solution, the velocity at a given x coordinate may be found by numerical solution to arbitrary precision, and from it, any of the other solution variables. Figure F.1 shows the velocity profile through the shock, both by numerical integration of the variable-viscosity equation (F1.19) with $n = 0.76$ and by the analytic solution with constant viscosity given by equation (F1.20). Note that the constant-viscosity profile has a steeper slope.

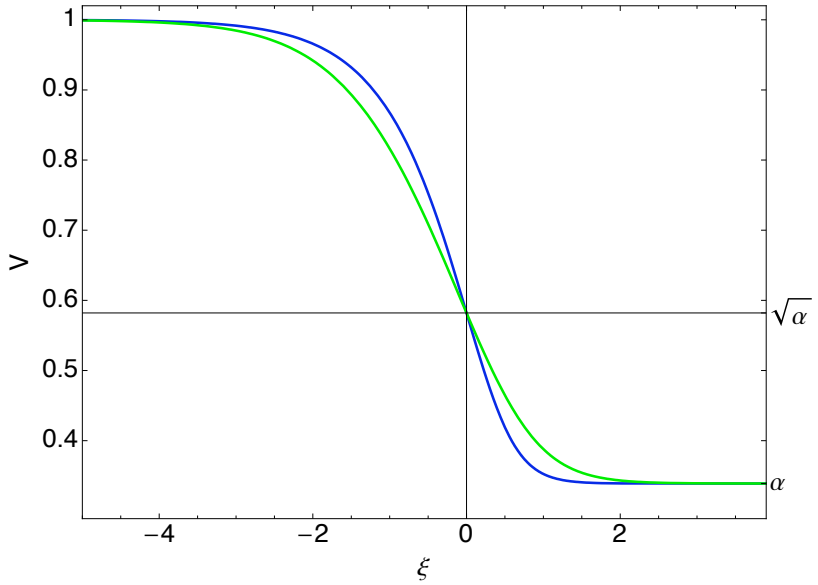

Figure F.1: Navier-Stokes shock velocity profiles for $M_0 = 2.2$: the variable viscosity solution is shown in green, the constant viscosity solution in blue.

Finally, note that by integrating the entropy equation,

$$[\rho u s]_{-\infty}^{\infty} = \int_{-\infty}^{\infty} \frac{1}{T}\left[\frac{4}{3}\mu\left(\frac{\mathrm{d}u}{\mathrm{d}x}\right)^2 + \kappa\left(\frac{\mathrm{d}T}{\mathrm{d}x}\right)^2\right]\mathrm{d}x > 0, \tag{F1.21}$$

i.e., entropy increases across the shock, as expected.

F.1.2 Shock Thickness

An estimate for the thickness of a shock may be calculated from this solution. The simplest (and most conservative) thickness estimate is the tangent thickness, which is the distance between the points where the upstream and downstream states intersect a tangent line to the shock through the point of inflection (where $\xi = 0$ by choice of the origin). From this analysis, we obtain an estimate for the thickness Δ,

$$\frac{\Delta}{\ell_0} = \frac{1}{k_3 M_0} \frac{1+\sqrt{\alpha}}{1-\sqrt{\alpha}}, \tag{F1.22}$$

which, for weak shocks with $\epsilon = M_0 - 1 \ll 1$, may be approximated by

$$\frac{\Delta}{\ell_0} \approx \frac{\gamma+1}{M_0 - 1}, \tag{F1.23}$$

since $k_3 \approx 1$. It turns out that this is an excellent approximation to the shock thickness, up to at least $M = 1.5$. The mean free path may be estimated from the kinematic viscosity of the gas, by the following formula:

$$\ell_0 = \nu \frac{8}{5} \sqrt{\frac{2}{\pi R T_0}}. \tag{F1.24}$$

F.1.3 Reference Frames

While the Euler and Navier-Stokes equations are frame invariant, the solution presented here is clearly in a shock-stationary frame (where the solution is steady). To obtain the solution in a stationary frame (the lab frame), consider the general form of the transformation for a steady shock traveling at speed $U = M_0 a_0$:

$$x_L = Ut - x_S, \tag{F1.25}$$

$$u_L = U - u_S, \tag{F1.26}$$

where subscripts L refer to the lab frame and S to the shock frame (the time variable is the same in both frames). Applying this transformation to the shock solution, in the lab frame

$$V_L(\xi_L) = 1 - V(Ut - \xi), \tag{F1.27}$$

$$\rho(\xi_L) = \frac{1}{V(Ut-\xi)}, \tag{F1.28}$$

$$p(\xi_L) = \frac{1}{V(Ut-\xi)}\left[1 + \frac{\gamma-1}{2}M_0^2\left(1-[V(Ut-\xi)]^2\right)\right], \tag{F1.29}$$

where V and ξ are the shock-frame velocity and spatial coordinate, respectively, defined by equation (F1.20).

F.2 Lamb-Oseen Vortex Solution

The tangential velocity distribution for the Lamb-Oseen vortex (defined a priori) is

$$\frac{u_\theta}{u_0} = \frac{r_0}{r}\left(1 - \mathrm{e}^{-\frac{r^2}{r_0^2}}\right), \tag{F2.1}$$

where $u_0 = \Gamma_0/2\pi r_0$ is a velocity scale, and r_0 is the vortex core radius. Substituting into the compressible Euler equations in polar coordinates with $u_r = 0$, the continuity and θ-momentum equations reduce to show that $\rho = \rho(r)$ and $p = p(r)$. The remaining r-momentum equation gives

$$\frac{1}{\rho}\frac{\mathrm{d}p}{\mathrm{d}r} = \frac{u_\theta^2}{r}. \tag{F2.2}$$

To proceed, we assume an isentropic perfect gas such that $p/p_0 = (\rho/\rho_0)^\gamma$, where p_0 and ρ_0 are the far-field pressure and density, respectively. Substituting and rearranging, we obtain

$$\left(\frac{p}{p_0}\right)^{-1/\gamma}\mathrm{d}p = \frac{\rho_0 u_0^2}{p_0}\frac{r_0^2}{r^3}\left(1 - e^{-\frac{r^2}{r_0^2}}\right)^2\mathrm{d}r, \tag{F2.3}$$

which may be integrated to obtain the pressure distribution,

$$\frac{p}{p_0} = \left(1 - (\gamma-1)M_0^2\left[\frac{1}{2\eta^2}\left(1-\mathrm{e}^{-\eta^2}\right)^2 + \mathrm{Ei}\left(-2\eta^2\right) - \mathrm{Ei}\left(-\eta^2\right)\right]\right)^{\frac{\gamma}{\gamma-1}}, \tag{F2.4}$$

expressed in terms of the exponential integral function $\mathrm{Ei}(z)$, the normalized radius $\eta = r/r_0$ and the reference Mach number, $M_0^2 = \rho u_0^2/\gamma p_0$. The density profile is then

$$\frac{\rho}{\rho_0} = \left(1 - (\gamma-1)M_0^2\left[\frac{1}{2\eta^2}\left(1-\mathrm{e}^{-\eta^2}\right)^2 + \mathrm{Ei}\left(-2\eta^2\right) - \mathrm{Ei}\left(-\eta^2\right)\right]\right)^{\frac{1}{\gamma-1}}. \tag{F2.5}$$

Velocity and pressure profiles for this vortex are shown in Figure F.2.

The vortex flow has three regimes, determined by the value of M_0. With $\gamma = 1.4$, for $M_0 < 1.35$, flow is subsonic everywhere based on the local Mach number, $M = u_\theta \sqrt{\rho/\gamma p}$. This limiting value is determined numerically by finding M_0 such that the maximum value of the local Mach number is 1. In the range $1.35 < M_0 < 1.9$, flow is supersonic in an annulus, and subsonic elsewhere. The upper Mach number limit is also determined numerically, at the M_0 such that pressure and density are zero at the origin.

Hydrodynamic stability of the vortex is determined by the Rayleigh Discrminant (Drazin and Reid, 2004),

$$\Phi(r) = \frac{1}{r^3}\frac{\mathrm{d}}{\mathrm{d}r}\left(ru_\theta\right)^2 = \frac{1}{4\pi^2 r^3}\frac{\mathrm{d}}{\mathrm{d}r}\left(\Gamma^2\right), \tag{F2.6}$$

which, if negative, indicates that a flow is unstable to axisymmetric perturbation. For the Lamb-Oseen vortex,

$$\Phi(r) = \frac{4}{\eta^2} e^{-\eta^2}\left(1 - \mathrm{e}^{-\eta^2}\right), \tag{F2.7}$$

which is positive for all r; thus this flow is stable.

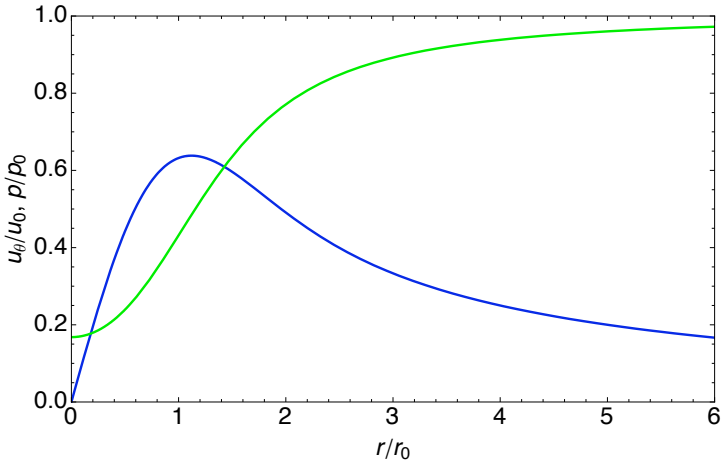

Figure F.2: Velocity (blue line) and pressure (green line) profiles of the Lamb-Oseen vortex, for a reference Mach number $M_0 = 1.2$.

Appendix G

Impulsive Model of the Richtmyer-Meshkov Instability

The original model of the acceleration of a perturbed interface by a shock was developed by Richtmyer (1960), who modeled the problem with an impulsively accelerated interface. Figure G.1 shows the problem in the stationary (lab) frame (cf. Figure 4.2), and the mapping to an impulsively accelerating frame. The interface is defined by $\xi = \xi(y, z, t)$.

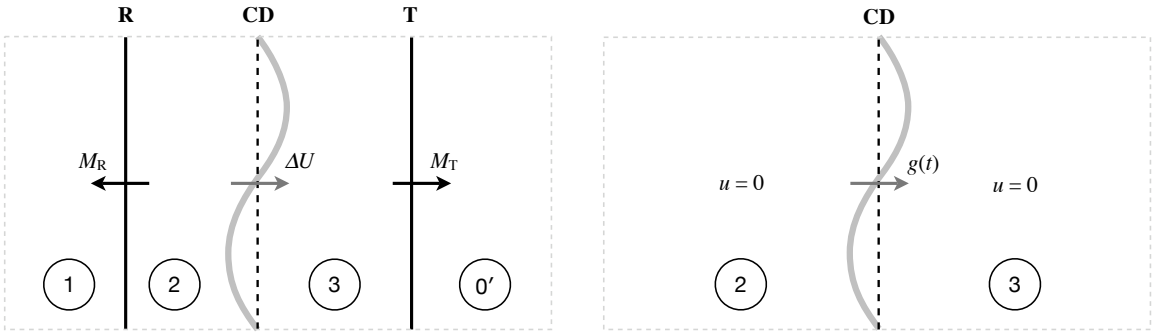

(a) stationary frame (b) accelerating interface frame

Figure G.1: The Richtmyer-Meshkov problem, mapped to an impulsively accelerated frame in which the flow is assumed to be potential.

By assuming incompressible flow in this frame, the flow is potential, so

$$\nabla^2 \phi_2 = 0, \quad x < \xi, \tag{G.1}$$

$$\nabla^2 \phi_3 = 0, \quad x > \xi, \tag{G.2}$$

with the boundary condition $\nabla \phi_i \to 0$ at $|\xi| \to \infty$. Note that this assumes that the shocks have no effect on the growth of the interface. The kinematic boundary condition at the

interface is given by

$$\frac{\partial \phi_i}{\partial x} = \frac{\mathrm{D}\xi}{\mathrm{D}t}\bigg|_{x=\xi} = \left(\frac{\partial \xi}{\partial t} + \frac{\partial \phi_i}{\partial y}\frac{\partial \xi}{\partial y} + \frac{\partial \phi_i}{\partial z}\frac{\partial \xi}{\partial z}\right)\bigg|_{x=\xi}, \tag{G.3}$$

for $i = 2, 3$. Bernoulli gives

$$p_i + \rho_i g(t)x + \frac{1}{2}\rho_i(\nabla^2\phi_i)^2 + \rho_i\frac{\partial \phi_i}{\partial t} = \rho_i C_i, \tag{G.4}$$

where C_i is a constant. This has the boundary condition that pressure be matched across the interface, so evaluating at $x = \xi$, we have

$$\rho_2\left[C_2 - \frac{1}{2}(\nabla^2\phi_2)^2 - \frac{\partial \phi_2}{\partial t} - g\xi\right] = \rho_3\left[C_3 - \frac{1}{2}(\nabla^2\phi_3)^2 - \frac{\partial \phi_3}{\partial t} - g\xi\right], \tag{G.5}$$

and from the unperturbed interface, $\rho_2 C_2 = \rho_3 C_3$.

Now we linearize, such that

$$\phi_i = \epsilon\phi_i', \quad \text{and} \quad \xi = \epsilon\xi',$$

where $\epsilon \ll 1$. The perturbed flow remains potential, with the same radiation boundary condition, but the kinematic boundary condition (G.3) reduces to

$$\frac{\partial \phi_i}{\partial x} = \frac{\partial \xi}{\partial t}. \tag{G.6}$$

Applying the linearization to equation (G.4),

$$\rho_2\left(\frac{\partial \phi_2}{\partial t} + g(t)\xi\right) = \rho_3\left(\frac{\partial \phi_3}{\partial t} + g(t)\xi\right). \tag{G.7}$$

We now define the impulsive acceleration as $g(t) = \Delta U\delta(t)$, where ΔU is the speed of the interface given by the solution of the Riemann problem. Assuming functions of the form

$$\phi_2' = \hat{\phi}_2(x)f_2(t)\mathrm{e}^{\mathrm{i}(\ell y + mz)}, \tag{G.8}$$

$$\phi_3' = \hat{\phi}_3(x)f_3(t)\mathrm{e}^{\mathrm{i}(\ell y + mz)}, \tag{G.9}$$

$$\xi' = h(t)\mathrm{e}^{\mathrm{i}(\ell y + mz)}, \tag{G.10}$$

with initial conditions $f_2(0^-) = f_3(0^-) = 0$, and $h(0)$ given, the problem may be solved. The solution has

$$h(t) = h(0)\left(1 + k\mathrm{A}\Delta U t\right), \tag{G.11}$$

which provides the interface growth rate (in the linear regime)

$$\frac{\mathrm{d}h}{\mathrm{d}t} = k\mathrm{A}\Delta U h(0), \tag{G.12}$$

where $k = \sqrt{\ell^2 + m^2}$, and the Atwood number is given by

$$\mathrm{A} = \frac{\rho_3 - \rho_2}{\rho_3 + \rho_2}. \tag{G.13}$$

More advanced models, discussed in Section 4.2, make various generalizations of these assumptions.

Appendix H

Validation Tests for the Richtmyer-Meshkov Simulation

Before solving the Richtmyer-Meshkov problem described in Section 4.4, a set of validation tests was performed on the implementation of the 2-D linearized problem. For the 1-D base flow, this had already been done using the analytic Navier-Stokes shock solution, but no such convenient test exists for the 2-D perturbation problem. Lacking any existing analytic solution, we generated our own by the method of manufactured solutions.

H.1 Manufactured Solutions

For the method of manufactured solutions, we begin with the full set of equations (4.3.12)–(4.3.18), adding a source term to each, as shown:

$$\frac{\partial \bar{\rho}}{\partial t} = -\frac{\partial(\bar{\rho}\bar{u})}{\partial x} + \bar{Q}_1, \tag{H1.1}$$

$$\frac{\partial(\bar{\rho}\bar{u})}{\partial t} = -\frac{\partial}{\partial x}\left(\frac{\bar{p}}{\gamma M_\mathrm{I}^2} + \bar{\rho}\bar{u}^2 - \frac{4}{3}\frac{1}{\mathrm{Re}}\frac{\partial \bar{u}}{\partial x}\right) + \bar{Q}_2, \tag{H1.2}$$

$$\frac{\partial}{\partial t}\left(\frac{\bar{p}}{\gamma M_\mathrm{I}^2} + \beta\bar{\rho}\bar{u}^2\right) = -\frac{\partial}{\partial x}\left(\frac{\bar{p}\bar{u}}{M_\mathrm{I}^2} + \beta\bar{\rho}\bar{u}^3 - \frac{1}{\mathrm{PrRe}M_\mathrm{I}^2}\frac{\partial \bar{T}}{\partial x} - \frac{4}{3}\frac{\gamma-1}{\mathrm{Re}}\bar{u}\frac{\partial \bar{u}}{\partial x}\right) + \bar{Q}_3, \tag{H1.3}$$

$$\frac{\partial \rho'}{\partial t} = -\frac{\partial}{\partial x}\left[\bar{\rho}u' + \rho'\bar{u}\right] - \mathrm{i}k\bar{\rho}v' + Q_1', \tag{H1.4}$$

$$\begin{aligned}\frac{\partial}{\partial t}\left(\bar{\rho}u' + \rho'\bar{u}\right) = &-\frac{\partial}{\partial x}\left[\frac{p'}{\gamma M_\mathrm{I}^2} + \rho'\bar{u}^2 + 2\bar{\rho}\bar{u}u' - \frac{1}{\mathrm{Re}}\left(\frac{4}{3}\frac{\partial u'}{\partial x} + \mathrm{i}kv'\right)\right] \\ &- \mathrm{i}k\bar{\rho}\bar{u}v' - \frac{1}{\mathrm{Re}}k^2u' + Q_2',\end{aligned} \tag{H1.5}$$

$$\frac{\partial}{\partial t}\left(\bar{\rho}v'\right) = -\frac{\partial}{\partial x}\left[\bar{\rho}\bar{u}v' - \frac{1}{\mathrm{Re}}\left(\frac{\partial v'}{\partial x} + \mathrm{i}ku'\right)\right] - \mathrm{i}k\frac{p'}{\gamma M_\mathrm{I}^2} - \frac{4}{3}\frac{1}{\mathrm{Re}}k^2v' + Q_3', \tag{H1.6}$$

$$\frac{\partial}{\partial t}\left(\frac{p'}{\gamma M_{\mathrm{I}}^2}+\beta\left(\rho'\bar{u}^2+2\bar{\rho}\bar{u}u'\right)\right)$$
$$=-\frac{\partial}{\partial x}\left[\frac{p'\bar{u}+\bar{p}u'}{M_{\mathrm{I}}^2}+\beta\left(\rho'\bar{u}^3+3\bar{\rho}\bar{u}^2u'\right)-\frac{1}{\mathrm{PrRe}M_{\mathrm{I}}^2}\frac{\partial T'}{\partial x}-\frac{4}{3}\frac{\gamma-1}{\mathrm{Re}}\left(\bar{u}\frac{\partial u'}{\partial x}+u'\frac{\partial\bar{u}}{\partial x}\right)\right]$$
$$-\mathrm{i}kv'\left(\frac{\bar{p}}{M_{\mathrm{I}}^2}+\beta\bar{\rho}\bar{u}^2\right)-\frac{1}{\mathrm{PrRe}}k^2\frac{T'}{M_{\mathrm{I}}^2}+\frac{\gamma-1}{\mathrm{Re}}\bar{u}\left(\mathrm{i}k\frac{\partial v'}{\partial x}-k^2u'\right)+Q_4'. \tag{H1.7}$$

H.1.1 Manufactured Solution I

The 1-D compressible Navier-Stokes equations of the base flow have only derivative terms, so admit a constant solution with zero source terms. This reduces the 2-D linearized equations in the perturbed quantities to a system of linear partial differential equations with constant coefficients. Thus we choose a base flow

$$\bar{\rho}=\bar{\rho}_0=1,\quad \bar{p}=\bar{p}_0=1,\quad \bar{u}=\bar{u}_0.$$

The value of $\bar{u}_0$ may be chosen to give either subsonic or supersonic boundary conditions. Since the code is currently set up to deal with both sub- and supersonic cases at the inlet, but only subsonic at the outlet, we choose $\bar{u}_0<1/M_{\mathrm{I}}$ such that both boundaries are subsonic. For testing, we choose $\bar{u}_0=0.3$ with $\bar{\rho}_0=\bar{p}_0=1$, for a subsonic base flow.

For the perturbed quantities, we first consider a solution with the velocity components set to zero, i.e., $u'=v'=0$. With the constant-valued base flow as described, the equations (H1.4)–(H1.7) reduce to

$$\frac{\partial\rho'}{\partial t}=-\bar{u}_0\frac{\partial\rho'}{\partial x}+Q_1', \tag{H1.8}$$
$$\bar{u}_0\frac{\partial\rho'}{\partial t}=-\frac{\partial}{\partial x}\left(\frac{p'}{\gamma M_{\mathrm{I}}^2}+\rho'\bar{u}_0^2\right)+Q_2', \tag{H1.9}$$
$$0=-\mathrm{i}k\frac{p'}{\gamma M_{\mathrm{I}}^2}+Q_3', \tag{H1.10}$$
$$\frac{\partial}{\partial t}\left(\frac{p'}{\gamma M_{\mathrm{I}}^2}+\beta\rho'\bar{u}_0^2\right)=-\frac{\partial}{\partial x}\left(\frac{p'\bar{u}_0}{M_{\mathrm{I}}^2}+\beta\rho'\bar{u}_0^3-\frac{1}{\mathrm{PrRe}M_{\mathrm{I}}^2}\frac{\partial T'}{\partial x}\right)-\frac{1}{\mathrm{PrRe}}k^2\frac{T'}{M_{\mathrm{I}}^2}+Q_4'. \tag{H1.11}$$

From equation (H1.10), it is clear that for $Q_3'=0$, $p'=0$, which in turn implies

$$p'=\rho'\bar{T}+\bar{\rho}T'=0,$$

so only ρ' and T' are nonzero perturbed quantities. With some additional algebra, we have the three simple equations (after setting $Q_1' = 0$)

$$\frac{\partial \rho'}{\partial t} + \bar{u}_0 \frac{\partial \rho'}{\partial x} = 0, \tag{H1.12}$$

$$\frac{\partial^2 T'}{\partial x^2} - k^2 T' = Q_4', \tag{H1.13}$$

$$T' = -\rho', \tag{H1.14}$$

using that $\bar{T}_0 = \bar{\rho}_0 = 1$. From (H1.12), it is clear that $\rho' = f(x - \bar{u}_0 t)$. The solution to (H1.13) is of the form

$$T'(x) = C_1 \mathrm{e}^{kx} + C_2 \mathrm{e}^{-kx}, \tag{H1.15}$$

but this cannot satisfy a radiation boundary condition (i.e., it does not have a solution of compact support) for a given value of k. Instead, we choose a compact function for ρ', and add a source term to the energy equation (H1.11) to satisify (H1.13).

For the following example, we choose a Gaussian for ρ', such that:

$$\rho'(x,t) = h_0 \mathrm{e}^{-k^2(x-\bar{u}_0 t)^2}, \tag{H1.16}$$

$$T'(x,t) = -h_0 \mathrm{e}^{-k^2(x-\bar{u}_0 t)^2}, \tag{H1.17}$$

where h_0 is an amplitude parameter. The required source term for the energy equation is then

$$Q_4' = -h_0 \frac{k^2}{\mathrm{PrRe}M_\mathrm{I}^2}(3 - 4k^2(x - \bar{u}_0 t)^2)\mathrm{e}^{-k^2(x-\bar{u}_0 t)^2}. \tag{H1.18}$$

Since this solution has compact support, zero boundary conditions are sufficient for the perturbed fields as long as the solution does not approach the boundaries too closely.

H.1.2 Manufactured Solution II

Having assumed zero velocity and pressure perturbations for the first manufactured solution, we seek a second solution that exercises the remaining terms of the linearized equations. For now, we continue to assume that the base flow is constant, and use the same subsonic conditions as before.

We now choose nonzero u' and v' and assume that $\rho' = 0$ to find

$$p' = \bar{\rho}T' = T'. \tag{H1.19}$$

Substituting this ansatz into the linearized equations, we first see from continuity that

$$\frac{\partial u'}{\partial x} = -\mathrm{i}kv', \tag{H1.20}$$

where we set $Q_1' = 0$. Using this, and after a little algebra, we obtain from the remaining equations of motion the equations

$$\frac{\partial u'}{\partial t} + \bar{u}_0\frac{\partial u'}{\partial x} = \frac{1}{\mathrm{Re}}\left(\frac{1}{3}\frac{\partial^2 u'}{\partial x^2} - k^2u'\right) - \frac{1}{\gamma M_\mathrm{I}^2}\frac{\partial p'}{\partial x} + Q_2', \tag{H1.21}$$

$$\frac{\partial v'}{\partial t} + \bar{u}_0\frac{\partial v'}{\partial x} = \frac{1}{\mathrm{Re}}\left(\frac{\partial^2 v'}{\partial x^2} - \frac{1}{3}k^2v'\right) - \mathrm{i}k\frac{p'}{\gamma M_\mathrm{I}^2} + Q_3', \tag{H1.22}$$

$$\frac{\partial p'}{\partial t} + \bar{u}_0\frac{\partial p'}{\partial x} = \frac{\gamma}{\mathrm{PrRe}}\left(\frac{\partial^2 p'}{\partial x^2} - k^2p'\right) + Q_p'. \tag{H1.23}$$

The left-hand sides of (H1.21)–(H1.23) support convecting solutions, of the form

$$u'(x,t) = u'(x - \bar{u}_0 t), \text{ etc.}, \tag{H1.24}$$

while the right-hand sides suggest a solution somewhat similar to equation (H1.15). Since we once again seek a solution of compact support (so perturbations are zero at the domain boundaries), the simplest answer is to specify a Gaussian solution and balance each equation with the source term. Starting with

$$u' = h_0\mathrm{e}^{-k^2(x-\bar{u}_0t)}, \tag{H1.25}$$

$$p' = \gamma M_\mathrm{I}^2 h_0\mathrm{e}^{-k^2(x-\bar{u}_0t)}, \tag{H1.26}$$

we obtain from equation (H1.20),

$$v' = -2\mathrm{i}k(x - \bar{u}_0t)h_0\mathrm{e}^{-k^2(x-\bar{u}_0t)}, \tag{H1.27}$$

where h_0 is again an amplitude parameter. Substituting these solutions into the equations

(H1.21)–(H1.23), we find corresponding source terms

$$Q_2' = -\left[2(x-\bar{u}_0 t) - \frac{1}{3\mathrm{Re}}\left(5 - 4k^2(x-\bar{u}_0 t)^2\right)\right] k^2 h_0 \mathrm{e}^{-k^2(x-\bar{u}_0 t)}, \tag{H1.28}$$

$$Q_3' = \left[1 - \frac{2k^2}{\mathrm{Re}}\left(\frac{19}{3} - 4k^2(x-\bar{u}_0 t)^2\right)(x-\bar{u}_0 t)\right] \mathrm{i}k h_0 \mathrm{e}^{-k^2(x-\bar{u}_0 t)}, \tag{H1.29}$$

$$Q_p' = \frac{\gamma}{\mathrm{PrRe}}\left(3 - 4k^2(x-\bar{u}_0 t)^2\right) k^2 h_0 \mathrm{e}^{-k^2(x-\bar{u}_0 t)}. \tag{H1.30}$$

For the full energy equation, the source term is given by

$$Q_4' = \bar{u}_0(\gamma-1)Q_1' + Q_p', \tag{H1.31}$$

following the derivation of equation (H1.23).

H.1.3 Manufactured Solution III

For the final test, we impose a nonconstant base flow that mimics the Navier-Stokes shock solution with a smoothed-step function. The Navier-Stokes shock solution itself is not used, because while an analytic solution exists in 1-D, the flow field is known only as an implicit function of the spatial coordinate. For simplicity in the perturbed flow, only u' is chosen to be nonzero.

We begin by assuming a general solution for the velocity in a "shock"-fixed frame, $V(\xi)$, similar to the shock solution of Appendix F.1. Translating this into a stationary frame by $\xi = t - x$, the flow feature moves across the domain with a convection velocity of 1, giving the base flow solution

$$\bar{\rho}(x,t) = \frac{1}{V(t-x)}, \tag{H1.32}$$

$$\bar{u} = 1 - V(t-x), \tag{H1.33}$$

$$\bar{p} = \frac{1}{V(t-x)}\left[1 + \frac{\gamma-1}{2}M_\mathrm{I}^2(1 - V(t-x)^2)\right]. \tag{H1.34}$$

If $V(\xi)$ is the Navier-Stokes shock solution, the equations for the base flow are satisfied

exactly, but in general, we have the source terms for (H1.1)–(H1.3):

$$\bar{Q}_1 = 0, \tag{H1.35}$$

$$\bar{Q}_2 = \frac{\gamma+1}{2\gamma}\left(\frac{\alpha}{V^2}-1\right)\frac{\mathrm{d}V}{\mathrm{d}\xi} + \frac{4}{3}\frac{1}{\mathrm{Re}}\frac{\mathrm{d}^2V}{\mathrm{d}\xi^2}, \tag{H1.36}$$

$$\bar{Q}_3 = (\gamma-1)\bar{Q}_2, \tag{H1.37}$$

where

$$\alpha = \frac{2+(\gamma-1)M_\mathrm{I}^2}{(\gamma+1)M_\mathrm{I}^2},$$

from the Rankine-Hugoniot relations for the velocity ratio across a shock M_I, and we have assumed that $\mathrm{Pr} = 3/4$, as in the analytic shock solution.

For the perturbed solution, we choose to set all perturbed quantities but u' to zero for all time, and use the familiar Gaussian form for the velocity perturbation, i.e.,

$$u' = h_0 \mathrm{e}^{-k^2(x-\bar{u}_0 t)}. \tag{H1.38}$$

Substituting this with the manufactured base flow into the linearized equations, we find

$$Q_1' = \left(\frac{1}{V} + 2k^2(t-x)\right)\frac{u'}{V}, \tag{H1.39}$$

$$Q_2' = \left[\frac{1}{V^2}\frac{\partial V}{\partial \xi} + 2k^2(t-x)\left(\frac{1}{V}-2\right) + \frac{k^2}{3\mathrm{Re}}\left(11-16k^2(t-x)^2\right)\right]u', \tag{H1.40}$$

$$Q_3' = -\frac{2\mathrm{i}}{\mathrm{Re}}k^3(t-x)u', \tag{H1.41}$$

$$\begin{aligned} Q_4' = \Bigg[&\frac{\alpha(\gamma+1)}{V}\left(k^2(t-x)+\frac{1}{2V}\frac{\partial V}{\partial \xi}\right) + \frac{\gamma-1}{V}\left((1-4V+2V^2)k^2(t-x)+\frac{1-2V^2}{2V}\frac{\partial V}{\partial \xi}\right) \\ &-\frac{\gamma-1}{3\mathrm{Re}}\left(k^2(V-1)(11-16k^2(t-x)^2)+16k^2(t-x)\frac{\partial V}{\partial \xi}-4\frac{\partial^2 V}{\partial \xi^2}\right)\Bigg]u'. \end{aligned} \tag{H1.42}$$

All that remains is to specify the base flow function $V(\xi)$. For the convergence results shown in tables H.3 and H.4, an error function of the form

$$V(\xi) = \frac{1+\alpha}{2} - \frac{1-\alpha}{2}\,\mathrm{erf}(\xi) \tag{H1.43}$$

was used, with corresponding derivatives, to fully specify the source terms. The boundary

conditions are the same as those for the Navier-Stokes shock, with supersonic upstream and subsonic downstream flows.

With these three tests problems, the discrete implementation of every term in the full set of equations (4.3.12)–(4.3.18) has been tested and verified.

H.2 Convergence Testing

Tables H.1–H.4 show convergence results from each of the manufactured solutions. In each case, the grid is uniform and results are gathered at time $t = 400$, such that the pulse has travelled a distance equal to its width. For manufactured solutions I and II, perfect fourth-order convergence is obtained, the first-order perturbation equations being linear with constant coefficients in these cases. For solution III, near-fourth order convergence is obtained for both base and perturbed solutions.

Additionally, convergence results for the unperturbed Navier-Stokes shock are presented in Tables H.5 and H.6. This is the problem described in Section 2.6.2, and is solved here on similar grids with the same parameter values ($\gamma = 1.4$, $M_\mathrm{I} = 2.20$). Convergence of this problem verifies the base flow calculation on both uniform and locally refined grids. The locally refined grid in this case has three blocks, with a factor four refinement in the block centered on the shock inflection point. In both cases, fourth-order convergence is observed.

Finally, convergence results based on the Richtmyer-Meshkov problem follow in Tables H.7 and H.8. The problem solved was that with $M_\mathrm{I} = 2.20$ and $\mathrm{A} = 0.2$, described in Table 4.1. Because no analytic solution exists in this case, comparison is made to a more refined numerical solution, in this case at resolution $\Delta x = 1/16$. The grid is uniform for each case. At the coarsest resolution tested, the transmitted shock extends over only 5–6 nodes, which causes nonphysical oscillation in the solution at its trailing edge. This is detrimental to the convergence rate of the solution, but at higher resolutions the oscillation disappears, and if the nodes covering the transmitted shock are excluded, the proper fourth-order rate is recovered in the average slope (see Figure H.1). All results are shown for a solution at time $t = 1000$. Some reduction in the CFL number at high resolution was found to be necessary for stability.

	Error based on ρ'				Error based on u'			
Δx	$\log_{10}(L_2)$	rate	$\log_{10}(L_\infty)$	rate	$\log_{10}(L_2)$	rate	$\log_{10}(L_\infty)$	rate
8/25	−6.095		−6.618		−7.147		−7.634	
1/4	−6.524	4.00	−7.046	4.00	−7.576	4.00	−8.063	4.00
4/25	−7.299	4.00	−7.821	4.00	−8.351	4.00	−8.838	4.00
1/8	−7.727	4.00	−8.250	4.00	−8.780	4.00	−9.267	4.00
2/25	−8.502	4.00	−9.025	4.00	−9.555	4.00	−10.04	4.00
rate		4.00		4.00		4.00		4.00

Table H.1: Convergence results for manufactured solution I

	Error based on ρ'				Error based on u'			
Δx	$\log_{10}(L_2)$	rate	$\log_{10}(L_\infty)$	rate	$\log_{10}(L_2)$	rate	$\log_{10}(L_\infty)$	rate
8/25	−5.513		−6.053		−5.792		−6.328	
1/4	−5.942	4.00	−6.482	4.00	−6.221	4.00	−6.757	4.00
4/25	−6.717	4.00	−7.257	4.00	−6.996	4.00	−7.532	4.00
1/8	−7.146	4.00	−7.686	4.00	−7.424	4.00	−7.960	4.00
2/25	−7.921	4.00	−8.461	4.00	−8.200	4.00	−8.735	4.00
rate		4.00		4.00		4.00		4.00

Table H.2: Convergence results for manufactured solution II

	Error based on $\bar{\rho}$				Error based on $\bar{u}$			
Δx	$\log_{10}(L_2)$	rate	$\log_{10}(L_\infty)$	rate	$\log_{10}(L_2)$	rate	$\log_{10}(L_\infty)$	rate
8/25	−2.094		−2.076		−2.849		−2.838	
1/4	−2.495	3.75	−2.412	3.14	−3.263	3.86	−3.221	3.58
4/25	−3.243	3.86	−3.147	3.79	−4.021	3.91	−3.966	3.84
1/8	−3.665	3.93	−3.549	3.75	−4.444	3.95	−4.374	3.80
2/25	−4.433	3.97	−4.316	3.96	−5.214	3.97	−5.140	3.95
rate		3.89		3.74		3.93		3.83

Table H.3: Convergence results for the base flow from manufactured solution III

	Error based on ρ'				Error based on u'			
Δx	$\log_{10}(L_2)$	rate	$\log_{10}(L_\infty)$	rate	$\log_{10}(L_2)$	rate	$\log_{10}(L_\infty)$	rate
8/25	−2.349		−2.347		−2.890		−2.854	
1/4	−2.748	3.73	−2.705	3.34	−3.309	3.91	−3.266	3.84
4/25	−3.487	3.81	−3.436	3.77	−4.066	3.91	−3.985	3.71
1/8	−3.907	3.91	−3.845	3.82	−4.489	3.94	−4.403	3.90
2/25	−4.674	3.96	−4.593	3.86	−5.258	3.97	−5.165	3.93
rate		3.86		3.75		3.93		3.83

Table H.4: Convergence results for the perturbed flow from manufactured solution III

	Error based on $\bar{\rho}$				Error based on $\bar{u}$			
Δx	$\log_{10}(L_2)$	rate	$\log_{10}(L_\infty)$	rate	$\log_{10}(L_2)$	rate	$\log_{10}(L_\infty)$	rate
1/4	−2.219		−2.085		−3.005		−2.923	
1/5	−2.571	3.63	−2.428	3.54	−3.377	3.83	−3.309	3.98
1/8	−3.343	3.78	−3.138	3.48	−4.173	3.90	−4.071	3.73
1/10	−3.715	3.84	−3.510	3.84	−4.549	3.88	−4.428	3.69
1/16	−4.526	3.97	−4.316	3.95	−5.366	4.00	−5.238	3.97
rate		3.83		3.69		3.92		3.82

Table H.5: Convergence results for the constant-viscosity Navier-Stokes shock of $M_\mathrm{I} = 2.20$ on a uniform grid

	Error based on $\bar{\rho}$				Error based on $\bar{u}$			
Δx	$\log_{10}(L_2)$	rate	$\log_{10}(L_\infty)$	rate	$\log_{10}(L_2)$	rate	$\log_{10}(L_\infty)$	rate
1/2	−2.898		−3.158		−3.408		−3.754	
1/3	−3.583	3.89	−3.826	3.79	−4.100	3.93	−4.437	3.88
1/4	−4.070	3.90	−4.318	3.94	−4.589	3.91	−4.926	3.91
1/6	−4.747	3.84	−4.985	3.79	−5.263	3.83	−5.595	3.80
1/8	−5.225	3.83	−5.472	3.89	−5.745	3.86	−6.079	3.87
rate		3.87		3.84		3.88		3.86

Table H.6: Convergence results for the constant-viscosity Navier-Stokes shock of $M_\mathrm{I} = 2.20$ on a three-block refined grid. Δx is the coarse grid scale.

	Error based on $\bar{\rho}$				Error based on $\bar{u}$			
Δx	$\log_{10}(L_2)$	rate	$\log_{10}(L_\infty)$	rate	$\log_{10}(L_2)$	rate	$\log_{10}(L_\infty)$	rate
1/2	−0.667		−0.730		−1.682		−1.736	
1/4	−1.527	2.86	−1.378	2.15	−2.571	2.95	−2.467	2.43
1/8	−2.614	3.61	−2.350	3.23	−3.726	3.84	−3.538	3.56
1/12	−3.424	4.60	−3.143	4.50	−4.554	4.70	−4.370	4.72
rate		3.52		3.07		3.67		3.36

Table H.7: Convergence results for the Richtmyer-Meshkov base flow, where the reference solution is the numerical solution on a grid of $\Delta x = 1/16$

	Error based on ρ'				Error based on u'			
Δx	$\log_{10}(L_2)$	rate	$\log_{10}(L_\infty)$	rate	$\log_{10}(L_2)$	rate	$\log_{10}(L_\infty)$	rate
1/2	−1.965		−2.083		−2.815		−2.881	
1/4	−2.588	2.07	−2.507	1.41	−3.445	2.09	−3.343	1.53
1/8	−3.578	3.29	−3.324	2.71	−4.433	3.28	−4.183	2.79
1/12	−4.365	4.47	−4.086	4.33	−5.221	4.48	−4.954	4.38
rate		3.06		2.53		3.07		2.62

Table H.8: Convergence results for the Richtmyer-Meshkov perturbed flow, where the reference solution is the numerical solution on a grid of $\Delta x = 1/16$

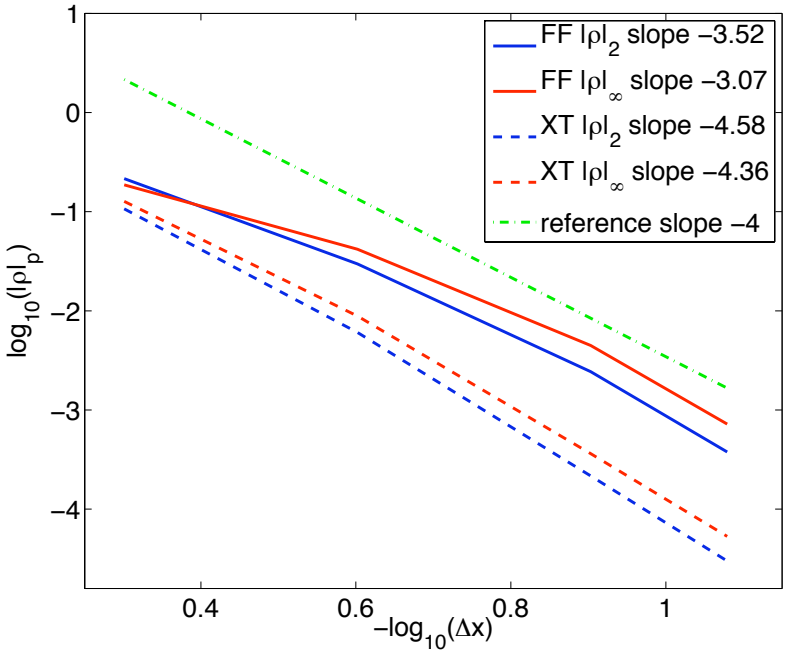

Figure H.1: Comparison of convergence of the RM-problem based on the full-field solution (FF), and on the solution excluding the transmitted shock (XT) which is underresolved at the coarsest grid resolutions. Between 5 and 25 nodes are removed from the solution for the XT case.

Bibliography

Abarbanel, S. S. and Chertock, A. E., 2000. Strict stability of high-order compact implicit finite-difference schemes: The role of boundary conditions for hyperbolic PDEs, I. *J. Comput. Phys.*, 160:42–66.

Ames, W. F., 1977. *Numerical Methods for Partial Differential Equations.* Boston: Academic Press, second edition.

Berger, M. J., 1985. Stability of interfaces with mesh refinement. *Math. Comput.*, 45(172):301–318.

Berger, M. J. and Colella, P., 1989. Local adaptive mesh refinement for shock hydrodynamics. *J. Comput. Phys.*, 82(1):64–84.

Berger, M. J. and Oliger, J., 1984. Adaptive mesh refinement for hyperbolic partial-differential equations. *J. Comput. Phys.*, 53(3):484–512.

Brouillette, M. and Sturtevant, B., 1994. Experiments on the Richtmyer-Meshkov instability: single-scale perturbations on a continuous interface. *J. Fluid Mech.*, 263:271–292.

Browning, G., Kreiss, H.-O., and Oliger, J., 1973. Mesh refinement. *Math. Comput.*, 27(121):29–39.

Butcher, J. C., 2003. *Numerical Methods for Ordinary Differential Equations*, pages 86–88. Hoboken, NJ: J. Wiley.

Carlès, P. and Popinet, S., 2001. Viscous nonlinear theory of Richtmyer-Meshkov instability. *Phys. Fluids.*, 13(7):1833–1836.

Carpenter, M. H., Gottlieb, D., and Abarbanel, S., 1993. The stability of numerical boundary treatments for compact high-order finite-difference schemes. *J. Comput. Phys.*, 108:272–295.

Carpenter, M. H., Gottlieb, D., and Abarbanel, S., 1994. Time-stable boundary conditions for finite difference schemes solving hyperbolic systems: Methodology and application to high-order compact schemes. *J. Comput. Phys.*, 111(2):220–236.

Cathers, B. and Bates, S., 1995. Spurious numerical refraction. *Int. J. Numer. Meth. Fluids*, 21:1049–1066.

Choi, D.-I., Brown, J. D., Imbiriba, B., Centrella, J., and MacNeice, P., 2004. Interface conditions for wave propagation through mesh refinement boundaries. *J. Comput. Phys.*, 193(2):398–425.

Ciment, M., 1971. Stable difference schemes with uneven mesh spacings. *Math. Comput.*, 25(114):219–227.

Ciment, M., 1972. Stable matching of difference schemes. *SIAM J. Numer. Anal.*, 9(4):695–701.

Collino, F., Fouquet, T., and Joly, P., 2003. A conservative space-time mesh refinement method for the 1-D wave equation. Part II: Analysis. *Numer. Math.*, 95:223–251.

Collins, B. D. and Jacobs, J. W., 2002. PLIF flow visualization and measurements of the Richtmyer-Meshkov instability of an air/SF_6 interface. *J. Fluid Mech.*, 464:113–136.

Drazin, P. G. and Reid, W. H., 2004. *Hydrodynamic stability.* New York: Cambridge University Press.

Duff, R. E., Harlow, F. H., and Hirt, C. W., 1962. Effects of diffusion on interface instability between gases. *Phys. Fluids.*, 5(4):417–425.

Engquist, B. and Sjögreen, B., 1998. The convergence rate of finite difference schemes in the presence of shocks. *SIAM J. Numer. Anal.*, 35(6):2464–2485.

Erpenbeck, J. J., 1962. Stability of step shocks. *Phys. Fluids.*, 5(10):1181–1187.

Ferm, L. and Lötstedt, P., 2004. Accurate and stable grid interfaces for finite volume methods. *App. Num. Math.*, 49:207–224.

Fornberg, B., 1988. Generation of finite-difference formulas on arbitrarily spaced grids. *Math. Comput.*, 51:699–706.

Gerritsen, M. and Olsson, P., 1998. Designing and efficient solution strategy for fluid flows: II. Stable high-order central finite difference schemes on composite adaptive grids with sharp shock resolution. *J. Comput. Phys.*, 147(2):293–317.

Gustafsson, B., 1975. The convergence rate for difference approximations to mixed initial boundary value problems. *Math. Comput.*, 29(130):396–406.

Gustafsson, B., Kreiss, H.-O., and Sundström, A., 1972. Stability theory of difference approximations for mixed initial boundary value problems. II. *Math. Comput.*, 26(119):649–686.

Herrmann, M., Moin, P., and Abarzhi, S. I., 2008. Nonlinear evolution of the Richtmyer-Meshkov instability. *J. Fluid Mech.*, 612:311–338.

Hill, D. J., Pantano, C., and Pullin, D. I., 2006. Large-eddy simulation and multiscale modelling of a Richtmyer-Meshkov instability with reshock. *J. Fluid Mech.*, 557:29–61.

Hill, D. J. and Pullin, D. I., 2004. Hybrid tuned center-difference-WENO method for large eddy simulations in the presence of strong shocks. *J. Comput. Phys.*, 194:435–450.

Honein, A. E. and Moin, P., 2004. Higher entropy conservation and numerical stability of compressible turbulence simulations. *J. Comput. Phys.*, 201:531–545.

Jameson, L., 2003. AMR vs high order schemes. *J. Sci. Comp.*, 18(1):1–24.

Jones, M. A. and Jacobs, J. W., 1997. A membraneless experiment for the study of Richtmyer-Meshkov instability of a shock-accelerated gas interface. *Phys. Fluids.*, 9(10):3078–3085.

Kramer, R. M. J., Pantano, C., and Pullin, D. I., 2007. A class of energy stable, high-order finite-difference interface schemes suitable for adaptive mesh refinement of hyperbolic problems. *J. Comput. Phys.*, 226:1458–1484.

Kreiss, H.-O. and Scherer, G., 1974. Finite element and finite difference methods for hyperbolic partial differential equations. In *Mathematical Aspects of Finite Elements in Partial Differential Equations*. New York: Academic Press.

Landau, L. D. and Lifshitz, E. M., 1959. *Fluid Mechanics*, pages 325–329. London: Pergamon.

Lele, S. K., 1992. Compact finite difference schemes with spectral-like resolution. *J. Comput. Phys.*, 103:16–42.

Lomax, H., Pulliam, T. H., and Zingg, D. W., 2001. *Fundamentals of Computational Fluid Dynamics*. New York: Springer.

Lombardini, M., 2008. Richtmyer-Meshkov instability in converging geometries. Ph.D. thesis, California Institute of Technology.

Lötstedt, P., Söderberg, S., Ramage, A., and Hemmingsson-Frändén, L., 2002. Implicit solution of hyperbolic equations with space-time adaptivity. *BIT*, 42(1):134–158.

Mattsson, K. and Nordström, J., 2004. Summation by parts operators for finite difference approximations of second derivatives. *J. Comput. Phys.*, 199:503–540.

Meshkov, E. E., 1969. Instability of the interfce of two gases accelerated by a shock wave. *Soviet Fluid Dyn.*, 4(5):151–157.

Mikaelian, K. O., 1991. Density gradient stabilization of the Richtmyer-Meshkov instability. *Phys. Fluids A*, 3(11):2638–2643.

Mikaelian, K. O., 1993. Effect of viscosity on Rayliegh-Taylor and Richtmyer-Meshkov instabilities. *Phys. Rev. E*, 47:375–383.

Nordström, J. and Carpenter, M. H., 1999. Boundary and interface conditions for high-order finite-difference methods applied to the Euler and Navier-Stokes equations. *J. Comput. Phys.*, 148:621–645.

Nordström, J. and Gustafsson, R., 2003. High order finite difference approximations of electromagnetic wave propagation close to material discontinuities. *J. Sci. Comp.*, 18(2):215–234.

Pantano, C., Deiterding, R., Hill, D. J., and Pullin, D. I., 2007. A low numerical dissipation patch-based adaptive mesh refinement method for large-eddy simulation of compressible flows. *J. Comput. Phys.*, 221(1):63–87.

Richtmyer, R. D., 1960. Taylor instability in shock acceleration of compressible fluids. *Comm. Pure Appl. Math.*, 13:297–319.

Scherer, G., 1977. On energy estimates for difference approximations to hyperbolic partial differential equations. Ph.D. thesis, Department of Scientific Computing, Uppsala University.

Sebastian, K. and Shu, C.-W., 2003. Multidomain WENO finite difference method with interpolation at subdomain interfaces. *J. Sci. Comp.*, 19(1):405–438.

Strand, B., 1994. Summation by parts for finite difference approximations for d/dx. *J. Comput. Phys.*, 110(1):47–67.

Svärd, M., Carpenter, M. H., and Nordström, J., 2007. A stable high-order finite difference scheme for the compressible Navier-Stokes equations, far-field boundary conditions. *J. Comput. Phys.*, 225:1020–1038.

Trefethen, L. N., 1985. Stability of finite-difference models containing two boundaries or interfaces. *Math. Comput.*, 45(172):279–300.

Vichnevetsky, R., 1987. Wave propagation and reflection in irregular grids for hyperbolic equations. *App. Num. Math.*, 3:133–166.

Whitham, G. B., 1974. *Linear and Nonlinear Waves*. New York: Wiley.

Wouchuk, J. G., 2001a. Growth rate of the linear Richtmyer-Meshkov instability when a shock is reflected. *Phys. Rev. E*, 63(5):056303.

Wouchuk, J. G., 2001b. Growth rate of the Richtmyer-Meshkov instability when a rarefaction is reflected. *Phys. Plasmas*, 8(6):2890–2907.

Wouchuk, J. G. and Nishihara, K., 1997. Asymptotic growth in the linear Richtmyer-Meshkov instability. *Phys. Plasmas*, 4(4):1028–1038.

Yang, Y., Zhang, Q., and Sharp, D. H., 1994. Small amplitude theory of Richtmyer-Meshkov instability. *Phys. Fluids.*, 6(5):1856–1873.

Yee, H. C. and Sjögreen, B., 2007. Simulation of Richtmyer-Meshkov instability by sixth-order filter methods. *Shock Waves*, 17:185–193.

Zhang, Q. and Sohn, S., 1997. Nonlinear theory of unstable fluid mixing driven by shock wave. *Phys. Fluids.*, 9(4):1106–1124.